

Monoscopic Analysis of H.E.S.S. Phase II Data on PSR B1259–63/LS 2883

DISSERTATION

zur Erlangung des akademischen Grades

Dr. rer. nat.
im Fach Physik

Spezialisierung:
Experimentalphysik

eingereicht an der
Mathematisch-Naturwissenschaftlichen Fakultät
Humboldt-Universität zu Berlin

von

M. Sc. Thomas Murach

Präsident der Humboldt-Universität zu Berlin:
Prof. Dr.-Ing. Dr. Sabine Kunst

Dekan der Mathematisch-Naturwissenschaftlichen Fakultät:
Prof. Dr. Elmar Kulke

Gutachter:

1. Prof. Dr. Thomas Lohse
2. Prof. Dr. Adrian Biland
3. Prof. Dr. Elisa Bernardini

eingereicht am: 30.09.2016

Tag der mündlichen Prüfung: 23.05.2017

Abstract

Imaging atmospheric Cherenkov telescope (IACT) arrays can detect the faint Cherenkov light emitted by air showers that were created by interactions of cosmic very-high-energy (VHE, with energies of $\mathcal{O}(100\text{ GeV})$ – $\mathcal{O}(100\text{ TeV})$) particles with atomic nuclei in the Earth’s atmosphere. While aiming for the detection of Cherenkov light emitted by gamma ray-initiated air showers, the vast majority of all detected showers are initiated by charged cosmic rays, which hence provide the dominant background. The most successful IACT to date is the H.E.S.S. observatory in Namibia. Starting regular observations in 2004 with four telescopes with reflector areas of approximately 100 m^2 each, a much larger fifth telescope was added to the centre of the four other telescopes in 2012. Due to the very large mirror area of approximately 600 m^2 , the energy threshold of this telescope is the lowest of all IACTs.

In this dissertation, a fast algorithm is presented that can reconstruct fundamental properties of the primary VHE gamma rays like their direction or their energy based on the distribution of measured intensities in the camera of the new telescope. Furthermore, this algorithm, which is called MonoReco, can distinguish between air showers initiated either by gamma rays or by charged cosmic rays. All those tasks are accomplished with the help of artificial neural networks, which use moments of the intensity distributions as input. At zenith angles of 0° , the resulting energy threshold is as low as 59 GeV , and at zenith angles of 40° it is 178 GeV . Depending on the energy and the pointing position of the telescope, angular resolutions of 0.1° – 0.3° are reached. In case of the energy reconstruction, the bias is usually at the level of a few percent, with large bias values occurring only at the edges of this energy range. The energy resolution is at the level of 20% – 30% . Steady sources of VHE gamma-ray emission can be detected with a significance of 5σ within 50 h of observations if their flux reaching Earth is at least 2% of the flux of the Crab Nebula.

With the MonoReco algorithm, data taken around the 2014 periastron passage of the gamma-ray binary PSR B1259–63/LS 2883 were analysed. Among the small group of gamma-ray binaries, five sources are established and two additional candidates were identified recently. PSR B1259–63/LS 2883 is the only member of this group for which the nature of the compact is known. In this case it is a neutron star in an orbit with a period of 3.4 yr around a massive star with a circumstellar disk consisting of gas and plasma. For the first time the differential photon spectrum of this source could be measured down to below 200 GeV with H.E.S.S. Furthermore, fluxes could be measured very close to periastron for the first time, exhibiting a local flux minimum at this time. Also certain times during the flare observed in the high-energy gamma-ray band (with photon energies between $\mathcal{O}(100\text{ MeV})$ and $\mathcal{O}(100\text{ GeV})$) were sampled for the first time contemporaneously to observations with *Fermi*-LAT. Both at this time and also shortly before the first crossing of the neutron star through the disk, high flux states were observed, with flux levels being comparable to the maximum fluxes measured around the disk crossings. A good agreement between measured energy fluxes and predictions of a leptonic model is found.

Kurzfassung

Abbildende atmosphärische Cherenkov-Teleskope (IACTs) sind in der Lage, das schwache Cherenkovlicht aus Teilchenschauern zu detektieren, die bei Kollisionen von sehr hochenergetischen (mit Energien von $\mathcal{O}(100 \text{ GeV})$ – $\mathcal{O}(100 \text{ TeV})$), kosmischen Teilchen mit Atomkernen in der Erdatmosphäre produziert werden. Das Ziel ist die Detektion von Cherenkovlicht aus Schauern, die von Gammastrahlen erzeugt wurden, jedoch stammt der größte Teil der Schauer von geladenen Teilchen, die somit den dominanten Untergrund bilden. Das bisher erfolgreichste IACT ist das in Namibia befindliche H.E.S.S.-Observatorium. Reguläre Observationen begannen im Jahr 2004 mit vier Teleskopen mit Spiegelflächen von je circa 100 m^2 . Im Jahr 2012 wurde das Observatorium um ein fünftes Teleskop mit einer Spiegelfläche von circa 600 m^2 ergänzt. Aufgrund dieser großen Spiegelfläche besitzt dieses Teleskop die niedrigste Energieschwelle aller IACTs.

In dieser Dissertation wird ein schneller Algorithmus präsentiert, der grundlegende Eigenschaften der Gammastrahlen wie ihre Energien und Ankunftsrichtungen mithilfe der gemessenen Intensitätsverteilungen in der Kamera des neuen Teleskops rekonstruieren kann. Dieser MonoReco genannte Algorithmus kann weiterhin zwischen Schauern unterscheiden, die von Gammastrahlen bzw. geladenen Teilchen der kosmischen Strahlung initiiert wurden. Diese Aufgaben werden mit mithilfe von künstlichen neuronalen Netzwerken erfüllt, welche die Momente der Intensitätsverteilungen analysieren. Bei Zenitwinkeln von 0° liegt die resultierende Energieschwelle bei 59 GeV , bei 40° liegt sie bei 178 GeV . Abhängig von der Energie und von der Beobachtungsrichtung des Teleskops werden Richtungsauflösungen von 0.1° – 0.3° erreicht. Die systematische Abweichung der Energierekonstruktion liegt meist bei einigen Prozent. Nur am Rand des der Rekonstruktion zugänglichen Energiebereichs sind größere Abweichungen vorzufinden. Die Energieauflösung liegt bei 20% – 30% . Stetige Gammastrahlungsquellen können innerhalb von Beobachtungszeiten von 50 h mit einer statistischen Signifikanz von 5σ detektiert werden, wenn ihr Fluss auf der Erde mindestens 2% des Krebsnebelflusses entspricht.

Mit dem MonoReco-Algorithmus wurden Daten, die in der Zeit um das Periastron des Gammastrahlungs-Binärsystems PSR B1259–63/LS 2883 im Jahre 2014 genommen wurden, analysiert. Zur kleinen Gruppe dieser Binärsysteme gehören fünf Quellen sowie zwei kürzlich identifizierte Kandidaten. Nur für PSR B1259–63/LS 2883 ist die Art des kompakten Objekts bekannt. Es handelt sich um einen Neutronenstern, der sich in einem 3,4-Jahres-Orbit um einen massereichen Stern mit einer den Stern umgebenden Scheibe aus Gas und Plasmen befindet. Zum ersten Mal konnte H.E.S.S. das Spektrum bei Energien unterhalb von 200 GeV messen. Weiterhin konnte die Quelle zum ersten Mal sehr nah am Periastron selbst beobachtet werden, wobei zu dieser Zeit ein lokales Flussminimum gemessen wurde. Auch zu bestimmten Zeiten während des sehr hohen Flusses im hochenergetischen Gammastrahlungsbereich (zwischen $\mathcal{O}(100 \text{ MeV})$ und $\mathcal{O}(100 \text{ GeV})$) wurden zum ersten Mal Daten gleichzeitig mit H.E.S.S. und *Fermi*-LAT genommen. Sowohl zu dieser Zeit als auch kurz vor dem ersten Durchqueren des Neutronensterns durch die Scheibe wurden Flüsse gemessen, die vergleichbar hoch waren wie die maximalen Flüsse nach den Scheibendurchquerungen. Ein Vergleich der gemessenen Flüsse mit Vorhersagen eines leptonischen Modells zeigt gute Übereinstimmungen.

Contents

1	Introduction	1
2	Gamma-Ray Astronomy	3
2.1	Cosmic-Ray Physics	4
2.2	Charged Particle Acceleration	6
2.3	Cosmic Ray Propagation	9
2.4	VHE Gamma-Ray Production	10
2.5	VHE Gamma-Ray Propagation	14
2.6	Astrophysical Sources of VHE Gamma Rays	14
2.6.1	Supernova Remnants	14
2.6.2	Pulsar Wind Nebulae	14
2.6.3	Active Galactic Nuclei	15
2.6.4	Other Source Classes	15
2.7	Gamma-Ray Binaries	16
2.8	PSR B1259–63/LS 2883	18
2.8.1	Neutron Stars	20
2.8.2	LS 2883	24
2.8.3	Radio Observations	25
2.8.4	Optical Observations	26
2.8.5	X-Ray Observations	26
2.8.6	High-Energy Gamma-Ray Observations	29
2.8.7	Very-High-Energy Gamma-Ray Observations	29
2.8.8	Models of the System	30
2.9	Detection of Gamma Rays	33
3	The H.E.S.S. Experiment	39
3.1	The Atmosphere	39
3.2	The H.E.S.S. Phase I Telescopes	41
3.3	The H.E.S.S. Phase II Telescopes	43
3.4	The Central Data Acquisition System	44
3.5	Calibration of the Data	47
4	Monoscopic Reconstruction	51
4.1	Monte Carlo Simulations of Gamma-Ray Air Showers	52
4.2	Artificial Neural Networks	56
4.3	Direction Reconstruction	62
4.4	Energy Reconstruction	66

Contents

4.5	Particle Identification	67
4.6	Cut Optimisation	72
4.7	Interpolation	78
5	Reconstruction Performance	81
5.1	Direction Reconstruction Performance	81
5.2	Energy Reconstruction Performance	86
5.3	Particle Discrimination Performance	89
5.4	Effective Area	90
5.5	Radial Acceptance	92
5.6	Sensitivity	94
5.7	Analysis of Observations of the Crab Nebula	98
6	Analysis of the 2014 PSR B1259–63/LS 2883 Data	103
6.1	Source Morphology	106
6.2	Spectrum	115
6.3	Variability	121
6.4	Discussion	128
6.4.1	Multi-Wavelength Spectral Energy Distribution	128
6.4.2	VHE Gamma-Ray Luminosity	130
6.4.3	Multi-Wavelength Light Curve	132
6.4.4	Comparison of Energy Fluxes with Model Predictions	134
6.4.5	Future Improvements	138
7	Conclusion	139

1 Introduction

In the years 1911 and 1912, Victor Franz Hess conducted several balloon flights up to heights of more than 5300 m, in an endeavour to measure the level of ionising radiation as a function of the height with the help of an electrometer [1]. Contrary to the common belief at that time, the level of such radiation did not decrease with increasing altitude, but it increased, excluding the decay of radioactive isotopes in the crust of the Earth as the primary source of this radiation. Also the sun could be excluded as the principal source, since the level of ionisation did not decrease when measured during a partial solar eclipse. Hence it was concluded that this ionising radiation must have its origin in outer space. For the discovery of this extraterrestrial nature of what is now referred to as cosmic rays, Victor Hess was awarded the Nobel Prize in Physics in 1936. Thorough studies of the secondary particles created by interactions of the cosmic rays with the atoms and molecules in the atmosphere lead to the discovery of several new particles like the positron, the muon, the pion or the kaon, contributing significantly to the progress of the young field of research of particle physics in the 1930s and 1940s. Despite the great success of experimental physics initiated by the discovery of cosmic rays more than 100 years ago, the question of the origin of cosmic rays is still not answered conclusively. The main reason for this is that over the largest part of the range of energies of cosmic rays, which extends over more than eleven orders of magnitude, the charged cosmic rays are deflected sufficiently by galactic and intergalactic magnetic fields to prevent tracing them back to their origins.

To resolve the long-standing enigma of the origin of cosmic rays, new detection techniques relying on different types of messenger particles were established. Gamma rays are good candidates for this, since they are neutral particles which are not deflected by magnetic fields. In this work, especially gamma rays with energies higher than approximately 100 GeV will be discussed. These can be produced via several processes from charged particles with even higher energies close to the acceleration site of the latter. By detecting the Cherenkov light emitted by secondary particles created by scattering processes of such gamma rays with atomic nuclei in the atmosphere, the energy and direction of the primary particles can be reconstructed accurately. Current-generation detectors have angular resolutions of approximately 0.07° , allowing for identifications of individual sources. After the initiation of this young field of astronomy in the late 1980s and 1990s, a wealth of more than 170 new gamma-ray sources was discovered by observatories like the High Energy Stereoscopic System (H.E.S.S.) [2; 3]. The most extreme objects in the universe belong to those sources, including neutron stars, remnants of supernova explosions, supermassive black holes in the centres of galaxies or binary systems consisting of massive stars and neutron stars or black holes. By detecting the non-thermal gamma-ray emission from such objects and characterising their

1 Introduction

various properties, gamma-ray astronomy has become an independent and vibrant field of research with a scope extending far beyond the determination of the origin of cosmic rays.

In Chap. 2, an overview over the physics of cosmic rays and VHE gamma rays is presented, including the acceleration of charged particles up to highest energies and the creation of gamma rays by those particles. The particular source class of gamma-ray binaries and especially the binary system PSR B1259–63/LS 2883 will be introduced in more detail. General concepts of detecting gamma rays will also be explained in this chapter.

The experimental setup of the H.E.S.S. telescope system is described in detail in Chap. 3. The new, large telescope added to the H.E.S.S. array in 2012 will be introduced in more detail, since data from this telescope is the subject of later chapters.

A new algorithm capable of reconstructing fundamental parameters of individual gamma rays from the data collected by the new, large telescope alone is presented in Chap. 4. This algorithm, which is called MonoReco, is based on the use of artificial neural networks. With the help of this algorithm, the energy range accessible for the H.E.S.S. array can be extended to unprecedentedly low energies. In Chap. 5, the performance of this algorithm is discussed in detail. Also an analysis of data obtained from observations of the Crab Nebula is presented to illustrate the good performance of the MonoReco algorithm.

In Chap. 6, an analysis of data taken around the 2014 periastron passage of the binary system PSR B1259–63/LS 2883 using both the MonoReco algorithm and stereoscopic algorithms is presented. In particular the light curve will be discussed, also in the context of results from other parts of the electromagnetic spectrum. Furthermore, the results are compared with model predictions.

2 Gamma-Ray Astronomy

Since the discovery of cosmic rays in 1912, the fields of astroparticle physics and especially gamma-ray astronomy have evolved greatly. In this chapter, special attention will be paid to high-energy (HE) gamma rays with energies between $\mathcal{O}(100 \text{ MeV})$ and $\mathcal{O}(100 \text{ GeV})$ and very-high-energy (VHE) gamma rays in the range of $\mathcal{O}(100 \text{ GeV})$ – $\mathcal{O}(100 \text{ TeV})$.

The Crab Nebula, the first astrophysical object from which VHE emission was detected, was discovered in this energy range in 1989 by Weekes et al. [4]. Since then, a total of 176 sources have been detected at VHEs, firmly establishing a new field of astronomy. 103 of these objects have been discovered in the VHE regime by the H.E.S.S. experiment. Approximately 50 of these sources have been identified as active galactic nuclei (AGN), 34 have been identified as pulsar wind nebulae (PWNe) and 24 as supernova remnants (SNRs) [5]. 35 objects are still unidentified, mostly because no counterparts at other wavelengths have been detected. The remaining sources are of different types, like galaxy clusters, starburst galaxies, binary systems, stellar clusters or pulsars. These object classes will be described in more detail in Sec. 2.4 and, in case of binary systems, in Sec. 2.7.

Most of the galactic sources of VHE emission are located at a distance of order 1 kpc from Earth. A large fraction of them appear extended in instruments with angular resolutions of $\sim 5'$, which implies a scale for the size of the emission regions of order 10 pc [6]. Despite being emitters of VHE gamma rays, none of the known sources was found to be capable of accelerating hadrons up to energies of order 1 PeV. The only exception is the recently discovered source of hadrons with PeV energies in the galactic centre [7]. Furthermore, there is evidence for electrons accelerated to energies of about 100 TeV [8; 9] or even $\mathcal{O}(1 \text{ PeV})$ in the Crab Nebula [10].

In addition to individual sources of VHE emission, diffuse emission from the galactic plane has been searched for by the H.E.S.S. experiment, which is described in detail in Chap. 3. All photons not associated with known sources could be attributed to unresolved sources and to products of interactions of cosmic rays with diffuse matter and photon fields [11; 12]. In contrast to the lack of detected diffuse emission at VHEs, diffuse emission from the galactic plane dominates the sky at HEs [12]. The *Fermi*-LAT experiment, a satellite-borne HE gamma-ray observatory that will be described briefly in Sec. 2.9, reported that roughly 80% of all detected photons originate from the galactic diffuse emission in the respective energy range [5]. Of the more than 3000 sources detected at HEs (in this case between 100 MeV and 300 GeV) by *Fermi*-LAT within four years of observations, about one third are AGN. For another third, there is no counterpart at other wavelengths and the type of source is not clear. The largest galactic source class is represented by pulsars of which 147 have been identified. 68 sources have been identified as SNRs or PWNe [13; 14].

VHE gamma-ray emission from other types of objects or environments is also searched for. Most prominently, VHE gamma-ray emission from gamma ray bursts (GRBs) has not been discovered yet, although *Fermi*-LAT detected photons with energies up to 100 GeV from one GRB already [15] and although models predict emission up to the VHE regime [16]. Also VHE emission from dark matter annihilation has not been observed yet, which helped setting competitive upper limits on the dark matter annihilation cross section for dark matter particles with masses in the TeV range.

In the following sections, the basics of cosmic-ray physics and the acceleration and propagation of charged particles in astrophysical environments will be discussed. Afterwards the creation and propagation of VHE gamma rays will be explained. Special attention will be paid to gamma-ray emitting binary systems, in particular to PSR B1259–63/LS 2883. At the end of this chapter, the concepts of gamma-ray detection will be explained.

2.1 Cosmic-Ray Physics

The Earth's atmosphere is constantly hit by cosmic rays consisting of a variety of particles. The vast majority of 99.8% of these particles is charged, the rest consists of photons, which are called gamma rays at high energies. Approximately 1% are electrons and positrons, the rest is composed of atomic nuclei. Protons make up the largest fraction (87%), Helium nuclei contribute 12% and the remaining fraction consists of heavier nuclei [17]. The cosmic-ray composition varies with energy. At energies accessible to the H.E.S.S. experiment, between about 50 GeV to tens of TeV, the overall proton fraction is above 75% [18]. At the lower end of this range the Helium fraction is about 50 to 60%, and heavier elements have an effect similar to a 60% increased Helium rate on measurements of the cosmic ray flux with observatories like H.E.S.S. or MAGIC [19]. The influence of nuclei heavier than protons on measurements performed with such experiments is limited, because the nucleons within the nuclei presumably scatter independently and thus distribute the total energy of the nucleus among them [18; 20].

The cosmic-ray spectrum is shown in Fig. 2.1, which displays the differential diffuse particle flux as a function of the energy per nucleus. This is one of the most famous graphs in physics, depicting the remarkably regular power law-like drop-off of the cosmic-ray flux over at least eleven orders of magnitude in energy. The spectral index is approximately 2.7 below the so-called knee at 3 PeV where the spectral index softens to approximately 3.1. A second spectral break can be seen at the so-called ankle at about 3 EeV where the index hardens from 3.1 back to approximately 2.7.

Particles with energies above a few GeV but below the knee are believed to be of galactic origin. SNR shocks are thought to be the main source of these particles, with contributions from pulsars and PWNe [8; 22]. A typical supernova releases about 10^{51} erg as kinetic energy of ejecta. Due to shock acceleration, explained in more detail in Sec. 2.2, the energy is transferred to kinetic and thermal energy of particles of the interstellar medium (ISM). Given an average residence time of 10^7 yr of cosmic rays in the galaxy

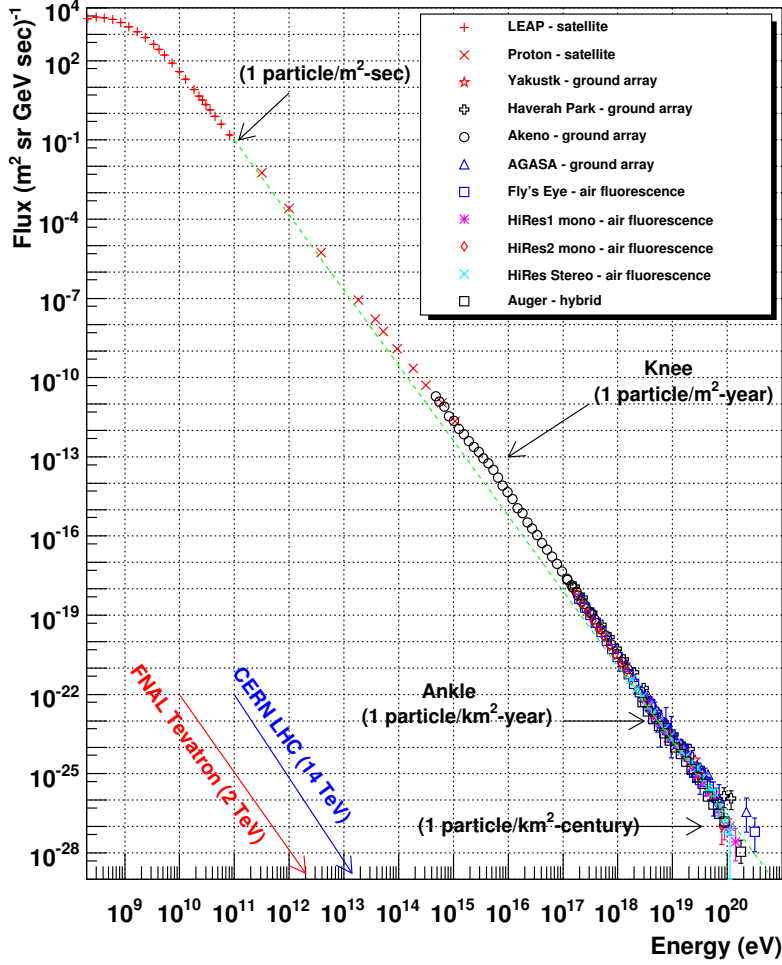


Figure 2.1: Differential diffuse cosmic ray flux as a function of the energy per nucleus. Different experiments have contributed data to this graph according to the respective energy ranges. The graph was taken from Hanlon [21].

and a cosmic ray energy density of approximately 1 eV/cm^3 , the total energy flux that has to be provided by cosmic ray sources is on the order of $5 \times 10^{40} \text{ erg/s}$. Given a supernova rate of two to three per century leads to the conclusion that about 10% of the energy released in a supernova need to be converted to cosmic rays to provide the estimated energy flux [6].

Particles with energies above the knee and below the ankle are thought to be of extragalactic origin because the galactic magnetic fields are so weak that the gyroradii of such high energy particles are larger than the galaxy itself. Therefore these particles escape from the galaxy, rendering the observable fluxes too low to be compatible with the spectrum shown in Fig. 2.1 [17]. Large extragalactic structures and higher magnetic fields found in extragalactic environments may allow for particle acceleration to higher energies [23]. AGN and their jets are prime candidates for such objects.

Ultra-high-energy cosmic rays (UHECRs) with macroscopic energies of $\gtrsim 100$ PeV are also thought to originate from AGN and AGN jets, as well as from GRBs or from galaxy merger shocks [10]. The origin of the spectral break at the ankle is still under debate. Above the ankle, the spectrum ends at $\lesssim 1$ ZeV despite instruments being sensitive enough at these energies. The lack of detections may have two reasons. The first one is the fact that even the most powerful particle accelerators in the universe might not be able to produce particles with energies higher than this threshold. The other one is related to the energy loss of particles on their way to the observer, resulting in the so-called Greisen–Zatsepin–Kuzmin (GZK) cut-off, which will be introduced briefly in Sec. 2.3.

2.2 Charged Particle Acceleration

Diffusive shock acceleration (DSA), also called first-order Fermi acceleration, is the prime candidate for particle acceleration in astrophysical contexts [10]. Historically, the so-called second-order Fermi acceleration [24] was proposed first. In this section, these processes and the emergence of cosmic-ray power-law spectra are described. Also alternative models will be introduced.

In the context of the second-order Fermi process, charged particles gain energy when interacting with interstellar or intergalactic plasma clouds containing magnetic fields. Assuming random motion of such clouds, the frequency of head-on collisions of particles with clouds exceeds the frequency of tail encounters, thus there is a net energy gain across many collisions [24; 23]. The downsides of this model are the long involved time scales for acceleration and the rather inefficient particle energy gain, which is proportional to $(\frac{u}{v})^2$, where u is the speed of the respective cloud and v is the much larger velocity of the particle [24; 25].

In contrast, the first-order Fermi acceleration occurs at collisionless plasma shock waves [23]. Shock fronts emerge whenever a supersonic flow collides with a flow of different direction or velocity such that the relative velocity is faster than the speed of sound in the medium. A sketch of such a configuration is shown in Fig. 2.2. The upstream flow with supersonic speed u_1 in the shock reference frame often originates from astrophysical objects like pulsar emitting relativistic winds or supernova remnants. The downstream flow of speed $u_2 \ll u_1$ could be matter from the interstellar medium or a stellar wind from a companion in a binary system. The shock front emerges where the pressures of the two flows balance each other, forming a contact discontinuity.

Particles of speed $v_0 \gg u_1$ diffuse in the upstream region of the shock due to collisions with magnetic turbulences in the plasma until they eventually cross the shock, effectively experiencing a plasma moving towards the particles with a velocity proportional to $|u_1 - u_2|$. In the downstream region they move diffusively as well. This diffusion leads to an isotropisation of their angular distributions in the corresponding plasma rest frame, leading to a net particle energy increase in the shock rest frame. The energy gain is always positive because the particles experience head-on collisions on both sides of the shock. The average relative energy gain of a particle over a full cycle from the upstream

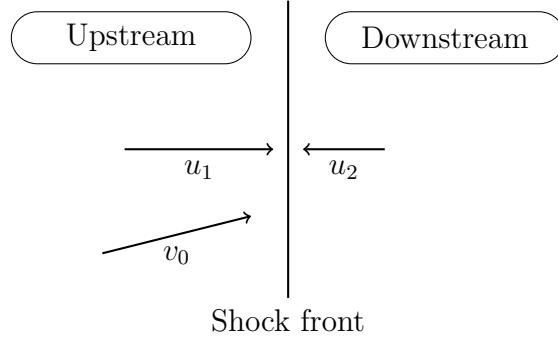


Figure 2.2: Sketch of a shock front between two flows of different directions and velocities u_1 and u_2 in the shock rest frame. The speed of a particle in the upstream region is denoted as v_0 .

region to the downstream region and back is

$$\left\langle \frac{\Delta E}{E} \right\rangle = \frac{4}{3} \frac{u_1 - u_2}{c}, \quad (2.1)$$

with c being the speed of light [26; 25; 27]. In this process, collisions with magnetic perturbations are dominant, Coulomb scattering is negligible [23]. Such perturbations in the upstream region are often plasma waves called Alfvén waves which have been generated by fast particles during their propagation through the plasma [28].

The probability P_{esc} with which particles can escape the shock region is

$$P_{\text{esc}} = 4 \frac{u_2}{rc}, \quad (2.2)$$

where $r = \frac{u_1}{u_2}$ is the shock compression ratio [26]. In this model, the escaped particles can be observed as cosmic rays. According to Eq. (2.2) the escape probability only depends on quantities which can, at first order, be assumed to be constant over time, thus a power-law spectrum

$$\frac{dN}{dE}(E) = N_0 \left(\frac{E}{E_0} \right)^{-\Gamma} \quad (2.3)$$

$$\text{with index } \Gamma \approx \frac{r+2}{r-1} \quad (2.4)$$

naturally emerges [6]. The speed of sound in the interstellar medium is on the order of a few km s^{-1} , which is very small compared to common shock front speeds u_s of thousands of km s^{-1} observed in supernova remnants [29]. For such high-Mach number shocks the compression ratio can be approximated to have the value 4, thus the spectral index is approximately $\Gamma \approx 2$. Assuming a spectral steepening of about 0.7 in the index Γ due to propagation effects, this is in good agreement with the observed cosmic ray spectral shape [10].

Several factors limit the maximal achievable particle energy. Finite shock lifetimes limit the maximum number of shock crossings, which is the dominant factor for accelerated hadrons, resulting in maximum energies well below the knee [6; 10]. In case of accelerated hadrons, weak magnetic fields can cause the gyroradii to be larger than the shock size, so that particles escape quickly. Then the maximum energy can be calculated as $E_{\max} \sim u_s^2 t_s B$. Here t_s is the age of the shock, u_s is the shock front speed in the ISM reference frame and B is the magnetic field strength. Energy losses due to radiation emission play a minor role for hadrons [14]. In case of electrons and positrons, from now on referred to as electrons only if not stated otherwise, energy loss via synchrotron radiation limits the maximum energy according to $E_{\max} \sim u_s B^{-1/2}$ [6]. In galactic environments like supernova remnants energies up to hundreds of TeV can be achieved.

In environments with at least one relativistic flow with $u_1 \gtrsim 0.1c$ the situation is more complicated. The assumption of isotropy is not valid in such cases, as the shock moves too fast for most particles to catch up with it. Therefore the escape probability is much larger in such cases, leading, together with relativistic boosting of particles crossing the shock, to different spectral indices than in the non-relativistic case described above [23].

Modern enhancements of the DSA theory consider the dynamical effects of the pressure induced by the cosmic rays themselves on the shock, the Alfvén wave generation by accelerated particles in the upstream flow and the dynamical amplification of the magnetic field. For example, a precursor shock can develop on the upstream side of the shock. In this precursor the particle density is increased, leading to a deceleration of fast particles [30]. The magnetic field in the vicinity of the shock are thought to be amplified due to fast particles moving through the plasma, causing the growth of resonant magnetic perturbations called streaming instabilities [10]. This way magnetic fields exceeding 100 μG can be created in the context of supernova remnant shocks [14]. Such high magnetic fields are needed to accelerate cosmic rays up to the knee.

A very different approach to particle acceleration is taken by the magnetic reconnection theory. Here acceleration is thought to happen in regions where two magnetic fluxes of opposite polarity encounter. In such cases the magnetic fields annihilate at a discontinuity surface, leading to the formation of a strong electric field. In this so-called current sheet, charged particles are accelerated normal to the magnetic field direction. Magneto-hydrodynamic (MHD) simulations are necessary to extract information about the energy spectra resulting from such configurations, which show that power-law cosmic ray spectra emerge. As encountering magnetic fields are a very frequent phenomenon in the universe, particle acceleration by magnetic reconnection is supposed to occur in a variety of sources and environments. If plasma turbulences are present in the reconnection area the acceleration is efficient, thus a part of the observed cosmic ray spectrum may be provided this way [31].

Every current model of astrophysical particle acceleration faces issues. The DSA theory results are derived for cases where energy losses during the acceleration process are negligible, which is very often not a valid assumption [29]. Also DSA is only efficient in accelerating electrons above energies of about 20 MeV. Below this threshold the electrons also cannot cross the shock, whose thickness usually corresponds to several ion gyroradii, equivalent to several thousand electron gyroradii [29]. Currently it is

unclear how electrons are accelerated up to that threshold energy [23]. Furthermore it is currently debated how particles can be accelerated up to energies significantly exceeding 100 TeV.

2.3 Cosmic Ray Propagation

The charged cosmic-ray particles observable on Earth have to travel from the place of their acceleration through the interstellar or intergalactic medium. During the propagation process, these particles are deflected by magnetic fields, such that the particles measured on Earth have lost most or all of their direction information, depending on the particle energy. Also the cosmic ray composition and energy spectrum may change due to interactions with atomic nuclei or photons. As the products of such spallation processes are, on average, lighter than the original particles, the fraction of light particles in the measured spectrum is most likely larger than in the original spectrum delivered from the sources of cosmic rays [17].

In all energy bands the question whether cosmic rays arriving on Earth are isotropic or not has been investigated. The average interstellar magnetic field strength of roughly $3 \mu\text{G}$ corresponds to Larmor radii of 0.4 kpc for protons with kinetic energies of 1 PeV [32; 33], which is much smaller than the size of the Milky Way. Therefore isotropy at energies below this value is expected as long as there are no cosmic ray sources very close to the solar system [34].

The origin of extragalactic magnetic fields is still debated. They might be leftovers of the early, primordial universe, or they might be created by jets of AGN, among other options. The field strength varies greatly, depending on the environment. In galaxy cluster cores field strengths of about 10^{-8} G can be reached, whereas in less dense areas the field strength is much weaker, on the order of 10^{-16} G – 10^{-9} G [32]. UHECRs, which are believed to be of extragalactic origin, can help to determine the properties of extragalactic magnetic fields by means of a tentative anisotropy. Indeed, the Yakutsk array has measured a hint of anisotropy above 10 EeV with a chance probability of observing a clustering of cosmic ray directions in case of actually isotropic cosmic rays of roughly 2% [35]. The Pierre Auger Observatory and the Telescope Array observatory have both reported anisotropies in a similar energy range. Below approximately 60 EeV there are hints of correlations with AGN positions with chance probabilities of 0.2% and 1.4%, respectively [36].

While propagating through the universe, UHECRs scatter with ambient photons, so that even in the coldest and emptiest regions of the universe the mean free path length of such particles is on the order of tens of Mpc [8]. The cosmic microwave background and magnetic fields are the dominant factors limiting UHECR propagation [32]. The GZK cut-off mentioned above is a result of such scattering processes, and the shape of the measured cut-off is in agreement with the hypothesis of uniformly distributed cosmic ray sources [36].

At lower energies, between tens of GeV and hundreds of TeV, both the Milagro and ARGO-YBJ experiments have reported large- and medium-scale anisotropy. One excess

and one deficit region have been identified in the sky. The anisotropy amplitudes are on the order of 10^{-4} – 10^{-3} only [33].

2.4 VHE Gamma-Ray Production

In Sec. 2.2, the acceleration of charged particles to high energies has been discussed. As mentioned earlier, these charged particles often lose their direction information during their propagation through the universe due to interaction with magnetic fields. Thus, in order to study properties of individual sources, observations utilising neutral messenger particles like neutrinos or photons are needed. In this section, the creation of VHE gamma rays in the vicinity of astrophysical objects will be explained.

Photons, as neutral particles, cannot gain energy by electric or magnetic fields directly. Instead they can gain energy by scattering processes with energetic particles, or they can be produced at high energies by means of various processes. Two general scenarios are adopted to explain the production of VHE gamma rays, which differ in the type of charged particles responsible for the creation of such gamma rays. These are called hadronic and leptonic scenario, where protons and electrons play the main roles, respectively.

In the hadronic scenario, VHE protons with energy E_p collide with other particles like photons from ambient photon fields or with other protons or nuclei. In such inelastic scattering processes, a multitude of secondary particles is produced. The number of secondary particles increases with E_p . Usually about one half of the energy of the VHE proton is carried away by a single nucleon during one scattering interaction. The remaining half is split among pions and other mesons. Among these, a fraction of roughly $\frac{1}{6}E_p$ is deposited into neutral pions. As each of these neutral pions decays into two photons with a probability of about 99%, roughly $\frac{1}{6}E_p$ is carried away by several gamma rays [6]. The resulting gamma ray flux is proportional to both the cosmic ray and target densities. The shape of the HE part of the emerging gamma-ray spectrum is equal to the shape of the hadronic energy spectrum, which usually is a power law $E^{-\Gamma}$ as explained above. The spectrum will also have a peak at half the neutral pion rest mass if the pion movement is isotropic, otherwise the peak position will be shifted towards higher energies due to relativistic boosting. A sketch of a typical hadronic spectral energy distribution (SED) is shown in Fig. 2.3. The high-energy peak caused by neutral pion decay can be clearly identified.

In the leptonic scenario, electrons produce gamma rays in several ways. Inverse Compton (IC) scattering is responsible for the highest-energy part of the gamma-ray spectrum. In this process, a relativistic electron upscatters a photon from the cosmic microwave background (CMB) or ambient infrared, optical or X-ray photon fields. The resulting gamma-ray flux is proportional to the electron density [6].

There are two different energy regimes in which the integrated Compton and IC scattering cross section can be approximated. In the low-energy regime, where the energy of the photon is small compared to the electron rest mass m_e in the rest frame of the electron, the cross section can be approximated as being energy-independent and identical

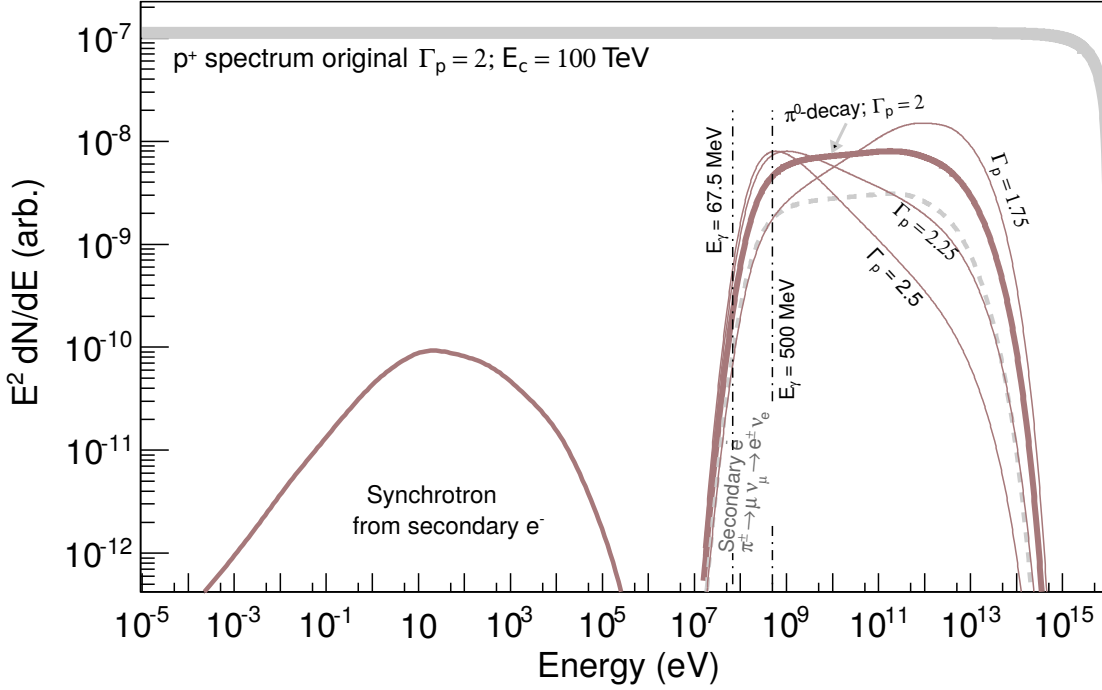


Figure 2.3: Sketch of a hadronic spectral energy distribution for a source of an age of 1000 yr. A magnetic field strength of $30 \mu\text{G}$ was assumed. At the top of the figure, the proton SED is shown. A spectral index of 2.0 and a cut-off energy of 100 TeV were assumed. The higher-energy peak of the gamma-ray SED is caused by π^0 decay. The shape of the peak depends on the proton spectral index Γ_p . The proton spectrum cut-off is reproduced by the gamma-ray spectrum. The much weaker low-energy peak is caused by synchrotron emission from secondary electrons which have been produced in the scattering processes between protons and target particles. Adapted from Funk [14].

to the classical Thomson cross section σ_T . At higher energies, where the abovementioned condition is not fulfilled anymore, the Klein-Nishina regime sets in. Then the cross section is modified according to the relation

$$\sigma_{\text{KN}} = \frac{3}{8} \sigma_T \frac{m_e c^2}{E_\gamma^0} \left(\ln \left(\frac{2E_\gamma^0}{m_e c^2} \right) + \frac{1}{2} \right). \quad (2.5)$$

Here E_γ^0 is the energy of the photon before the scattering. According to this formula, the IC process will be less efficient at scattering photons up to highest energies, leading to a steepening of the spectral energy distribution towards the VHE regime. At the same time this also means that the electrons lose less energy per shock crossing, so that they can reach higher energies [26]. The threshold at which the Klein-Nishina correction becomes significant depends on the energy of the target photons. For scattering of electrons with

photons from the CMB, the threshold is at approximately 300 TeV, while it is at 30 GeV for photons with wavelengths in the optical domain [6].

The energy of the scattered photon is on the order of $\gamma^2 E_\gamma^0$ in the Thomson approximation. In the Klein-Nishina regime, the photon is scattered such that it reaches, on average, an energy comparable to the electron rest mass in the rest frame of the highly relativistic electron. In the laboratory frame, this corresponds to an energy of $\gamma m_e c^2$, where γ is the Lorentz factor of the electron [26]. The resulting gamma-ray spectrum will show a spectral break in the transition regime between the two cross section domains. If the electron spectrum has a spectral index Γ_e , then the gamma-ray spectrum is harder than that in the Thomson regime, with the differential flux being proportional to $E^{-\frac{\Gamma_e+1}{2}}$ [37]. In the Klein-Nishina regime, the spectral index softens by $\Delta\Gamma \approx \frac{\Gamma_e}{2}$ [6]. Due to this spectral softening, a peak in the resulting gamma-ray spectral energy distribution is predicted. Assuming mono-energetic electrons with an energy E_e scattering on target photons with energies following, for example, a black-body spectral distribution, the resulting peak of the IC scattering gamma-ray spectrum will be located at an energy

$$E_{\text{IC}} = 5 \times 10^9 \frac{\langle E_\gamma^0 \rangle}{10^{-3} \text{ eV}} \left(\frac{E_e}{1 \text{ TeV}} \right)^2 \text{ eV}, \quad (2.6)$$

where $\langle E_\gamma^0 \rangle$ is the expectation value of the photon energy distribution [14].

An important factor for the shape of the resulting gamma-ray spectrum is the time after which the electrons lose their energy due to IC scattering processes. This cooling time $\tau = E_e / \dot{E}_e$ depends on the intensity U_{rad} of the radiation field and on the electron energy E_e like $\tau \propto (U_{\text{rad}} E_e)^{-1}$ in the Thomson regime. In the Klein-Nishina regime, the proportionality is modified by a factor $(1 + 40(E_e/1 \text{ TeV})(kT/1 \text{ eV}))^{-1.5}$, where k is the Boltzmann constant and T the temperature of the radiation field [6]. Due to this additional factor the cooling time increases in the Klein-Nishina regime, so that electrons lose their energy more slowly at higher energies.

Apart from IC scattering, electrons can emit photons via bremsstrahlung and synchrotron processes. When electrons interact with atomic nuclei in matter or dense plasmas, they emit bremsstrahlung photons. These photons can have up to one third of the energy of the electron, thus bremsstrahlung photons can reach VHEs [29]. The produced spectra follow a power-law distribution if the energy spectrum of the electrons follows one as well. Also the spectral index will be identical [6].

If electrons propagate within magnetic fields they will emit synchrotron emission. The energy of the synchrotron photons can be calculated as

$$E_{\text{sync}} = 0.2 \frac{B}{10 \mu\text{G}} \left(\frac{E_e}{1 \text{ TeV}} \right)^2 \text{ eV}, \quad (2.7)$$

where B is the magnetic fields strength. For a typical field strength of 10 μG in the vicinity of astrophysical acceleration sites and electrons with energies $E_e = 1 \text{ TeV}$, the synchrotron peak will be at around 0.2 eV. The spectral index of the synchrotron photons is $\Gamma_{\text{sync}} = \frac{\Gamma_e+1}{2}$ up to the peak, with Γ_e being the spectral index of the electron energy distribution [14]. Above the peak, the index softens to a value of $\Gamma_{\text{synchr}} = \frac{\Gamma_e+2}{2}$,

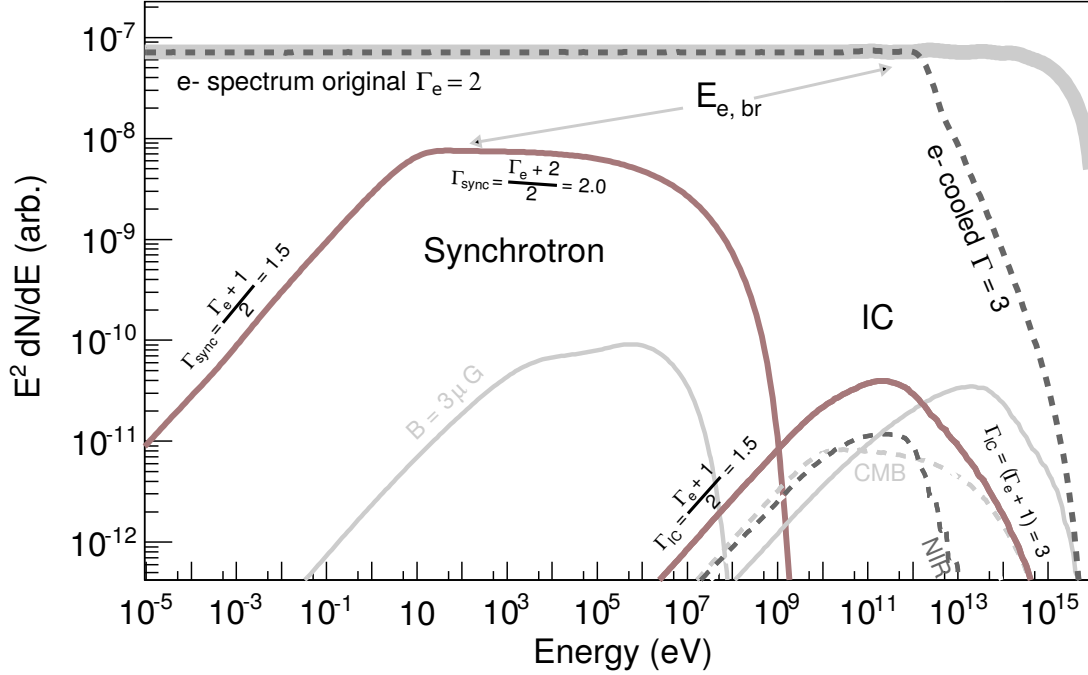


Figure 2.4: Sketch of a leptonic spectral energy distribution. At the top, an electron SED with a spectral index of 2 with a cut-off at 100 TeV is shown (grey band) together with an alternative scenario in which cooling effects are taken into account (dashed grey line). The IC gamma-ray peak is visible at high energies. Scenarios taking into account IC scattering of different photon fields are displayed as well. At low energies, a stronger and broader peak can be seen. The corresponding photons have been produced via synchrotron radiation. For both peaks, a source with an age of 1000 yr and a relatively high magnetic field strength of 100 μG has been assumed. An alternative scenario with a weaker magnetic field of 3 μG is shown as well in light grey. Adapted from Funk [14]

reproducing the break in the electron energy spectrum introduced by cooling effects. VHE electrons are needed to produce synchrotron radiation in the X-ray band. The emission in this regime thus depends on the highest-energy end of the electron spectrum [29]. The high-energy ends of both photon SED peaks depend on electron cooling. If the energy loss time scale is similar to the age of the source of accelerated electrons, then the electron index changes significantly above a break energy. This produces cut-offs or spectral breaks in the photon SEDs [6].

An example of an idealised leptonic SED is shown in Fig. 2.4. In this plot, the characteristic double-peak structure of leptonic SEDs caused by synchrotron radiation and IC scattering can be seen. Bremsstrahlung contributions are not visible due to the lack of dense material with which the VHE electrons could interact in the model calculations from which the curves above have been derived.

2.5 VHE Gamma-Ray Propagation

While propagating through the universe, the mean free path of VHE gamma rays is limited by interactions with photons from the extragalactic background light (EBL). The EBL consists of low-energy photons representing the red-shifted emission from the universe, integrated over the entire cosmic history. Thus the photons of this electromagnetic field have low energies, with spectral peaks at wavelengths on the order of micrometers. When these low-energy photons scatter off gamma rays, pairs of charged fermions like electrons and positrons are created, completely absorbing all the energy of the original VHE photon. For example, the range of a 100 GeV gamma ray corresponds to a redshift of $z \approx 1$, whereas the range of a 10 TeV gamma ray is only $z \approx 0.03$. At PeV energies, the gamma-ray range is limited to galactic distances [6].

2.6 Astrophysical Sources of VHE Gamma Rays

In the following sections, the production of gamma rays in several prominent types of astrophysical objects will be discussed briefly.

2.6.1 Supernova Remnants

As mentioned earlier, SNRs are believed to be dominant contributors to the observed cosmic ray spectrum. This hypothesis can be investigated by observations of SNRs in the gamma-ray regime. Observations of the peaks caused by pion decay would be a strong argument for the observed source being a hadron accelerator. Up to now two sources have been found which show such a spectral feature. The *Fermi*-LAT collaboration have discovered it in W44 and in IC 443 [38; 39]. In the latter SNR, the Agile collaboration [40] have seen the peak, too [41; 38]. Both sources are roughly 10 kyr old SNRs, the ejecta of which are interacting with a molecular cloud. In fact, most SNRs detected in the gamma-ray regime interact with such clouds [22]. From these observations it can be concluded that, at least to a certain fraction, cosmic rays are accelerated in SNRs and also that they can escape from the source [37].

Most observed SNR gamma-ray spectra are steeper than the spectra predicted by the DSA theory with an index of 2.0. In case of W44, the spectral index measured by *Fermi*-LAT is approximately 3 [22; 37]. Further investigations are needed to explore the origin of this discrepancy.

2.6.2 Pulsar Wind Nebulae

Pulsar wind nebulae form the most abundant source class of galactic gamma rays at TeV energies. They host the most relativistic shocks in nature, and direct evidence for particles with PeV energies exists only for this source class [42]. They consist of a neutron star (see Sec. 2.8.1 for details) which has been formed in a supernova explosion and a nebula around the neutron star. Most of the rotational energy of the neutron star is converted into kinetic energy of accelerated particles, which form the highly

magnetised pulsar wind. In case of young neutron stars and PWNe, the relativistic particle wind, which has Lorentz factors on the order of 10^4 – 10^6 , is confined by the SNR, which expands at much lower velocities of order 10^3 km s^{-1} . A shock forms where the ram pressures of the two flows balance each other, creating a region where particles can be accelerated efficiently up to TeV or PeV energies as explained in Sec. 2.2 [10; 42]. If the SNR has vanished already, the shock will form where the pulsar wind collides with the PWN formed in the past. The particles accelerated at such shocks are responsible for the majority of the nebular emission, while the luminosity of the pulsed emission from the pulsar is much lower. Via processes described above they can emit photons at all wavelengths. In PWNe, approximately 1%–10% of the total spin-down power of the pulsar can be emitted as gamma rays [5].

2.6.3 Active Galactic Nuclei

Most galaxies are believed to host supermassive black holes with millions or even billions of solar masses in their centres. Around some of these black holes accretion disks form, in which the infalling matter gathers and heats up. Perpendicular to the accretion disk plane, two collimated, highly relativistic outflows called jets emerge from the poles of the black holes. It is not clear how the formation of jets works in detail. The luminosity of the accretion disk together with the jet dominates the electromagnetic emission from the host galaxy, thus these objects are called active galactic nuclei (AGN). Most of the AGN detected at VHEs until now are blazars, a subset of AGN for which the direction of the jet corresponds to the line of sight of the observer [5].

The SEDs of most AGN exhibit a typical double-peak shape, similar to the SEDs shown in Fig. 2.3 or Fig. 2.4. The luminosities of AGN are not constant in time but show variability on all time scales down to minutes [8]. In some AGN, the spectral shape changes with luminosity. The VHE emission is thought to be produced by blobs of high-energy particles moving along the jets, thereby forming shock fronts within the jet. Several models exist trying to explain the acceleration of these blobs, including shock-wave acceleration in MHD turbulences within the jet and centrifugal acceleration along the rotating magnetic field found in the vicinity of the central black hole [6]. When electrons are injected into the blobs, rapid flares and variable light curves emerge naturally. The magnetic field strength within the blobs is thought to be on the order of 0.01 G–1 G, which is very high compared to the field strengths of order $10 \mu\text{G}$ reached in galactic objects. The particle content of the blobs is still disputed. Both leptonic and hadronic VHE gamma-ray emission scenarios are possible, although the observation of rapid flares strongly favours the former scenario.

2.6.4 Other Source Classes

There are several classes of sources of VHE gamma-ray emission which do not fit into the source classes mentioned above. One of them are starburst galaxies, which are galaxies with a star formation rate much higher than in other galaxy types. Due to the higher abundance of massive stars in such galaxies, the rate of supernovae is higher than in

Name	Compact Object	Companion	P_{orb}
PSR B1259–63/LS 2883	pulsar	Be star	1236.7 d
HESS J0632+057	unknown	Be star	315 d
LS I +61°303	unknown	Be star	26.5 d
1FGL J1018.6–5856	unknown	O star	16.6 d
LS 5039	unknown	O star	3.9 d
HESS J1832-093	unknown	unknown	unknown
CXOU J053600.0-673507	unknown	O star	10.3 d

Table 2.1: Overview over the five binary systems known to emit VHE gamma rays, together with two newly identified gamma-ray binary candidates listed in the two bottom rows. P_{orb} is the orbital period of the binary. Adapted from Dubus [45].

galaxies of comparable mass. This, together with collective wind effects, gives rise to the assumption that gamma-ray emission should be produced in such systems [26], of which only a few have been detected at VHEs so far. Similar reasoning applies to galaxy clusters and stellar clusters, of which several have been detected at VHEs [6; 3].

PWNe were introduced as emitters of VHE gamma rays already. However, the central source of these objects, the pulsars, very often exhibit a lack of pulsed VHE emission. Their spectra usually show a break at energies around a few GeVs, thus only very few of those, like the Crab pulsar and the Vela pulsar, have been detected at VHEs [14].

2.7 Gamma-Ray Binaries

A separate class of gamma-ray emitting objects are the so-called gamma-ray binaries. While about 70% of all stars in our galaxy are part of bound states of two or more stars [26], only few more than ten binary systems are known to emit HE gamma rays, and only five binary systems have been detected at VHE gamma rays. In addition, two new gamma-ray binary candidates were identified recently. Those two candidates will not be discussed further, instead the reader is referred to the literature [43; 44]. Because the emission above 1 MeV dominates the SEDs of these systems they are conventionally called gamma-ray binaries [45]. In the following, the term gamma-ray binary will refer to the VHE gamma ray emitting binaries only. The remaining five gamma ray emitting binaries known today are listed in Tab. 2.1. These sources have many properties in common. They all lie within 1° of the galactic plane, and they all consist of a compact object and a main sequence star with a mass of $\mathcal{O}(10)$ solar masses (M_\odot) and surface temperatures between 20×10^3 and 40×10^3 K. The nature of the compact object is known for PSR B1259–63/LS 2883 only, where it is a neutron star [46; 45]. In case of LS 5039 and LS I +61°303 there are hints for the existence of relativistic jets, indicating the presence of stellar-mass black holes. In this case the sources would belong to the class of microquasars. It should be noted, however, that other explanations for jet-like

structures are possible. For example a tail of shocked pulsar wind material extruded by the stellar wind pressure might mimick a jet [46]. Indeed, observations of LS I +61°303 revealed bursts similar to those expected from magnetars, a type of neutron stars with extremely strong magnetic fields [45]. Future observations will certainly help to clarify the nature of the compact objects in the respective four systems.

All systems show flux variability at all wavelengths over the course of one orbit, and some even show superorbital flux modulation such that there is a periodic change of flux levels over the course of many binary orbits [45; 47].

A striking difference between those systems is the duration of one orbit. The shortest orbit has been measured in the system LS 5039, which has an orbital period of less than 4 d. The longest period was found in PSR B1259–63/LS 2883, where one orbit takes approximately 3.4 yr. This already indicates that the compact object experiences very different environments in these systems. Compared to PSR B1259–63/LS 2883, the compact objects are much closer to the companion star in the other sources. Thus the much denser stellar wind that the compact objects experience would absorb a large fraction of pulsed emission if the compact objects were to be pulsars. Therefore the environment would prevent the detection of pulsed radio emission, complicating the object classification [45].

The multiwavelength spectra and light curves of gamma-ray binaries show several remarkable features. All systems have been detected in the radio wavelength regime. This is very unusual among the members of the related class of high-mass X-ray emitting binaries (HMXBs). These consist of a compact object and a massive companion star and exhibit an intensity maximum located in the X-ray regime. Only 9 out of 117 galactic HMXBs in the catalogue aggregated by Liu et al. [48] were found to emit radio waves. In case of gamma-ray binaries, this emission is attributed to synchrotron radiation [46].

Another interesting property is the fact that often the VHE spectra are not just simple extrapolations of the HE spectra, but features like spectral breaks are found [45]. Also the flux levels in these energy domains are not always correlated. In case of LS 5039, a clear anticorrelation was observed. Currently, there is no model which can explain all spectral and flux variability features [47].

The gamma-ray binary phase is believed to be an intermediate stage only. Supposedly these systems started as colliding wind binaries, of which Eta Carinae is a famous example, consisting of two very massive stars with tens of solar masses each. In the wind collision zone a shock can form, such that these systems are in principle able to accelerate particles to very high energies. Via IC scattering, gamma rays can be produced. Only one colliding wind binary system, Eta Carinae, was found to emit gamma rays so far [47]. Eventually, one of the two massive stars will end its life in a supernova explosion. The resulting compact object, often a neutron star, will then orbit the remaining massive star. The newly formed gamma-ray binary is believed to have a rather short life time of typically 10^5 yr– 10^6 yr, because a high spin-down luminosity only provided by young pulsars is needed for gamma-ray emission. This also explains why so few gamma-ray binaries were discovered so far. The emission of gamma rays in such binaries will be described below. In the last phase presented here, the neutron star will have slowed down its rotation. The pulsar wind pressure will have decreased enough to not prevent

accretion of stellar wind or stellar material into an accretion disk and eventually onto the neutron star surface anymore. Hence, an HMXB has been formed [46; 47]. At this point the evolution is not over, but out of scope for this thesis. For further information see, for example, the overview articles by Dubus [46], Lamberts [47] or Harding [49].

There are two scenarios for the explanation of gamma-ray emission from gamma-ray binaries, differing in the type of the compact object. If this is a black hole, then there will be strong X-ray emission originating from the accretion disk and VHE photons from the relativistic jet, similar to the mechanism occurring in AGN. If the binary hosts a pulsar, both the pulsar wind and the stellar wind will form a shock region where both wind pressures equalise. This contact discontinuity is the origin of VHE particles. Non-thermal electromagnetic emission is thought to be produced as synchrotron emission and via IC scattering [47]. More detailed models will be presented in context of the description of PSR B1259–63/LS 2883 in Sec. 2.8.8.

Gamma-ray binaries provide unique laboratories to test particle acceleration and interactions under different conditions in a single system. Often the radiation field of the companion star is known rather well, so that from the observed electromagnetic emission the properties of the HE particles can be probed directly [45]. Furthermore, pulsar winds are not visible in most wavelength bands because the electrons are tied to the magnetic field lines, preventing the emission of synchrotron radiation. In case of binaries, the bright stars close to the pulsars provide dense radiation fields on the order of 1 erg/cm^3 , so that the up-scattered photons can be measured, providing insight into the details of pulsar winds [6]. Also the involved length scales are much shorter than in isolated PWNe. For example, the extension of the Crab Nebula is on the order of 10 ly, whereas the maximum separation within PSR B1259–63/LS 2883 is on the order of 10 AU. Thus the high magnetic field strengths all involved particles encounter are on the order of mG up to several G, resulting in rapid energy losses of accelerated particles and hence high gamma-ray luminosities [6].

Observations at gamma-ray wavelengths are of particular importance because at these energies emission can be observed even when radio signals are hidden due to free-free absorption in stellar winds. Furthermore, the IC scattered stellar photons enable studies of the properties of the free pulsar wind, as mentioned earlier. Also the maximum energy particles can achieve in such contexts and the efficiency with which particles are accelerated can be extracted from observations of HE and VHE gamma ray [45]. By studying the flux variability, the timescales of the involved acceleration and radiation processes can be deduced, which further enhances the understanding of this source class.

2.8 PSR B1259–63/LS 2883

PSR B1259–63/LS 2883, also known under the name PSR J1302-6350/LS 2883 [50], has been observed at VHEs by the H.E.S.S. experiment around the times of periastron in 2004 [51], 2007 [52], 2010 [53] and 2014. An analysis of the 2014 data will be presented in Chap. 6. In the current section, the properties of this famous gamma-ray binary system will be presented together with models aiming to explain the emission mechanisms at

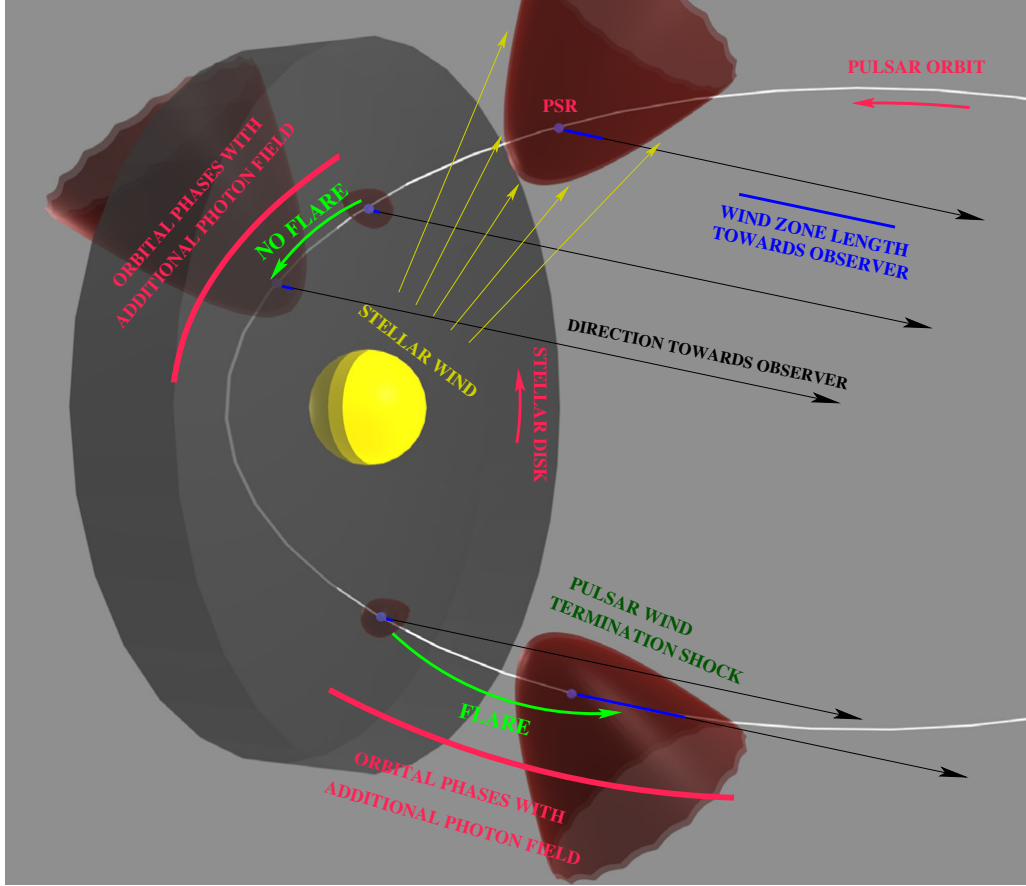


Figure 2.5: Sketch of the PSR B1259–63/LS 2883 binary system configuration. The pulsar orbits the star counterclockwise along the sketched white line. The shock structure is indicated in dark red. During most parts of the orbit, a bow-like structure is found, but during the disk crossings a cavity forms. The length of the pulsar wind zone in the direction of the observer is indicated as blue lines. Adapted from Khangulyan et al. [56].

work.

This binary system is thought to be part of the Cen OB1 stellar cluster, which is located at a distance of $d = 2.3$ kpc [54]. It consists of the pulsar PSR B1259–63 and a massive Be star called LS 2883 in an elliptic orbit with an eccentricity of $e = 0.87$ [55]. The configuration is sketched in Fig. 2.5. The stellar disk is inclined with respect to the orbital plane at an angle of approximately $\omega_D \approx 35^\circ$. The semimajor axis of the orbit deviates from the line of sight by approximately $i_O \approx 23^\circ$. Given the measured value of roughly 1300 light-seconds for the projected semimajor axis α , the true size of the orbital semimajor axis is approximately 6.5 AU [57]. Hence the distance between the two stars varies from 13 to 0.9 AU during the course of one orbit. Around periastron, the binary separation corresponds to approximately 24 stellar radii only. The radius

of the Be star disk, explained in more detail in Sec. 2.8.2, is approximately 25 stellar radii, thus the pulsar probes an environment with very dense matter and radiation fields [58; 50]. In that phase of the orbit, the radio pulsations are eclipsed for approximately 30 d due to free-free absorption [45]. The HE and VHE gamma-ray flux detected from the source increases significantly around periastron. VHE emission was predicted by Tavani and Arons [59] in 1997 already, which could be confirmed by the measurement with the H.E.S.S. observatory in 2004 [51].

In this section, first the two constituents of the binaries will be presented in some detail. Afterwards observational data from several wavelength bands gathered over the course of many orbits is presented. At the end, several approaches of modelling the emission of electromagnetic radiation from this source are presented.

2.8.1 Neutron Stars

Stars with masses exceeding $8 M_{\odot}$ end their lives in a supernova explosion when the thermal pressure from the vanishing nuclear fusion decreases, leading to a collapse of the core of the massive star. As a result of this collapse, the stellar core gets compressed until the gravitational pressure is balanced by the neutron degeneration pressure caused by the quantum-mechanical exclusion principle. When the outer parts of the star fall towards the core they are reflected and sent back outwards, where they collide with other, still infalling stellar envelopes. Thus a very dense and compressed shock wave propagates outwards, further accelerated due to interactions with neutrinos coming from the core. Initially, the velocity of these expanding envelopes is on the order of 10 % of the speed of light. During such an explosion, a total energy of about 10^{53} erg is released. About 1 % is carried away as kinetic energy of the expanding envelopes, and only 0.01 % are released as electromagnetic radiation. The vast majority of the entire energy is carried away by neutrinos [60].

Neutron stars as dense remainders of supernova explosions have been predicted in the 1930's already [61; 62]. Typically, their radii are of order 10 km, while the range of possible neutron star masses is $0.1 M_{\odot}$ – $2.5 M_{\odot}$. Neutron stars heavier than the given upper limit would transition to a black hole. Often neutron star masses are assumed to be $M_{\text{NS}} = 1.4 M_{\odot}$, which is adopted in this work as well. Given these estimates, the average neutron star density is on the order of 10^{15} g cm⁻³, equivalent to three times the density ρ_0 of heavy atomic nuclei [60]. The angular momentum and the magnetic field of the progenitor are preserved, thus the much smaller neutron star rotates rapidly and has a strong magnetic dipole field. Rotation periods lie in a range between approximately 1 ms and 10 s. The magnetic field strengths cover the range between 10^8 and 10^{15} G. A typical neutron star has a field strength of 10^{12} G [49; 60]. At early stages of a neutron star's life, the surface temperature can be as high as 10^{10} K– 10^{11} K. All these parameters depend on the formation history of the neutron star and on its age.

The origin of the strong magnetic field strengths is still under debate, as they cannot be derived from first principles. Several approaches exist, trying to explain the magnetic fields by compression of the progenitor star's magnetic field, differential rotation of layers within the star, convection or by thermodynamic effects, but no model can explain all

aspects of the observed variety of neutron star magnetic fields [60].

The structure of neutron stars is thought to be understood to some extent, although large uncertainties exist in the description of the innermost parts. At first approximation, they consist of a core and an envelope. The core is divided into an inner and an outer core, the envelope consists of a solid crust and a liquid ocean. Above the ocean, a layer called atmosphere can be found [60].

The atmosphere is only about 1 cm thick. It consists of a layer of plasma which emits the thermal part of the electromagnetic spectrum of the pulsar. This spectrum contains information about, among other properties, the surface temperature of the neutron star, the chemical composition and the magnetic field strength. The ocean layer is some tens of meters thick. It consists of atomic nuclei surrounded by degenerate electrons. The nuclei form a Coulomb liquid [60].

Below the ocean, the several kilometer thick crust is found, consisting of the solid outer crust and a superfluid inner crust. In the outer crust, the nuclei form a crystal structure. This is where the star's magnetic field is believed to be anchored [60; 63]. In the inner crust, the atomic nuclei are embedded in free neutrons and electrons. At the inner boundary of the inner crust, the nuclei form a homogeneous mass. Above this boundary, the nuclei exist as separate particles [60].

Neutron star cores have radii of several kilometers and matter densities of a few times ρ_0 . The nucleons in the outer core form a strongly interacting Fermi liquid, and here as well as in the inner core, pions and other mesons make up a fraction of the hadronic composition. This is energetically favourable because the Fermi energy of the core particles is very high, an order of magnitude higher than the kinetic thermal energy. This also leads to the conversion of nucleons to hyperons in the inner core, mediated by the weak force [60].

Most neutron stars known today have been found to emit radiation mainly in the form of two beams. If the directions of these beams deviate from the rotational axis and occasionally match the line of sight of an observer, this radiation is detected as pulsed emission. As an example, in case of the polar cap scenario introduced later, most of the radiation is emitted along the magnetic field axis sketched in Fig. 2.6. Pulsed emission was first discovered by Hewish et al. [64] in 1967. Today, more than 2400 pulsars have been identified by the detection of pulsed radio emission. Interestingly, only 230 of them were found to be part of a binary system [63]. At HEs, the fraction of detected pulsars in binaries increases to 55 out of 161 [45].

Pulsars have spin-down powers on the order of 10^{30} W– 10^{32} W, calculable as

$$\dot{E} = 4\pi^2 I \frac{\dot{P}}{P^3}. \quad (2.8)$$

P is the pulsar's rotational period, \dot{P} is the period change caused by the loss of rotational energy, and $I \approx 1 \times 10^{45}$ g cm² is the rotational momentum of inertia [26; 66]. In context, the sun releases about 10^{26} W in form of electromagnetic emission [67]. The emission spectrum is dominated by X-rays and gamma rays, while a fraction of only 10^{-4} – 10^{-6} is emitted at radio wavelengths [49; 63]. After pulsars have released most of their rotational energy, their luminosities decrease drastically, so that their pulses cannot be detected

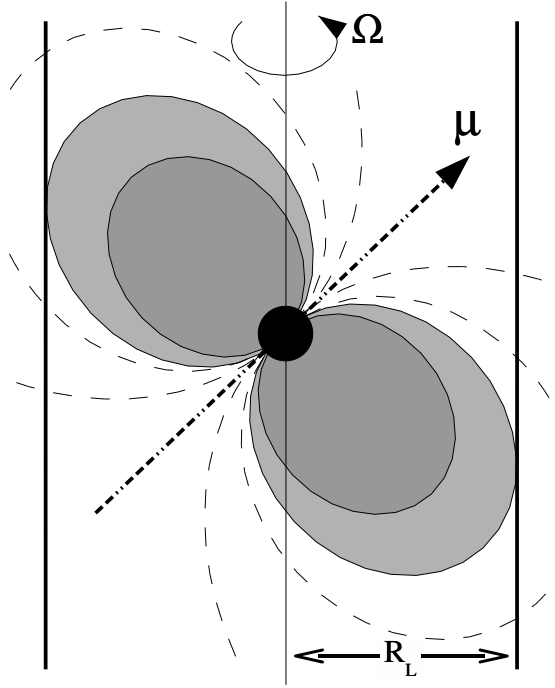


Figure 2.6: Sketch of a pulsar. The rotational axis Ω and the magnetic field axis μ are shown. Closed magnetic field lines are indicated by solid lines enclosing a grey area, open field lines are shown as dashed lines. The last open field line defines the location of the light cylinder at a distance R_L from the rotational axis. Figure taken from De Naurois [65].

anymore. It can be estimated that about 10^8 – 10^9 extinguished pulsars exist in the Milky Way [63; 68].

An important subject of pulsar emission models is the magnetosphere. This region around the neutron star is dominated by the strong magnetic field and the existence and creation of electron-positron pairs. The rotating magnetic field induces an electric field

$$\vec{E} = \vec{\Omega} \times \vec{r} \times \vec{B} \quad (2.9)$$

at the point \vec{r} . \vec{E} , \vec{B} and $\vec{\Omega}$ are the electric field, the magnetic field and the angular velocity, respectively [49]. The electric field strength is large enough to extract electrons and protons from the neutron star surface and to accelerate them to relativistic energies. For magnetic field axes with $\vec{\Omega} \cdot \vec{\mu} > 0$, electrons are extracted from regions close to the pole and protons are extracted from regions in the open magnetosphere closer to the equator. If the alignment condition given above is not fulfilled, electrons and protons switch origins [69]. Either way a charge separation emerges in the magnetosphere. Deflected by the magnetic fields, the electrons emit synchrotron radiation up to gamma-ray energies [60; 67]. These photons can create more electrons via pair production when interacting with the magnetic field [63]. About 10^4 – 10^7 pairs can be created by a single

electron extracted from the surface, making pulsars the main antimatter source in the galaxy [67; 10]. These pairs form a charge distribution that compensates the induced electric fields [69]. The charge density has been calculated from MHD calculations by Goldreich and Julian [69] as

$$\rho_{\text{GJ}} = \frac{\nabla \cdot \vec{E}}{4\pi} = -\frac{\vec{\Omega} \cdot \vec{B}}{2\pi c} \left[1 - \left(\frac{\vec{\Omega} r}{c} \right)^2 \sin^2 \theta \right]. \quad (2.10)$$

Here, θ is the polar angle with respect to the rotational axis.

The accelerated particles are trapped by the closed magnetic field lines, but they can escape from the pulsar along so-called open field lines. Due to the pulsar's rapid rotation, at a distance

$$R_L = \frac{cP}{2\pi} \quad (2.11)$$

from the rotational axis the field lines co-rotating with the pulsar reach the speed of light. This distance defines the so-called light cylinder. Thus one can define one last closed field line, touching the light cylinder at the field line's maximum distance from the pulsar's rotational axis. Field lines reaching further out are called open field lines. These field lines are spun up until they eventually return through the rotational equator [67]. They form a toroidal magnetic field which reverses direction in the equatorial plane [70]. A current sheet is thought to be created at the boundary between the open and the last closed field lines [71].

Particles propagating along open field lines can escape the light cylinder, forming the pulsar wind [49]. The corresponding current density can be estimated as

$$J_{\text{GJ}} = \rho_{\text{GJ}} \cdot c. \quad (2.12)$$

This pulsar wind dominates the energy loss of the pulsar. Electromagnetic dipole emission is the second-most important energy loss process.

The large multiplicities of electron-positron pairs in the magnetosphere lead to efficient screening of electric fields. Therefore, efficient particle acceleration is prevented in most regions. Only thin zones, called gaps, where the plasma charge densities are too low to screen the electric field because the currents flow out of the light cylinder are believed to be dominant sites of acceleration and thus of directed photon emission [60; 71]. In these regions the electric field is strong enough to accelerate particles efficiently. The location of these gaps are still subject to debate. In the frequently invoked polar cap model [72; 73], the voltage drop between the regions of open and closed magnetic field lines is considered to be the place of efficient particle acceleration [49]. The accelerated particles travel along the magnetic field lines and hit the star's surface close to the magnetic poles, which are heated up to temperatures of millions of Kelvin in this process and thus emit a broad thermal spectrum [60]. Several competing models exist, in particular the outer gap model [74] and the slot gap model [75; 76]. For details the reader is referred to the referenced literature. All models predict distinct luminosities, pulse profiles and spectral features like cut-offs or breaks. Observations show that all models can predict many aspects correctly, but no model can explain all observed features.

2.8.2 LS 2883

The massive companion star LS 2883 in the binary system PSR B1259–63/LS 2883 is a mag-10 star with a mass of $20 M_{\odot}$ – $30 M_{\odot}$ and is often classified as a Be star or as a late Oe star [57; 54; 77]. Be stars are B-type stars that show or at some point of their history showed strong atomic emission lines in their spectra, like H I, He I or Fe II lines. Such lines can disappear and reappear during the star’s life. These stars also rotate at approximately 70%–80% of their breakup velocities, thus properties of polar and equatorial regions differ significantly [58]. In case of LS 2883, the star is very oblate, with a polar radius of $R_{\text{pole}} = 8.1 R_{\odot}$ and an equatorial radius of $R_{\text{eq}} = 9.7 R_{\odot}$. Correspondingly, the temperatures are $T_{\text{pole}} = 34\,000$ K at the pole and $T_{\text{eq}} = 27\,500$ K at the equator [54]. The luminosity of LS 2883 is 6.3×10^4 times that of the sun, with flux variability observed on time scales ranging from minutes to days [78; 79; 80]. Occasionally also pulsations have been observed.

From the polar region of Be stars, a hot but relatively thin stellar wind with velocities of order 10^3 km s^{-1} emerges, whereas a high-density equatorial disk with a temperature of 4×10^3 K surrounds the star [80; 81; 82]. Close to the star’s surface, particle densities of 10^8 – 10^{10} cm^{-3} are found in the disk [58]. The density drops off radially following to a power law with an index of 2–4 [83; 80]. The streaming velocities in Be star disks are smaller than a few km s^{-1} , much lower than in the polar wind region. Overall, the winds cause a mass-loss rate of $\dot{M} \approx 4 \times 10^{-8} M_{\odot} \text{ yr}^{-1}$ [57; 81]. The main contributors to the stellar wind acceleration are the scattering of electrons on thermal stellar light, ionisation of hydrogen atoms and the absorption of UV light by atoms. The stellar matter participating in these processes is ejected from the star due to thermal and rotational movement [82].

The gaseous disk-like structure around the equator is a common feature of Be stars. These disks are thin, with opening angles of a few or sometimes up to a few tens of degrees. The radial movement of matter in the disks is slow, as mentioned above [80]. The mechanism of the formation of Be star disks is not clear yet. The collision of winds from both poles could in principle form a disk as the result of a shock-formation process [84]. Careful analyses of the influence of stellar rotation and magnetic fields together with the fact that the polar and equatorial flow speeds are drastically different lead to the conclusion that this scenario is unlikely. Alternative models explain the disk formation by diffusion of matter from the star by virtue of turbulent MHD effects in the viscous disk environment. This model can explain many aspects, but it has the problem that it cannot explain how particles gain enough angular momentum to diffuse far out into the disk [80; 81]. More research is needed to get a complete understanding of the Be disk phenomenon.

Due to the star’s oblateness a quadrupole term $\propto 1/r^3$ occurs in the star’s gravitational potential. This causes, among other effects, apsidal precession of the disk, which in turn leads to particle pile-up and thus to the formation of one-armed density waves within the disk [58; 80]. These waves can lead to year-long growth and decay phases of the disk [47]. In contrast, the interaction of the disk with the pulsar in the binary system can lead to the formation of two-armed spiral waves [81].

The quadrupole term can also lead to a precession of the orbital plane if the orbital axis is misaligned from the star’s spin axis [58; 57]. This precession can be measured as variations of the position of the periastron and the projected size of the binary orbit. Such variations have indeed been observed [57].

Be stars like LS 2883 are believed to evolve in binary systems. The development of a normal star to a rapidly rotating Be star is thought to happen as follows. The future Be star accretes mass from its giant companion of roughly $25 M_{\odot}$, the latter of which overfilled its Roche lobe. Thereby the smaller, future Be star accretes mass on the order of a few solar masses and gains angular momentum. The resulting angular velocity is close to the break-up velocity. Later the giant star explodes in a supernova, ejecting roughly half the system’s mass and thereby leaving the stars in a very eccentric orbit [55; 50].

2.8.3 Radio Observations

Results from radio observations of the binary system formed by the pulsar and the Be star introduced above are of fundamental importance for the determination of all basic orbital parameters. Also the identification of the compact object as a pulsar was possible because of the detection of pulsed emission in the radio wavelength band. Pulsations were not found in any other wavelength band.

The pulse period was determined to be 47.76 ms. The spin-down power of the pulsar is $\dot{E} = 8.3 \times 10^{35} \text{ erg s}^{-1}$, causing the pulsar to slow down its rotation, which is changing at a rate of $\dot{P} = 2.28 \times 10^{-15}$ [57; 50; 46]. From the pulsation parameters the characteristic age of the pulsar t_{psr} can be calculated as

$$t_{\text{psr}} \equiv \frac{P}{2\dot{P}}. \quad (2.13)$$

In case of PSR B1259–63, this value is $t_{\text{psr}} = 330 \text{ kyr}$.

The pulsation period also changed abruptly by $\lesssim 0.1\%$ in a glitch event in 1997 [58]. The period derivative did not change permanently in this event [57]. The physics of pulsar glitches is not understood completely yet. Attempts to explain this phenomenon consider starquakes caused by surface cooling leading to changes of the crustal structure or shape, phase transformations in the neutron star core or the adjustment of the crust rotation rate to the rotation of the superfluid core as possible glitch explanations [60; 85; 49]. After a few weeks, pulsars’ rotation periods recover from those events.

With the angular resolution of current radio telescopes and detector arrays it is possible to study the morphology of objects like PSR B1259–63/LS 2883. The size of the radio emission region is found to be approximately 120 AU in diameter, which is significantly larger than the binary orbit. The peak of the radio emission actually comes from outside the orbit. The morphology is consistent with a cometary tail of long-lived particles extending behind the pulsar [86; 54; 87].

The distance of the binary system from Earth can be derived from the dispersion measure. This is a measure of the integrated electron content along the line of sight. It is measured by comparing the times of arrival of radio pulses at different radio frequencies,

which differ due to dispersion effects when electromagnetic waves of different wavelengths propagate through a medium or electron gas. Comparing measurements with theory predictions allows deriving distance estimates. Depending on the model, values between 1.5 kpc and 4.6 kpc are calculated, favouring the lower end of this range [50; 88].

The evolution of fluxes at radio, X-ray, HE and VHE gamma-ray energies around periastron is shown in Fig. 2.7. In the radio wavelength band, the flux is comparatively low before the first disk crossing. Between the first and the second disk crossing, the flux rises significantly. The maximum flux, reached at the end of the second disk crossing, is roughly twice as large as the flux between the first disk crossing and periastron.

Radio measurements are used to define the times of the disc crossing indicated in Fig. 2.7. 16 d before periastron, the pulsed emission becomes undetectable. Approximately 15 d after periastron, the strength of the pulsed radio emission has increased enough to be measurable again. It can be expected that the pulsar enters the disk slightly earlier and also leaves the disk slightly later than these times suggest, but since the described method is the most well-defined way of determining one aspect of the disk crossing procedure known today these values are used frequently as references.

2.8.4 Optical Observations

Observations in the optical wavelength band help to deduce several parameters of PSR B1259–63/LS 2883. Most importantly, the companion star type was derived from spectral lines. The Be-star disk size mentioned above can be inferred from the width of the H_α line, and also the distance of the binary system from Earth can be deduced from optical observations [50]. Using absorption lines caused by interstellar gas limits the distance to $2 \text{ kpc} \lesssim d \lesssim 2.8 \text{ kpc}$ [54], which is well in agreement with the distance inferred from the association with the Cen OB1 cluster.

The rotational velocity of LS 2883 can be derived from measured spectral line widths. Depending on the spectral lines chosen for the analysis, projected rotational velocities up to $v_{\text{rot}} \sin(\omega_D) = (260 \pm 15) \text{ km s}^{-1}$ are measured. This corresponds to a deprojected velocity of 450 km s^{-1} [54]. This is almost identical to this star's breakup velocity.

Assuming that changes in the equivalent width of the H_α line are caused by growth or decay of the Be star disk, the disk mass evolution can be estimated from measurements. Before the interaction with the pulsar, the disk had a mass of $2 \times 10^{-8} M_\odot$. Within five days after the so-called Fermi flare that will be introduced in more detail in Sec. 2.8.6, the disk mass was reduced by a factor of five [79].

2.8.5 X-Ray Observations

Several orbits including periastron passages of PSR B1259–63/LS 2883 have been observed already. X-ray emission from this system can be detected during the entire orbit, with altering flux levels during the orbit. The observed light curves are stable across orbits, as shown in Fig. 2.7. The flux peaks around the times of the disk crossings and has a local minimum at the time of the periastron. Similar to the radio light curve, the observed flux is higher at the time of the second disk crossing.

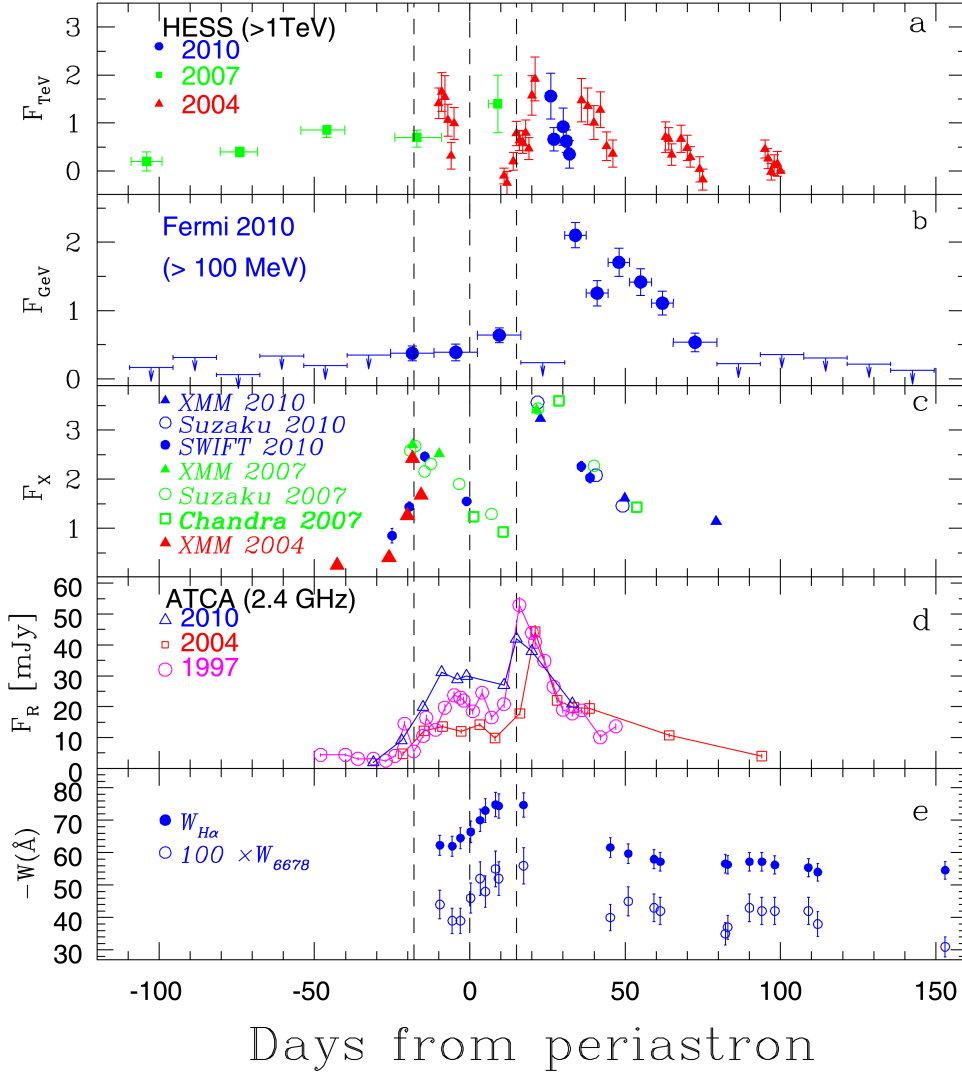


Figure 2.7: Light curves from several periastron passages for different wavelength bands are shown. In panel *a* the VHE flux, in panel *b* the HE gamma-ray flux, in panel *c* the X-ray flux and in panel *d* the radio flux is shown. Panel *e* is not relevant for the discussion here. Upper limits are marked by arrows. Black, dashed lines indicate, from left to right, the times of the first disc crossing, the periastron and the second disc crossing. Figure taken from Chernyakova et al. [86].

Together with the flux level, also the observed X-ray spectral index changes significantly over the course of an orbit. The spectrum is softest around periastron, with an index of approximately 2.0, while 266 d after the periastron, a remarkably hard index of 0.42 is attained [89; 86].

Current-generation X-ray observatories like the satellite-borne Chandra X-ray Obser-

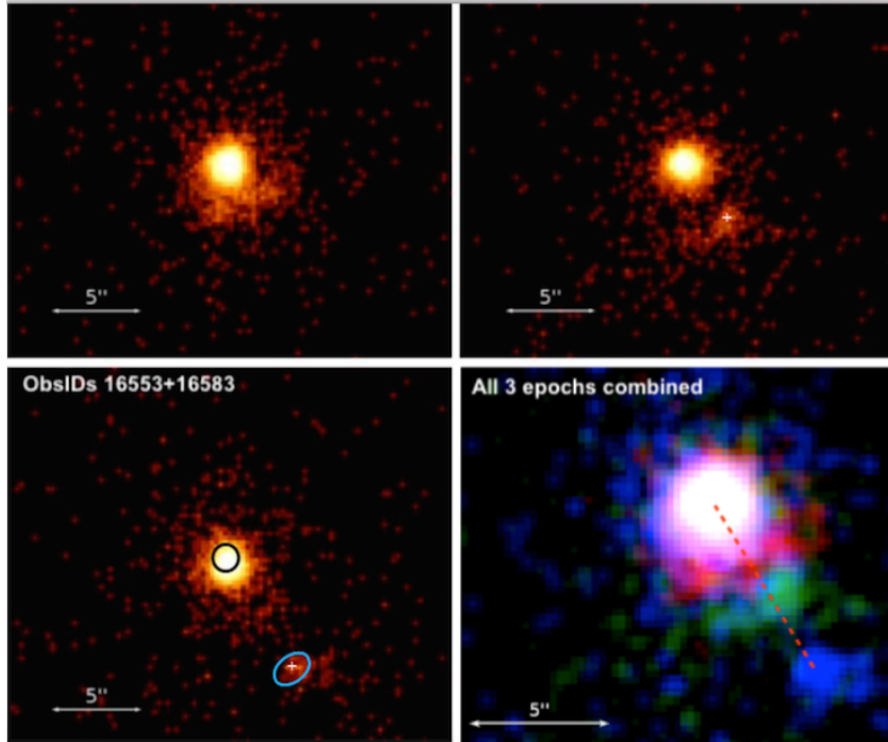


Figure 2.8: X-ray images showing the movement of a bright object away from the binary. The second image (*top right*) was recorded 519 d after the first image (*top left*). The last image was taken another 265 d later. All images in colour coded form are overlaid in the last picture (*bottom right*). Image taken from Pavlov et al. [78].

vatory [90] have angular resolutions small enough to allow studying the morphology of PSR B1259–63/LS 2883 in the corresponding wavelength band. With this instrument, hints of an elongated structure and an extended, compact object were found [89]. There have been proposals to associate these features with a jet created by either the pulsar or a shock remnant. Later observations showed that the extended, compact object is moving at a speed of $0.07c$, with a hint of acceleration [78]. Chandra images from several observation campaigns are shown in Fig. 2.8, visualising the object movement and the decrease of the object’s luminosity. Pressure from the Be star wind can in principle explain the emission of parts of the shocked pulsar wind. Around apastron, the pulsar and stellar winds mix quickly, thereby forming a fast and inhomogeneous outflow of material moving into the direction of the point of apastron. The object is believed to contain shocks, such that acceleration of electrons can occur inside. The emission of X-rays is most likely caused by synchrotron processes [89; 91].

In an alternative model, the object is interpreted as plasma created by the pulsar interacting with the disk. Disk matter can be accreted onto the pulsar’s magnetosphere. The pulsar then enters the so-called propeller regime, in which the accreted matter does

not reach the neutron star’s surface but is expelled in two ways. Due to centrifugal forces, most of the matter leaves the pulsar in an equatorial disk-like structure, while about 10 % can be accelerated to high velocities in form of a jet along the pulsar’s spin axis. A shock forms at the collision zone of the pulsar wind with the jet, in principle enabling the acceleration of particles to energies high enough to emit X-ray synchrotron radiation. Problems of this model are that neither the pulsar orbit nor the pulsar’s spin period changed during the disk crossings, which would be expected due to drag forces [78].

2.8.6 High-Energy Gamma-Ray Observations

In the HE gamma-ray band, the light curves are dominated completely by flaring events first detected after the time of the 2010 periastron passage [92]. As shown in Fig. 2.7b, PSR B1259–63/LS 2883 is not detected before the first disk crossing. At the time of the second disk crossing, the flux is about twice as large as the flux at periastron and at the first disk crossing. Approximately 35 d after periastron, just after the second disk crossing, the flux rises rapidly to ten times the periastron flux level, which was not expected beforehand. At all other wavelengths, the flux does not increase during that time. In fact, the start of the HE gamma-ray flare is coincident with the start of the decline of the X-ray flux.

The flare reoccurred at a similar orbital position in 2014 [93]. The measured spectrum, the flare duration and the average flux level were similar to the 2010 flare, but the flux evolution was different. While the shape of the 2010 flare resembled an exponential decay, the flux stayed almost constant during the 2014 flare. Also the shape of the onset of the flare differ marginally. In 2010/11, 36 d after the periastron, the flux has risen rapidly and monotonically to the maximum value of about 70 % of the pulsar’s spin-down power. In 2014, the flux formed a small plateau until 34 d after periastron, then rising to the maximum value corresponding to 50 % of the pulsar’s spin-down power approximately 38 d after periastron [94].

2.8.7 Very-High-Energy Gamma-Ray Observations

PSR B1259–63/LS 2883 was the first variable galactic source detected at VHEs by the H.E.S.S. observatory. The measured spectrum has a power law index of $2.7 \pm 0.2_{\text{stat}} \pm 0.2_{\text{sys}}$ [51]. The light curve across several periastron passages is shown in Fig. 2.7a. It can be seen that the flux increases towards the first disk crossing. Then it falls quickly before periastron, after which it rises again, reaching a maximum several days after the second disk crossing. There is no flux increase at the time of the flare detected by *Fermi*-LAT. The ratio of the fluxes above 1 TeV during and before the time of the flare is smaller than 3.5 at the 99.7 % confidence level [95].

A more detailed description of results of analyses of VHE gamma-ray data obtained from observations with H.E.S.S. data will be presented in Chap. 6.

2.8.8 Models of the System

The complex environment within PSR B1259–63/LS 2883, consisting of a very compact object, a massive and rapidly rotating star with strong stellar winds and a dense circumstellar disk, strong magnetic fields, an energetic pulsar wind and a changing binary separation over the course of one orbit requires detailed models to describe the interaction of the involved components and the resulting non-thermal emission. It is clear that the involved stellar and pulsar winds play an important role in the acceleration process. For both winds, the ram pressures exerted by the winds superseed the magnetic pressure [82]. Although the energy content carried by the pulsar wind is larger than the energy content of the stellar wind, the latter is more dense and thus has a higher thrust. The pressures of the pulsar and stellar winds are given by

$$p_{\text{PW}} = \frac{\dot{E}}{4\pi R^2 c} \quad (2.14)$$

$$\text{and } p_{\text{SW}} = \rho_w v_w^2 = \frac{\dot{M} v_w}{4\pi(d - R)^2}, \quad (2.15)$$

where d is the binary separation, R is the distance of the discontinuity from the pulsar and $v_w \approx 2400 \text{ km s}^{-1}$ is the estimated stellar wind speed [46; 91]. The location of pressure equilibrium can be determined by equating p_{PW} and p_{SW} , resulting in

$$R = \frac{d}{1 + \sqrt{\frac{\dot{M} c}{\dot{E} v_w}}} \approx 0.17d. \quad (2.16)$$

Thus the shock discontinuity forms at roughly 17% of the binary separation d measured from the pulsar along the connecting line. In a three-dimensional model, the shock forms a hollow cone pointing away from LS 2883 as indicated in Fig. 2.5. From the system's parameters also the question whether accretion occurs onto the neutron star's surface can be answered. The radius within which accretion occurs can be approximated as

$$R_{\text{ac}} \approx \frac{2GM_{\text{NS}}}{v_w^2} \approx 6.5 \times 10^7 \text{ m}, \quad (2.17)$$

where G is the gravitational constant [46]. Accretion is prevented if $p_{\text{PW}} > p_{\text{SW}}$ at R_{ac} , which is fulfilled in case of PSR B1259–63/LS 2883 because $R_{\text{ac}} \ll 0.17d$ at every point of the orbit.

The conical shape of the shock changes to a spherical shape when the pulsar passes through the disk. Then the pulsar wind is confined completely by the disk material, forming a sphere with a diameter of approximately 10% of the disk radius [51; 82]. According to MHD simulations, the interaction of the pulsar wind with the disk leads to a local truncation of the disk. Additionally, due to tidal effects the disk is warped at each crossing. The disk disturbance is larger during the second disk crossing due to cumulative effects of tidal torques [81].

The radiation detected from the binary system is affected by the geometry of the shock region. Due to the alignment of the orbital major axis with the observer's line

of sight the radio pulses propagate through the low-density pulsar wind region without being absorbed by the much denser Be star wind. The optical depth of the stellar wind at radio wavelengths can be of the order of several thousand at distances of 1 AU from the star. The pulse disappearance could then be caused by the absorption by the disk as well as the cone’s rotation away from the line of sight [81].

In order to explain the emission of radiation at higher energies, both leptonic and hadronic scenarios are, in principle, possible candidates. Hadronic scenarios as presented, for example, in Kawachi et al. [96], are generally disfavoured, though, because several predictions do not match observations. Most importantly, the Larmor radii of the 100 PeV hadrons needed for the creation of the observed VHE gamma rays would be larger than the shock size [46]. Furthermore, PSR B1259–63/LS 2883 can be detected at VHEs several months before periastron, when the density of the stellar wind is still too low to provide a sufficient amount of scattering targets. Thus almost all current models involve leptonic synchrotron radiation and IC scattering as main radiative processes. The dominance of one of the radiation mechanism depends on the respective cooling times. The synchrotron and IC cooling times in the Klein-Nishina regime are, respectively, given as

$$\tau_{\text{synchr}} = 6\pi \frac{m_e^2 c^4}{\sigma_{\text{T}} c E_e B^2} \approx 400 E_{e,\text{TeV}}^{-1} B_G^{-2} \cdot 1 \text{ s} \quad (2.18)$$

$$\tau_{\text{IC}} = 3.2 \times 10^3 \frac{E_{e,\text{TeV}} d_{13}^2}{\ln(30.6 E_{e,\text{TeV}}) - 1.4} \cdot 1 \text{ s} \quad (2.19)$$

according to Blumenthal and Gould [97] and Aharonian et al. [51]. In these equations, $E_{e,\text{TeV}}$ is the electron energy in TeV, B_G is the local magnetic field in G and d_{13} is the orbital separation of the pulsar and LS 2883 in units of 10^{13} cm. The magnetic field strengths are not known very well. The field strength close to the pulsar is approximately 3.3×10^{11} G, the Be star’s field strength on the surface is of order 1 G, but the field strength farther away from the objects is not determined precisely [88]. Above an electron break energy of roughly 25 GeV, the Klein-Nishina regime sets in, leading to longer electron cooling times in the IC scattering process, so that above this energy, synchrotron emission is dominant [46]. The IC gamma-ray spectral index transitions from Γ_e to $\Gamma_e + 1$ at the break energy, where Γ_e is the power-law index of the electron energy distribution. From H.E.S.S. observations at intermediate wavelengths a value of $\Gamma_e \approx 2.2$ can be derived from the photon index of $\Gamma = \Gamma_e + 0.5 \approx 2.7$ [51].

The location of the zone of emission of radiation differs across wavelength bands. X-ray emission is believed to originate from pulsar wind electrons in the shock region [59; 78]. The HE gamma-ray emission instead is believed to stem from the unshocked pulsar wind or from within the light cylinder. Inside the light cylinder the electrons emit low-energy curvature radiation as they follow the movement of the magnetic field lines. The strong radiation field present in binary environments provides IC scattering targets to the cold, unshocked pulsar wind, contributing to the HE gamma-ray emission. At VHEs, the emission is believed to come from IC scattering of shock-accelerated, multi-TeV electrons and stellar photons; see e.g. Tavani and Arons [59], Kirk et al. [98],

Dubus [99] or Khangulyan et al. [100] for corresponding models. Hence the populations responsible for HE and VHE gamma-ray emission are different, which is an important fact to consider when trying to explain the differing flux evolution in these energy bands [46; 54].

The simplified view presented so far has to be extended in order to explain the observed spectra and light curve shapes. First of all, the disk provides an additional infrared target photon field in addition to the stellar photon field [101]. Furthermore, pulsar wind particles can be advected away into a direction roughly pointing away from the companion star by crossing the shock into the domain of the stellar wind if the shock is not spherically symmetric. Thereby energy is lost due to non-radiative, adiabatic MHD processes. The characteristic energy loss time related to this process is

$$t_{\text{ad}} = \frac{3\varepsilon}{\text{div}\vec{u}} \approx \varepsilon \times 350 \frac{\Delta l}{2 \times 10^{12} \text{ cm}} \cdot 1 \text{ s} \quad (2.20)$$

with $\Delta l \approx \mathcal{O}(10^{12} \text{ cm})$ being the distance the shocked pulsar wind can propagate into the domain of the wind of the stellar companion, \vec{u} being the speed of the flow across the shock and ε being an efficiency factor incorporating details of the MHD flow. Remarkably, the resulting loss time is smaller than the IC energy loss time but comparable to the synchrotron loss time [51; 100].

Also the effect of relativistic boosting has strong influence on the observed synchrotron flux levels and likely contributes to the observed flux variability [46]. If relativistic boosting is not considered, the HE gamma-ray emission caused by IC scattering should peak before periastron if the assumption holds that HE electrons close to the pulsar are responsible for this emission. This contradicts the observed HE gamma-ray light curve, which peaks roughly 30 d after periastron at an unfavourable IC scattering angle. This, together with the observed peak luminosity, can be explained better if boosting is taken into account [45; 92].

Valuable observational input comes from the HE flare detected during the previous two periastron passages. Several models predict, or can be refined to predict, a similar light curve feature. These models try to explain the flare as a result of Doppler-boosted synchrotron emission from electrons with energies up to 100 TeV (e.g. Kong et al. [102]), IC scattering of GeV electrons on UV photons provided by the star and the disk which is heated up by the interaction with the pulsar (e.g. Khangulyan et al. [56]) or by the destruction of the regular bow-shock (e.g. Chernyakova et al. [79]). Models based on Doppler-boosting appear disfavoured because then the X-ray flux should be affected in a similar way, which is incompatible with observations.

In the model proposed by Khangulyan et al. [56], electrons from the unshocked pulsar wind with Lorentz factors of order 10^4 scatter via the IC process on ambient photons. As the unshocked wind is cold, no contemporaneous synchrotron flare is expected, which matches observations well. In this model the rapid transformation of the shock structure at both the pulsar's entrance into and the departure from the disk as indicated in Fig. 2.5 leads to HE gamma-ray flux increases similar to those observed. The flare that is predicted to occur, in principle, also at the time of the first disk crossing, but then it

is not visible on Earth due to an unfavourable geometry. Within the disk, IC scattering involving pulsar wind particles is suppressed because the high particle density and ram pressure in this region confine the wind, thereby reducing the volume in which IC scattering can occur. Close to the disk, the radiation field produced by the disk heated up by the interaction with the pulsar is very intense. Due to these radiation fields the optical depth for IC scattering is larger than one, so that the production of HE emission is very efficient. The gamma-ray flux during the flare is a natural consequence of the re-opening of the shock cone at the time of the pulsar's departure from the disk, as then the relativistic pulsar wind is allowed to travel further along the line of sight. Thus the amount of relativistic electrons IC scattering on photons from the intense photon field provided by the disk changes rapidly, in turn leading to an increased gamma-ray flux. The 15 d delay between the appearance of radio pulses and the start of the HE gamma-ray flare poses a problem to this and other models. Another important ingredient in this model is the creation of an intense photon field from the heated disk. It is unclear if the heated disk can provide a sufficient amount of photons. Alternatively, in a similar model according to which the HE gamma-ray flare is based IC scattering, the target photon field stems from the cometary tail of shocked pulsar wind material [56; 103].

The transformation from a bow-shaped shock to a confined, non-spherical shock inside the disk prevents the unshocked pulsar wind from escaping. Thus the pulsar deposits its entire energy loss into the system. According to the model by Chernyakova et al. [79], this can already lead to the observed fluxes corresponding to 50 %–70 % of the pulsar's spin-down power.

In conclusion, the complex environment found in PSR B1259–63/LS 2883 makes it difficult to describe all observed properties within a simple model. Especially the details of the binary's constituents, like spiral waves within the Be star disk, density variations in the stellar wind or cycles in the stellar mass-loss rate lead to deviations of the calculated light curves from the observed light curves [45]. Results from observations of the HE and VHE gamma-ray part of the spectrum of PSR B1259–63/LS 2883 already provided valuable input to the models introduced above and will continue to do so in the future. An overview of the experimental approaches taken to detect such gamma rays will be given in the next section.

2.9 Detection of Gamma Rays

Gamma rays can be observed by space-based and ground-based experiments. As a rule of thumb, space-based experiments cover the HE gamma-ray range, whereas ground-based experiments have better sensitivities than satellite-borne experiments at VHEs.

At energies below $\mathcal{O}(100 \text{ GeV})$, the gamma-ray flux is large enough to be detected by experiments like *Fermi*-LAT [104], which has an effective detection area of $\lesssim 1 \text{ m}^2$ and a large field of view covering approximately 20 % of the sky [105]. The detection principle of this observatory is relatively similar to that of particle detectors used at collider experiments. Particles can enter the telescope through an opening at the front, pass through a tracker system in which a magnetic field deflects charged particles, so

that the ratio of their charge and mass can be determined, and afterwards they deposit their energy in a calorimeter. Separating gamma rays from charged cosmic rays is a relatively simple task here due to the very different signatures in the detector. The angular resolution, defined as the radius in which 68 % of the reconstructed directions are located around the true direction of a source is on the order of 0.5° above 1 GeV.

Ground-based experiments are built very differently from space-based experiments because the atmosphere is opaque for gamma rays and cosmic rays, hence they cannot be detected directly. Instead, the showers consisting of secondary particles produced by interactions of the primary particles with atomic nuclei in the atmosphere are detected. The development of a gamma-ray induced air shower can be seen as a sequence of pair production and bremsstrahlung emission close to atmospheric nuclei. In this process, the number of particles in the shower grows exponentially until the average particle energy is sufficiently low for ionisation to become the dominant process through which particles lose energy. This is where the shower has its maximum number of constituents of up to $\mathcal{O}(10^4)$ particles for gamma rays with TeV energies, afterwards the number of particles decreases due to scattering and absorption [26]. The shower maximum is reached at a height of approximately 10 km in case of an incident gamma-ray photon with an energy of 1 TeV [6]. Non-imaging detectors of extended air showers (EASs) like ARGO-YBJ [106] or HAWC [107] sample radiation emitted by shower particles as they pass through a detector. In contrast, imaging atmospheric Cherenkov telescopes (IACTs) sample the Cherenkov light emitted as the shower particles travel through the atmosphere. A sketch of the detection principle is shown in Fig. 2.9. The pioneering IACT experiment was the Whipple observatory, a telescope with a 10 m reflector and a camera consisting of 109 photomultiplier tubes (PMTs) that started observing in the 1980s [108]. In the 1990s, the HEGRA experiment introduced the concept of stereoscopy, which greatly helped to improve the gamma-hadron separation as well as the direction reconstruction [109]. Three experiments, MAGIC [110], VERITAS [111] and H.E.S.S., belong to the current generation of IACTs, making use of large mirrors, finely pixelated cameras, stereoscopy and advanced analysis techniques. They are the most sensitive experiments for the detection of VHE gamma rays currently operating. The H.E.S.S. experiment will be described in detail in Chap. 3. The next-generation experiment, the Cherenkov Telescope Array (CTA) is currently planned and is foreseen to begin observations in 2017.

IACTs collect Cherenkov light emitted by atmospheric atoms and molecules when charged particles, mostly electrons and positrons, pass by with a velocity v fulfilling the condition

$$v \geq \frac{c}{n(\lambda)}, \quad (2.21)$$

where c is the speed of light in vacuum and $n(\lambda)$ is the wavelength-dependent refractive index of the respective medium. The relativistic particles polarise the atoms, which, as they return to the equilibrium state, emit radiation. If this condition is fulfilled, the wave fronts of light emitted by many atoms or molecules interfere such that light is emitted in form of a cone around the direction of the relativistic particle. For electrons at 10 km above sea level, the condition is fulfilled if their corresponding energy exceeds roughly

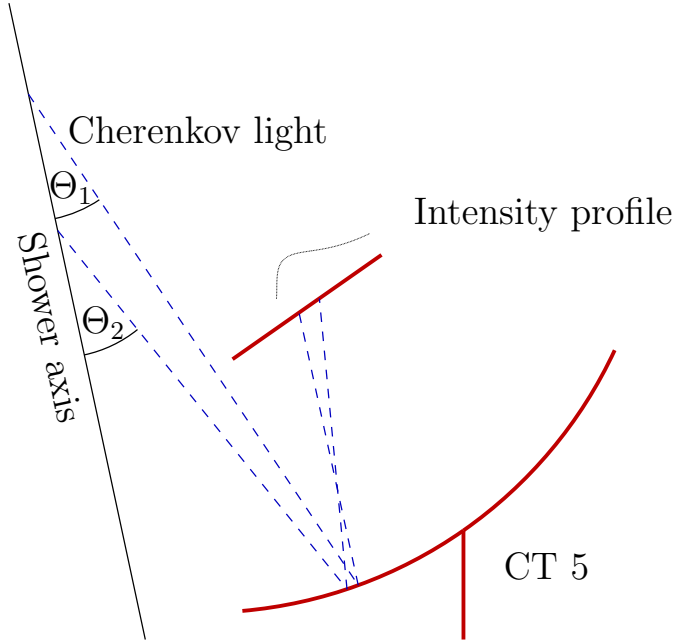


Figure 2.9: Sketch of an imaging atmospheric Cherenkov telescope called CT 5 with a spherical mirror. The Cherenkov photons emitted at different angles are focussed onto the pixelated camera, where the intensity distribution is measured and recorded. See the main text for details of the telescope setup and the measurement process.

40 MeV. The angle θ_C between the particle trajectory and the wave number vector is given by the relation

$$\cos \theta_C = \frac{c}{n(\lambda)v}. \quad (2.22)$$

For electrons propagating through air, this angle is $\lesssim 1^\circ$. Depending on the height of the experiment detecting air showers, the corresponding light pool has a diameter of approximately 100 m–150 m [112; 113; 114; 6]. The shower profile and the resulting Cherenkov light density depends on the type of the initial particle. In case of gamma rays, the vast majority of all interactions are electromagnetic interactions, whereas in case of protons and hadrons, a substantial fraction are strong interactions. In strong interactions, the transverse momentum of scattering products with respect to the shower axis can be much larger than in electromagnetic scatterings, thus hadronic air showers produce a wider light pool. Furthermore, the much larger variety of possible decay channels and interactions causes hadronic showers to be less regular than gamma-ray air showers, which can be seen in Fig. 2.10.

The energy emitted in form of Cherenkov radiation per unit length and frequency is given as

$$\frac{dE}{dx d\omega} = \frac{q^2}{4\pi} \mu(\omega) \omega \left(1 - \frac{c^2}{v^2 n^2(\omega)} \right). \quad (2.23)$$

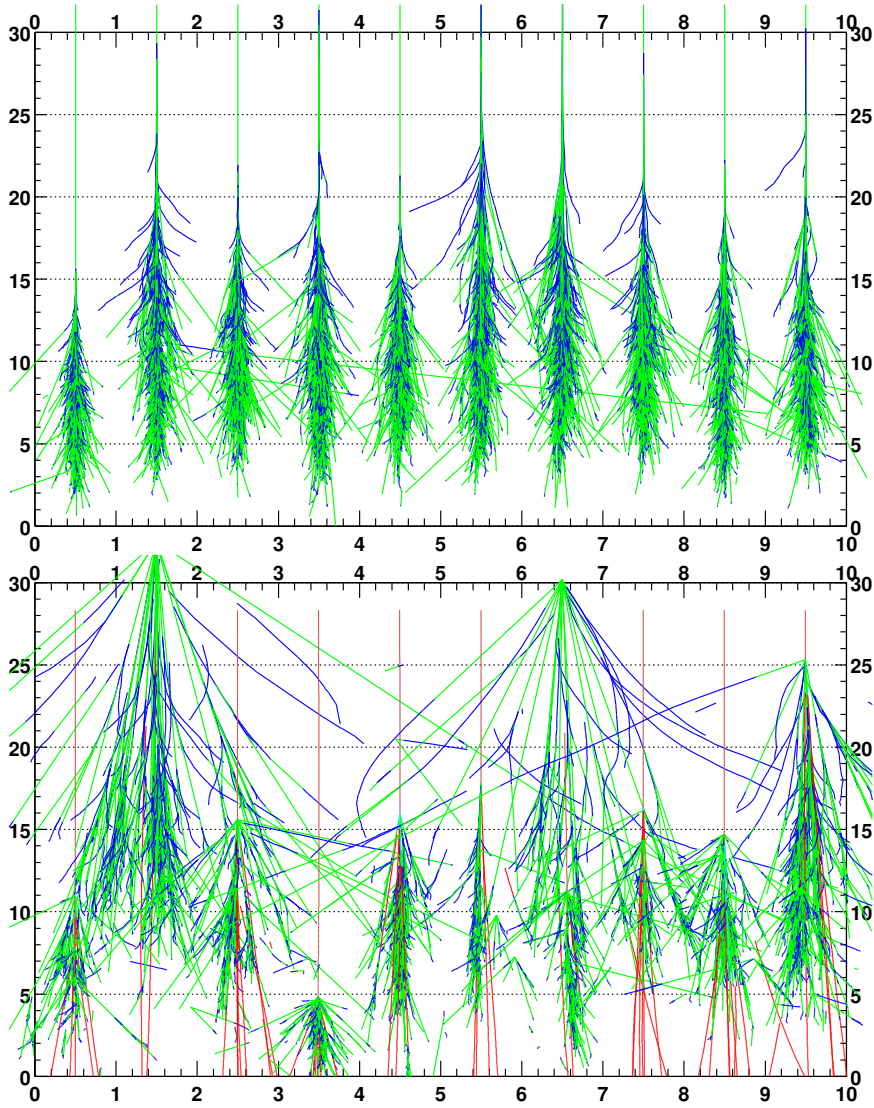


Figure 2.10: Simulated air showers initiated by gamma rays (*top*) and protons (*bottom*), each with an energy of 300 GeV. The unit of the values on both axes is kilometres. Green lines represent photons, blue is for electrons and positrons, thick red lines are for protons, other colors stand for muons, pions and other particles. The much larger irregularity and intrinsic spread of proton showers is obvious. Figure taken from De Naurois [65].

This is the so-called Frank-Tamm formula [115]. In this formula, $\mu(\omega)$ and $n(\omega)$ are the frequency-dependent permeability and refractive index of the medium, q is the charge of the relativistic particle. To calculate the energy emitted per unit length, the above formula needs to be integrated over all frequencies for which the condition given in Eq. (2.21) is fulfilled.

A related quantity which is important for the detection of air showers is the number

of Cherenkov photons emitted per unit length. This can be calculated as

$$\frac{dN}{dx} = 2\pi\alpha q^2 \int_{\lambda_1}^{\lambda_2} \left(1 - \frac{c^2}{(vn(\lambda))^2}\right) \frac{1}{\lambda^2} d\lambda, \quad (2.24)$$

where α is the fine structure constant. The integration range is defined by the wavelengths between which the Cherenkov condition is fulfilled [114]. As an example, a gamma-ray photon with an energy of 1 TeV produces showers yielding approximately ten detected Cherenkov photons per square meter in the center of the Cherenkov light pool [6].

The amount of Cherenkov light reaching the ground depends on several parameters. Most importantly, atmospheric properties like the density profile, water vapour content and the temperature profile can change the light pool density by up to 60% when comparing extremes like an antarctic winter atmosphere with a tropical atmosphere. Also seasonal changes can have an influence of up to 20%. In addition, the height in which the experiment is located has an influence due to the stronger light absorption in the thicker atmosphere at low altitudes and due to the geometric widening of the light pool. A 10% change in the light pool density is found for experiments at 2.4 and 1.8 km a.s.l. The scattering and refraction of light play a negligible role. Light scattering influences the arrival time of the photons, so that photons scattered by more than $\sim 3^\circ$ arrive too late to be part of the recorded image (see Chap. 3 for more details on the image recording). Only $\lesssim 0.1\%$ of all photons are lost due to scattering [114].

3 The H.E.S.S. Experiment

The H.E.S.S. telescope array is located in the Khomas highland in Namibia at an altitude of 1835 m. This site provides a more favourable view of the galactic plane including the galactic center compared to sites in the northern hemisphere. The high altitude reduces absorption of light as it propagates through the atmosphere. It also leads to smaller and therefore denser light pool on the ground since the dispersion of photons away from the shower axis is limited. Both effects result in larger amounts of light collectable by telescopes at higher altitudes compared to lower-altitude sites. Furthermore the weather conditions are well-suited for astronomical experiments as the sky is very clear most of the time. Last but not least the population density is very low in this area. Therefore the light pollution is very low, which is important for experiments as sensitive as IACTs.

The construction of the array started in 2002. The first telescope was finished in September 2002, the fourth and last telescope of the H.E.S.S. Phase I array was finished in December 2003 [116]. These four telescopes were given the shorthand names CT 1 to CT 4, “CT” standing for “Cherenkov Telescope”. These telescopes are arranged in a square with a side length of 120 m. This array has an energy threshold of approximately 100 GeV and already provided an entirely new view of the universe in the VHE gamma-ray domain with the detection of more than sixty new sources during a survey of the galactic plane [117; 118] and morphological studies of extended objects like the shell-type supernova remnant RX J1713.7-3946 [9]. More recently, the first source of particles with PeV energies was found with the H.E.S.S. telescopes [7]. Given the great success of this experiment already in its first years it was decided in 2005 to enhance the array by a much larger fifth telescope placed in the centre of the array to further decrease the energy threshold down to approx. 50 GeV. With the inauguration of the new telescope named CT 5 in 2012 the H.E.S.S. experiment entered Phase II. This array, shown in Fig. 3.1, is the only hybrid array currently existing.

In the following sections the telescopes will be described in more detail. First the calorimeter of the experiment, the atmosphere, will be described. Then the properties of the telescopes of Phase I and Phase II will be detailed. At the end of this chapter the central data acquisition system and the calibration of data will be described.

3.1 The Atmosphere

The Cherenkov photons emitted in air showers travel through the atmosphere before reaching the ground, where they can be detected by IACTs. The atmosphere consists of 78 % nitrogen, 21 % oxygen and 1 % trace gases. In addition to these gas molecules, solid or liquid particles are suspended in the troposphere, that is the lower ~ 2 km layer of the atmosphere. Such particles are called aerosols and can consist of various types of

3 The H.E.S.S. Experiment

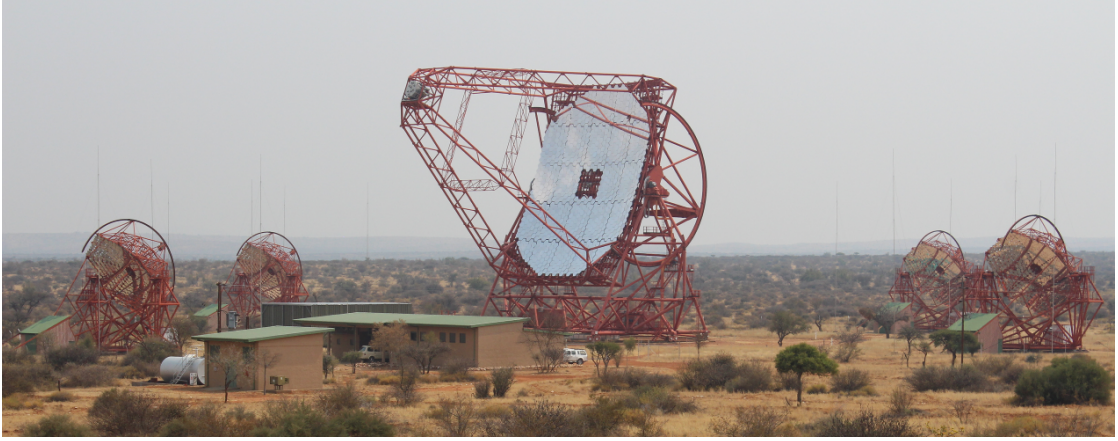


Figure 3.1: The H.E.S.S. array on a hazy day. From left to right there are CT 4, CT 3, CT 5, CT 2 and CT 1. CT 1 to 4 are parked in, whereas CT 5 is pointing towards the south for tests of the drive system. The building in front of the array hosts the control room and the local computing farm.

particles like desert sand or pollen. Their typical radii are on the order of nanometers up to millimeters [119; 113]. Water droplets and ice crystals contribute to the aerosol content of the atmosphere as well. Their radii are on the order of 1 to 50 μm [120; 113].

Two different types of scattering processes occur as the Cherenkov photons propagate through the atmosphere. Rayleigh scattering [121] is dominant for photons scattering off particles with sizes in the nanometer regime like atmospheric molecules. The light is scattered isotropically, but the intensity is strongly wavelength dependent with a proportionality to the inverse of the fourth power of the wavelength. Mie scattering [122] is dominant for larger particles of a size comparable to the wavelength of the Cherenkov light, like aerosols. In this scenario the light is mostly scattered forward. At wavelengths larger than 400 nm Mie scattering dominates over Rayleigh scattering [113]. These scattering processes lead to a lower Cherenkov photon density in the light pool on the ground, so that the trigger rates and energy thresholds of IACTs are influenced negatively.

Several atmospheric properties are monitored constantly at the H.E.S.S. site. The weather station placed next to the telescopes records the air temperature and air pressure, the wind speed and the wind direction and the relative humidity. Furthermore a light detection and ranging device (LIDAR) is installed on site to determine the aerosol content and cloud coverage above 1 km. This is done by analysing the light scattered back from those particles when they are hit by laser pulses [123; 113]. Currently the LIDAR is not operative due to issues with broken hardware. Six infra-red radiometers are also deployed on site to measure the temperature of the atmosphere above the site. They provide valuable information for shift crews operating the experiment to base decisions on whether the weather is sufficiently good to perform observations or whether there is a risk of rain, in which case the telescopes have to be parked to prevent damage to the hardware. Furthermore the telescopes must not be operated if the wind speed

constantly exceeds 10 m s^{-1} to prevent damage to the drive systems.

3.2 The H.E.S.S. Phase I Telescopes

The telescope dishes of CT 1–CT 4 are supported by alt-azimuth mounts which enable the telescopes to be moved to any point in the sky. The dishes are attached to the mounts by two bearings forming the axis of the altitude movement. Circular rails form the contact of the telescopes with the ground. On these rails the telescopes, weighing 60 t each, can rotate in azimuthal direction. The nominal slewing speed of the telescopes around each axis is $100^\circ \text{ min}^{-1}$ [124], so that every point in the sky can be reached in approximately two minutes [125]. When observing a source the telescope is moved such that the target position remains at a constant position in the camera, i.e. the telescope follows the movement of the object in the sky.

The telescope dishes are made from steel and provide stable structures to the reflectors and also hold the support arms carrying the cameras. The red colour of these structures was chosen as a compromise between the optimal heating and cooling behaviour together with the fact that the radiated wavelengths are very different from the maximum of the cameras' efficiency of a brighter red or pink colour on the one hand and subjective impressions on the other hand [126; 124]. The shadowing for Cherenkov photons caused by the camera support structures and the camera itself is on the order of 5 % [124].

The 107 m^2 reflectors are tessellated and consist of 380 facets each. The mirror facets themselves have a round shape as a compromise between the better areal coverage of e.g. hexagonal mirrors and costs. Indeed the loss in effective area due to this compromise amounts to 10 % [124]. The facets are arranged on a sphere according to the Davies-Cotton design [127]. The radius of this sphere as well as the focal length f of the spherically shaped facets is 15 m. In this design a point-like focus can be achieved for rays travelling close to the optical axis of the telescope. To be able to fine position and adjust the orientation of the individual facets actuators are mounted on the mirror support structures. The orientation of the mirrors is verified on a regular basis. The root mean square (rms) of the supposedly Gaussian optical point-spread function (PSF) of the telescope, defined as the image of a point light source at infinity [124], is 0.28 mrad. The mirror facets are made of aluminised glass with quartz coating and show only mild dependence of their reflectivity in the relevant wavelength range of 300 up to 600 nm. Due to degradation the mirrors lose a few percent of reflectivity every year, but over the years all mirrors have been recoated to remedy this process.

The light reflected by the mirror then reaches the camera, which consists of 960 Winston cones and PMTs, electronics, cooling systems and mechanical structures. The overall weight of each camera is 1 t, the volume is $1.6 \times 1.6 \times 1.5 \text{ m}^3$. The field of view (FoV) is 5° . The Winston cones guide the light to the PMTs, which represent the pixels of the cameras. The cones are made from plastic with quartz coating and aluminised inner sides. The aperture shape is hexagonal with a flat-to-flat distance of 41 mm (corresponding to a pixel size of 0.16°) at the entrance facing the mirror and a flat-to-flat distance of 21.5 mm at the end towards the PMTs. The cones effectively cover

3 The H.E.S.S. Experiment

95 % of the camera surface. The transmissivity between 300 and 500 nm is between 65 and 80 %. The cones have a cutoff angle of 27° to reduce the amount of albedo light reaching the PMTs [124].

The light reaching the PMTs can produce one photoelectron (p.e.) or more inside the PMT through the photoelectric effect. As PMTs are very sensitive instruments they are automatically switched off if they are illuminated by light coming from bright stars to avoid damage [128]. In the remaining devices, the produced photoelectrons are accelerated in high voltage cascades. When they hit the dynodes inside the PMTs they produce several secondary electrons, so that the current inside the PMTs increases following a power law. The voltage difference occurring as the generated current passes a resistor is measured, creating a voltage signal proportional to the amount of incident light. The overall quantum efficiency of the PMTs is approximately 25 % [128]. The PMTs are sensitive in a spectral range of 270 nm–650 nm, the peak efficiency is at 420 nm [128]. Combining the optical efficiencies of all involved components, the overall optical efficiency of the mirror-camera systems is on the order of 10 % [129].

The signals from the PMTs are sampled every nanosecond using analogue ring samplers (ARs) [116]. To reduce the amount of data that has to be stored, the PMT values are only read out if certain trigger criteria are fulfilled. One camera triggers only if the values of at least 3 PMTs in a camera region corresponding to 64 pixels called sector exceed the value of 4 p.e. within a time window of roughly 1.3 ns on average. The values have been chosen to suppress triggers by the so-called night sky background (NSB), which consists of star light, stray light from distant cars or houses or similar, efficiently. This is necessary as the trigger rate per pixel due to NSB is on the order of 9×10^7 p.e. s⁻¹ [116].

After a camera trigger occurred, a signal is sent to the central trigger of the H.E.S.S. array. This central trigger checks if other cameras have triggered in a time window of 80 ns around the time of the corresponding camera trigger. The delay caused by different fiber lengths and photon arrival times depending on the observation direction is taken into account. If at least two telescopes triggered within the time window, a sample corresponding to 16 ns around the time of the respective camera trigger is read out, processed and sent to the data acquisition system. The width of the time window was chosen such that only negligibly few accidental coincidences are found while not discarding any real coincidences [116]. Requiring stereoscopy helps to lower the energy threshold by a factor of roughly two by suppressing the dominant background of hadronic air showers as these tend to be more irregular than gamma-ray air showers. In the following sections the information recorded by the cameras and stored on disk after a positive decision of the central trigger will be referred to as an *event*.

The single-telescope trigger rate is usually at a level of 600–1000 Hz. The average dead time during which the cameras are busy processing an event and reading out the data is 460 μ s [128]. The overall trigger rate of this array configuration is on the order of 100–300 Hz, demonstrating the efficiency of the background suppression through requiring stereoscopy.

Currently the hardware of the H.E.S.S. Phase I cameras are undergoing an upgrade procedure. While the PMTs will not be exchanged the electronics hardware is substi-

tuted by more modern components with the main aim of decreasing the dead time. The upgrade is foreseen to be completed by the end of 2016. In this work only data from all four H.E.S.S. Phase I cameras before the upgrade is used.

3.3 The H.E.S.S. Phase II Telescopes

In Phase II of the H.E.S.S. experiment, a large, fifth telescope that has been added to the array joined operations, so that the new array consists of the four older telescopes and the new one next to them. In the following, only CT 5 will be described in detail and compared to CT 1–4 as necessary.

The design of CT 5 has been optimised for a good low-energy sensitivity and fast slewing speed in order to increase the chance of detecting transient events after receiving an alert. In order to lower the energy threshold significantly, the total reflector area has been increased up to 614.5 m^2 [128], making CT 5 the largest IACT ever built. An alt-azimuth mount is used similar to the H.E.S.S. Phase I telescopes. Despite the much larger mirror area and the large mass of approximately 600 t [130] the maximum slewing speed of CT 5 is $100^\circ\text{ min}^{-1}$ in both directions, equal to the slewing speed of CT 1–4. In order to further decrease the time needed to slew to a certain observation position CT 5 is operated in reverse mode under certain conditions like during observations of gamma ray bursts (GRBs). The average time needed to slew to a target can be reduced by a factor of two if the reverse mode is used, so that 90 % of sources distributed randomly across the sky can be slewed to within 52 s [130].

The mirror has a roughly rectangular shape with side lengths of 24.3 and 32.6 m, approximately 8 % of the corresponding area are shadowed by the camera and support structures. The mirror is made of 875 hexagonal facets [125]. Each facet has a flat-to-flat distance of 90 cm. A parabolic mirror was chosen for CT 5 due to the isochronous imaging properties of such a design. The camera of CT 5 can record, among other shower properties, the time of the maximum signal strength per readout window per pixel. In case of H.E.S.S. Phase I, the time dispersion at the camera due to the Davies-Cotton design for photons arriving at the mirror as a planar wavefront is on the order of 1 ns, which corresponds to the intrinsic spread of the photons in the Cherenkov wavefront of air showers [124]. The larger mirror of CT 5 would have enhanced this temporal spread even further due to the dependency of the temporal spread on the square of the mirror diameter, thus a parabolic design was deployed. The individual facets are spherical reflectors with varying focal lengths depending on the radial distance to the optical axis of the telescope.

The focal length of the telescope is roughly 36 m [130]. The exact position of the camera can be varied along the optical axis using a focus system [131]. Currently the focus is set to a fixed value which corresponds to a distance of 15 km, but in principle it can be adjusted depending on the observation position. Monte Carlo simulations show that the angular resolution can be improved up to 10 % at low energies if the focus is adjusted according to the observation conditions [131].

The camera consists of 2048 pixels and has a FoV of 3.2° averaged over the entire

3 The H.E.S.S. Experiment

camera. Its overall mass is 3 t, the total volume is $227 \times 240 \times 184 \text{ cm}^3$ [128]. Similar to the H.E.S.S. Phase I cameras, Winston cones are used to guide the incoming light to the PMTs. These cones have a hexagonal aperture with a flat-to-flat distance of 42 mm, corresponding to a FoV of 0.07° per pixel. The cones' cutoff angle is 30° , approximately the same value as for the smaller telescopes' cones. Small cutoff angles adapted to the size of the telescope mirror greatly help to reduce the amount of stray light entering the camera. A new coating provides a 10% higher transmission yield below 400 nm with respect to the older Winston cones. The PMTs used in CT5 are a minor update to the PMTs used in the smaller cameras, the only major difference being the quantum efficiency which increased from 25 to 30%. The spectral range of the PMTs is 270 nm–650 nm, with a peak efficiency at 420 nm. Groups of 16 PMTs are connected to one drawer, similar to the case of the H.E.S.S. Phase I cameras. These drawers provide signal amplification, sampling, signal conversion from analog to digital values and provide triggers at the PMT level. The camera triggers if at least 3 pixels belonging to one sector measured values of at least 4 p.e. [128]. Until a decision made by the central trigger arrives at the camera the individual PMT values are stored in a swift analogue memory (SAM) chip, a newly designed replacement for the ARSs used in the other cameras. The central trigger has been modified to allow several trigger modes, one being a usual stereoscopic trigger requiring at least two out of all five telescopes to have triggered within a time window of 80 ns and the other one being a monoscopic trigger requiring only CT5 to have triggered. The latter mode is particularly important for measurements of low-energy air showers that produce too little Cherenkov light to be detected by the smaller telescopes.

The trigger rate of the CT5 camera can be as high as 5000 Hz. The dead time of this new camera is 15 μs and the readout time is only 2 μs , resulting in an effective dead time of less than 1% at the maximum trigger rate [128]. As the cameras continue data taking after the data have been read out even though the data are still being processed by the cameras themselves the overall trigger rate of CT5 is not influenced by the much higher dead time of the old cameras. Thus the overall trigger rate of the full array is usually on the order of 1 kHz.

3.4 The Central Data Acquisition System

The data from the cameras are sent to the central data acquisition system (DAQ), which receives those data, processes them and writes them to disk. Though this is the most important task of the DAQ, there are several other tasks like instructing the involved hardware, starting and stopping observations, providing an interface to the shift personnel or the handling of errors. In this section, the DAQ is described in detail.

H.E.S.S. observations are grouped in shift periods starting and ending at full moon periods. During the shift breaks the experiment cannot take observational data. In these breaks the non-expert shift personnel changes and maintenance tasks are executed. In the remaining shift periods observations are performed during times of astronomical darkness and sufficiently good meteorological conditions. Given these constraints, ap-

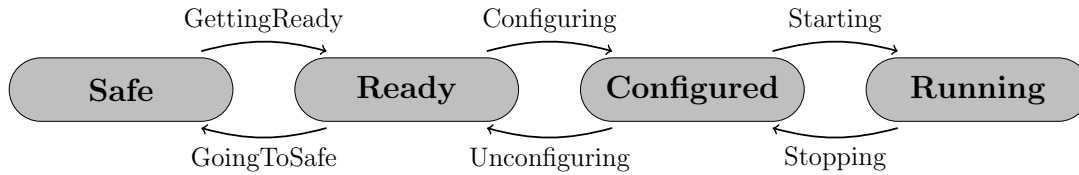


Figure 3.2: Sketch of the states of hardware controllers and software processes used in the DAQ. The transitions between the states are indicated by arrows.

proximately 1000 h of dark time are available per year.

Due to the limited FoV of the H.E.S.S. telescopes, targeted observation campaigns are executed. These campaigns are structured in so-called observation runs, each run usually taking 28 min. The DAQ is responsible for starting and stopping those runs. The observation targets are defined before each moon period and stored in a database which is looked up at the beginning of each night. The DAQ asks for the corresponding parameters at the beginning of each run and distributes those to the involved hardware, like the drive systems or cameras. The DAQ creates one so-called SubArray for each group of telescopes jointly performing one run. A SubArray is a software process managing and supervising other software processes belonging to the same run. It is possible to use arbitrary but disjoint groups of telescopes at the same time. For example it would be possible to perform calibration runs with CT 1–4 while observing a target with CT 5 [132]. In such a setup, the DAQ would create one SubArray for each telescope group.

The software processes managed by the DAQ serve a variety of purposes. One fundamental purpose is the communication with hardware. The hardware involved in the H.E.S.S. experiment ranges from weather stations to complex pieces of hardware like Cherenkov cameras. Each piece of hardware is abstracted and presented to the DAQ as a so-called controller with which the DAQ communicates. A fundamental design feature of the DAQ is the existence of controller states as shown in Fig. 3.2. The default is the Safe state. In this state no high voltage is supplied to any piece of hardware, and every component is in a state of minimal activity [132]. When preparing for calibration or observation runs, all involved software and hardware components are sent to Ready, which is an intermediate step in which the hardware is prepared for data taking and slow control data is taken. The last intermediate state before data taking is the Configured state. In this state the hardware has received all necessary information from the controllers to be able to start data taking. The final step in this chain is the Running state, in which information is read out from the hardware, the DAQ processes data and stores data on hard disk. The DAQ is also responsible for creating and managing the chain of transitions of the involved processes including dependencies between them. There are several types of dependencies among the processes. One trivial example is the fact that, during observation runs, the camera should not start triggering before high voltage is provided to the PMTs, which is a strict requirement. There are also optional dependencies for non-critical components like weather monitoring. If such optional requirements cannot be fulfilled within a certain amount of time, the DAQ will ignore this and continue with the chain of transitions. Optional processes are allowed to re-join the SubArray once they become ready. Lastly there are so-called disturbing processes, like calibration light

3 The H.E.S.S. Experiment

sources which should not be running during normal observations.

Errors can, in principle, occur at any time in any of the involved components. While the controllers and firmware of the hardware devices are responsible for their own safety they do report errors to the DAQ in such cases. The DAQ then informs all other processes and takes care of bringing the entire SubArray or array, depending on the severity of the error, to a safe state [132]. For offline debugging and for the information of the shift crew, a sophisticated logging system has been developed. The log entries have accurate timestamps assigned to them, so that the chain of actions or incidents leading to an error (or to successful operations) can be recovered afterwards.

As the DAQ is a multi-machine, multi-threaded, multi-process software, redundancy and easy recoverability were primary design goals [132; 133]. The software processes are running on a computing cluster consisting of ten eight-core worker nodes, seven four-core servers and several control room machines used for displaying information to the shift crew. The distribution of processes to the nodes is specified in a database, so that in case of a severe hardware failure only a database entry has to be modified such that other nodes take over tasks of the broken node. The $\gtrsim 200$ software programs running on the nodes communicate with each other through a CORBA [134] implementation called omniORB [135]. The nodes host the vast majority of these processes. They are responsible for processing the data received from the cameras and writing these processed data to disk and for hosting the various software processes needed for data taking. Several of the nodes host additional services like web servers which provide access to the various types of data stored on site for collaboration members off-site. The servers deployed on site in Namibia serve a variety of tasks, mostly providing infrastructure and storage capacity to the DAQ. Among the tasks of the servers the most important ones are the configuration of the six virtual networks used on site, the hosting of virtual machines which store operating system images used by e.g. the cameras, the hosting of the central MySQL [136] database containing configuration data for many software and hardware instances and the provision of storage capacity for the data processed by the nodes and for the log files mentioned above. Three servers are involved in storing data from the H.E.S.S. array. They use the distributed file system GlusterFS [137], which is configured such that the nodes write to the global GlusterFS interface and the file system takes care of distributing the received data to the three data servers. A similar approach was chosen for the two servers storing the log files. The major advantage of such distributed file systems is the easy extensibility of the cluster and the increased speed with which data can be written to disk by using multiple servers together. The current maximum data rates of 70 MB s^{-1} can be provided in the current setup. To prevent data loss caused by failures of individual hard drives all servers use redundant arrays of disks. To further increase the resilience of the cluster a sophisticated backup scheme was put into place, so that every important component of the cluster is backed up on a separate GlusterFS instance regularly. As a result of the stability of the DAQ software and the redundancy of the involved components, less than 1% of the overall loss of dark time is due to problems caused by the DAQ [133].

Apart from the low-level tasks described before, the DAQ is also responsible for the interaction of the shift crew with the experiment. It provides an easy-to-use graphical

interface as well as many displays and text information reflecting the state of the array at any time. The interface was designed to be usable by non-expert personnel.

Special attention was paid to the correct and especially fast handling of target of opportunity (ToO) alerts sent to the H.E.S.S. experiment by other observatories via the GCN network [138]. Such alerts are sent in case a GRB is detected. In case of such events the array has to react as quickly as possible, because the time scale of such events is on the order of 30s. When such an alert arrives it is first checked if the position of the source is visible at all, and what type of alert it was. If, according to defined rules, the target is considered worth observing, a special procedure is started. CT 5 starts slewing immediately, while the previous run is stopped and a new one is prepared by the DAQ. If the array is in a transition when an alert arrives, then the current transitions are finished in order to guarantee a consistent state of the hardware and software. The smaller telescopes are treated as optional processes, so that they don't delay the start of the observations. The high voltage supplied to the PMTs is not turned off, only the data taking is stopped until the target is in the FoV of the camera of CT 5. Usually the accuracy of the target position is increased after a short time. If an updated position is sent to the DAQ via the GCN network, the data taking is not stopped but the telescopes reposition while continuing observations [133]. So far no GRB has been detected by H.E.S.S., but given the large effective area of the experiment and the availability of the fast-track procedure described above, interesting science results are imminent. Apart from GRBs, also other types of ToO alerts exist, which often are issued if an astronomical object like an AGN is flaring, i.e. if its flux level increases on short time scales. Such events can last up to several days, hence the reaction time is not as crucial as in case of GRB alerts. Therefore a different procedure is applied, usually involving human decisions on whether to observe the ToO or not.

In the course of this work several improvements have been made to the DAQ. This includes an updated layout of the computing networks, the commissioning of new servers, a revision of the backup scheme deployed on site, the introduction of the GlusterFS file system as well as the addition of new run types dedicated to special purposes and numerous corrections and improvements of the DAQ software. Furthermore assistance has been provided to shift crews as well as to maintainers of hardware components.

3.5 Calibration of the Data

After the data are written to disk, they have to be calibrated offline to account for technical and experimental effects like properties of the trigger, the readout electronics or non-homogeneous PMT responses across the camera.

One important task is to flag unusable pixels as such so that they are discarded in high-level analyses. Reasons for pixels being unusable might be that they were exposed to bright star light, or there might have been problems with the high voltage supply. If the high voltage turns out to be unstable across a run, with a deviation of > 10 V, the pixel is flagged as unusable. The same holds for pixels with very low rates of signals exceeding > 30 p.e. [139], which also indicates hardware problems.

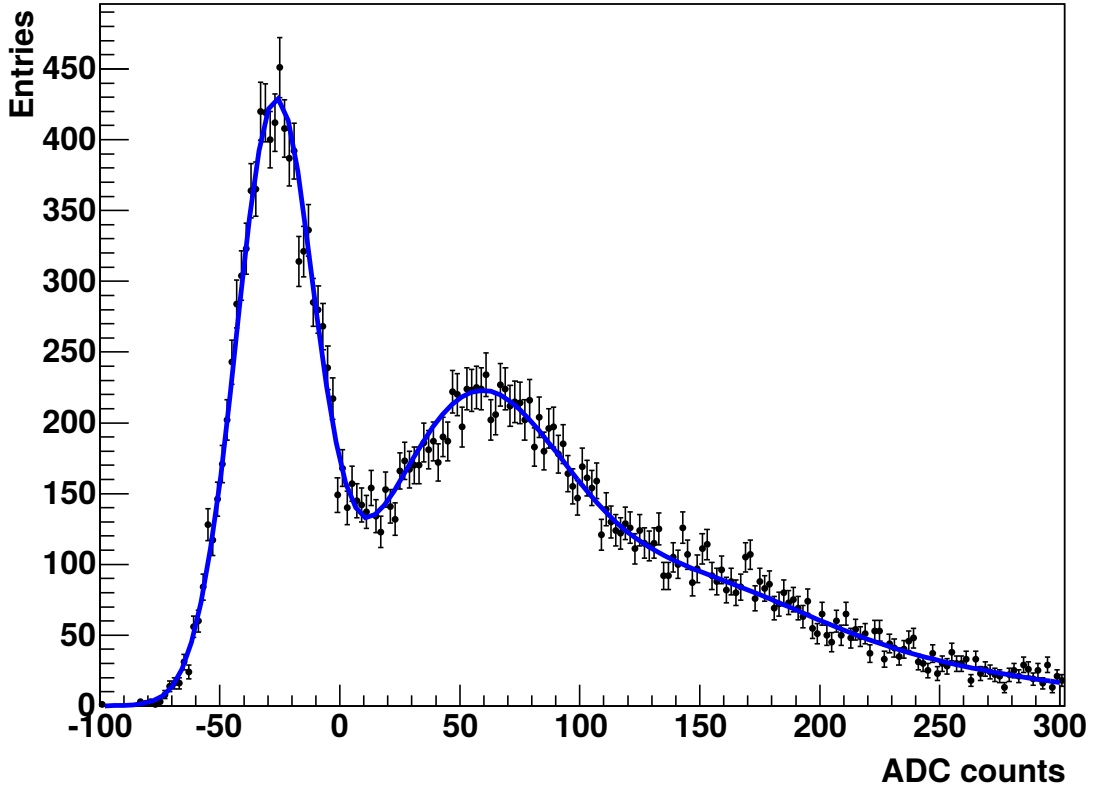


Figure 3.3: ADC count distribution for a single pixel recorded during a SinglePhotoElectron run [139]. See main text for details.

The remaining pixels then have to be calibrated further in order to derive the correct number of photoelectrons corresponding to the measured and digitised PMT signals stored as Analogue to Digital Converter (ADC) counts. Two data acquisition channels are used per pixel differing in their gains, providing a high dynamical range from very low up to very high intensities. The so-called high-gain (HG) channel can be used up to ADC count values corresponding to 200 p.e. for the H.E.S.S. Phase I cameras (400 p.e. for CT 5), the so-called low-gain (LG) channel can be used for signals between 15 and 1600 p.e. (5000 p.e. for CT 5). Outside of these bounds the PMT response does not scale linearly with the amount of incident light anymore.

From the pixel amplitude measured in ADC counts a conversion to the more physically motivated unit of photoelectrons is needed for later use in analyses. This conversion can be derived from distributions similar to the one shown in Fig. 3.3. There the distribution of ADC counts in the HG channel for one pixel recorded during a so-called SinglePhotoElectron run is displayed including a fit using the PMT response function which will not be explained here. For further information about this function the reader is referred to Aharonian et al. 2004 [139]. In SinglePhotoElectron runs, which are performed every few days, the camera is illuminated uniformly by LED pulsers located several meters in front of the cameras in each of the camera shelters. On average, each pixel is illumi-

nated by light with a wavelength of 340 nm [128] with an intensity on the order of 1 p.e. [139]. Two peaks can be seen in Fig. 3.3. The one on the left is the so-called pedestal peak caused by electronic noise in the absence of any light. The position and width of this peak can also be determined from other run types like observation runs where it is determined roughly every minute for both the HG and the LG channels. The second peak is caused by the illumination of the PMT with one photon, causing the emission of one photoelectron. The difference of the positions of this peak and the pedestal peak defines the conversion factor from ADC counts to photoelectrons called gain.

The pixel amplitudes in photoelectrons can be derived from the ADC counts as

$$A^{\text{HG}} = \frac{ADC^{\text{HG}} - P^{\text{HG}}}{\gamma_e^{\text{ADC}}} \times FF \quad (3.1)$$

$$A^{\text{LG}} = \frac{ADC^{\text{LG}} - P^{\text{LG}}}{\gamma_e^{\text{ADC}}} \times \frac{HG}{LG} \times FF. \quad (3.2)$$

Here $P^{\text{LG/HG}}$ is the pedestal position in the respective channel, γ_e^{ADC} is the gain of the HG channel in ADC counts per p.e., HG/LG is the amplification ratio between the HG and the LG channels and FF is the so-called flat-field coefficient which will be explained below [139]. The determination of P and the gain γ_e^{ADC} has been discussed above. The HG/LG ratio is derived during observation runs from the overlap region of the two channels. The region between 30 and 150 p.e. is used for this purpose.

Depending on the amount of incident light hitting the pixel, one or two channels provide estimates of the light intensity. The HG channel is used exclusively up to ADC values corresponding to $A_{\text{max}}^{\text{HG}} = 130$ p.e., from $A_{\text{min}}^{\text{LG}} = 180$ p.e. onwards the LG channel is used solely. In the overlap region where both the HG and LG channels are usable the overall pixel amplitude A in p.e. is calculated for all telescopes as a weighted mean according to

$$A = (1 - \varepsilon) \cdot A^{\text{HG}} + \varepsilon \cdot A^{\text{LG}} \quad \text{with} \quad (3.3)$$

$$\varepsilon \approx \frac{A^{\text{HG}} - A_{\text{max}}^{\text{HG}}}{A_{\text{min}}^{\text{LG}} - A_{\text{max}}^{\text{HG}}}. \quad (3.4)$$

A^{HG} and A^{LG} are the reconstructed PMT amplitudes in p.e. in the respective HG and LG channels [139]. The amplification factors with which the nominal PMT gain value of 2×10^5 is multiplied are 10.1 and 16 for the HG channel and 4 and 0.4 for the LG channel for CT 1–4 and CT 5, respectively [139; 128].

The flat-field coefficient is a quantity assigned to each pixel that is used to describe the deviation of the Winston cone collection efficiencies and photocathode efficiencies of individual pixels from the mean of the camera [139]. Dedicated runs are performed every few days to measure these coefficients. In the corresponding runs, LED flashers for CT 1–4 and a pulsed laser for CT 5 illuminate the cameras uniformly with a high intensity of $\mathcal{O}(200)$ p.e. per pixel [128]. The illumination devices are located in the centres of the telescope dishes. The wavelength of the emitted light is between 390 and 420 nm for the smaller telescopes and at 532 nm for CT 5.

3 *The H.E.S.S. Experiment*

After calibrating the pixels of the cameras also the degradation of the optical efficiency of the Winston cones, PMT windows and especially the mirrors can be corrected for. For this purpose the ring-like images produced by muons passing very close to the telescope are used. As these muons travel through the atmosphere at nearly constant speed the angle at which Cherenkov light is emitted stays almost constant. Given the imaging properties of the telescope mirrors, photons arriving from the same direction are imaged to the same pixel, thus the Cherenkov photons emitted by muons form ring- or arc-like images in the cameras, depending on the impact parameter of the muon with respect to the telescope position. As the emission of Cherenkov photons by muons is understood very well and as all necessary muon properties can be derived from the shape of the images, the intensity of the image can be calculated and compared to the measured intensity [129]. The ratio of these values gives the efficiency coefficient with which all measured shower images have to be scaled. With such an approach the amount of light lost due to degradation can be corrected for in case of air showers which triggered the cameras, but obviously some events will not trigger the cameras anymore if too little light reaches the PMTs. Thus the event statistics will suffer from degradation of the equipment.

4 Monoscopic Reconstruction

The new, large telescope that has been added to the H.E.S.S. telescope array requires new analysis techniques to be developed, because its much larger reflector area leads to a significantly lower energy threshold compared to the smaller telescopes. Currently, three approaches to data analysis utilising the new telescope exist. In the so-called *hybrid* mode, previously existing H.E.S.S. I analysis chains are adapted to be able to work on data from CT 5. Data analysed in this mode needs to be taken with at least two telescopes, as stereoscopy is demanded by the analyses. A different analysis approach is taken in the *mono* mode. In this case data from CT 5 alone is analysed, regardless of the availability of data from CT 1–4. It is obvious that this analysis mode is the only option for lowest-energy gamma-ray air showers which produce so little Cherenkov light that only CT 5 can detect them. Such air showers make up a fraction of more than 60 % of all events accepted by the central trigger. Furthermore, the H.E.S.S. DAQ allows for split observations in several SubArrays as explained in Sec. 3.4, with, for example, CT 5 observing a different source than the other telescopes. This is a reasonable strategy if two astrophysical objects have favourable observation conditions at the same time, and in particular if the low- and high-energy ends of the spectra are of interest, respectively. An example of such a situation would be the contemporaneous observation of a pulsar and a potential PeVatron, the latter being an object capable of accelerating particles up to PeV energies. Another use case for a mono analysis is the analysis of data taken after a GRB alert triggered observations of a specific region in the sky. Due to the significantly faster reaction time and, additionally, the lower energy threshold of CT 5 compared to the smaller telescopes, GRB observations start as soon as the big telescope has reached the observation position, as explained in Sec. 3.4. Such data can be analysed by a monoscopic reconstruction only. The third analysis mode is the so-called *combined* mode, which makes use of both hybrid and mono analyses. In this mode, the availability of data from each telescope is checked on an event-by-event basis, and depending on a certain criterion either a monoscopic or a stereoscopic reconstruction is performed. While the latter analysis type is the desired one, the analysis software infrastructure is not ready yet, so that such an analysis cannot be performed at the time of writing.

In this chapter, a monoscopic reconstruction algorithm called *MonoReco* is presented. Historically, this algorithm evolved from the analysis technique presented in Murach [140], but it has been developed further such that none of the reconstruction approaches remained unchanged. It has already been presented at an international conference [141].

The three key properties any shower reconstruction algorithm has to reconstruct are the direction, the energy and the type of the primary particle which initiated observed air showers. In the analysis presented here the multivariate analysis toolkit TMVA [142] implemented within the ROOT [143] software framework is made use of to reconstruct

all these basic properties. Simulated gamma rays are used to train the neural networks provided by the TMVA toolkit, such that in a later data analysis measurable quantities can be used as input for the trained neural networks which then calculate parameters needed for the reconstruction of the mentioned properties. For the discrimination of gamma rays and hadrons two sets of input data are used. For the gamma-ray part, Monte Carlo simulations are used to provide input distributions, while data from regions in the sky without known gamma-ray sources are used to provide parameter distributions for the measurements' background.

In all separate parts of the reconstruction, the calculation of the desired gamma-ray properties and the input parameters of the neural networks are based on the moments of the intensity distribution recorded by the camera of CT 5. Information from individual pixels is not used directly, since this would require more complex reconstruction concepts in order to not be affected by shower fluctuations or by variations of the images with respect to the location of the image in the camera plane. More sophisticated reconstruction techniques like the ImPACT reconstruction algorithm [144; 145] or the Model++ analysis [146] exist which are based on the analysis of the intensity information stored for each pixel. Working with intensity distribution moments and artificial neural networks only makes the reconstruction algorithm presented here very fast compared to those more advanced techniques. While the ImPACT algorithm takes roughly 20 s to analyse 5000 events, the MonoReco algorithm needs only 1.5 s, thus the execution speed is lower by a factor of more than ten. This is the reason why the latter algorithm is used for on-site analyses providing real-time physics results to the shift personnel and to all members of the H.E.S.S. collaboration. Based on such results, decisions can be made whether a target of observations should be continued to be monitored.

In contrast to the cameras of CT 1–4, the CT 5 camera stores information about the temporal aspects of the recorded image in its output data. For each pixel, the time at which the maximum of the recorded signal was reached within the 16 ns readout window introduced in Sec. 3.2 and the time the signal exceeded the threshold value is stored. None of the reconstruction techniques currently in use for analyses of data recorded with the H.E.S.S. telescopes make use of these data.

In the following sections, the simulation of gamma-ray air showers and of the detector response is explained. Then, in Sec. 4.2, the concept of the neural networks used within the algorithm presented here are discussed. In the subsequent sections, the application of neural networks in the context of direction and energy reconstruction tasks is described, followed by a description of the particle discrimination process. Afterwards, the optimisation of cut values is discussed. In Sec. 4.7, an interpolation procedure used when applying the algorithm presented here to real data is described.

4.1 Monte Carlo Simulations of Gamma-Ray Air Showers

Monte Carlo simulations of EASs and the corresponding detector responses are of great importance in IACT experiments like H.E.S.S. Due to the lack of a direct calibration, which in principle could be provided by means of an artificially created VHE gamma-ray

Parameter	Value														
θ / [°]	0	10	20	30	35	40	45	50	55	60	63	65	67	69	
φ / [°]								0	180						
o / [°]					0.0	0.5	1.0	1.5	2.0	2.5					
MuonPhase					199	200	201	202							

Table 4.1: Angles specifying the directions of the simulated gamma rays used in the presented reconstruction algorithm. θ is the zenith angle, φ is the azimuth angle and o is the offset angle. Also the MuonPhases are listed. See the main text for a definition of these quantities. Simulations for all possible combinations of these values are used in this work.

beam currently not producible, the detector response and fundamental detector properties like the energy-dependent effective area can only be studied through simulations. Furthermore, all shower reconstruction techniques used within the H.E.S.S. experiment are based on simulation results.

The simulation of the detection process is generally separated into two independent parts. First an air shower is simulated, afterwards the detector response to this shower is calculated [147].

At the beginning of the first step, a gamma ray with an energy chosen from a power law-shaped random distribution with an index of 2.0 is simulated. Simulations are grouped with respect to the directions of the gamma rays to be able to understand the impact of the effects of the geomagnetic field and the changing atmospheric depth encountered by the showers at different observation positions. The magnetic field leads to deflections of electrons and positrons in the extended air showers in opposite directions, which alters the photon density in the light pool on the ground. Compared to a shower development without any geomagnetic field, the width of the light pool is increased by up to 20% [148]. Hence also the images recorded by IACTs get broader and less dense, which holds in particular for low-energy events. Images from hadron-induced air showers are less affected since they are, in general, broader than images from gamma ray-initiated air showers anyway. Both the zenith angle, measured from the vertical direction at the position of the observer, and the azimuth angle, measured clockwise from north, influence the orientation of the magnetic field and the atmospheric depth encountered by showers within the field of view of the telescopes. The zenith and azimuth angles for which gamma rays have been simulated are given in Tab. 4.1. Due to the approximated $1/\sin(90^\circ - \theta)$ -dependence of the atmospheric depth the zenith angle spacing decreases with increasing θ .

The simulations of gamma rays and of the development of air showers are performed by the CORSIKA [149] software package. All relevant physical processes are taken into account, most importantly the propagation of particles, the deflection of charged particles in the geomagnetic field, interactions with other particles and scattering processes, particle decays, the energy loss due to ionisation and the emission of Cherenkov light [147].

4 *Monoscopic Reconstruction*

The calculations are sufficiently accurate so that the systematic uncertainty contributed by them are much smaller than the uncertainties introduced by the assumptions about atmospheric conditions. Most of the involved processes listed above are intrinsically of stochastic nature. Thus it is not sufficient to simulate only one air shower per gamma ray energy and arrival direction, but many air showers need to be simulated to understand the level of fluctuation that has to be expected when observing showers from otherwise identical gamma rays. Within the H.E.S.S. experiment, Monte Carlo simulations are used to accomplish that goal. Such simulations make use of the well-known physical formulae and probability density functions describing the stochastic processes mentioned above to calculate the outcome of the individual interactions within the air shower. As an example, based on the decay law of unstable particles created inside the showers the decay or non-decay of a particle within a certain time span is calculated. Therefore the shower development differs from one gamma ray to the next. Usually $\mathcal{O}(10^6)$ gamma rays including the respective air showers are simulated per incident direction.

In the interactions listed above, atmospheric conditions play an important role, as the atmosphere provides scattering targets and as it influences the absorption and scattering of light by large amounts, as stated in Sec. 2.9. Within the simulations used in this work a tropical atmosphere with absorption characteristics caused by aerosol particles similar to a typical desert environment has been assumed. Seasonal variations are not taken into account. The wind speed, which also influences the visibility, is assumed to be 0 m s^{-1} , and the atmospheric temperature profile is set to the average night time temperature profile in Windhoek, which is located approximately 120 km from the H.E.S.S. site. The refractive index of the atmosphere is assumed to be constant in the wavelength range between 300 and 600 nm. Also its dependence on the pressure, temperature and water vapour content is neglected, only the dependence on the density is taken into account [114].

In the second step of the simulation chain the detector response to a gamma ray air shower is calculated. Here the trajectories of the Cherenkov photons reaching the telescopes are traced until they get absorbed either at any interaction with the telescope structures or in the air. At each step the reflectivities and transmissivities of the involved components like mirrors or Winston cones are taken into account. As the mirrors degrade in time the simulations have been repeated several times with different assumptions concerning the reflectivity to compensate for this effect. Tab. 4.1 lists the experimental phases for which simulations are used in this work. These phases are referenced by the so-called MuonPhase, a name indicating the fact that the mirror reflectivities can be measured by comparing images produced by muons passing close to the telescope with images derived from analytic calculations as explained in Sec. 3.5. MuonPhase 200 is the first phase in which CT 5 was part of regular observations starting at June 1, 2013 [150]. Simulations from within MuonPhase 199 are applicable for observations taken during the commissioning phase of CT 5 starting at January 1, 2013. MuonPhase 201 corresponds to a readjustment of the gains of the CT 5 camera on May 22, 2014 and the remaining phase 202 started after a cleaning of the Winston cones on November 11, 2014.

Apart from the optical properties of the involved components also mechanical effects

like the bending of the telescope structures depending on the observation position are taken into account [147]. The bending model is supported by real measurements performed in advance. Also the variable camera position can be specified in the simulations. Here a value corresponding to a focus at 15 km has been assumed as this is the current, fixed focus position.

The detection of the photons by the PMTs is simulated according to the specifications of the PMTs. If a photon has invoked a PMT output signal, the electronics analysing that signal are simulated consecutively. This includes the voltage levels at the involved comparators and discriminators, the response times of all components, the output voltage levels, the time over certain thresholds needed for a signal to pass the respective electronic component, signal digitisation and electric pulse shapes. In summary, all involved electronics in the cameras and the different triggers are simulated to best knowledge [147; 151]. Also pixel shut-down caused by the exposure to bright light from stars is simulated.

The simulation of the detector response is performed in the adaption of `sim_telarray` [152] called `sim_hessarray`, which is a generalised implementation of the `sim_telarray` programme originally written for the HEGRA experiment [147]. As the calculation of the detector response is significantly faster than the simulation of the air shower development it is computationally beneficial not to simulate gamma rays with fixed directions at different points of entry into the atmosphere but to simulate only one gamma ray and the corresponding air shower and to then displace the simulated experiment within a circular area with a radius r_{sim} around the shower axis. This radius depends on the observation direction, in particular on the zenith angle θ , as shown in Fig. 4.1. Furthermore, different pointing positions of the telescopes for a fixed gamma-ray air shower direction can be simulated, so that the location of the gamma-ray source varies in the cameras. The angular distance of the source position from the camera centre is called offset o . The values used in this work are listed in Tab. 4.1.

In addition to the simulation of the air shower development and the simulation of the detector response the effect of the night sky background, introduced in Sec. 3.2, on the detector is taken into account. In the simulations used in this work an NSB rate of approximately 8.8×10^7 p.e. s⁻¹ per pixel of the CT5 camera was assumed. In case of CT 1–4 the rate is approximately 6×10^7 p.e. s⁻¹ per pixel. The effect of the NSB photons on the data is significant, increasing the width of the pedestal distribution depending on the strength of the NSB signal and contributing approximately 1 p.e. per pixel per readout window of 16 ns [139]. Pixels directly illuminated by stars are affected even more. For example, a star of magnitude 4 induces NSB levels of roughly 2.5×10^8 p.e. s⁻¹ in the H.E.S.S.-I cameras. In principle simulations can account for different NSB levels found in different regions in the sky, but at the time of this writing, no such simulations were available. Extending the configurations indicated in Tab. 4.1 by another dimension would be very simple.

An important simulation result is the detected gamma-ray spectrum at the central trigger level. While the input distribution follows a pure power law with a spectral index of 2.0, the spectrum of events which have triggered the cameras such that the central trigger accepts the events shows the intrinsic acceptance of the experiment before

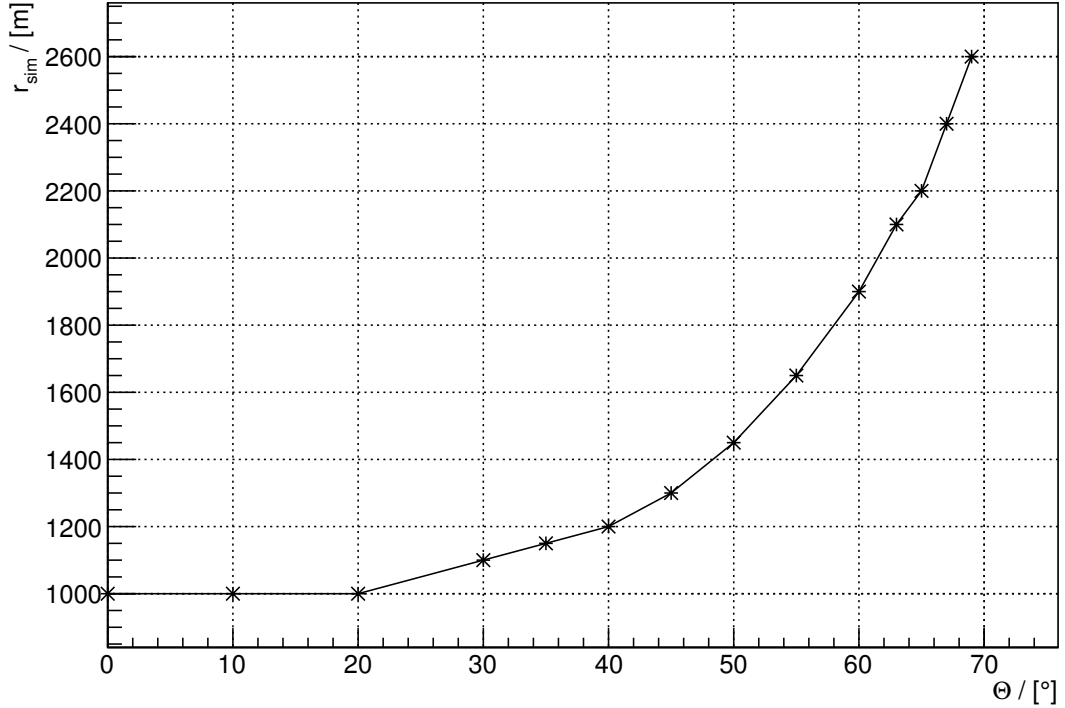


Figure 4.1: Simulated radius around the shower axis within which the simulated telescope array was placed as a function of the zenith angle at which the gamma rays were simulated. The points are connected for better visibility.

applying any selection cuts or reconstruction techniques. A plot comparing the two distributions is shown in Fig. 4.2. It can be seen that the majority of all events does not lead to positive decisions of the involved triggers, especially at low energies, but also at medium and high energies. At the lowest energies, the efficiency is on the order of $4 \times 10^{-3} \%$, at 40 GeV it is roughly 3% and even at the highest energies it is only 12%. In total the efficiency is 0.9%. At low energies the small efficiency is caused by low Cherenkov light intensities. Towards higher energies the intensities the light intensities increase such that they are always sufficient to trigger the cameras in case they light hits the telescope reflector. Since the showers were simulated with fixed incoming directions but varying positions with respect to the location of the telescope array as discussed above, a majority of all simulated showers is too far away from the telescopes to be detectable.

4.2 Artificial Neural Networks

All of the reconstruction concepts introduced in the next sections are based on the usage of artificial neural networks implemented within the TMVA framework. Depending on the use case, two fundamentally different tasks can be accomplished with neural networks. In the first case a real number can be reconstructed, whereas in the second case

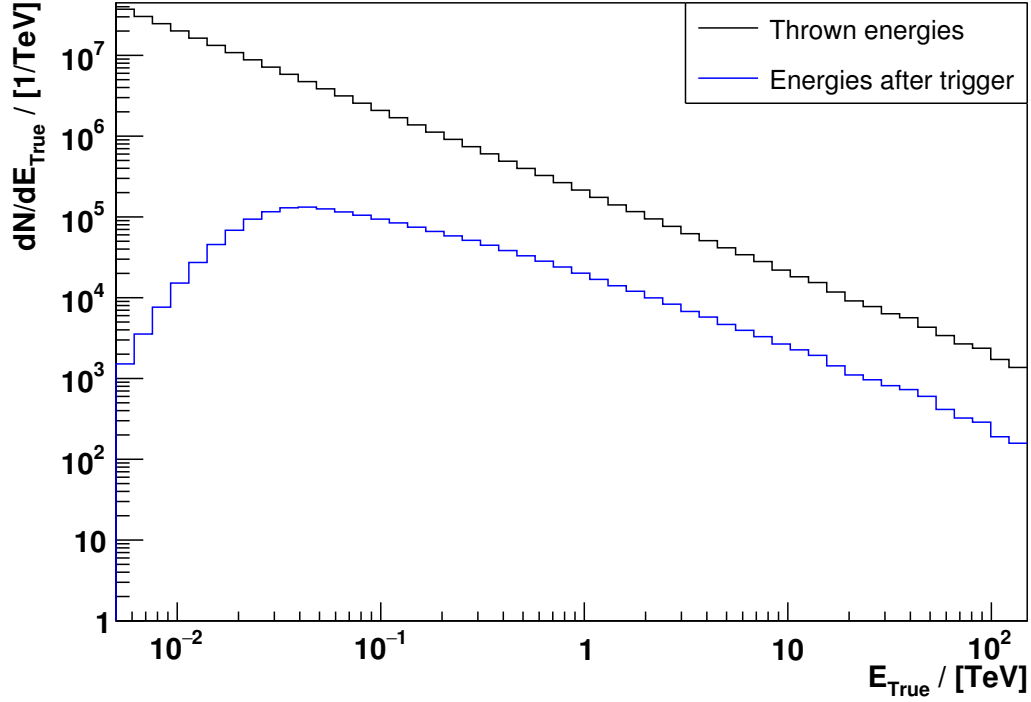


Figure 4.2: Energy distributions at the stage of simulating gamma rays (black) and after passing trigger criteria (blue). These distributions follow from simulated observations at 20° zenith, 0° azimuth and a source offset of 0.5° during MuonPhase 200.

a binary decision can be made. The first case is the method of choice when reconstructing gamma-ray properties like the energy. This mode is called *regression mode*. The second case can be used, for example, to discriminate gamma rays from the dominant background consisting of charged cosmic rays. Hence this mode is called *classification mode*.

In both operating modes there are two distinct phases when working with neural networks. The first phase is called training phase. During this phase the neural network is taught event properties, consisting of both the future input parameters $\vec{p} = p_1, \dots, p_N$ and the future output parameters $\vec{O} = O_1, \dots, O_m$ which later need to be reconstructed with the help of the neural network. Thus all these parameters must be known during the training stage. In this work $m = 1$ and $O \equiv O_1$ in all cases. Usually the input events to the training process come from simulations similar to those described in the previous section, as in case of simulated events all event properties are known. Depending on the type of measurement that has to be performed also real, measured data can be used as input if the data source can be controlled, such that, for example, the direction or the type of particle are known. Internally the neural network then tries to find correlations between the input parameters and the target parameter that it later has to reconstruct based on the input parameters. After the training stage the neural network is ready to be used also with real data. In order to retrieve the output value O , the set of

4 Monoscopic Reconstruction

measured parameters or parameters directly derived from measurements \vec{p} is used as input to the neural network, which then reconstructs the desired value based on the network configuration determined during the training phase.

Before discussing the training phase in more detail, the general layout of a neural network needs to be introduced. Such networks consist of simulated neurons often called nodes that are connected to each other. For simplicity's sake only the layout of a *multilayer perceptron* (MLP), the type of neural networks used in this work, will be discussed, although very different network layouts exist as well. In case of MLPs the neurons are arranged in layers, where each neuron is connected by synapses to every neuron in neighbouring layers but not to neurons in other layers, including the layer the neuron itself is part of. An example of such a layout is shown in Fig. 4.3, where the network used to reconstruct gamma-ray energies is depicted. This network was configured to consist of four layers in total. The first layer is called input layer, the last layer is the output layer and the remaining layers are called hidden layers. Each layer comprises a certain number of neurons, which calculate an output value from a number of input parameters. In case of the neurons in the input layer, the input parameter is one of the input parameters \vec{p} . Thus the input layer consists of N neurons; one extra neuron called bias node that is part of all but the last layers will be discussed later.

In principle the number of nodes in the two hidden layers can be defined freely, but in general it is advisable to use a number greater than the number of input parameters N as this simplifies the detection of hidden correlations between the input parameters, provided that the number of simulated events usable during the training process is large enough. In this work the number of neurons was set to $N_1 = N + 5$ and $N_2 = N + 4$ for the first and second hidden layer, respectively. The number of hidden layers can be chosen freely. According to the Weierstrass approximation theorem one layer with a sufficiently large number of nodes suffices, but in practice two layers with less neurons in total yield the same performance at faster training speeds [153]. The output layer comprises only one neuron, whose output defines the network's response to the set of input parameters \vec{p} . For neurons part of hidden layers or the output layer the input is calculated from the output values of all neurons in the previous layer.

Each neuron is defined by a so-called activation function $A(x)$, $x \in \mathbb{R}$, which defines how the neuron's output is calculated based on the input parameters. The activation function $A_L(x)$ of the neurons in the input and the output layers are fixed within TMVA to be linear functions. The corresponding functions of neurons in the hidden layers can be selected from a set of options. In this work, these activation functions were chosen to be of a hyperbolic tangent form

$$A_H(x) = \frac{e^{2x} - 1}{e^{2x} + 1}. \quad (4.1)$$

While the actual choice of the activation function has limited influence on the performance of the neural network based reconstruction algorithm it is advisable to choose a sigmoidal function in order to gain stability of the network with respect to large fluctuations of the input parameters.

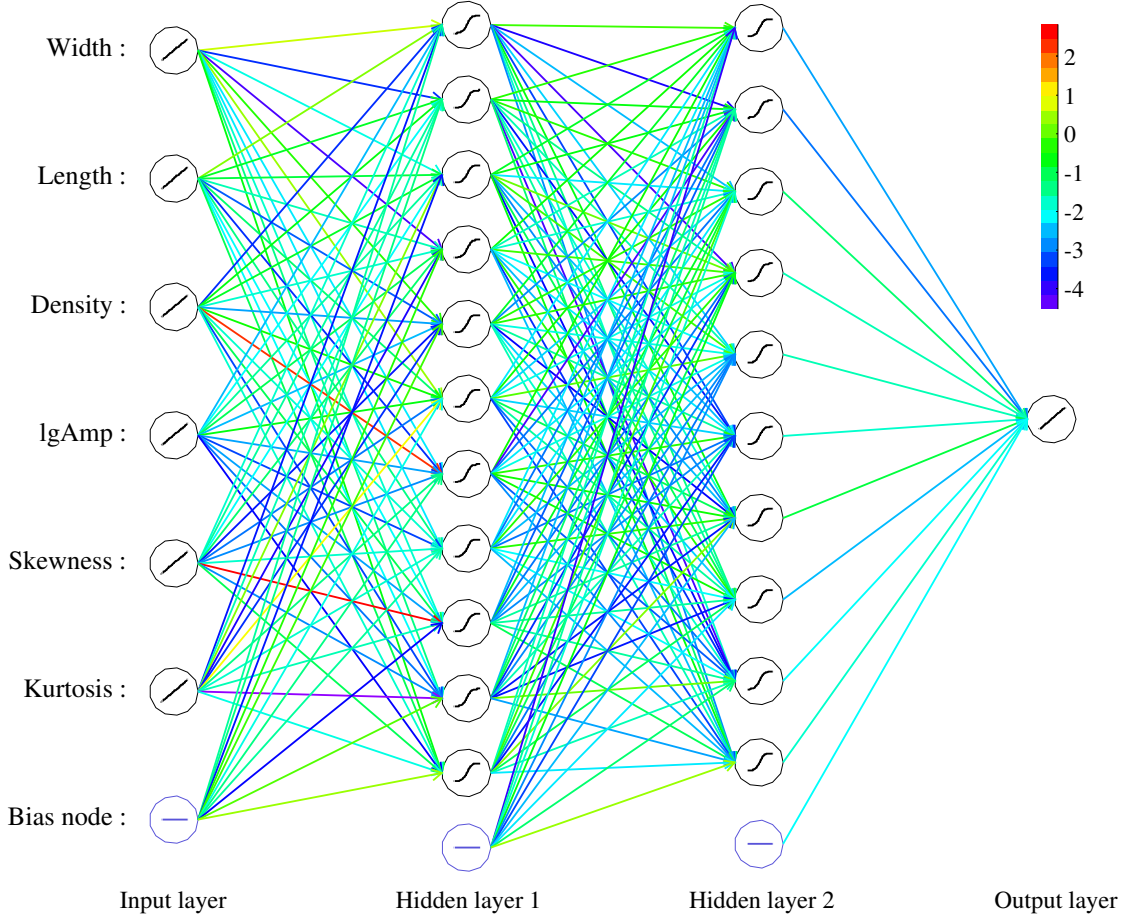


Figure 4.3: Sketch of a neural network as used in this work. The displayed network is used for reconstructing the energies of gamma rays. Input parameters are fed into the input layer on the left, the network's output can be retrieved from the neuron in the output layer on the right. The names of the input parameters are listed on the left. The neurons' activation functions are sketched in the centres of the nodes. The colours of the node connections represent the synapse weight values according to the colour scale shown in the top right corner.

As indicated earlier, the calculation of the neuron's response based on its input parameters depends on the layer it is located in. In the input layer, each neuron uses one of the values \vec{p} as input parameter. The input x_i^I to node i in layer I being one of the hidden layers or the output layer is the weighted sum of outputs of the nodes in the previous layer according to the equation

$$x_i^I = \sum_{j=1}^{N_{I-1}} w_{ji}^{I-1} A_{j,I-1} (x_j^{I-1}), \quad (4.2)$$

4 Monoscopic Reconstruction

where w_{ji}^{I-1} is the weight with which the output of node j in the previous layer $I - 1$ is weighted when used as input to neuron i in the current layer. $A_{j,I-1} \left(x_j^{I-1} \right)$ is the output of node j in layer $I - 1$, calculated using the corresponding activation function. The weights are determined during the training phase such that the network's output value O matches the desired value for all given sets of input parameters \vec{p} and known output values O . Details of the training procedure will be described later.

In addition to the neurons discussed so far, the last neuron in all layers except for the output layer is the so-called bias node. As the output of these neurons does not depend on any input their activation functions provide a constant value as input to neurons in the next layer. While the usage of bias nodes is not strictly necessary it simplifies the training procedure since only one more weight needs to be adjusted instead of re-evaluating the weights of all connections reaching the neuron if a general shift of the input level of one node is needed during the training procedure.

As mentioned earlier, a fundamental part of the training procedure is the determination of the synapse weights. In this work the Broyden-Fletcher-Goldfarb-Shanno (BFGS) method [154; 155; 156; 157] is used for this purpose. This method belongs to the class of supervised learning methods, which makes use of the fact that the target value O_i is known for each set of input parameters \vec{p}_i in both the regression and the classification mode. Based on this knowledge, the weights can be adapted such that they minimise the error function

$$E(\vec{p}_1, \dots, \vec{p}_N | \vec{w}) = \sum_{i=1}^N \frac{1}{2} (O_i - \hat{O}_i(\vec{p}_i | \vec{w}))^2. \quad (4.3)$$

Here N is the number of training events, \vec{w} is the vector of all synapse weights in the network, O_i is the known output value which the network should reconstruct to satisfactory precision and $\hat{O}_i(\vec{p}_i | \vec{w})$ is the network's output for the set of input parameters \vec{p}_i given the current set of weights \vec{w} [153]. Several numerical approaches exist for the determination of the synapse weight values which minimise the error function. The BFGS method makes use of the Hessian matrix H of second derivatives of this function in an iterative process to achieve this goal. In the first step of each iteration the vector of weight changes \vec{D} between iterations $k - 1$ and k is calculated as $\vec{D} = \vec{w}^{(k)} - \vec{w}^{(k-1)}$. \vec{D} contains one element for each synapse in the network. Then the vector containing the gradient errors \vec{Y} is calculated as $\vec{Y} = \vec{g}^{(k)} - \vec{g}^{(k-1)}$, where $\vec{g}^{(i)} = -\nabla E(\vec{p}_1, \dots, \vec{p}_N | \vec{w}^{(i)})$ is the gradient describing the direction in the weight space along which the minimum of the error function can be found starting from the point $\vec{w}^{(i)}$. For the first iteration of the algorithm the vectors \vec{w} and \vec{g} need to be guessed. Within the BFGS method all their elements are set to zero.

Then the inverse Hessian matrix $H^{-1(k)}$ in iteration k can be approximated as

$$H^{-1(k)} = \frac{\vec{D}^{(k)} \cdot \vec{D}^{(k)T} \cdot (1 + \vec{Y}^{(k)T} \cdot H^{-1(k-1)} \cdot \vec{Y}^{(k)})}{\vec{Y}^{(k)T} \cdot \vec{D}^{(k)}} - \vec{D}^{(k)} \cdot \vec{Y}^{(k)T} \cdot H^{(k-1)} + H^{(k-1)} \cdot \vec{Y}^{(k)} \cdot \vec{D}^{(k)T} + H^{-1(k-1)}, \quad (4.4)$$

where the superscript T denotes a transposed vector [153]. The matrix H describes the second derivative of the error function with respect to its parameters \vec{p}_i . The derivation of an exact Hessian matrix is computationally expensive and also only possible if the error function is differentiable at least twice. Thus, in this approach, the Hessian matrix is never calculated directly but approximated as shown in Eq. (4.4). There the matrix is modified by adding correction terms to it in each iteration, which is very fast. Initial values for H and for \vec{w} can be guessed. Often they are chosen to be the identity matrix and a vector containing zeroes, respectively.

Using H^{-1} a new estimate of $\vec{D}^{(k)}$ can be calculated according to the formula

$$D^{(k)} = -H^{-1(k)}Y^{(k)}. \quad (4.5)$$

Afterwards a line search algorithm is applied to find the next estimate of the minimum of the error function. In this iteration step the error function is locally approximated by a parabolic function. By calculating the first and second derivatives the minimum of this parabolic function can be found. This minimum is not necessarily identical with the minimum of the original error function. An estimate of the true minimum can now be derived by evaluating points along a line constructed from the gradient of the error function in the weights space. In the next iteration the newly found point $\vec{w}^{(k)}$ can be used. At this stage the iteration is complete and can be repeated if the improvement of the error function value is large enough to justify another iteration.

The algorithm presented above can be applied at two stages during the training phase. In the bulk learning mode, the algorithm is applied after all training events have been processed, whereas in the online learning mode the algorithm is executed each time a new training event has been processed. With the latter choice the training procedure is slower, but it is also more accurate. Therefore the latter mode is used in the TMVA implementation.

Several other parameters can be specified to adapt the training procedure to the specific use case. First it is specified that each of the input parameters and, in case of the regression tasks performed within MonoReco, also the output parameter are normalised to an interval $[-1; 1]$. This is of little importance for the resulting performance, but this way the weights are easier to compare to each other. Another set of options specifies the treatment of the input data. In order to obtain performance estimates from a statistically independent data set the available data is separated into a training set and a testing set. In this work a fraction of 30% of all available events is randomly chosen for the actual training, while the remaining data is used for the determination of the performance of the MLP network. The performance and especially the convergence is tested after every sixth iteration of the BFGS learning algorithm, which is a good compromise between the time needed for the training and the resulting performance. The overall number of iterations of the BFGS algorithm is limited to 2000. Finally the evaluation of the convergence of the BFGS algorithm can be influenced by parameters. In this work the training is defined to have converged when fifteen iterations in a row have failed to improve the found minimum of the error function by at least 10^{-6} .

After the training phase has completed the neural network is ready to use. It should be noted that also combinations of input parameter values which did not occur during

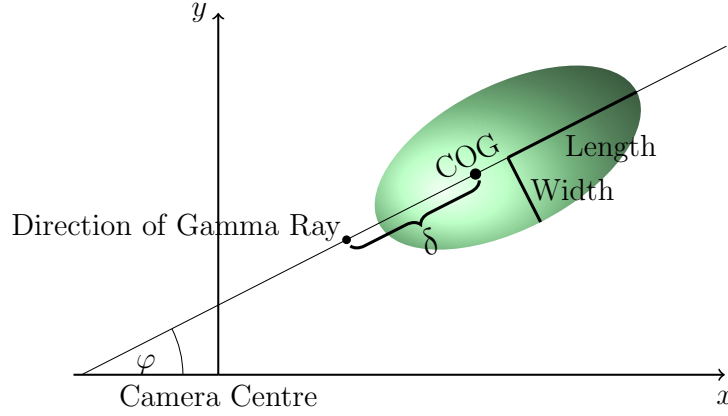


Figure 4.4: Sketch of an elliptical shower image in the camera plane. Brighter colours represent higher intensities measured by individual pixels. The centre of gravity (COG) of the intensity distribution as defined in the main text and the direction of the initial gamma ray are both shown as points along the major axis of the ellipse. Their angular distance is called δ .

the training phase will produce a reasonable network output value because of the shape of the activation functions of the neurons and the linear dependence of the input value x of an activation function on the output values of the nodes in the previous layer. This robustness is important because in the application of MLP networks in the context of air shower reconstruction the parameter phase space can only be covered sparsely during the Monte Carlo simulation phase due to limited computation power.

4.3 Direction Reconstruction

Several properties of the particles initiating air showers need to be reconstructed to enable later high-level analyses. In the reconstruction algorithm presented in this work, the property that is reconstructed first is the direction of the incident particle under the assumption that it was a gamma ray that led to the formation of the observed air shower. The direction reconstruction as well as all other reconstruction parts developed in the context of this work are based on the so-called Hillas parameters, which comprise the moments of the intensity distribution in the camera. Since the image of a gamma ray-initiated air shower is expected to be of a regular, elliptical shape, a Hillas ellipse can be defined by the determination of the centre of gravity (COG) and the lengths of the semi-major and semi-minor axes of the ellipse. The latter two properties are from now on called length L and width W , respectively. An example of such an ellipse is shown in Fig. 4.4. From the intensity distribution, the coordinate corresponding to the centre of gravity can be calculated by determining the intensity-weighted average of the pixel coordinates. In order to calculate the width and the length of the shower image, first the orientation of the major axis of the ellipse, expressed in terms of the angle φ , is determined. Then all higher moments of the intensity distribution are calculated with respect to this major axis. In this frame, the length and the width can be calculated as

the second order moments of the intensity distribution. The third-order and fourth-order moments are the skewness and the kurtosis, respectively.

During the calculation of the Hillas parameters, not all pixel amplitudes are taken into account. Prior to the Hillas parameter determination, an image cleaning procedure is applied. Only pixels with an intensity of at least 5 p.e. which have at least one neighbouring pixel with an intensity of 10 p.e. or vice versa are kept for later analyses. Intensities of pixels failing this image cleaning criterion are set to zero. The main purpose of this procedure is the removal of fluctuations caused by NSB photons. As mentioned in Sec. 4.1 a measured intensity of approximately 1 p.e. per pixel per readout window of 16 ns is expected, thus this noise needs to be removed. The actual signal strength measured in pixels passing the image cleaning criterion is influenced by NSB as well, which is taken into account by Monte Carlo simulations.

After cleaning the image, several other requirements need to be fulfilled for an event to either be used in the training phase or to be analysed further when working with measured data. First it is ensured that parameters like the width or the location of the COG have been assigned non-zero values, which is a technical requirement implemented to avoid working with events that have not been processed correctly. Then two physically motivated requirements need to be fulfilled. The integrated intensity recorded by the camera, called amplitude A from now on, needs to be greater than 60 p.e. after the image cleaning procedure has been applied to guarantee a minimum of information which can be analysed. A second cut requiring a minimum of four pixels contained in the image after the image cleaning is applied with the same intention. Lastly, the angular distance of the position of the COG from the centre of the camera, called nominal distance, needs to be smaller than 1.15° . This requirement is a trade-off, since as few events as possible should be rejected by such cuts and at the same time showers whose images have been cropped significantly by the edges of the camera should be rejected. Given a FoV of the CT5 camera of roughly 3.2° and an average shower size of $2 \cdot L \approx 0.4^\circ$ the given cut value is considered appropriate.

From the Hillas parameters derived from the cleaned images the direction can be reconstructed by following geometrical considerations. Conceptionally, the direction reconstruction is based on the fact that the shower direction is a point that can be expected to be located along the major axis of the elliptical image. This assumption is based on the expected lateral symmetry of the air shower. Thus it is possible to derive the direction from the location of the COG and the orientation of the major axis of the Hillas ellipse, which are measurable quantities, and a displacement value δ , which cannot be measured directly. The latter value can be retrieved from an artificial neural network working in regression mode which has an identical layout as the network shown in Fig. 4.3 apart from the weight values. This network is provided with six input parameters which are correlated with the output parameter. The correlation of the input parameters \vec{p} and the target O can be quantified by the correlation coefficient ρ , which is defined as

$$\rho(p_i, O) = \frac{\text{cov}(p_i, O)}{\sigma_{p_i} \sigma_O}. \quad (4.6)$$

In this equation, σ_{p_i} and σ_O are the standard deviations of the distributions of the

Rank	Variable	Corr. coeff. ρ
1	Length	0.57
2	$\log(A)$	0.26
3	Width	0.09
4	Kurtosis	0.07
5	Skewness	0.07
6	Density	0.03

Table 4.2: List of input parameters to the MLP network used for the reconstruction of the direction of gamma rays together with the correlation coefficients ρ introduced in Eq. (4.6). The listed variables are introduced in the main text. The correlation coefficients describe the correlation of the input parameters with the output parameter δ . The given variable ranking and the correlation coefficients in particular are valid for a training configuration corresponding to a zenith angle of 20° , an azimuth angle of 0° , an offset angle of 0.5° and a MuonPhase of 200.

respective input parameters p_i and the output parameter O [153]. Ordered by decreasing correlation coefficients, the input parameters used to determine the displacement value δ are listed in Tab. 4.2. All variables in this table have been introduced already except for the density D , which is calculated as

$$D = \log\left(\frac{A}{L \cdot W}\right). \quad (4.7)$$

As already mentioned in Sec. 4.1, differences in the recorded images introduced by varying directions of observation or ageing of the instrument for otherwise identical gamma ray air showers are dealt with by using several sets of Monte Carlo simulations. Consequently, one neural network used to reconstruct δ was trained for each combination of zenith, azimuth and offset angles and MuonPhases listed in Tab. 4.1. In principle the correlation coefficients and thus also the ranking of variables can differ from one set of observational parameters to another. The ranking presented in the table results from a training procedure for a zenith angle of 20° , an azimuth angle of 0° , an offset angle of 0.5° and a MuonPhase of 200, from now on called *standard configuration*. For different observation configurations the ranking does indeed change, but overall trends are not affected, so that more important variables are correlated strongly with the output parameter δ for other configurations as well.

The input parameters themselves can be correlated with each other as well. In general, multivariate analysis techniques may yield wrong results if the input parameters are correlated strongly. Despite the fact that MLP networks are not affected strongly by input parameter correlations [153] it is advisable to check for correlations between these variables. The correlation coefficients, given in percent, calculated for each pair of input parameters is shown in Fig. 4.5. Most variables are only mildly correlated with other

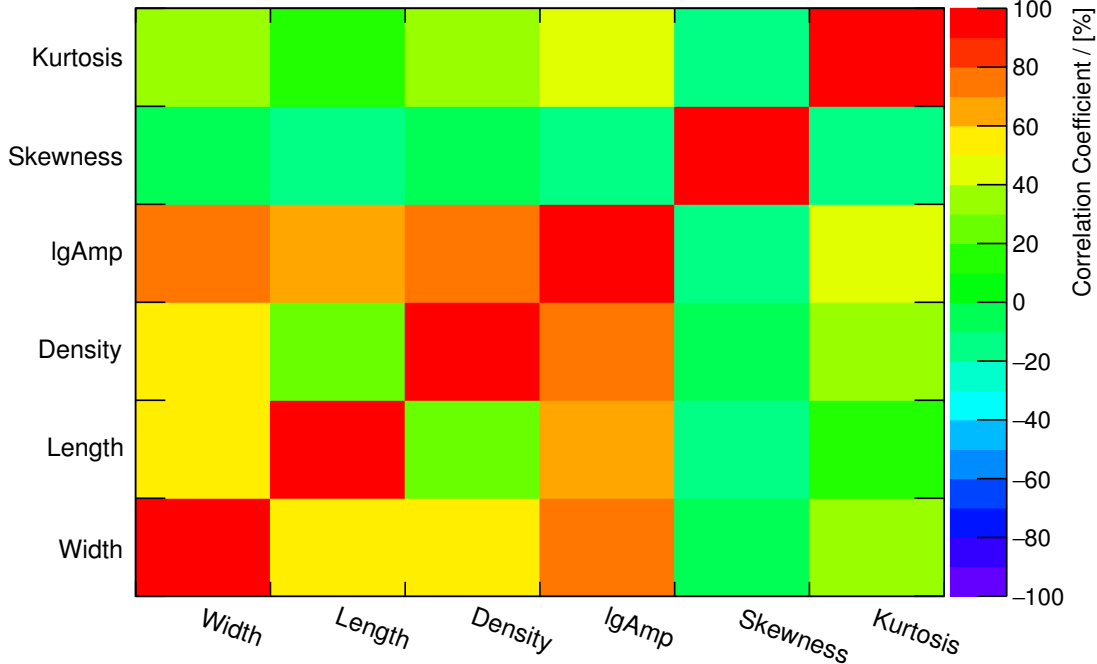


Figure 4.5: Correlations between the input parameters to the MLP networks used to reconstruct the direction and the energy of primary gamma rays given in percent. The logarithm of the amplitude is abbreviated as lgAmp in this plot. This histogram results from a training process corresponding to a zenith angle of 20° , an azimuth angle of 0° , an offset angle of 0.5° and a MuonPhase of 200.

variables. Only the logarithm of the image amplitude is correlated with several other variables at levels of $\gtrsim 60\%$. These variables are the density, the length and the width of the Hillas ellipse. The correlations are expected, since the amplitude is used to calculate the density according to Eq. (4.7), and longer and broader shower images tend to contain higher measured intensities. Nevertheless the image amplitude is an important parameter for the artificial neural networks used to determine δ or the energy of the initial gamma ray as shown in Tab. 4.2 and in Tab. 4.3, therefore the parameter is not removed from the set of input parameters to the neural networks. The correlation measures of the image amplitude with the kurtosis or of the width with the length and the density are on the order of 40–50%. Larger kurtosis values indicate more peaked intensity distributions, which are found in images with larger amplitudes. This hints towards the fact that the intensity maximum, which in turn corresponds to the height at which the air shower had its maximum number of particles, is more pronounced in brighter images. The correlation of the length and the width can be explained by a reasoning similar to the above argument given in the context of the discussion concerning the correlation of the image amplitude with various other parameters. Lastly, the positive correlation of the density and the width needs to be discussed. According to Eq. (4.7) the width appears in the denominator of the density calculation, leading to an anti-correlation.

But with increasing width values the amplitude increases more than linearly, hence the overall correlation is positive. All other correlation measures are comparatively small and will thus not be discussed here.

After providing this set of input parameters \vec{p} to the trained neural network and retrieving the displacement value δ , which is a positive number, from its output, an ambiguity needs to be resolved. There are two possible directions along the major axis in which the value δ can be added to the coordinate of the COG of the intensity distribution. Since the intensity profile is asymmetric, as indicated in Fig. 2.9, the skewness can be used to choose the correct direction. This way the reconstructed direction \vec{d} can be calculated as

$$\vec{d} = \vec{C} - \delta \cdot \begin{pmatrix} \cos(\varphi + \pi \cdot H(-S)) \\ \sin(\varphi + \pi \cdot H(-S)) \end{pmatrix}. \quad (4.8)$$

Here the Heaviside step function H takes as argument the skewness S multiplied by -1 . \vec{C} is the coordinate representing the COG.

The direction of the initial particle can be a point located within the Hillas ellipse or outside of it. This depends mostly on the impact parameter of the shower axis from the telescope. If the shower axis intersects with the telescope reflector then the direction will lie within the ellipse, otherwise it will be located outside of it. This can be explained by the fact that the telescope mirrors focus light beams of equal direction onto one point. Thus it is required that Cherenkov photons with directions deviating from the shower axis in all radial directions are collected by the mirror for the gamma-ray direction to be contained by the ellipse. This is not a strict statement, as shower fluctuations can extend the shower image to one side, so that the direction is contained within the ellipse even though the shower axis does not intersect the mirror. Also the scattering of Cherenkov light can lead to the same effect.

4.4 Energy Reconstruction

A second property of the initial gamma rays that needs to be reconstructed to allow for later high-level analyses is the energy. Instead of the energy itself the logarithm to base ten of this quantity is chosen as target parameter for the corresponding artificial neural network because the range of energies that need to be reconstructed covers about three orders of magnitude. By using the logarithm of the energy as target it is technically easier to weight the differences of shower images of gamma rays at low energies of, for example, 50 GeV and 60 GeV the same as for energies of 5 TeV and 6 TeV. Since especially monoscopic analyses should perform well at low energies the logarithmic approach is clearly desired. In the following the logarithm of the energy is referred to as energy if only qualitative statements are made.

The neural network used for reconstructing the energy is shown in Fig. 4.3. It should be noted that the set of input parameters is the same as used for the reconstruction of the direction of the primary particle. The correlations of the input parameters with the target parameters, however, differ between the two cases. Comparing the correlation coefficients listed in Tab. 4.3 with the values given in Tab. 4.2 it can be seen that

Rank	Variable	Corr. coeff. ρ
1	$\log(A)$	0.87
2	Length	0.71
3	Width	0.68
4	Density	0.60
5	Kurtosis	0.32
6	Skewness	0.13

Table 4.3: List of input parameters to the MLP network used for the reconstruction of the energy of gamma rays together with the correlation coefficients ρ introduced in Eq. (4.6). The listed variables are introduced in the main text. The given variable ranking and the correlation coefficients in particular are valid for a training configuration corresponding to a zenith angle of 20° , an azimuth angle of 0° , an offset angle of 0.5° and a MuonPhase of 200.

the parameters are correlated more strongly with the energy than with the displacement value δ . Consequently the weights assigned to the input parameters of the neural network responsible for the energy reconstruction deviate from the weights determined in the training process of the network reconstructing δ .

4.5 Particle Identification

A crucial and comparatively difficult task the MonoReco algorithm has to perform is the discrimination of gamma ray-induced air showers from hadron-induced air showers. As already mentioned in Sec. 3.2, air showers initiated by hadrons are, in general, more irregular than gamma ray air showers. This is the case because hadrons mostly interact strongly with the nuclei of atoms in the atmosphere. The secondary particles created in such scattering events have masses of order 0.1–1 GeV, which are not negligible with respect to the total transferred momentum. Hence the Lorentz boost they experience is smaller than it would be if lighter particles like electrons were created. Consequently the transverse momentum of the secondary particles with respect to the shower axis is, on average, larger. This leads to a wider distribution of angles with respect to the shower axis under which Cherenkov is emitted, yielding more extended and less regular shower images. Thus the shape of the shower images can be used to distinguish between gamma ray-induced air showers and hadronic air showers. Depending on the results of the first scattering process, however, also hadrons can induce air showers which are indistinguishable from gamma-ray air showers in case most of the energy of the primary particle is transferred to one (or more) neutral pions. These pions decay into two high-energy photons each in 99% of all cases, leading to the formation of an electromagnetic air shower as it would evolve from a primary gamma ray. Also if several sub-showers evolve from the strong, inelastic scattering processes and only one electromagnetic sub-shower is oriented such that it is visible by the IACT (or an

4 Monoscopic Reconstruction

array thereof) the recorded image cannot be discriminated from a gamma-ray air shower [18; 158]. Nevertheless most air showers initiated by hadrons deposit a significant fraction of their energy into hadronic sub-showers, hence they can be identified and discarded by the reconstruction algorithm. This holds especially for nuclei heavier than protons, since the chance of depositing most of the energy of the primary particle inducing the scattering process into one or more dominant neutral pions is on the order of 1%, and since each nucleon scatters independently from the other nucleons, the chance of creating only electromagnetic subshowers is on the order of 0.01^N for a nucleus consisting of N nucleons [18].

To illustrate the importance of a powerful particle discrimination one can compare the rates at which hadronic showers and gamma-ray showers are recorded by CT5. Usual trigger rates are on the order of 1 kHz. This can be put into perspective by calculating a rough estimate of the rate of gamma rays within the effective area of the experiment, a quantity that will be introduced in more detail in Sec. 5.4. From the numbers given in Sec. 4.1 for the average gamma-ray trigger efficiency $\bar{\varepsilon}_\gamma$ of approximately 1% and for the radius $r_{\text{sim}} \approx 1000$ m, an estimate of an energy-independent effective detection area \bar{A}_{eff} can be calculated as

$$\bar{A}_{\text{eff}} = \bar{\varepsilon}_\gamma \cdot \pi r_{\text{sim}}^2 \approx 3 \times 10^4 \text{ m}^2. \quad (4.9)$$

Assuming an integrated photon flux from a strong gamma-ray source, in this case the Crab Nebula, of approximately $\Phi_\gamma = 3 \times 10^{-10} \text{ cm}^{-2} \text{ s}^{-1}$ above an energy of 200 GeV, the rate of detected gamma rays R_γ within the effective area is

$$R_\gamma = \Phi_\gamma \cdot \bar{A}_{\text{eff}} \approx \mathcal{O}(0.1) \gamma/\text{s}. \quad (4.10)$$

A proper calculation would involve an integration over the energy of the differential photon flux and the effective area, but this estimate is sufficient for the purpose of comparing orders of magnitude. Since the calculated number is much smaller than the total trigger rate it can be deduced that most of the triggered events were initiated by hadrons. Hence the separation needs to be as accurate as possible.

In MonoReco, this task is accomplished using an artificial neural network in classification mode. The general network layout is similar to the network shown in Fig. 4.3, only the input parameters differ partly. In contrast to the training procedure for regression networks, two types of input events are used to train the classification network. Monte Carlo simulations of gamma-ray air showers are used to provide the input parameters for the signal type of events, whereas real, so-called OFF data are used as background events. One part of the latter are recorded during dedicated observations of regions in the sky without any known source of VHE gamma rays, while the other part of the OFF data is recorded during observations of known gamma-ray sources. In order to avoid contamination with gamma-ray air shower images, the direction of each event is reconstructed under the assumption that it is a gamma ray, and only those images are analysed further which have reconstructed directions outside a circular sector containing the source of VHE gamma rays [159]. By excluding sectors from the field of view the radial symmetry of the distribution of reconstructed directions of background events is

Rank	Variable	Importance I
1	Width	235.7
2	LoS	98.8
3	Length	91.3
4	Kurtosis	42.7
5	Density	10.0
6	Skewness	0.8

Table 4.4: List of input parameters to the MLP network used for the discrimination between gamma-ray and hadronic air showers. The listed importance I is introduced in Eq. (4.12). The given variable ranking and the importance values are valid for a training configuration corresponding to a zenith angle of 20° , an azimuth angle of 0° , an offset angle of 0.5° and a MuonPhase of 200.

preserved. A set of approximately 600 of such runs lasting 28 min each were used in the training process described here. Events contained in each of these runs were arranged such that they correspond to the observational angles listed in Tab. 4.1. For both the zenith and the azimuth angles the events were grouped such that the angle ranges are centred around the fixed values given in the table. As an example, events observed at zenith angles between 15 and 25° were assigned to the 20° zenith band. Since the best-suited angle band can change over the course of one observation run the assignment is performed eventwise. A MuonPhase assignment is not performed for OFF data because the phase space set up by the parameters from Tab. 4.1 cannot be covered sufficiently by the available data. Also an offset angle separation is not performed since the particles of the diffuse charged cosmic rays arrive from all directions within the FoV and selecting only those showers with a certain reconstructed offset greatly reduces the available statistics. At the same time the gain is limited since the reconstructed direction does not depend strongly on the properties of the OFF events since the direction reconstruction is performed under a gamma-ray hypothesis. Therefore it is more useful to increase the event statistics by analysing all OFF events regardless of their reconstructed direction.

Signal and background events are parameterised using a set of variables listed in Tab. 4.4. All variables have been introduced before apart from a variable abbreviated as LoS, which stands for *length over size*. It is calculated as

$$\text{LoS} = \frac{L}{\log(A)}. \quad (4.11)$$

The linear correlation of the input parameters listed in the table is shown in Fig. 4.6. Most correlations have been discussed in Sec. 4.3 already. Only the variable LoS, which is not used as input to the artificial neural networks performing regression tasks needs to be studied. This new variable is correlated strongly with the length of the Hillas ellipse, which is expected due to the construction the variable as shown in Eq. (4.11). It also is mildly anticorrelated with the density. This is also expected as the density D as defined in Eq. (4.7) increases with increasing A/L , whereas LoS decreases when A/L increases.

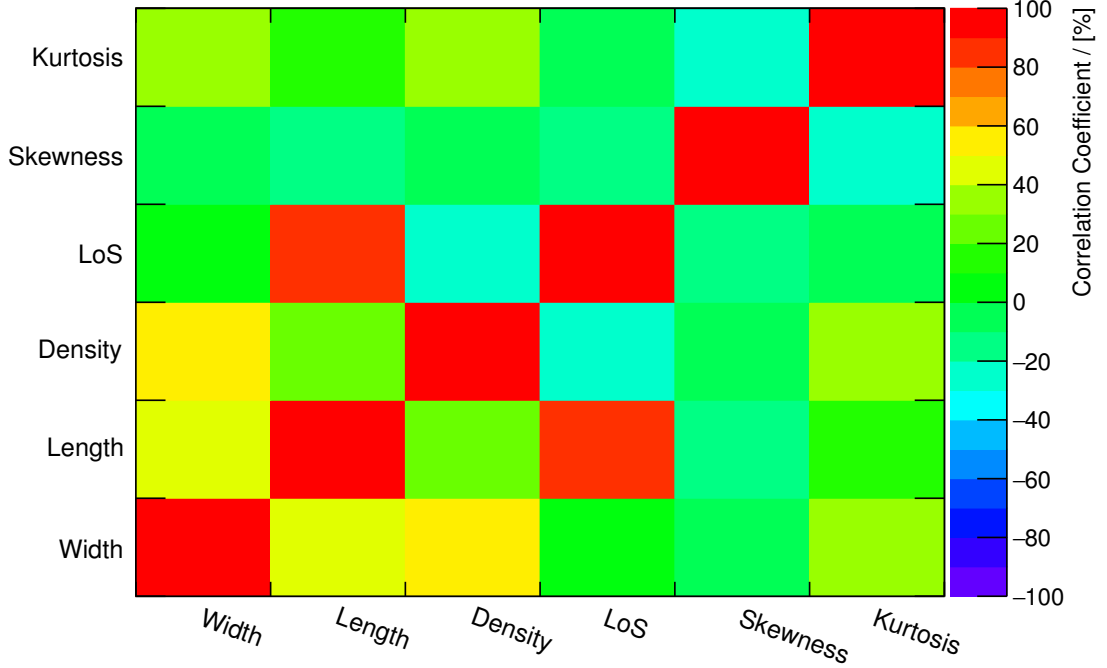


Figure 4.6: Correlations between the input parameters to the MLP network used to differentiate between gamma ray- and hadron-induced shower images given in percent. This histogram results from a training process for a zenith angle of 20° , an azimuth angle of 0° , an offset angle of 0.5° and a MuonPhase of 200.

Examples of the input parameter distributions for signal and background events for the standard angle configuration are shown in Fig. 4.7. The more the signal and background distributions differ the better the respective variable is suited as an input parameter. A measure for the separation power is the importance I_i assigned to each variable i . It is calculated as

$$I_i = \bar{x}_i^2 \sum_{j=1}^{n_h} \left(w_{ij}^{(1)} \right)^2, \quad (4.12)$$

where \bar{x}_i is the mean value of the distribution of the input variable i [153]. The weight of the synapse between node i in the input layer and node j in the first hidden layer is denoted as $w_{ij}^{(1)}$.

From the signal and background parameters the neural network calculates an output parameter ζ . In the training process the weights in the network are adapted such that the ζ distributions for signal and background events differ maximally. This is accomplished by setting the target output value O_i from Eq. (4.3) for event i to 0 for background-type events and to 1 for signal-type events. For the standard angle configuration, the resulting ζ distributions are shown in Fig. 4.8. It can be seen that the distributions belonging to either background or signal events differ significantly. Hence the parameter ζ can be used to discriminate between these event types. The process of determining

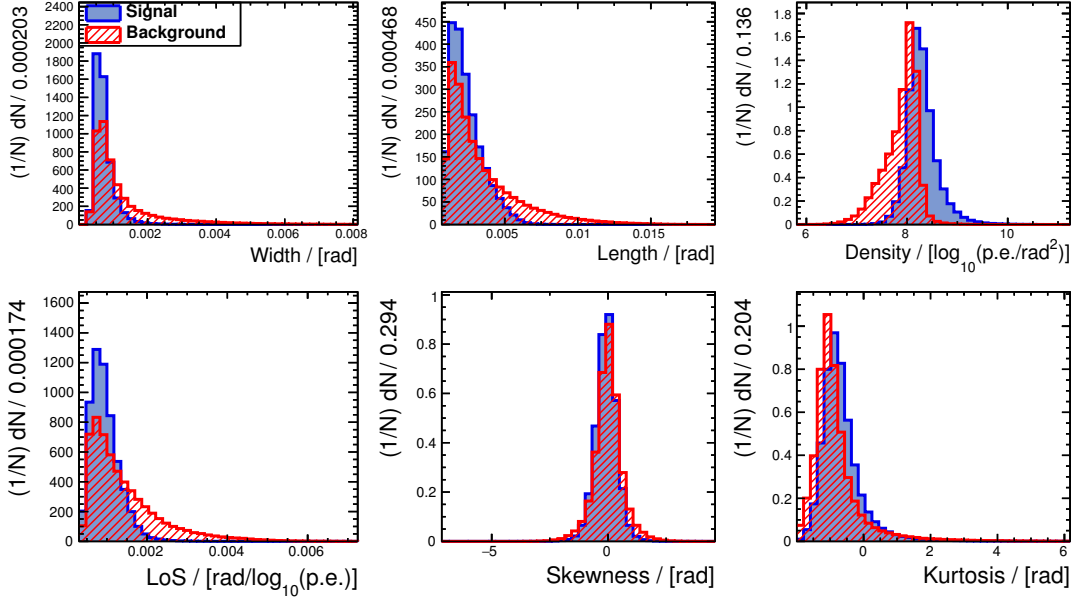


Figure 4.7: Input parameter distributions for the particle discrimination network. Blue histograms represent gamma-ray air shower parameters, red histograms represent the OFF data parameters. The histograms result from a training process corresponding to a zenith angle of 20° , an azimuth angle of 0° , an offset angle of 0.5° and a MuonPhase of 200.

a cut value ζ_0 is explained in more detail in Sec. 4.6. Apart from the two peaks at ζ values around 0 and 1 another, much smaller peak emerges in both distributions at around $\zeta \approx 0.5$. This peak is considered an artifact of the training procedure without any physical meaning. Studying the correlation of the input parameters with ζ by means of the distributions shown in Fig. 4.9 reveals that the population of events forming the central peak consists of mostly small shower images with small values of L and W . Interestingly also the LoS variable is, on average, small for those events, meaning that also small shower images with relatively high intensities can contribute to the peak. Such events are most likely showers that are bright but far away from the telescope. Since small shower events, on average, were induced by low-energy gamma rays the above findings translate to an energy dependence of the zeta variable as shown in Fig. 4.10. In this figure the distribution of ζ values per bin in logarithmic, simulated energy is displayed. As expected, low-energy gamma-ray air showers form the central ζ peak.

In order to eliminate the extra peak in the ζ distribution several tests have been performed, including fine-tuning of network parameters or the addition of new variables based on Hillas parameters. None of those tests yielded the desired result. Only the addition of very powerful discriminant variables showed the desired effect. As an example the impact parameter is such a variable. It is known for simulated gamma rays and can be reconstructed using an MLP network in regression mode. The distributions of the simulated gamma-ray impact parameter and the reconstructed hadron impact parameter differ significantly. However, in applications to data the impact parameter needs to be

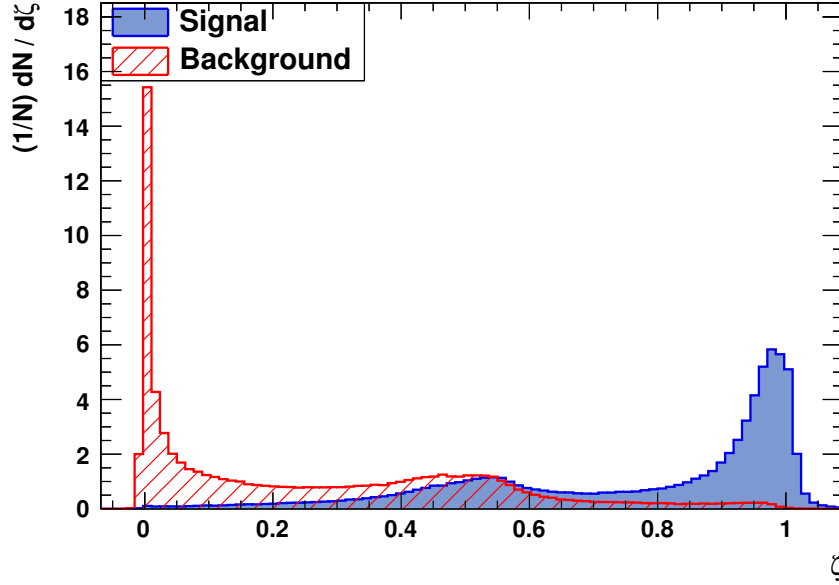


Figure 4.8: Distributions of the discriminant variable ζ for signal (blue) and background (red) events. The histograms result from a training process for a zenith angle of 20° , an azimuth angle of 0° , an offset angle of 0.5° and a MuonPhase of 200.

reconstructed also for gamma-ray showers, hence the impact parameter distribution for such events is different from the simulated distribution and closely resembles the background distribution. Therefore the performance expected from the usage of the simulated distributions cannot be met in reality. If, however, variables providing a separation power similar to the case just described are found in the future, the central peak can be eliminated.

4.6 Cut Optimisation

In the previous section the discriminant variable ζ was introduced. Based on this parameter a decision can be made whether an event shall be considered a gamma-ray or a background event by comparing the calculated value with a cut value ζ_0 . In this section the determination of an optimised cut value is described. Apart from the cut value on the ζ parameter the cut values A_0 on the amplitude A introduced in Sec. 4.3 and on the so-called Θ_0^2 cut parameter need to be optimised. The latter parameter describes the size of the circular region in the camera plane centred on the assumed source position within which the reconstructed direction of an air shower needs to be located. That region is called ON region and has a radius $\Theta_0 = \sqrt{\Theta_0^2}$. A sketch of the camera plane with labelled regions is shown in Fig. 4.11. It should be noted that the position of a source moves in the camera plane due to the rotation of the sky, which is accounted for. By construction the events with reconstructed directions inside the ON region that have been recorded during real measurements will be both gamma-ray and background

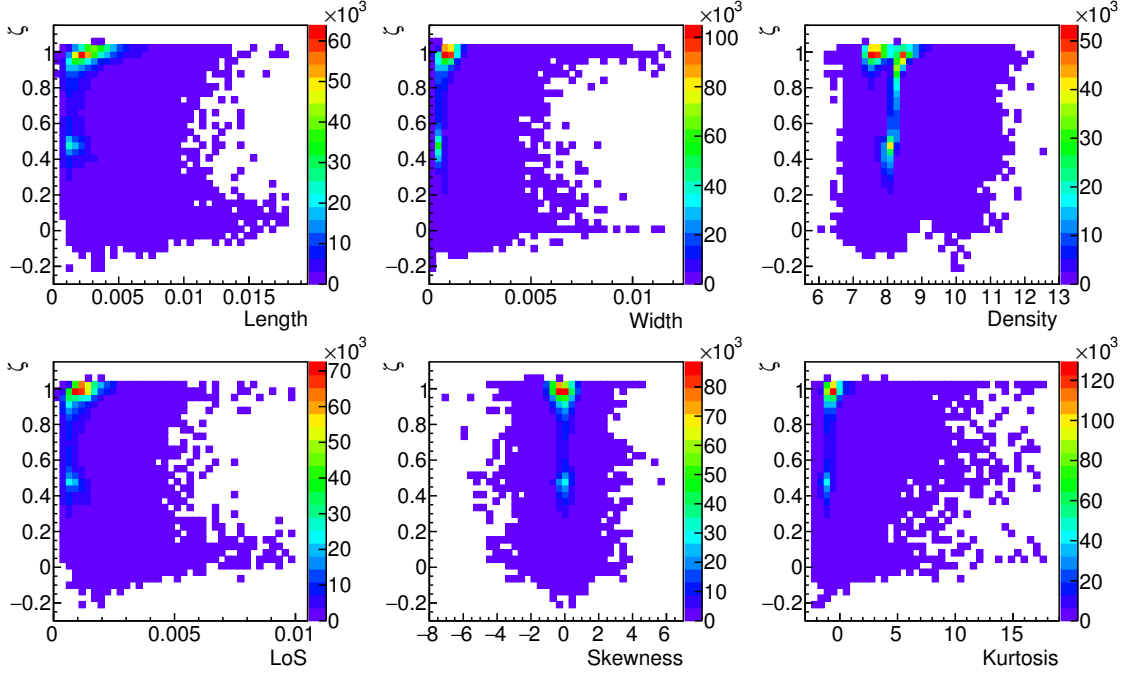


Figure 4.9: Two-dimensional distribution of gamma-ray air shower parameters. The abscissa is the corresponding input parameter of the neural network performing the particle separation, the ordinate is the discriminant variable ζ . Units are similar to those given in Fig. 4.7.

events. Since also a certain fraction of background events will pass the cut on the ζ variable the fractions of signal-type and background-type events are, a priori, unclear. To get an independent estimate of the number of background events a commonly chosen observation strategy is to conduct observations of sources with a wobble offset. In this mode the position of a source needs to be known beforehand, which often is the case since most objects have been detected by experiments covering different wavelength bands. Hence a position estimate is usually available. When observing a potential gamma-ray source with a wobble offset, the telescopes are pointed such that the source position is displaced from the camera centre by an offset o . The acceptance of an analysis like MonoReco is assumed to be radially symmetric with respect to the centre of the camera as will be discussed in Sec. 5.5. Therefore it is possible to define disjoint OFF regions located at a similar offset o in order to estimate the number of background events in the ON region, as indicated in Fig. 4.11. This general approach is also referred to as reflected-background technique [160]. The number of OFF regions depends on Θ_0^2 . In total the number of events with directions located inside one of the OFF regions passing all cuts is N_{OFF} . Since the combined exposure of all OFF regions E_{OFF} is different from the exposure of the ON region E_{ON} , an exposure ratio

$$\alpha = \frac{E_{\text{ON}}}{E_{\text{OFF}}} \quad (4.13)$$

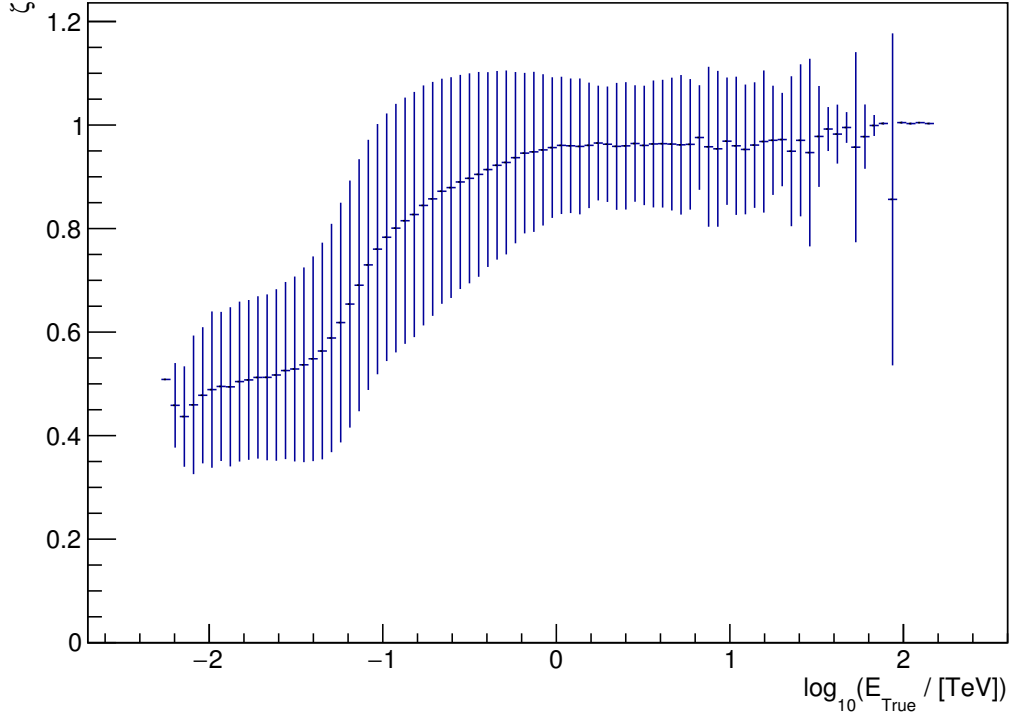


Figure 4.10: Discriminant variable ζ as a function of the simulated energy E_{True} . The points denote the average ζ value per bin in logarithmic energy. Vertical error bars represent the standard deviation of the ζ distribution around the average value per bin in energy. Only shower images passing the basic cuts introduced in Sec. 4.3 are considered in this plot.

is defined to compensate for that difference. With this definition the number of excess events in the ON region ϵ can be calculated as

$$\epsilon = N_{\text{ON}} - \alpha N_{\text{OFF}}, \quad (4.14)$$

where N_{ON} is the total number of events with reconstructed directions inside the ON region. According to Eq. 17 of Li and Ma [161], the significance S of this excess can be estimated as

$$S = \sqrt{2} \cdot \sqrt{N_{\text{ON}} \cdot \ln \left[\frac{1 + \alpha}{\alpha} \frac{N_{\text{ON}}}{N_{\text{ON}} + N_{\text{OFF}}} \right] + N_{\text{OFF}} \cdot \ln \left[(1 + \alpha) \frac{N_{\text{OFF}}}{N_{\text{ON}} + N_{\text{OFF}}} \right]}. \quad (4.15)$$

During the cut optimisation procedure the cut parameters A_0 , ζ_0 and Θ_0^2 are varied, and for each combination of cut parameters the significance is calculated according to Eq. (4.15). The combination of parameters that maximises the significance of the gamma-ray excess is then used as cut parameters.

It is possible to perform this optimisation on real data, for example data from observations of the Crab Nebula. This source is a natural candidate, since it is very luminous

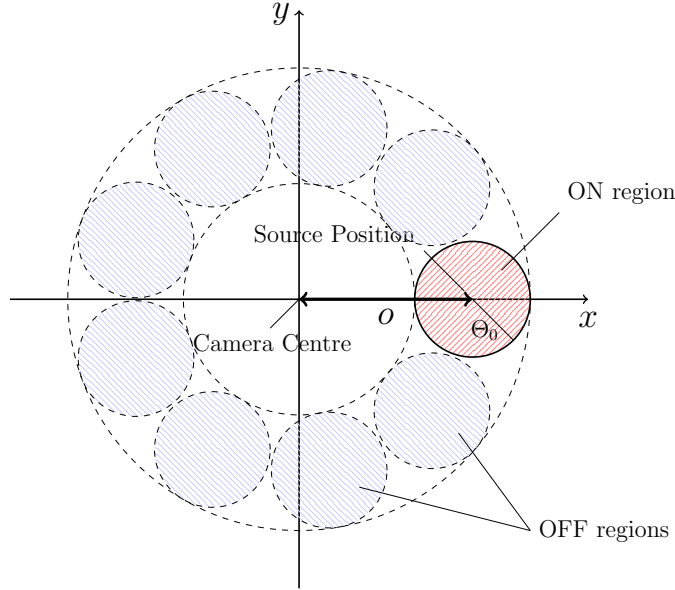


Figure 4.11: Sketch of the camera plane with indicated ON and OFF regions. Each of these regions is displaced from the camera centre by an offset o . The ON region is centred at the location of the previously known position of the (potential) gamma-ray source. The radius of each region is called Θ_0 . The number of OFF regions depends on the choice of Θ_0 .

in the VHE gamma-ray wavelength band, and the index of the differential energy spectrum is typical for galactic sources. A disadvantage of using data from a real source directly is the fact that there might be regions in the sky which need to be excluded from the analysis, so that the ON and OFF regions do not intersect the excluded regions. Regions are excluded if they host either a known gamma-ray source, which would then artificially increase the estimated number of background events inside the ON region and thus influence the significance estimate, or a bright star. In the latter case the NSB level is very high in the corresponding part of the camera. This leads to the camera triggering on NSB-only events not being images of air showers and to an increased intensity of parts of air shower images coincident with the location of the bright star. By excluding such regions of the sky from the analysis these problems are avoided, but then the number of OFF regions is reduced, which increases α . The number and positions of excluded regions is different for each source. In case of the Crab Nebula, two stars need to be excluded. To be able to determine an optimal set of cut parameters independently from the features of the area close to one source a different approach is chosen. In this approach the signal part is taken from Monte Carlo simulations and the background estimate is taken from OFF runs performed in different regions of the sky. Therefore the influence of exclusion regions located in different areas of the sky is reduced, and the freedom to optimise cuts for different spectral assumptions is preserved. The total number of ON events then is the sum of simulated events passing all cuts added to the number of background events inside the ON region, which is estimated as $\alpha \cdot N_{\text{OFF}}$. It is

4 Monoscopic Reconstruction

clear that the numbers of signal and background events depend on the available amount of data, hence, in order to get a realistic ratio of the number of events of each class, the number of signal events needs to be scaled. As a reference, the ratio of the number of signal and background events passing reference cuts of $A_0 = 60$ p.e., $\zeta_0 = 0.9$ and $\Theta_0^2 = 0.016^{\circ 2}$ cuts resulting from a monoscopic analysis of Crab Nebula data is on the order of five. Because the Crab Nebula is the brightest source of VHE gamma rays in the sky a smaller ratio is more realistic for any other source. In the optimisation procedure presented here a ratio of approximately 10% of the value mentioned above is used as target ratio when applying the same cuts.

In order to simulate a typical source spectrum, each simulated gamma-ray event was assigned a weight according to its simulated energy such that the parameter distributions resemble those of a source with a spectral index of 2.7. Other spectral indices are used to optimise cuts for different target classes with, for example, larger spectral indices. The resulting cut sets will not be discussed in this work.

An optimal set of parameters can be found for each different combination of zenith angles, azimuth angles, offset angles and MuonPhases, but the framework called H.E.S.S. Analysis Program (HAP) in which the MonoReco algorithm is integrated does not offer the option to define varying cut values based on the observation position. Therefore the cut definition procedure described above is performed for the standard configuration only. Therefore the performance of the algorithm for other configurations will not be optimal.

During the optimisation, the ζ_0 parameter is varied in steps of 0.01 and limited to values below 0.9, since a cut value above this number would lie inside the peak of the gamma-ray ζ distribution. When analysing real data, the exact shape of this peak depends on many aspects like the atmospheric conditions or the number and position of switched-off pixels in the camera. Thus defining a cut value in a region where the ζ distribution changes rapidly reduces the comparability of results from simulations and from real observations, which has to be averted. Θ_0^2 is varied in steps of $0.002^{\circ 2}$ and A_0 is varied in steps of 10 p.e. For the standard configuration, the significance as a function of the ζ_0 and Θ_0^2 cut values and for a size cut of $A_0 = 60$ p.e. is shown in Fig. 4.12. Along the ζ_0 dimension, the significance increases mostly monotonously, which is expected given the shapes of the ζ distributions of signal and background events. Around the central peak of the ζ distributions, the significance decreases by ten percent, because not only the number of background events but also the number of signal events decreases in this region. The significance is largest at large ζ_0 cut values, since then still a large fraction of gamma-ray air shower images pass all cuts, while most background events are removed. Along the Θ_0^2 dimension, the significance shows various features that need to be discussed. As a general trend, the significance decreases with increasing Θ_0^2 cut values. This is due to the fact that the simulated gamma-ray source is point-like, hence the reconstructed directions are, on average, close to the centre of the ON region. For background events there is no preferred reconstructed direction, thus the number of OFF events is proportional to Θ^2 . Therefore decreasing the size of the ON and OFF regions reduces the number of background events faster than the number of signal events, leading to an increased significance. Only at very small cut values the number of signal

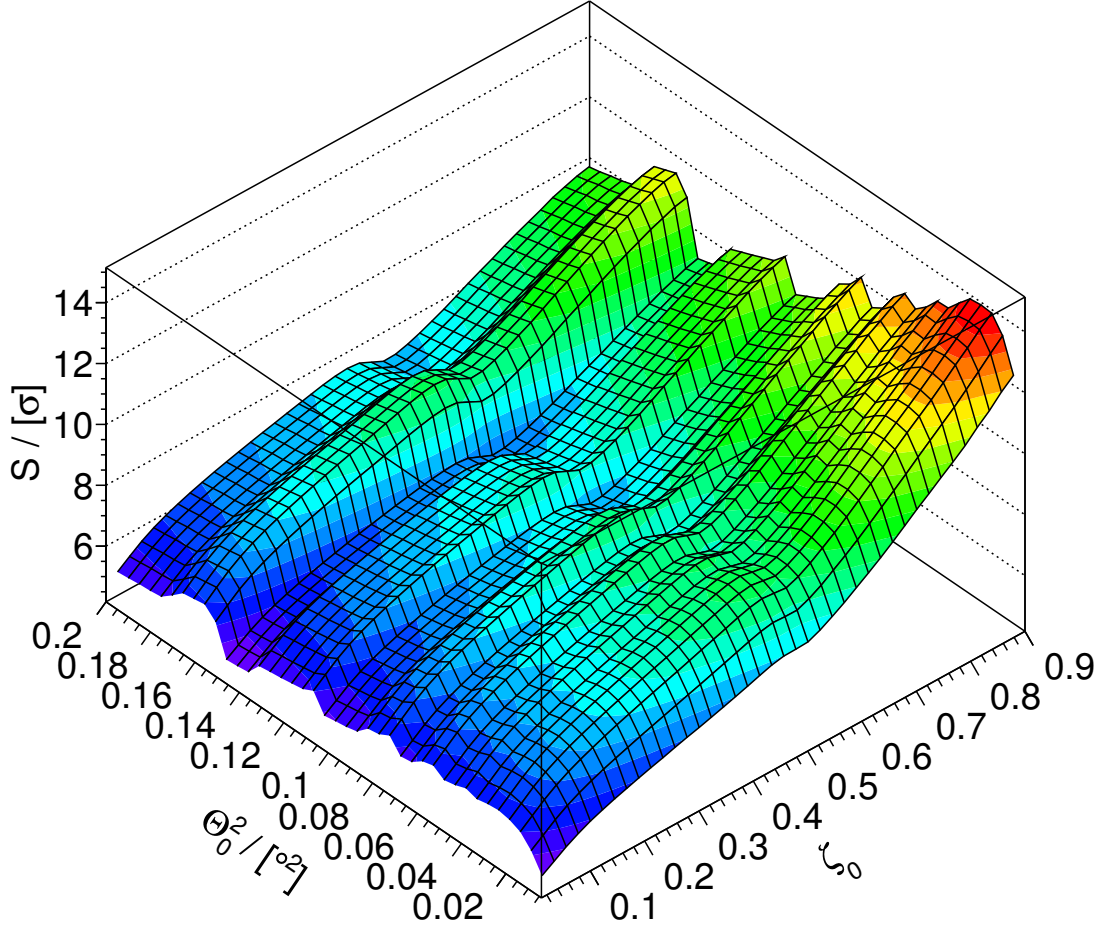


Figure 4.12: Significance S as a function of the ζ_0 and Θ_0^2 cut values. The colour code represents the values on the vertical axis. This surface results from an optimisation procedure performed with a size cut of $A_0 = 60$ p.e.

events is reduced drastically, because the direction reconstruction has a finite resolution. Hence the significance drops rapidly at very small Θ_0^2 values. Another feature apparent in Fig. 4.12 is the existence of discrete steps along the Θ_0^2 direction. This is caused by the discrete number of OFF regions. When increasing the Θ_0^2 cut, the integer number of OFF regions decreases in steps of one. Thus the exposure ratio α , which is a parameter of the significance S , increases in steps as well, while the numbers of ON and OFF events increase smoothly.

The maximum overall significance results from the set of cut parameters listed in Tab. 4.5. The Θ_0^2 value of $0.016^{\circ 2}$, corresponding to a radius of the ON region of $\Theta_0 \approx 0.13^\circ$, is small enough to allow for finding OFF regions during analyses of observational data taken with wobble offsets of usually 0.5° . It should also be noted that the value of the cut parameter A_0 does not have a significant influence on the optimised values of the other two cut parameters and also not on the maximum significance, despite the fact that the shape of the optimisation surfaces resulting from optimisation

Cut Parameter	A_0	ζ_0	Θ_0^2
Cut Value	60 p.e.	0.9	0.016°^2

Table 4.5: Optimised cut values for the three cut parameters A_0 , ζ_0 and Θ_0^2 . These values are derived using a zenith angle of 20° , an azimuth angle of 0° , an offset angle of 0.5° and a MuonPhase of 200.

procedures conducted with different size cuts differ significantly. This is due to the large value of the cut parameter ζ_0 , because such a cut already removes shower images with small amplitudes. Only at size cut values larger than 60 p.e. the maximum significance starts to decrease slightly, by approximately one percent. Hence the mentioned value is chosen as a compromise between large significances and stability against fluctuations of the performance of the gamma-hadron separation caused by variations of atmospheric conditions or broken pixels in the camera.

4.7 Interpolation

All neural networks presented above were trained individually for each of the observational parameters listed in Tab. 4.1. When performing real observations, parameters like the observation position will, however, differ from that discrete set of configurations. To compensate for this a simple, linear interpolation algorithm is made use of. The concept is shown in Fig. 4.13. For a set of parameters for a certain observation configuration θ_C, φ_C and o_C , the available adjacent configurations listed in Tab. 4.1 are determined. Thus for each of the zenith, azimuth and offset dimensions there are two neighbouring parameters for which a neural network has been trained. In total this results in eight neighbours which can be displayed as corners of a cuboid as indicated in the sketch. Depending on the distance of the angles describing the observation position to the observation positions the networks were trained for, the neural network response value for each of the eight corners is assigned a weight. The final parameter to be determined corresponding to the actual observation position is then calculated as the weighted average of the corner values. This procedure is applied whenever one of the parameters δ , the energy or ζ is reconstructed. These final parameters are then used for comparisons with cut values or for the reconstruction of physical parameters like the energy or the direction of the incident gamma ray.

Even though trained neural networks are provided for the entire reasonable phase space of zenith, azimuth and offset angles the algorithm can also be used for configurations outside of the parameter range listed in Tab. 4.1. In such cases the closest available value for the corresponding dimension is used for all corners of the cuboid.

The MuonPhase parameter is not included in the interpolation algorithm. This parameter is used to compensate for variations of the optical efficiency of the telescope and is assigned to observation runs taken in certain time intervals. The degradation of optical components over time influences the optical efficiency slowly but steadily, which

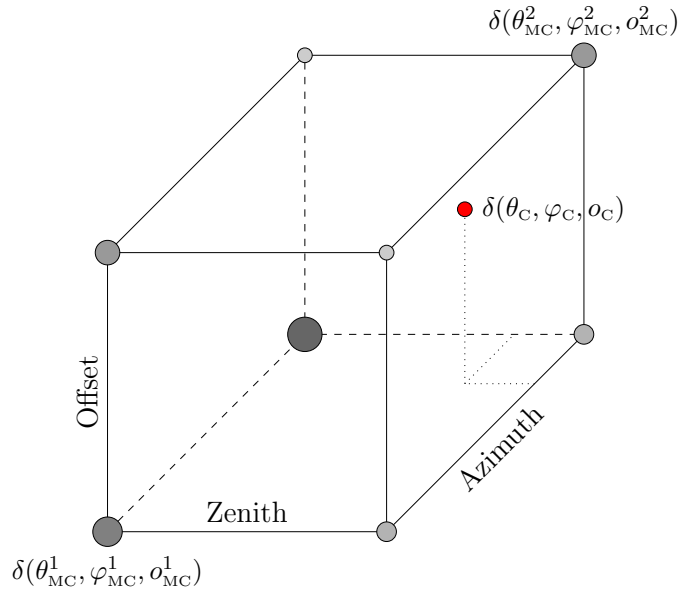


Figure 4.13: Illustration of the interpolation algorithm. In this example the displacement value δ , introduced in Sec. 4.3, at the current observation position θ_C, φ_C and o_C needs to be determined. For each of the neighbouring angle configurations consisting of triples of the angles $\theta_{MC}^{1/2}, \varphi_{MC}^{1/2}$ and $o_{MC}^{1/2}$, the neural networks that have been trained for these angles are used to determine the corresponding δ values. In this sketch the brightness and the size of the spheres in each corner represent the respective value of δ .

could in principle be taken into account by applying an interpolation. In contrast, also the cleaning of optical components or the recoating of mirrors can lead to sudden increases of the optical efficiency. In such situations an interpolation yields worse results, thus it was decided not to include this parameter in the interpolation algorithm.

5 Reconstruction Performance

With the MonoReco algorithm presented in the previous chapter, several parameters of the incident gamma rays can be reconstructed. In this chapter the performance of each of the components of the algorithm will be quantified and discussed. This includes the discussion of the performance of the direction reconstruction in Sec. 5.1, the energy reconstruction in Sec. 5.2 and the particle discrimination in Sec. 5.3. Also the interplay of the different components of the algorithm is explained when discussing effective areas, radial acceptance curves and sensitivity curves in Sec. 5.4, Sec. 5.5 and Sec. 5.6, respectively. Lastly, the performance of the MonoReco algorithm is evaluated on real data. In Sec. 5.7 results from observations of the Crab Nebula obtained from the MonoReco algorithm are compared to previously published H.E.S.S. results.

5.1 Direction Reconstruction Performance

To quantify the performance of the direction reconstruction algorithm, several parameter distributions need to be discussed. One very basic check concerns the distribution of reconstructed directions of simulated gamma rays passing all cuts listed in Tab. 4.5 apart from the Θ^2 cut. Such a distribution is shown in Fig. 5.1a for the standard configuration. Based on this distribution, three groups of events can be identified. The most numerous class of events forms the dominant peak at the simulated direction, which is the intended behaviour. Considering the distribution of reconstructed directions inside a circle of radius 0.8° around the maximum only, the rms of the distribution is approximately 0.11° in both the x- and y-direction. 90% of all events are contained in the mentioned circle. A second group of events forms a ring around the simulated direction. Approximately 8% of all events lie inside this ring, defined by an inner radius of 0.8° and an outer radius of 1.6° with respect to the simulated gamma-ray direction. This group consists of events with low-intensity shower images and only few pixels passing the image cleaning procedure. For such events the sign of the skewness is not a reliable indicator for the direction along the major axis of the Hillas ellipse along which the displacement parameter δ needs to be applied. Since the centres of gravity form a circle around the simulated source position with a radius of approximately 0.6° and a thickness of roughly 0.4° , the ring structure in Fig. 5.1a directly results from this symmetry. A third group of events reproduces the shape of the camera edge on the left side. Approximately 3% of all events contribute to this group. The existence of this group of events is a combined effect of the choice of the nominal distance cut value introduced Sec. 4.3, a wrong skewness sign determination and of the cropping of shower images at the edges of the camera. Due to the image cropping, the COGs are shifted towards the centre of the camera compared to the hypothetical case of having

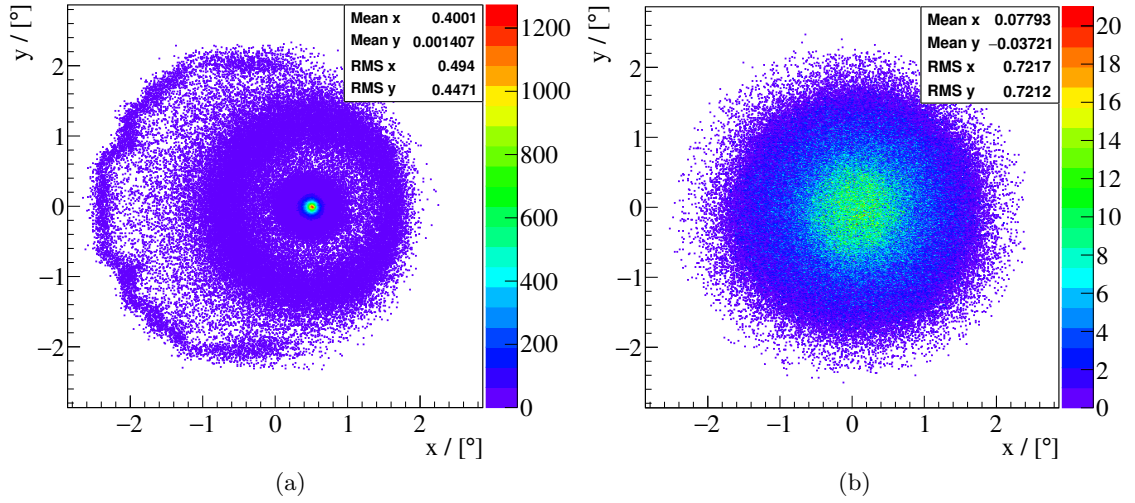


Figure 5.1: Reconstructed directions in the camera plane for shower images induced by simulated gamma rays (*left*) and by real, charged cosmic ray particles (*right*). The gamma rays were simulated at a zenith angle of 20° , an azimuth angle of 0° , an offset of 0.5° and a MuonPhase of 200. The distribution on the right results from 23 runs during which source-free regions of the sky were observed. These runs were conducted at zenith angles between 10° and 25° and azimuth angles between 110° and 250° . Most of these runs belong to MuonPhase 200, only four runs belong to MuonPhase 201.

a camera with a larger FoV. This leads to an aggregation of COGs close to the camera edges. The nominal distance cut is large enough to see the onset of this effect. From the distribution of directions and COGs it can be deduced that the image cropping has only a small effect on the determination of the orientation of the Hillas ellipses, because further checks showed that the lines connecting the reconstructed directions and the corresponding COGs intersect very close to the simulated position of the gamma-ray source. A more accurate determination of the skewness sign would thus remove this subset of events. Also reducing the nominal distance cut by 15% removes this third group of events, but this also leads to a reduction of the number of events passing the nominal distance cut by approximately 28%, which reduces the overall performance of the MonoReco algorithm drastically. Thus this solution is not adopted.

In case of measurements of incident directions of the cosmic-ray background a radially symmetric distribution of the reconstructed directions around the camera centre is expected since there is no preferred direction. Also the direction reconstruction is performed under the hypothesis that observed shower images are initiated by gamma rays, therefore the reconstructed directions are not intended to be correlated with the real incident direction. The distribution of reconstructed directions resulting from 23 observation runs at zenith angles of 10° – 25° is shown in Fig. 5.1b. In both the x- and y-directions, the mean of the distribution is compatible with zero. The fact that the number of entries decreases with increasing radial distance to the camera centre and the

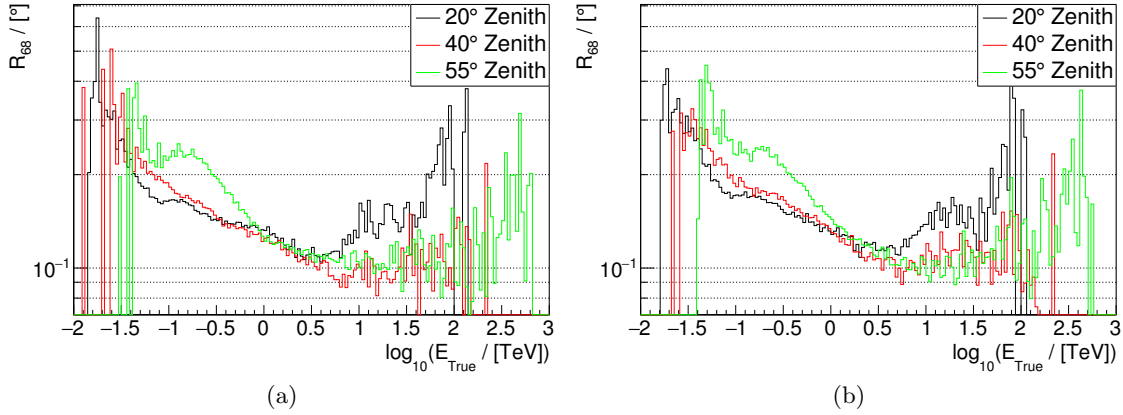


Figure 5.2: Angular resolution as a function of the energy of simulated gamma rays. The curves for simulated gamma-ray source positions at azimuth angles of 0° (*left*) and 180° (*right*) and zenith angles of 20° , 40° and 55° are shown. The offset of the direction of the gamma-ray source from the observation direction is 0.5° , and the MuonPhase is 200 in all cases.

radial symmetry of this distribution are discussed in Sec. 5.5.

An important measure used to quantify the quality of the direction reconstruction is the angular resolution R_{68} , defined as the radius of a circle around the simulated position of a gamma-ray source containing 68% of the reconstructed directions after applying the cuts listed in Tab. 4.5, apart from the cut on the Θ^2 parameter. In Fig. 5.2, this quantity is shown as a function of the energy of simulated gamma rays for several simulated zenith and azimuth angles. Regardless of the azimuth and zenith angles, the angular resolution improves with energy, which can be explained by the fact that shower images become bigger and more regular with increasing energies. The latter behaviour is due to the fact that the shower fluctuations are proportional to \sqrt{A} , so that the relative impact of these fluctuations scales with $\sqrt{A}/A = 1/\sqrt{A}$. At lowest energies, the reconstructed major axis of the Hillas ellipse often deviates significantly from the true orientation, hence the direction can not be reconstructed precisely with the general approach presented here. Furthermore shower images are dominated by fluctuations at low energies [162], thus it is difficult for the artificial neural network to reconstruct the displacement parameter δ reliably. At medium energies, the angular resolution decreases due to the increased regularity and larger amount of information contained in the shower images, mitigating the difficulties mentioned before. Towards high energies the angular resolution becomes larger again. This is an effect caused by image truncation, which is more likely to occur at high energies, since then the shower images consist of, on average, 100 pixels or more, so that despite the cut on the location of the COG discussed in Sec. 4.3 the shower images are large enough to extend over the edge of the camera. This also influences the reconstruction of the displacement value δ . Furthermore, the available event statistics are limited at highest energies due to the simulated power-law gamma-ray spectrum, rendering the neural network less optimised than it is for lower-energy events.

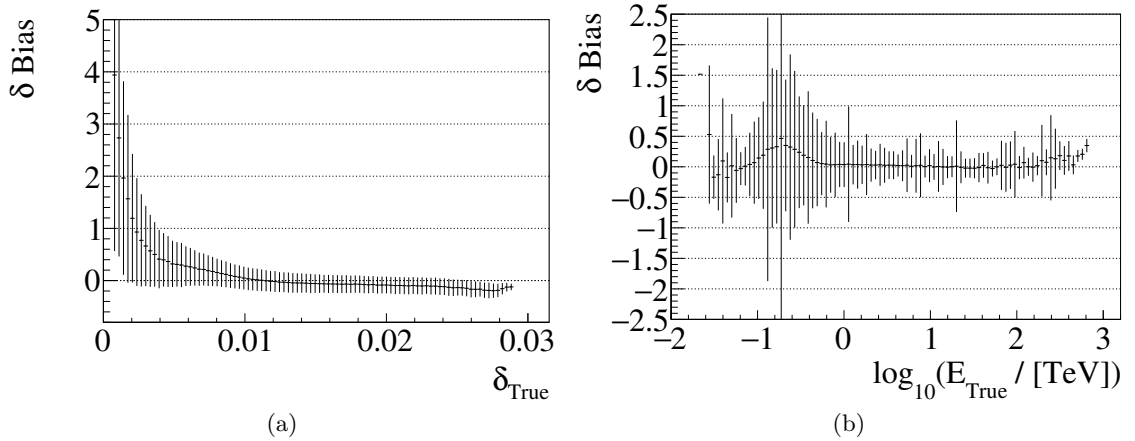


Figure 5.3: Reconstruction bias of the parameter δ needed for the direction reconstruction as a function of the true value of δ inferred from Monte Carlo simulations (*left*) and as a function of the simulated energy of the primary gamma ray (*right*). Error bars indicate the width of the bias distribution per bin on the abscissa. The plots correspond to a simulated zenith angle of 55° , an azimuth of 0° , an offset of 0.5° and a MuonPhase of 200.

Another feature of the curves shown in Fig. 5.2 is the difference between the distributions corresponding to different zenith angles. At energies around a few tens of GeV, the absorption of Cherenkov light in the atmosphere is small enough such that showers can still be reconstructed if gamma rays arrive from close to zenith, but with increasing zenith angle θ the absorption increases such that the same showers become too faint to be detectable. Thus the performance curves corresponding to low zenith angles extend to lower energies, a trend that can also be observed in all performance curves shown later. At higher energies, the stronger attenuation of the Cherenkov light at large zenith angles prevents the camera images from being cropped at the camera edges, thus leading to an improvement of the direction reconstruction performance at higher energies compared to lower zenith angle observations.

The influence of the azimuth angle on the shape of the angular resolution curves is limited. The geomagnetic field introduces an azimuth-dependent effect on the shower development and thus on the orientation of the Hillas ellipses [148; 162]. A comparison of the angular resolution curves in Fig. 5.2a with those in Fig. 5.2b shows that this effect is smaller than 10% in most energy bins.

In all curves shown in Fig. 5.2 a wiggly structure, consisting of a small local minimum followed by a local maximum, can be seen, most prominently in the 55° zenith curves at energies of approximately $10^{-0.5} \text{ TeV} \approx 300 \text{ GeV}$. This is caused by shower fluctuations, as can be inferred from Fig. 5.3a and Fig. 5.3b. In this figure, the bias of the δ reconstruction is shown. The bias is calculated as the mean of the distribution $(\delta_{\text{Reco}} - \delta_{\text{True}})/\delta_{\text{True}}$, with δ_{Reco} being the reconstructed δ value and δ_{True} being the true value of δ as derived from the simulated gamma ray shower images. This bias is plotted

as a function of δ_{True} and as a function of the simulated energy E_{True} , respectively. It can be seen that the bias is very large for very small δ_{True} values, whereas the bias as a function of the energy is, in general, comparatively small. There is a peak in the δ bias distribution occurring at the energies where the wiggle is found in Fig. 5.2. Because on average the reconstructed δ value is too large at these energies, the angular resolution becomes worse, resulting in the peak in the corresponding distributions. The large spread of bias values in the region of the peak indicates that the events contributing to the peak in Fig. 5.3b have very diverse true δ values. This can be explained by the fact that the peak occurs at energies where the shower development is still dominated by fluctuations, so that shower images with very different true δ values appear similar in the camera.

Based on the energy-dependent angular resolution values discussed above, a justification of the choice of the cut value of $\Theta_0^2 = 0.016^{\circ 2}$ can be made. For observations conducted at zenith angles of roughly 40° , the majority of all gamma-ray candidates passing all cuts for typical gamma-ray spectra have reconstructed energies of several hundred GeV. Assuming that the energy reconstruction is good enough to reconstruct the energy with low biases at such energies, which will be shown in Sec. 5.2, the majority of all these gamma rays will have real energies of the same order of magnitude. Hence the angular resolution is better than approximately 0.15° in this regime, which matches the size of the ON region of $\Theta_0 \approx 0.13^\circ$.

A function that is related to the angular resolution is the PSF of the gamma-ray reconstruction algorithm. The PSF describes the distribution of reconstructed directions of gamma rays coming from a point-like gamma-ray source located at infinity in the focal plane of the camera. More precisely, this function represents the expected number of events as a function of the squared angular distance of the reconstructed direction from the assumed target position, hence a radial symmetry is assumed when calculating the PSF. Since the angular resolution depends on parameters like the observation position or on the energy of the primary gamma rays, the PSF needs to be calculated individually for each set of observational data and for each assumed gamma-ray spectrum. For real observations the pointing position changes during the course of an observation run. Therefore the PSF is calculated as a weighted average of the PSFs pre-computed for the parameters listed in Tab. 4.1. For each of those parameter combinations, the energy-dependent PSF is used to calculate one energy-independent PSF based on an assumed spectral power-law index. The overall, averaged PSF is often assumed to follow a distribution called King's function [163], which is defined as

$$K(\Theta^2) = \frac{1}{\pi\sigma^2} \left(1 - \frac{1}{\gamma}\right) \cdot \left[1 + \frac{1}{2\gamma} \cdot \frac{\Theta^2}{\sigma^2}\right]^{-\gamma}. \quad (5.1)$$

In this formula, σ and γ are fit parameters describing the width and the slope of the profile, which depend on the performance of the direction reconstruction algorithm. The integral of this function is one, so it needs to be scaled to the maximum excess occurring in the FoV. Examples of the PSF will be shown when discussing results from analyses of real observations.

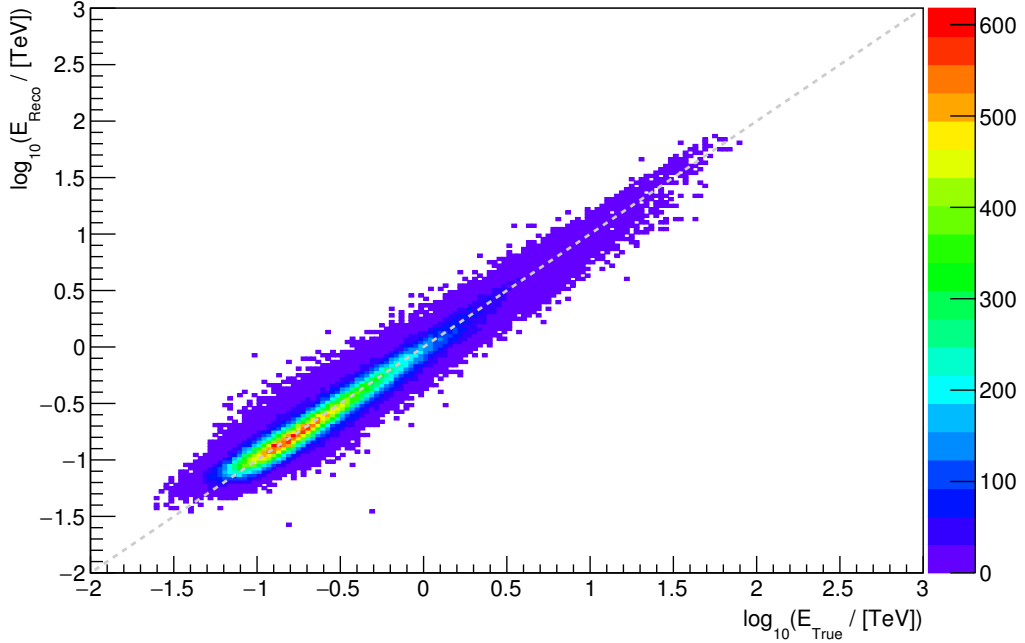


Figure 5.4: Reconstructed energy E_{Reco} as a function of the simulated gamma-ray energy E_{True} . The dashed line represents the identity relation. Colours denote the number of events per bin. The shown distribution corresponds to a zenith angle of 20° , an azimuth angle of 0° , an offset angle of 0.5° and a MuonPhase of 200.

5.2 Energy Reconstruction Performance

The discussion and quantification of the performance of the energy reconstruction is based on the two-dimensional distribution of reconstructed energies as a function of the true, simulated energy of gamma rays shown in Fig. 5.4. This distribution is often referred to as energy migration matrix. In the plot, the reconstructed energies of all simulated gamma rays whose shower images pass the quality criteria specified in Tab. 4.5 are visualised. Apart from the shape of the distribution, which will be discussed in the next paragraph, the number of events passing all cuts shall be discussed. Since the simulated differential gamma-ray spectrum is a power law with an index of -2 , the number of events passing all cuts should decrease accordingly with increasing simulated energy. At energies above several hundreds of GeV this behaviour is seen, but at energies lower than this, the number of events increases with simulated energy. This is due to the fact that shower images from gamma rays with very low energies are less likely to pass all cuts than shower images from high-energy gamma rays. The shape of the acceptance curve as a function of the energy is studied in more detail in Sec. 5.4.

Apart from the numbers of events, the shape of the distribution is of particular interest. Using an ideal energy reconstruction, the distribution would be a line similar to the dashed line shown in Fig. 5.4. The reconstruction algorithm implemented in MonoReco yields a distribution that follows the identity relation closely. In order to quantify the

agreement of the reconstructed energies with the simulated energies, the parameter

$$d_{ij} := \frac{E_{\text{Reco},ij} - E_{\text{True},i}}{E_{\text{True},i}} \quad (5.2)$$

is examined. This quantity d_{ij} is the relative deviation of the reconstructed energy $E_{\text{Reco},ij}$ from the true energy $E_{\text{True},i}$ in bin i along the abscissa and bin j on the ordinate. Based on the relation defined in Eq. (5.2), the energy reconstruction bias b_E and the energy resolution r_E can be constructed. The bias is defined as

$$b_{E,i} = \frac{1}{N_i} \sum_{j=1}^{N_i} d_{ij}, \quad (5.3)$$

where $b_{E,i}$ is the bias in bin i of the simulated gamma-ray energy E_{True} , N_i is the number of entries in the respective bin, and $E_{\text{True},i}$ is the centre of the bin on the abscissa. The energy resolution is defined as the standard deviation, calculated as the square root of the variance, of the distribution d_{ij} . The mathematical definition reads

$$r_{E,i} = \sqrt{\frac{1}{N_i} \sum_{j=1}^{N_i} d_{ij}^2 - \frac{1}{N_i} \cdot \left(\sum_{j=1}^{N_i} d_{ij} \right)^2}. \quad (5.4)$$

Similar to the energy reconstruction bias, this quantity is calculated for each bin i along the abscissa.

The distributions of b_E and r_E as functions of the simulated gamma-ray energies for events passing all cuts given in Tab. 4.5 are shown in Fig. 5.5 for various zenith and azimuth angles. In Fig. 5.5a and Fig. 5.5b it can be seen that the influence of the azimuth angle on the energy reconstruction is marginal. The energy threshold depends on the zenith angle, as already discussed earlier. At energies close to this threshold the energy reconstruction bias is large and positive, regardless of the zenith and azimuth angles. Fluctuations in the shower development cause this behaviour, since showers which produce more Cherenkov light at the same simulated gamma-ray energy have a much higher chance of being detected than the average shower at the same simulated energy. Thus only non-representative shower images resembling those of showers initiated by gamma rays with larger simulated energies are used to train the corresponding artificial neural network. With increasing energy the effect of these fluctuations close to a threshold vanishes, so that at energies of approximately 100 GeV the bias is smaller than 10% in case of observations at zenith angles of 20°. For all zenith angles, the bias then stays at a level of a few percent for two or more orders of magnitude in simulated energy. At the highest energies the statistics per bin become small, so that the statistical error on the bias estimate becomes larger. Also a trend towards large negative bias values can be observed. Similar to the situation at lowest energies, fluctuations in the shower development are the main reason for this behaviour, since showers which produce less Cherenkov light than the average shower at a certain simulated energy are more likely to be contained entirely in the camera. Therefore these events are less likely to be removed

5 Reconstruction Performance

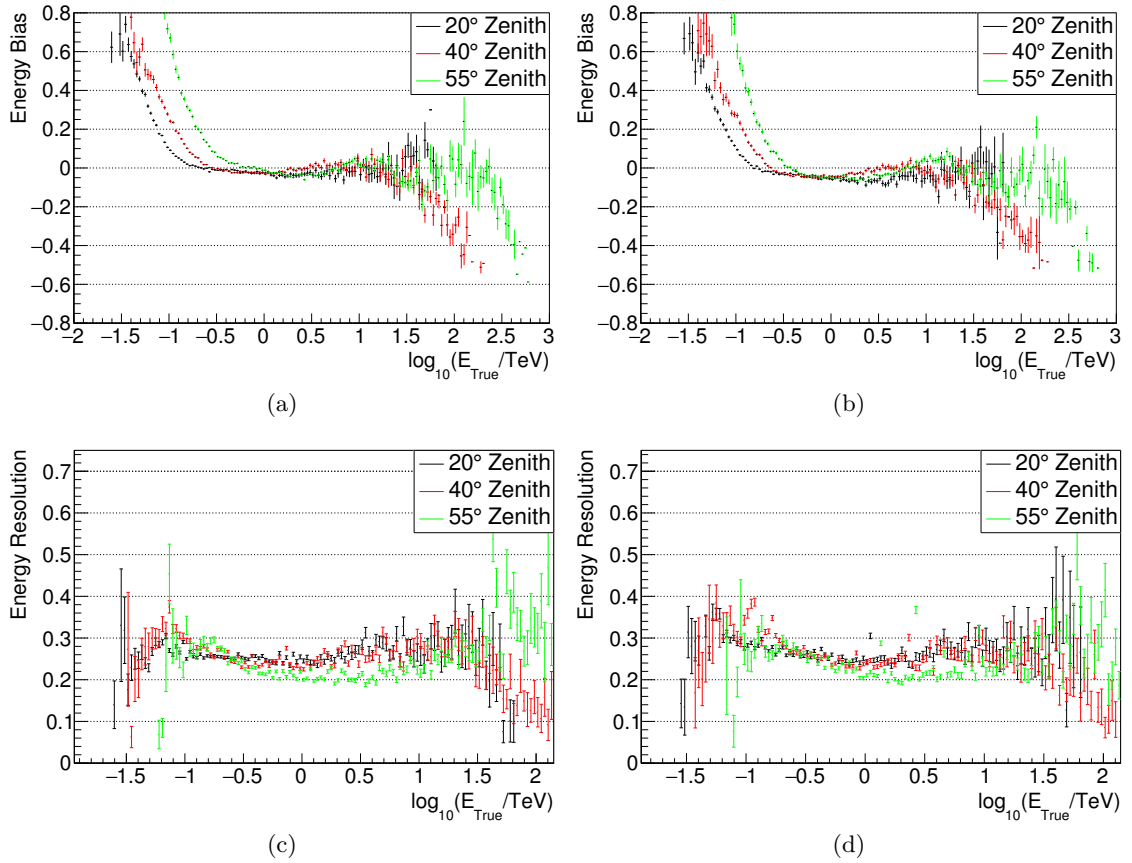


Figure 5.5: Energy reconstruction bias curves (*top left* and *top right*) and energy resolution distributions (*bottom left* and *bottom right*) for several zenith angles as indicated in the legends. Plots on the left (right) side correspond to azimuth angles of 0° (180°). The MuonPhase is 200 in all cases. Error bars denote the statistical error on the bias and on the resolution, respectively.

by the cut on the ζ parameter, so that the remaining events passing the cut have shower images which resemble those of the gamma rays with smaller simulated energies.

For a zenith angle of 20° , the energy resolution stays at a level of 30 % for more than three decades of simulated gamma-ray energies. At energies below $10^{-1.3} \text{ TeV} \approx 50 \text{ GeV}$, the resolution is still comparable to the level at higher energies, but due to the small number of events passing cuts at these energies, the statistical errors are very large. Furthermore the resolution changes significantly from one bin to the next, which is due to the fact that the Cherenkov light intensity is dominated by fluctuations at lowest energies. At the high end of the energy scale the same effects as discussed in the context of the energy bias lead to a rapid decrease of the resolution. Similar to previous performance curve comparisons, the azimuth angle has a very small influence on the energy resolution.

To put the performance of the energy reconstruction algorithm into perspective, one can compare the energy bias and resolution values to systematic uncertainties imposed on

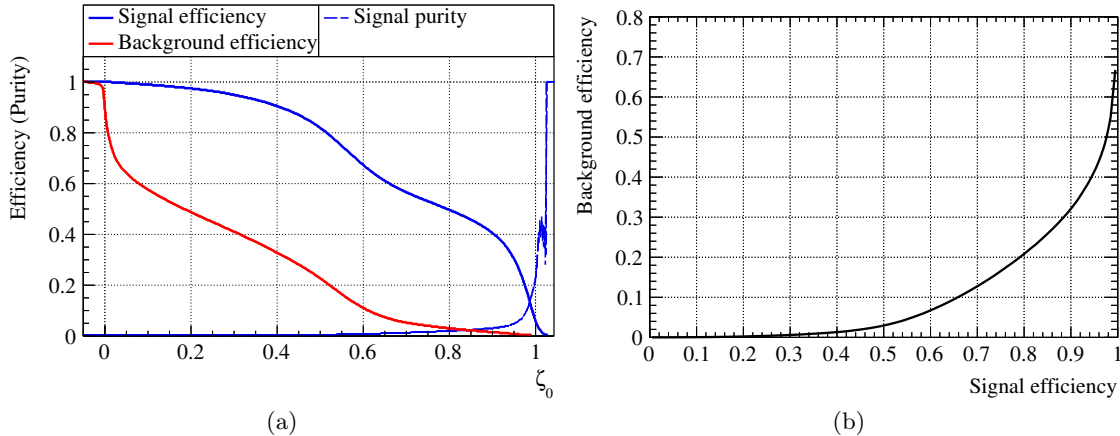


Figure 5.6: *Left*: Efficiency with which signal-type and background-type air shower images pass the cut on the ζ variable as functions of the cut parameter ζ_0 . In this plot also the purity is shown, which is defined as the fraction of signal events in the total sample of events passing the cut on ζ_0 . A ratio of the input number of signal events to the input number of background events of 10^{-3} was assumed. *Right*: Efficiency with which background events pass the cut on the ζ variable as a function of the signal efficiency. All distributions correspond to a zenith angle of 20° , an azimuth angle of 0° , an offset angle of 0.5° and a MuonPhase of 200.

measurements by instabilities of atmospheric conditions and effects of the geomagnetic field on the shower development. These sources of systematic uncertainties account for an uncertainty of the energy scale of approximately 20% [6]. This number needs to be compared to the energy bias, since the latter acts in the same way on the energy scale as the varying atmospheric conditions. Over most of the energy range, and in fact everywhere in the energy range relevant to most parts of standard data analyses as will be explained in Sec. 5.4, the systematic uncertainty dominates the overall uncertainty. The energy resolution is larger than the values obtained from stereoscopic measurements, where values of approximately 15% can be reached [164]. Introducing new, well-suited input parameters to the artificial neural network might help to approach this level in the future.

5.3 Particle Discrimination Performance

Several cuts are applied to reduce the number of background events while trying to keep a large fraction of the signal events. To study the performance of the neural-network based particle identification approach, the performance of the classification using the ζ parameter is discussed first. Using the MLP network presented in Sec. 4.5, the signal and background efficiency distributions shown in Fig. 5.6 result for the standard configuration. The efficiency is defined as the fraction of the number of signal-type and

background-type events which pass the cut on the ζ variable, respectively. The shape of the efficiency distributions shown in Fig. 5.6a follows directly from the shape of the gamma-ray and background ζ distributions shown in Fig. 4.8. For ζ_0 values close to zero, almost all gamma-ray air shower images pass the cut, while the number of background events is reduced significantly already. As ζ_0 approaches the cut value of 0.9, the number of background events approaches a level of a few percent. At $\zeta_0 = 0.9$, the background efficiency is only 1.3%, thus 98.7% of all background events are removed by the cut on ζ . The overall signal efficiency is much higher than the background efficiency. At the nominal cut value $\zeta_0 = 0.9$, the efficiency is still 40%. At even higher ζ_0 values, the background efficiency is not reduced significantly anymore, while the signal efficiency decreases drastically. In the plot shown in Fig. 5.6b it can be seen more clearly that the background efficiency decreases slowly for signal efficiency values below 40%.

When analysing data from real observations, the composition of the set of events that pass the cut on ζ depends on the ratio of the number of gamma-ray events S and the number of cosmic-ray events B . In Fig. 5.6a, an S/B ratio of 10^{-3} was assumed, which is roughly the ratio of trigger rates expected during observations of a strong gamma-ray source. The purity, defined as the fraction of the number of gamma-ray events passing the cut on ζ among all events that pass this cut is shown in the figure mentioned before. It can be seen that the purity is at a level of only a few percent for ζ_0 values smaller than 0.9. Even at this value, the purity is 3%. This is the result of the much larger rate at which cosmic ray-induced air showers trigger the camera compared to the rate at which gamma-ray air showers trigger the camera.

Since the resulting purity is low, additional cuts are required to reach an improved purity. For analyses of sources of VHE gamma rays with apparent extensions much smaller than the size of the PSF of the MonoReco algorithm, a simple way to improve the purity is to select events based on their reconstructed directions. If such point-like sources are observed with a wobble offset, the ON region with radius Θ_0 can be centred on the position of the gamma-ray source. As a result, the reconstructed directions of gamma-ray air showers have a much larger likelihood of lying inside the ON region than cosmic-ray air showers. For the assumed ratio of trigger rates specified above, an estimated purity of approximately 55% is achieved with the MonoReco algorithm.

To improve the particle identification, an input variable for the corresponding artificial neural network is needed which is able to discriminate gamma-ray induced air showers with energies below approximately 100 GeV from cosmic-ray air showers. According to Fig. 4.10, most of the low-energy events are removed by the cut on the ζ variable. This is compensated partly by the fact that the gamma-ray flux is much higher at lowest energies due to the power-law nature of most spectra of VHE gamma-ray sources, but an improvement at these energies is clearly desirable and will be subject of future work.

5.4 Effective Area

To further quantify the efficiency with which gamma rays pass the cuts listed in Tab. 4.5 including the Θ^2 cut a quantity called effective area $A_{\text{eff}}(E)$ is introduced. This variable

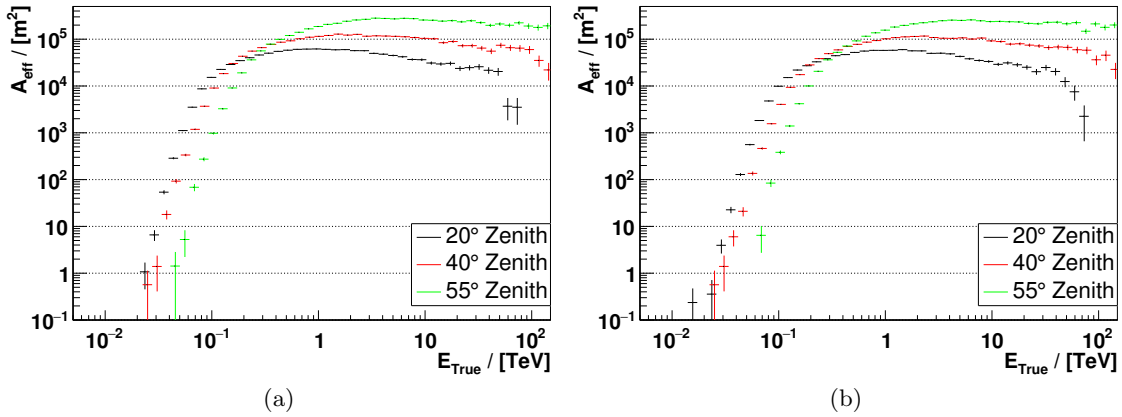


Figure 5.7: Effective area as a function of the simulated gamma-ray energy for three different zenith angles and an azimuth angle of 0° (left) or 180° (right). All distributions correspond to an offset angle of 0.5° and a MuonPhase of 200.

can be calculated either as a function of the simulated energy or as a function of the reconstructed energy of gamma rays. It is defined as

$$A_{\text{eff}}(E) = \varepsilon(E) \cdot \pi r_{\text{sim}}^2, \quad (5.5)$$

where $\varepsilon(E)$ is the energy-dependent gamma-ray detection efficiency and r_{sim} is the radius of the circular area around the telescope in which the simulated impact points of gamma-ray air shower axes were simulated, as discussed in Sec. 4.1. This definition of the effective area makes it suitable for simple calculations of the differential rate $R_{\text{det}}^\gamma(E)$ at which gamma rays are detected according to the formula

$$R_{\text{det}}^\gamma(E) = \Phi_\gamma(E) \cdot A_{\text{eff}}(E). \quad (5.6)$$

In this equation, $\Phi_\gamma(E)$ is the differential gamma-ray flux from an astrophysical source of VHE gamma rays observable at the position of the observer. As will be shown later, the fact that the effective area can be used in such calculations makes it an important property of any reconstruction algorithm.

Effective areas as functions of the simulated gamma-ray energy are shown in Fig. 5.7 for several zenith and azimuth angles. All those effective area curves exhibit similar trends. At very low energies, the effective area is very small because most air showers are too faint to either trigger the camera at all as explained in the discussion of Fig. 4.2 or to pass the basic cuts explained in Sec. 4.3. Still even at energies around 10 GeV there are events which fulfill these criteria, as can be seen e.g. in Fig. 4.10. Those events are removed by the cut on ζ and the Θ^2 cut, so that no images of air showers initiated by gamma rays with such energies pass all cuts. With increasing energy and therefore, on average, increasing intensities of Cherenkov light emitted by the air showers, the number of events passing the cuts increases quickly. In case of the effective area curve corresponding to a zenith angle of 20° and an azimuth angle of 0° , the maximum value

is reached at an energy of approximately 1 TeV. At this energy, the effective area is approximately $6.2 \times 10^4 \text{ m}^2$, which corresponds to a detection efficiency of about 2% given the simulated radius r_{sim} of 1000 m. At the same energy, the efficiency with which gamma-ray air showers trigger the camera is approximately 10%. Thus about 80% of all events which trigger the camera are removed by either the basic cuts, the cut on ζ or the Θ^2 cut. The basic cuts remove a fraction of roughly 10% of the events triggering the camera at energies above 100 GeV. At 1 TeV, this percentage shrinks to a few percent only. Thus at this energy, most shower images are rejected by either the cut on ζ or on Θ^2 . For the standard configuration, both cuts contribute equally.

At highest energies, the effective area stays relatively constant. Depending on the zenith angle it decreases slightly. This trend is caused by both the lower cut efficiency of the ζ cut and the Θ^2 cut, since very large and bright shower images tend to be cropped by the camera edges, so that the reconstruction of the ζ variable and the reconstruction of the δ parameter are unreliable, as discussed before. Therefore the trend is less pronounced at larger zenith angles, since there more Cherenkov light is absorbed by the atmosphere, preventing image cropping.

It can also be seen that the maximum effective area values increase with increasing zenith angle. This is due to the fact that the Cherenkov light pool on the ground becomes larger with increasing zenith angles, which increases the likelihood that the light pool contains the telescope, which then can record the event if trigger criteria are met. The fact that the light pool also becomes less dense at larger zenith angles lowers the effective area at small energies, but at energies above roughly 1 TeV the showers are bright enough to still be detected with a high efficiency.

The azimuth angle has a negligible effect on the effective area curves.

5.5 Radial Acceptance

The efficiency with which air shower images pass all cuts apart from the Θ^2 cut depends not only on the energy but also on the location of the reconstructed direction in the camera. A distribution of the event acceptance as a function of the squared angular distance of the reconstructed direction to the centre of the camera $\Delta\Psi$ is shown in Fig. 5.8 for four different zenith angles. These curves are generated using data from observation runs, while keeping only those shower images for which the reconstructed direction does not coincide with excluded regions around known VHE gamma-ray emitters or bright stars. Data recorded at various azimuth angles and during different MuonPhases contribute to each distribution, since in the HAP framework there is no infrastructure to allow for creating and using azimuth-dependent and MuonPhase-dependent acceptance curves. Only shower images which pass the cuts, in particular the cut on the ζ parameter, contribute to these curves. Thus such events are background events with shower images which are indistinguishable from gamma-ray air shower images. Therefore it can be expected that the shapes of the acceptance curves differ only marginally from those that would result from an analysis of gamma rays with isotropic directions.

In general the acceptance is a function of both the radial distance $\Delta\Psi$ and the az-

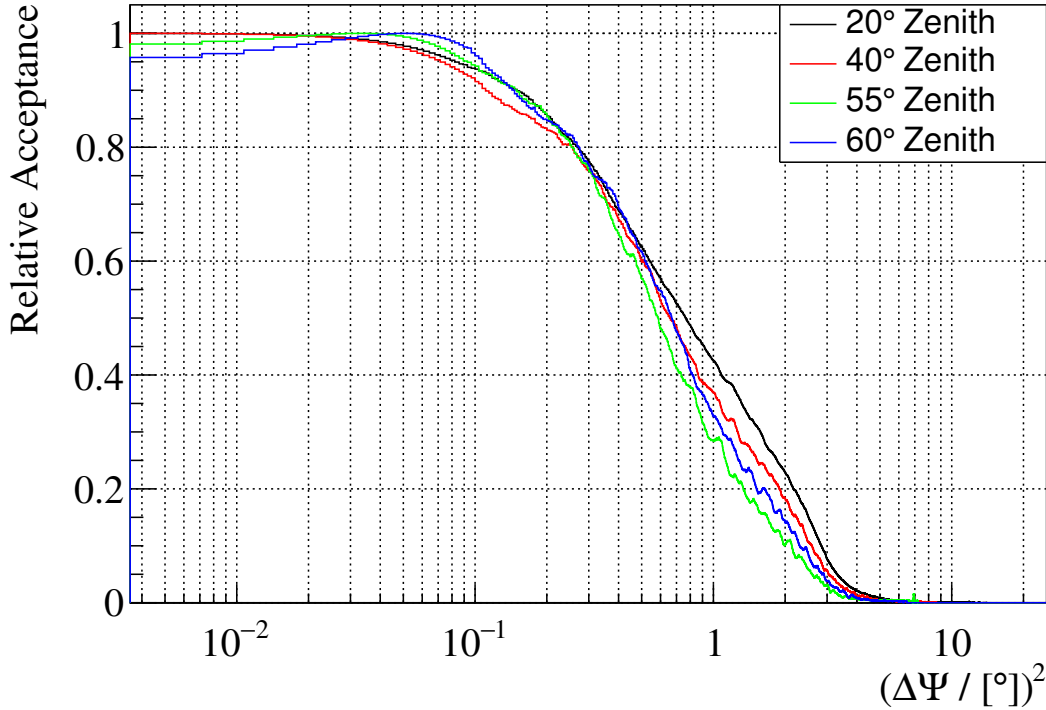


Figure 5.8: Radial acceptance in arbitrary units, scaled to have maximum values equal to one, as a function of the squared angular distance between the reconstructed direction of an air shower and the centre of the camera $\Delta\Psi$. Distributions are shown for four different zenith angles. Observational data from observations at various azimuth angles and MuonPhases contribute to each of these distributions.

imuthal angle between the line connecting the camera centre and the reconstructed direction and the abscissa of the camera coordinate system. Based on distributions as shown in Fig. 5.1b it is, however, generally assumed that the acceptance is radially symmetric, because in the direction reconstruction there is no preferred azimuthal angle in the camera plane. The facts that the mean values of the reconstructed directions in the directions of the abscissa and the ordinate in the referenced figure are very small compared to the size of the camera and that the rms values in both the x- and y-directions are almost identical support this assumption. Thus the acceptance shown in the figure is usually referred to as radial acceptance.

It can be seen that the acceptance is maximal in the centre of the camera for zenith angles below 40° . With increasing angular distance $\Delta\Psi$ from the camera centre the radial acceptance decreases. For a zenith angle of 20° , the acceptance is still above 80% of the maximum value at an angular distance of 0.5° . Towards larger distances the acceptance decreases further, so that the acceptance is at a level of a few percent at the camera edge ($\Delta\Psi \approx 1.7^\circ$). The general shape of the curves has several causes. The average displacement value δ is approximately 0.5° and the maximum value is 1.7° , so it is clear that air shower images with reconstructed directions close to the camera centre

have a larger probability of passing the nominal distance cut introduced in Sec. 4.3. At larger $\Delta\Psi$ values, also the already discussed effect of shower image truncation at the camera edges starts to further decrease the probability that the images pass all cuts. In addition, the number of possible locations of shower images in the camera with reconstructed directions close to a point at the camera edge is much smaller than for points close to the camera centre. It should be noted that the acceptance is non-zero even outside the camera. This is the case because the reconstructed direction can be outside the camera even if the shower image is well-contained in the camera.

At small values of $\Delta\Psi$ below $\sim \sqrt{0.5^\circ{}^2} \approx 0.7^\circ$, the shapes of the distributions related to different zenith angles are very similar. In this range, the deviation of the curves from each other is caused by the choice of the observation runs used to derive the respective curves. In order to keep the statistical uncertainties of the shapes of the acceptance distributions low, a large number of observation runs is needed as input, therefore also data from observations of emitters of VHE gamma rays are used as input for the calculation. As explained above, regions around those emitters are excluded from the analysis. Since those regions can, in principle, be located anywhere in the field of view of the telescope, the radial symmetry of the exposure can be broken. The current version of the HAP software framework does not allow for excluding circular sectors of the field of view during the calculation of radial acceptances, thus the distributions shown in Fig. 5.8 are susceptible to such asymmetries, which are of importance at small $\Delta\Psi$ values in particular. Also the fact that the acceptances corresponding to zenith angles of 55° and 60° increase slightly at the smallest $\Delta\Psi$ values is due to the fact that for a few observation runs excluded regions are located very close to the centre of the camera. Part of this behaviour is also due to the fact that at large zenith angles the part of the shower arriving from larger zenith angles is absorbed more than the part of the shower arriving from smaller zenith angles.

At larger values of $\Delta\Psi$, the relative acceptance differences are larger. More detailed studies are needed to determine the cause of this dispersion.

5.6 Sensitivity

Another important measure of the performance of the entire reconstruction and particle identification algorithm is the sensitivity. This quantity describes the lowest flux that can be detected with a significance greater than 5σ in a time T_{Obs} during which the astrophysical source of VHE gamma rays is observed. For the calculation of this quantity, simulated gamma rays are used to provide the signal-type air showers and observational data is used to provide background-type air shower images. All these events need to pass all cuts specified in Tab. 4.5, including the cut on Θ^2 . Therefore the sensitivity calculated here can only be used as an estimate for the sensitivity of the MonoReco algorithm for the detection of point-like gamma-ray sources. The sensitivity can be calculated as differential and as integral sensitivity. The former quantity represents the sensitivity per energy bin. Here a logarithmic binning is chosen, with five bins per decade. The integral sensitivity will be introduced at the end of this section.

The number of simulated gamma-ray showers which pass all cuts is proportional to the number of simulated events, which is a quantity without physical meaning. To calculate the sensitivity, a realistic gamma-ray spectrum needs to be assumed. In this case the differential energy spectrum of the Crab Nebula as measured by Aleksić et al. [165] is used, which is of log-parabolic form defined as

$$\left. \frac{dN}{dE}(E) \right|_{\text{Crab}} = \Phi_0 \cdot \left(\frac{E}{E_0} \right)^{a+b \cdot \log_{10}\left(\frac{E}{E_0}\right)}. \quad (5.7)$$

Here, $\Phi_0 = 3.23 \times 10^{-11} \text{ cm}^{-2} \text{ s}^{-1} \text{ TeV}^{-1}$ is the flux at the energy $E_0 = 1 \text{ TeV}$, and the spectral parameters are $a = -2.47$ and $b = -0.24$. E is the real gamma-ray energy. This differential spectrum is used to calculate the expected number of gamma rays $N_{\text{Crab}}^j(E)$ per area in the energy bin j according to the formula

$$N_{\text{Crab}}^j(E) = \int_{E_l^j}^{E_u^j} \left. \frac{dN}{dE}(E) \right|_{\text{Crab}} \cdot T_{\text{Obs}} dE. \quad (5.8)$$

In this equation, E_l^j and E_u^j are the lower and upper edges of the energy bin j , respectively. From this value the number of gamma-ray air showers passing all cuts per energy bin i is calculated as

$$N_{\gamma}^i(E_{\text{Reco}}) = \pi r_{\text{sim}}^2 \cdot \sum_{j=1}^{N_b} \frac{E_{\text{Mig}}^{ij}(E_{\text{Reco}}, E_{\text{True}})}{N_{\text{Sim}}^j(E_{\text{True}})} N_{\text{Crab}}^j(E). \quad (5.9)$$

Here, N_b is the number of bins per row in the energy migration matrix $E_{\text{Mig}}^{ij}(E_{\text{Reco}}, E_{\text{True}})$ presented in Sec. 5.2 and displayed in Fig. 5.4. Each column j of this matrix is normalised by the number of simulated gamma rays $N_{\text{Sim}}^j(E_{\text{True}})$ in energy bin j . Since the migration matrix is only filled if a shower image passes all cuts, the integral of all elements in each column j cannot be larger than $N_{\text{Sim}}^j(E_{\text{True}})$. Therefore the normalised migration matrix contains the detection efficiency, so that the resulting number $N_{\gamma}^i(E_{\text{Reco}})$ represents the expected number of detected gamma rays from a source like the Crab Nebula in a time T_{Obs} . To further calculate the number of events in the ON and OFF regions, also the number of background events needs to be determined. The number of events $N_{\text{BG}}^i(E_{\text{Reco}})$ in energy bin i in the OFF regions, sketched in Fig. 4.11, is retrieved from observations of regions in the sky free from known VHE gamma-ray sources. To account for the target observation time, the number of events needs to be scaled accordingly. Thus the number of events expected to be detected in the ON region is calculated as

$$N_{\text{ON}}^i(E_{\text{Reco}}) = N_{\gamma}^i(E_{\text{Reco}}) + \alpha N_{\text{OFF}}^i(E_{\text{Reco}}) \quad (5.10)$$

$$= N_{\gamma}^i(E_{\text{Reco}}) + \alpha \frac{T_{\text{Obs}}}{T_{\text{BG}}} \cdot N_{\text{BG}}^i(E_{\text{Reco}}). \quad (5.11)$$

In this equation, T_{BG} is the observation time corresponding to the real observations and α is the ratio of the ON and OFF exposures. From the number of ON and OFF

5 Reconstruction Performance

events and the exposure ratio α , the significance $S^i(E_{\text{Reco}})$ of the gamma-ray excess in each energy bin i is calculated according to an approximation of Eq. (4.15) for a simpler interpretation of the results. With this simplified formula, the significance is calculated as

$$S^i(E_{\text{Reco}}) \approx \frac{N_{\gamma}^i(E_{\text{Reco}})}{\sqrt{N_{\text{BG}}^i(E_{\text{Reco}})}}. \quad (5.12)$$

This significance can be translated to a sensitivity measure ζ^i according to the equation

$$\zeta^i(E_{\text{Reco}}) \approx \frac{5\sigma}{S^i(E_{\text{Reco}})}, \quad (5.13)$$

where the sensitivity is calculated in units of the differential gamma-ray flux of the Crab Nebula. The numerator of this equation represents the target significance. It should be noted that two additional requirements need to be fulfilled. Firstly, the number of photons $N_{\gamma}^i(E_{\text{Reco}})$ expected per energy bin i from a gamma-ray source like the Crab Nebula needs to be $N_{\gamma,\text{min}} \geq 10$ to not be dominated by systematic uncertainties. If this requirement is not met, the sensitivity is scaled, so that it is calculated as $N_{\gamma,\text{min}}^i(E_{\text{Reco}})/N_{\gamma}^i(E_{\text{Reco}})$. Also a systematic uncertainty of the number of background events of $p_{\text{BG}} = 5\%$ is assumed. Thus the number of gamma-ray events per energy bin i needs to exceed this percentage of the number of background events, otherwise the sensitivity is calculated as $p_{\text{BG}} \cdot \alpha N_{\text{OFF}}^i(E_{\text{Reco}})/N_{\gamma}^i(E_{\text{Reco}})$.

In Fig. 5.9, the differential sensitivity is shown for one set of observational conditions and for an observation time of $T_{\text{Obs}} = 50$ h. The differential sensitivity exhibits three domains with different functional dependence on the energy. At the lowest energies the number of gamma-ray air shower images which pass all cuts is very small, as was seen in the effective area distributions discussed in Sec. 5.4. At an energy of approximately 60 GeV, the differential sensitivity is similar to the flux of the Crab Nebula. With increasing energy, the gamma-ray detection efficiency increases, leading to a decrease, i.e. an improvement, of the sensitivity. At 100 GeV, the sensitivity is roughly 5% of the Crab Nebula flux already, making the H.E.S.S. experiment in phase II the most sensitive ground-based experiment to date. To improve the low-energy sensitivity further, a better acceptance of gamma-ray air showers needs to be accomplished. At intermediate energies, the sensitivity is roughly constant, in this case at a level of approximately 3–5% of the differential Crab Nebula flux. In this region, the sensitivity is limited by the number of background-type events which are misclassified as signal-type events. Improving the angular resolution or the performance of the neural network performing the particle classification would help to improve the sensitivity. At the high-energy end, the sensitivity is limited by the lack of gamma-ray air showers, caused by the steep decrease of typical gamma-ray spectra towards higher energies.

To put the differential sensitivity curve into perspective, also the sensitivity of the H.E.S.S.-I Model++ analysis [146] is shown in Fig. 5.9. The H.E.S.S.-I curve was obtained assuming an optical efficiency of 60%, which is roughly the optical efficiency of the telescopes in their current state. In the figure it can be seen that at energies below approximately $10^{-0.8}$ TeV ≈ 160 GeV the monoscopic reconstruction algorithm

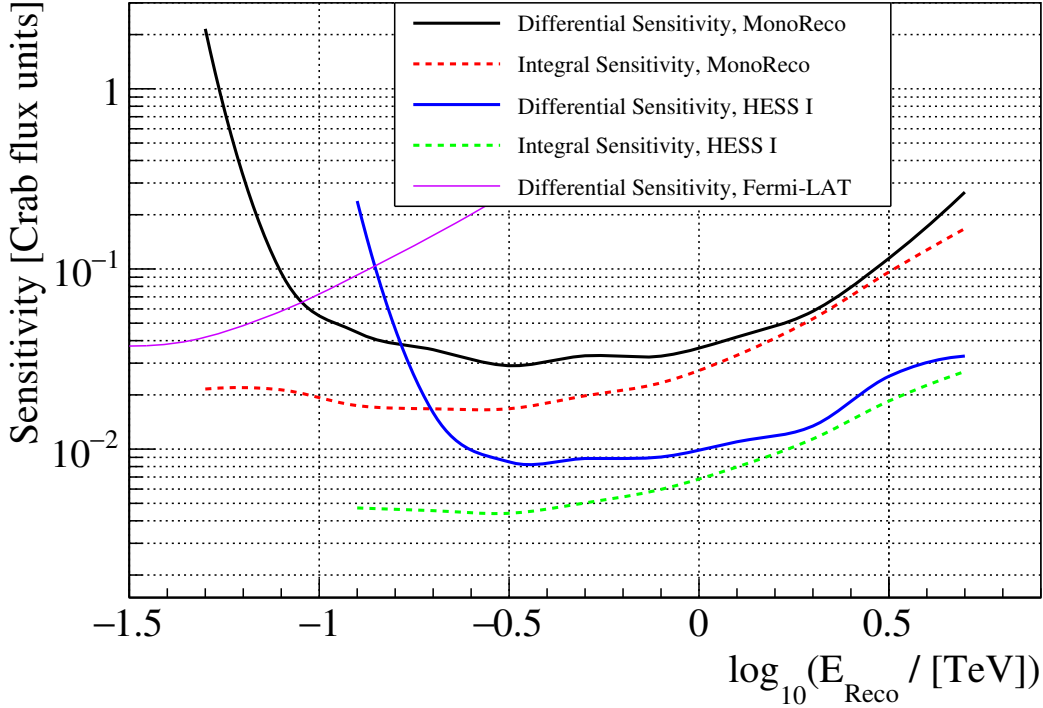


Figure 5.9: Differential and integrated sensitivity as a function of the reconstructed energy for a zenith angle of 20° , an azimuth angle of 180° , an offset angle of 0.5° , a MuonPhase of 200 and an observation time of 50 h. Curves obtained from the MonoReco algorithm are shown together with the distributions resulting from the H.E.S.S.-I Model++ analysis. Also the differential sensitivity of the *Fermi*-LAT satellite experiment for ten years of operation for detections of sources in the galactic plane is shown.

outperforms the stereoscopic analysis using data from the four smaller telescope only. At lowest energies, the strongest competitor of the H.E.S.S. II experiment is the satellite-borne *Fermi*-LAT, for which a part of the differential sensitivity curve for observations of sources in the galactic plane for ten years of operations is shown [166]. At energies below approximately 80 GeV, the *Fermi*-LAT sensitivity is better than the MonoReco sensitivity. This sensitivity comparison is, however, only possible for sources of gamma rays which exhibit only little flux variability. To be able to study transient, short-term phenomena and flux variability, the much larger effective area of ground-based experiments leads to a significantly higher sensitivity to such events.

At higher energies, the stereoscopic analysis greatly benefits from the better angular resolution, leading to a better background suppression and thus a sensitivity which is, over a large part of the energy range the H.E.S.S. experiment is sensitive to, a factor of 3–5 better than the monoscopic analysis.

In Fig. 5.9, also the integral sensitivities for both the MonoReco algorithm and the mentioned H.E.S.S.-I analysis is shown. The integral sensitivity is calculated similarly to the differential sensitivity, with the only difference being the definition of the upper

energy limit. Here, no binning is assumed, so that all events with energies above a threshold are taken into account in the above calculations. Thus the resulting integral sensitivity is a measure of the minimum integrated flux above a threshold that can be detected within 50 h with a significance of more than 5σ . The integral sensitivity reaches levels of less than 2% of the integral flux of the Crab Nebula in case of the MonoReco analysis, and values of 0.4–0.5% of the integrated Crab Nebula flux in case of the H.E.S.S.-I analysis.

5.7 Analysis of Observations of the Crab Nebula

Above photon energies of ~ 30 keV, the Crab Nebula is one of the brightest or, for example at VHEs, even the dominant point-like source of radiation in the sky [71]. It is a pulsar wind nebula, formed around a pulsar called Crab pulsar which was created in a supernova explosion in the year 1054, located at a distance of approximately 2 kpc [19].

The Crab pulsar's spin-down luminosity of $5 \times 10^{38} \text{ erg s}^{-1}$ is the highest spin-down luminosity known of any pulsar in the Milky Way. Approximately 1% of this energy is released by the system as electromagnetic radiation. The nebular emission dominates the energy output from the pulsar by a factor of ten [71]. From energies corresponding to radio wavelengths to MeV energies, the spectral energy distribution is thought to be dominated by synchrotron emission from leptons [165]. At higher energies, the emission is caused by IC scattering, with a peak of the emission at around 50 GeV. In the energy range dominated by synchrotron emission, the flux emitted by the Crab nebula is variable at all time scales [71]. Also flares lasting hours to a few days have been observed, with flux increases by factors up to thirty at the extreme upper end of the synchrotron emission energy range of approximately 1 GeV [5; 71]. Flares have not been observed in other wavelength bands like the optical regime, at radio wavelengths or at X-ray energies. At VHEs, however, where IC scattering dominates the gamma-ray emission, there is no sign of spectral or flux variability.

The magnetic field inside the nebula of $10^{-4} \text{ G} - 10^{-3} \text{ G}$ is so strong that it can only have been generated by the Crab pulsar [70; 167]. Most of the non-thermal emission is released in the UV and X-ray energy domains, which indicates that the synchrotron lifetimes are smaller than the age of the nebula in this energy regime. From this finding, it can be calculated that the relativistic electrons must have Lorentz factors of up to 10^8 , corresponding to an energy of 100 TeV [70]. Diffusive shock acceleration is not efficient enough to provide such energies [67]. Several acceleration processes like magnetic reconnection or magnetohydrodynamic acceleration are discussed in the literature. See e.g. Bühler and Blandford [71] for a review. In the following paragraphs, results from an analysis of observations of the Crab Nebula are presented.

Given the high intensity and the spectral stability at VHEs, the Crab Nebula is well-suited for cross-checking results from different experiments or analysis and reconstruction algorithms. As a first check, a sky map representing the two-dimensional significance distribution as a function of the celestial coordinates obtained from 16 good-quality observation runs, corresponding to a live time of 7.2 h, is shown in Fig. 5.10a. These

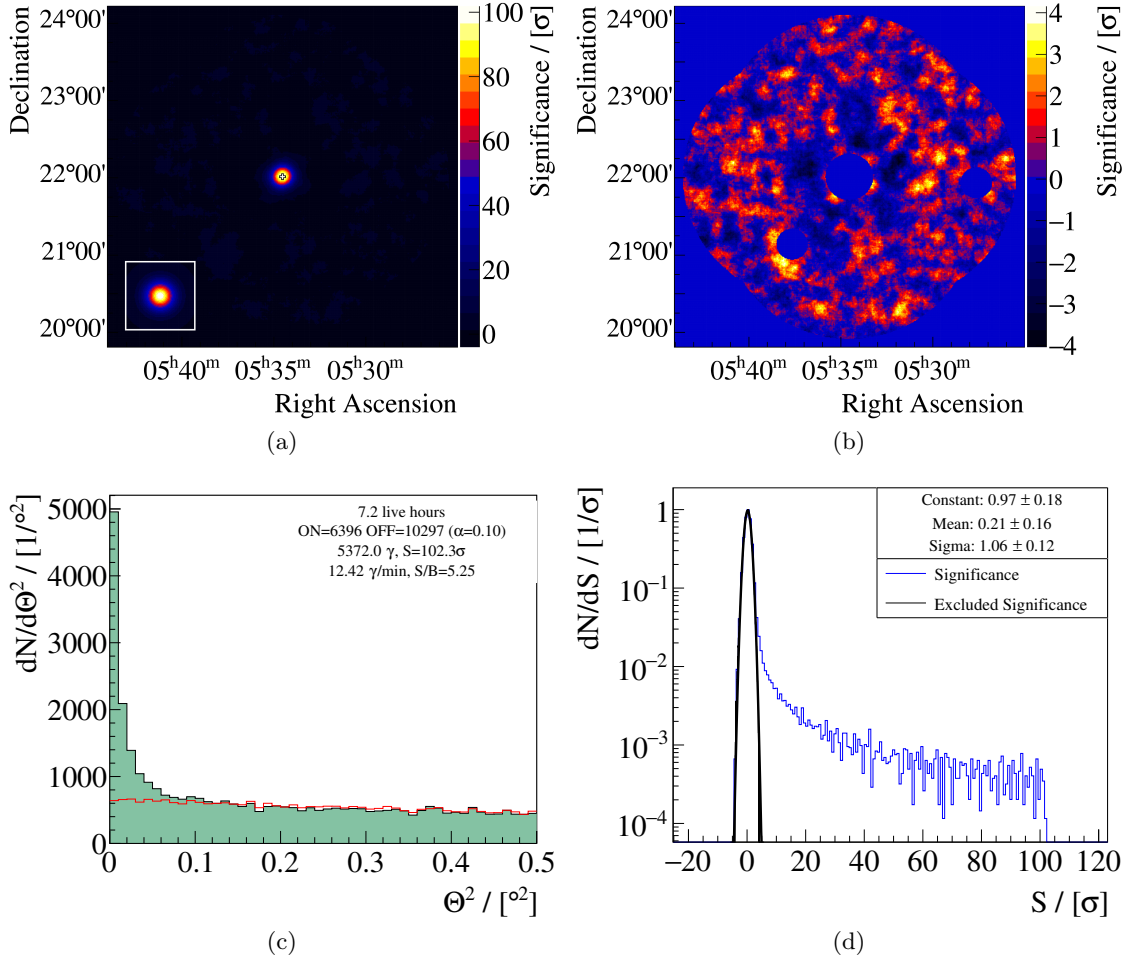


Figure 5.10: *Top left*: Significance distribution obtained with the ring-background technique. The black cross marks the position of the Crab pulsar. The inset in the lower left corner represents the PSF for comparison. *Top right*: The same distribution, with the difference that three regions, including the position of the Crab Nebula, are excluded. *Bottom left*: Distribution of the squared angular distances of the reconstructed directions from the test position for ON (black) and OFF events (red) obtained from the ring background algorithm. The numbers given in the inset are explained in the main text. *Bottom right*: One-dimensional significance distributions obtained from the top-left and top-right distributions.

significances are calculated using Eq. (4.15) from the number of events with reconstructed directions inside each bin of the sky map. The number of ON events is the number of events in a circle with a radius similar to the Θ_0 cut value around the respective bin i . The number of OFF events is estimated from the number of events in a ring with an inner radius of 0.4° and a thickness of 0.2° centred on bin i . Since the radial acceptance differs

5 Reconstruction Performance

across the FoV, the number of events in the respective areas are weighted accordingly, as described in Berge et al. [160]. The significance calculated for each bin is smoothed with a two-dimensional Gaussian distribution with a width of 0.1° .

From the distribution shown in Fig. 5.10a, it can be derived the significance is maximal within one bin width of 0.01° from the test position, which is the position of the Crab pulsar determined by VLBI measurements of $\alpha_{J2000} = 5\text{h}34\text{min}32\text{s}$ and $\delta_{J2000} = 22^\circ 0' 52''$ [168]. The variables α_{J2000} and δ_{J2000} represent the right ascension and the declination in the RaDec J2000 coordinate system, respectively. The negligible deviation of the maximum significance position from the test position indicates that the bias of the direction reconstruction is negligible also in applications of the MonoReco algorithm to real data. The distribution of the number of events as a function of the squared angular distance of the reconstructed direction from the test position is shown in Fig. 5.10c for both the ON and OFF events obtained from the ring background technique. Before producing the one-dimensional distribution shown in the plot, each bin in the OFF sky map is scaled by the exposure of the respective bin. A clear excess at small Θ^2 values can be seen, which becomes smaller with increasing angular distance. At approximately $0.3^\circ \approx \sqrt{0.1^\circ{}^2}$, the ON and OFF distributions are compatible with each other, indicating that there is no additional negative or positive excess in the region around the test position apart from the Crab Nebula itself. This can also be seen in Fig. 5.10b, where a significance distribution is shown with three circular regions excluded from the significance calculation. The central region is located at the position of the Crab Nebula. The remaining two regions cover the positions of two bright stars, since the light emitted by those stars causes an elevated NSB level. Around the lower-left exclusion region, a significance level of approximately 4σ is reached, which may be an effect of the high NSB. In a region of the sky without any gamma-ray source, a Gaussian distribution of significances is expected, which, by construction, has a mean value of zero and a width of one. Such a significance distribution is shown in Fig. 5.10d. For the excluded significance map, the distribution can be fit by a Gaussian distribution. The best-fit distribution has a mean of 0.21 ± 0.16 and a width of 1.06 ± 0.12 . While the width of the distribution is compatible within one standard deviation with the expected value, the mean is compatible with the expected value of zero at 1.3σ only. It can be assumed that this discrepancy is caused by the high NSB level induced by the star in the bottom-left corner of the sky map. For comparison, also the distribution of significances from the non-excluded sky map is shown, which extends up to the peak significance of 102σ .

An excess of approximately 5370 gamma-ray candidates in the circular ON region with a radius of $\Theta_0 \approx 0.13^\circ$ is calculated using the ring-background technique. This excess is equivalent to 12.4 gamma-ray candidates per minute, as indicated in Fig. 5.10c. The calculated excess corresponds to a signal to background ratio S/B of 5.25 and an overall statistical significance of 102σ with which the Crab Nebula is detected. This significance corresponds to a sensitivity of 1.9% of the Crab Nebula flux, which matches the estimated integral sensitivity of 2% of the integral flux of the Crab Nebula calculated in Sec. 5.6 very well, despite the fact that the observations of the Crab Nebula were performed at zenith angles between 45° and 60° , while the sensitivities calculated earlier were obtained assuming a zenith angle of 20° . Thus this agreement can be seen as an

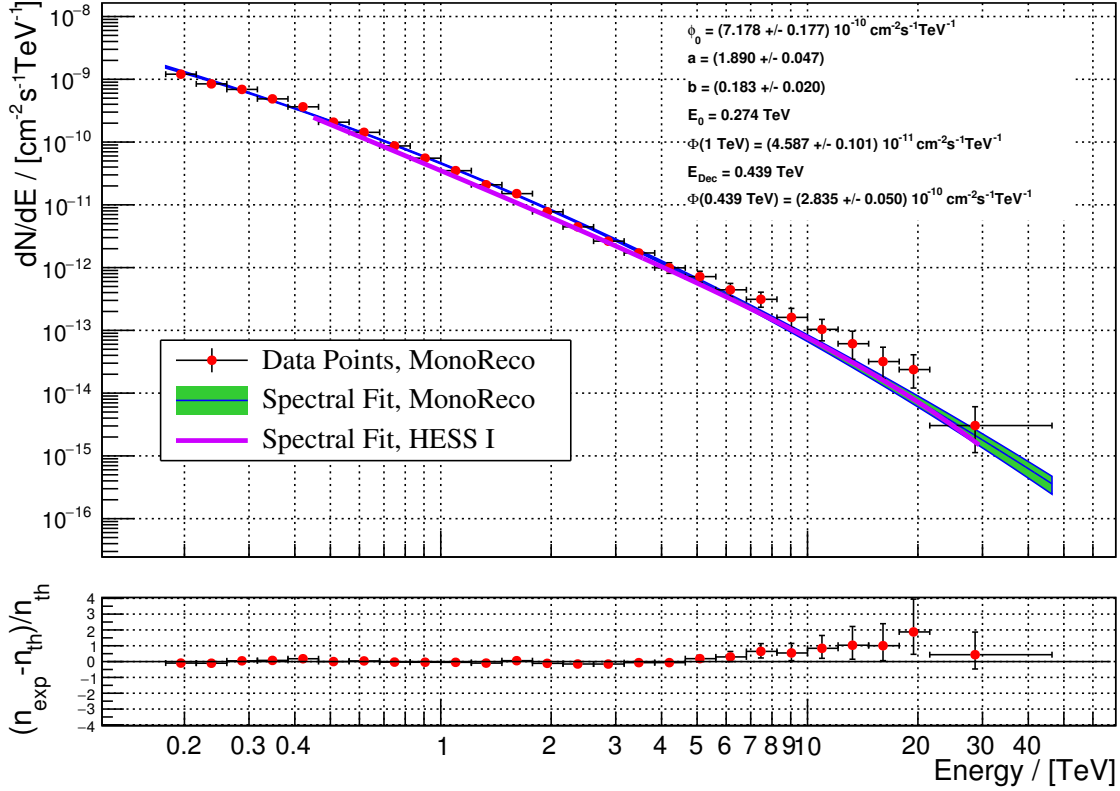


Figure 5.11: Differential energy spectrum obtained from observations of the Crab Nebula. Data points and the green uncertainty band correspond to the analysis conducted with the MonoReco algorithm, the purple line shown for comparison represents the spectrum published by the H.E.S.S. collaboration in 2006. The lower panel shows the fit residuals for the MonoReco analysis. Residuals are calculated as the relative deviation of the fit function from the data points.

indicator of a stable performance across large zenith angle ranges.

Another high-level check of the performance of the MonoReco algorithm concerns the reconstruction of differential gamma-ray spectra. A spectrum reconstructed from the sixteen observation runs targeted on the Crab Nebula introduced above is shown in Fig. 5.11. The data points shown in this plot represent the reconstructed differential gamma-ray flux values per bin with a width dE in reconstructed energy. They can in principle be calculated using the formula

$$\frac{dN}{dE}(E) = \frac{\frac{dN_{\text{ON}}}{dE}(E) - \alpha \frac{dN_{\text{OFF}}}{dE}(E)}{T_{\text{Obs}} A_{\text{eff}}(E)}. \quad (5.14)$$

Here N_{ON} and N_{OFF} are the numbers of ON and OFF events in the respective regions defined in Sec. 4.6 and α is the corresponding exposure ratio. Data points were rebinned such that the excess in each point is statistically significant at the level of 2σ or more. The

data points are fit with a log-parabolic function introduced in Eq. (5.7). The resulting fit function, as a main result of a data analysis, shall be a function of the real energy, e.g. to be able to compare the spectrum with results from other experiments. Since the energy bias can deviate from zero and especially since the energy resolution is so large that, in general, a non-negligible amount of the events inside a given energy bin can be events with true energies corresponding to a different bin. Thus the forward folding technique described in more detail in Piron et al. [169] is applied during the fitting procedure to take into account the full energy migration matrix introduced earlier. Fit results for the flux normalisation φ_0 at the reference energy E_0 , the photon index a and the curvature parameter b are given in the inset in Fig. 5.11. For a comparison, the fit result from the H.E.S.S. publication from 2006 is also shown [164]. This is a power law function with an exponential cutoff at 14.3 TeV. At the lowest and highest energies of the H.E.S.S. I spectrum, the agreement with the spectrum reconstructed with MonoReco is at a level of a few percent only. At intermediate energies, the flux deviation is $\lesssim 25\%$, which is on the order of the usually quoted systematic uncertainties of 20% in case of H.E.S.S. I analyses [164].

It should be noted that the energy range of the monoscopic analysis extends to significantly lower energies. While the H.E.S.S. I spectrum starts at approximately 440 GeV, the first bin of the MonoReco spectrum starts at roughly 177 GeV. This can even be considered a conservative estimate, because the lower energy threshold is defined as the energy where the effective area curve reaches 10% of its maximum value. This is an arbitrary definition agreed upon within the HAP analysis framework the MonoReco algorithm is implemented in. Extending the range to lower energies is possible if the number of events passing all cuts is sufficient to provide a reliable estimate of the energy bias and the energy reconstruction, given that the changing atmospheric conditions can be taken into account properly since they strongly influence the amount of light reaching the detector. As this is currently not the case, such a lowering of the energy threshold will, if at all, only be possible with an improved set of atmospheric monitoring instruments deployed at the H.E.S.S. site. The energy threshold furthermore depends on the zenith angle. While the value given above is valid for zenith angles of $\gtrsim 40^\circ$, the lowest threshold of 59.4 GeV is obtained at a zenith angle of 0° .

The overall deviation of the spectral fit function from the data points is very small, only at high energies there are several bins in which there is a systematic trend in which the fit function is compatible with the data points within two standard deviations only. This indicates that the effective area is underestimated at these energies. Alternatively the energy resolution could be overestimated, or the energy bias could be underestimated. Further investigations are needed to identify the main reason of this effect.

Apart from the fact that improvements are always possible, the overall performance of the MonoReco algorithm is considered competitive with other monoscopic reconstruction algorithms. Therefore a more detailed analysis of observational data using the MonoReco algorithm will be presented in the next chapter.

6 Analysis of the 2014 PSR B1259–63/LS 2883 Data

The gamma-ray binary system PSR B1259–63/LS 2883, which has been introduced already in Sec. 2.8, went through its most recent periastron passage on May 4, 2014. Previous observations with the H.E.S.S. experiment in phase I were conducted for the three periastron passages before the most recent passage. Those occurred on March 3, 2004, during which the source was firmly detected at VHEs for the first time [51], on July 26, 2007 [52] and on December 14, 2010 [53]. Data from the latter observation campaign will be referred to as 2010 data despite the fact that the actually recorded data is from January 2011. In 2014, the binary system was observed before, during and after periastron, and especially at the time of the anticipated reoccurrence of the Fermi flare starting approximately 30 d after the periastron passage. The periods during which PSR B1259–63/LS 2883 was observed are called P2014-02 through P2014-07. For each of those periods the visibility of PSR B1259–63/LS 2883 with zenith angles smaller than 50° and 45° is shown in Fig. 6.1. The general shape of the visibility curves is determined by the fact that this zenith angle condition needs to be fulfilled and by the limitation of the H.E.S.S. telescopes to observe during moonless parts of the night only. For reference, the maximum zenith angle that is typically allowed for observations is 60° . The fact that there are dips in between the observational periods without any possibility to observe the target is due to the visibility of the moon. From Fig. 6.1 it can also be seen that the time around periastron has not yet been sampled without gaps in the past. Especially before periastron, the visibility in 2014 matches those gaps very well. Furthermore, the periastron itself could be observed for the first time, and also during the time of the Fermi flare the source could be observed well for one entire moon phase period. It should be noted that significant parts of the time PSR B1259–63/LS 2883 was at favourable zenith angles were dedicated to observations of other targets.

The resulting numbers of runs fulfilling all quality criteria for either monoscopic or stereoscopic analyses are listed in Tab. 6.1 together with the corresponding live times and mean zenith angles of the observations. Quality criteria that need to be fulfilled for monoscopic, stereoscopic and H.E.S.S. I-type analyses are listed in Tab. 6.2. These criteria either apply to the entire telescope array or to individual telescopes. System-level criteria comprise a check of the relative atmospheric humidity, the minimum run duration and the number of telescopes which need to participate in an observation run. For obvious reasons the latter number depends on the type of analysis that is to be conducted. Furthermore, the trigger rate measured by the central trigger needs to be within the range of expected, reasonable rates given in the table. For monoscopic analyses, no such check is necessary because there is a check on the camera trigger rate. For stereoscopic

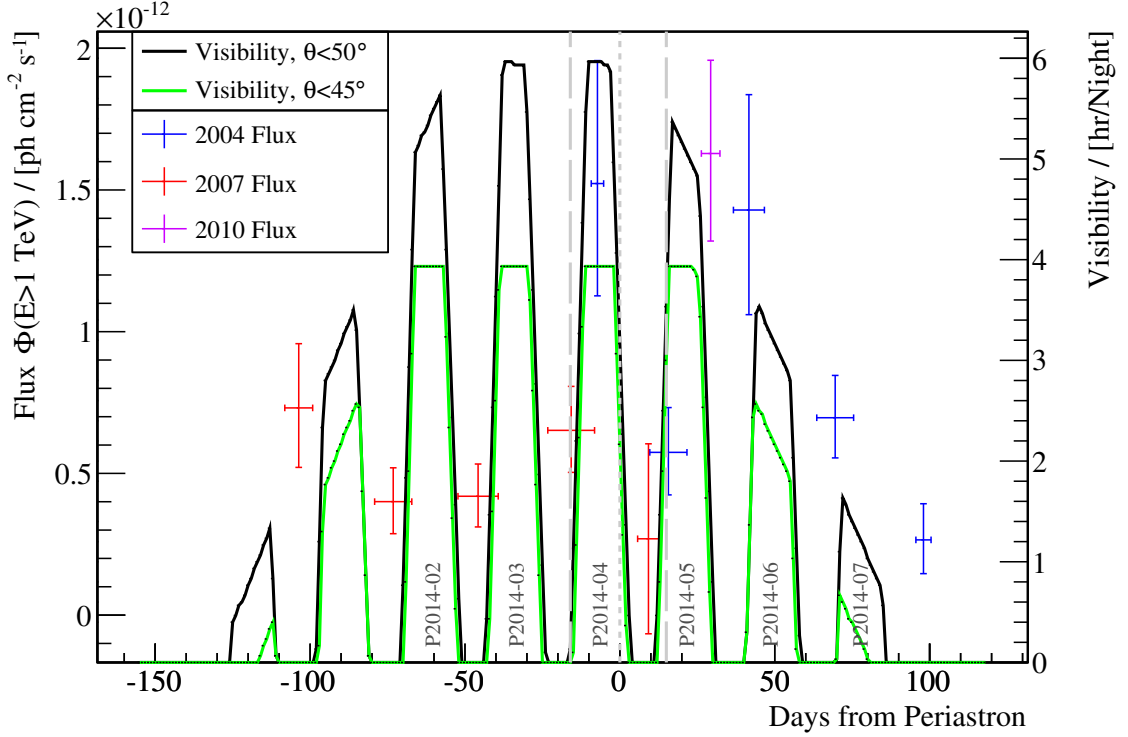


Figure 6.1: Visibility of PSR B1259–63/LS 2883 around the 2014 periastron in hours per night with zenith angles θ smaller than 50° and 45° . The time of the periastron passage is marked with a short-dashed line, the times of the disk crossings, here defined as the times the radio pulsations disappear, are marked by long-dashed lines. For reference, the monthly-binned fluxes above energies of 1 TeV obtained from a re-analysis of archival data around the previous periastron passages indicated in the legend are shown as well. Also the names of the periods during which observations were conducted in 2014 are displayed.

analyses performed with H.E.S.S. II, no dedicated criterion has been implemented yet. A further check on the stability of the system trigger rate ensures that the trigger rate is not influenced by rapidly changing atmospheric conditions or hardware issues like unstable camera readout. This check is, however, only available for H.E.S.S. I-type analyses. Lastly, the 2-fold dead time fraction, describing the fraction of the time during which at least one out of two telescopes is blocked by data read-out, needs to be smaller than 80%. For analyses of H.E.S.S. II data, no such check is currently in place.

For observation runs passing the system-level quality checks introduced before, each telescope is required to fulfill another set of criteria. If those are not met, data from the corresponding telescope is not included in the analysis. Depending on the analysis type, a minimum event rate has to be read out from each telescope. The higher rate expected from CT 5 is reflected by the cut values listed in the table. Another important criterion concerns the number of non-functional pixels. For each camera, the number of pixels labelled as broken, which can be caused by malfunctioning hardware like the

		P2014	P2014	P2014	P2014	P2014	P2014	Total
		-02	-03	-04	-05	-06	-07	
Mono	N_{Runs}	1	26	44	37	18	8	134
	$t_L / [\text{h}]$	0.5	11.8	19.4	16.6	7.9	3.6	59.8
	$\bar{\theta} / [^\circ]$	42.1	41.0	42.0	41.1	41.6	47.3	41.8
Stereo	N_{Runs}	0	25	50	37	20	8	140
	$t_L / [\text{h}]$	0	10.7	21.1	15.9	8.3	3.5	59.6
	$\bar{\theta} / [^\circ]$	-	41.0	42.1	41.1	41.5	47.3	42.1

Table 6.1: Number of available good-quality runs N_{Runs} , selected using the criteria for monoscopic and stereoscopic analyses detailed in the main text, corresponding live times t_L and the mean zenith angles of the ON region $\bar{\theta}$. Numbers are given for each observation period and also summed to give the total value.

Criterion	Mono	Stereo	H.E.S.S. I
<i>System-level Criteria</i>			
Relative humidity	$\leq 90\%$	$\leq 90\%$	$\leq 90\%$
Run duration	≥ 15 min	≥ 15 min	≥ 5 min
Number of telescopes	≥ 1 (CT 5)	≥ 3	≥ 3
Central trigger rate	-	-	100–600 Hz
Central trigger rate variation	-	-	$\leq 4\%$
2-fold dead time fraction	-	-	$\leq 80\%$
<i>Telescope-level Criteria</i>			
Zenith angle corrected trigger rate	≥ 1300 Hz	CT 5: ≥ 1300 Hz	100–300 Hz
Broken pixels	$\leq 17\%$	$\leq 20\%$	$\leq 20\%$
Pixels with broken HV	≤ 50	≤ 50	≤ 50
Trigger rate variation	-	-	$\leq 10\%$
Dead time fraction	-	-	$\leq 10\%$
Telescope participation fraction	-	-	≥ 0.4

Table 6.2: Quality criteria which have to be met in order to pass the run selection for each telescope and for the entire array for monoscopic, stereoscopic and H.E.S.S. I-type analyses. The criteria are explained in the main text.

readout electronics, and the number of pixels with non-functional high voltage supply are required to be smaller than the fiducial values given in Tab. 6.2. Pixels for which the high voltage supply was actively shut down due to images of bright stars located in the respective part of the camera are not taken into account by this check. Furthermore, the trigger rate per telescope needs to vary by less than 10% over the course of one observation run in case of H.E.S.S. I-type analyses. No such cut is defined yet for

analyses of H.E.S.S. II data. The same is true for the cuts on the dead time fraction and the telescope participation fraction, the former of which is self-explanatory. The latter cut assumes that on average 2.5 telescopes participate in the detection of an air shower. Dividing this number by the number of telescopes in the H.E.S.S.-I array gives a value of 0.625. Participation fractions much lower than this number indicate that there was a problem with the respective camera during the run, thus data from the corresponding telescope is excluded from the analysis. For further information about the stereoscopic H.E.S.S. I run selection, see Hahn et al. [170].

In the following sections, the analysis of the most recently taken data on PSR B1259–63/LS 2883 is described in detail. In Sec. 6.1, the detection of the source and the features of the sky map are discussed. In Sec. 6.2, the reconstruction of the gamma-ray spectrum of PSR B1259–63/LS 2883 is explained, and in Sec. 6.3, the flux evolution around the time of the 2014 periastron passage will be discussed. In the latter two sections, also comparisons with results from previous observation campaigns are made. A discussion of the results of the data analysis follows in Sec. 6.4.

6.1 Source Morphology

Using the entire data set available for a monoscopic analysis, the total number of excess events is 3370 ± 130 in a circle of radius $\Theta_0 \approx 0.13^\circ$ around the position of PSR B1259–63/LS 2883. This excess is equivalent to a significance of 27.6σ . The two-dimensional distribution of significances projected into the sky is shown in Fig. 6.2a. In this plot a smoothed significance map is shown. For the smoothing the same Gaussian distribution with a width of 0.1° was used as in the analysis presented in Sec. 5.7. The location of the maximum excess is, given the binning shown in the plot, identical to the test position. Apart from the clear excess around the position of PSR B1259–63/LS 2883, there is an additional excess at the 15σ level located roughly 0.6° to the north of it. This excess is associated with a pulsar wind nebula called HESS J1303–631, discovered by chance while observing PSR B1259–63/LS 2883 [171; 172]. It is an extended source exhibiting an energy-dependent morphology at VHEs [66]. The presence of this VHE gamma-ray source is the reason why the observations of PSR B1259–63/LS 2883 were performed with wobble offsets of $\pm 0.5^\circ$ along the right ascension axis only and not along the declination axis. The significance distribution is calculated using the ring-background technique [160] using an adaptive determination of an optimal size of the ring around the bin for which the excess significance is to be calculated. In the present analysis, a minimum inner ring radius of 0.4° , a maximum outer radius of 1.7° , a step size of 0.08° and a ring thickness of 0.2° are used. Within these constraints a ring geometry is chosen for each pixel in the map and for each observation run such that the ratio of the exposure of a circular region similar to the ON region shown in Fig. 6.2a around the pixel and the respective ring exposure is smaller than a threshold value of one. Such a condition is chosen to avoid background estimates with too low statistics due to a potential intersection of the ring with excluded regions or areas beyond the map. Since the resulting bin size is different for each bin, the ring-background OFF region circle

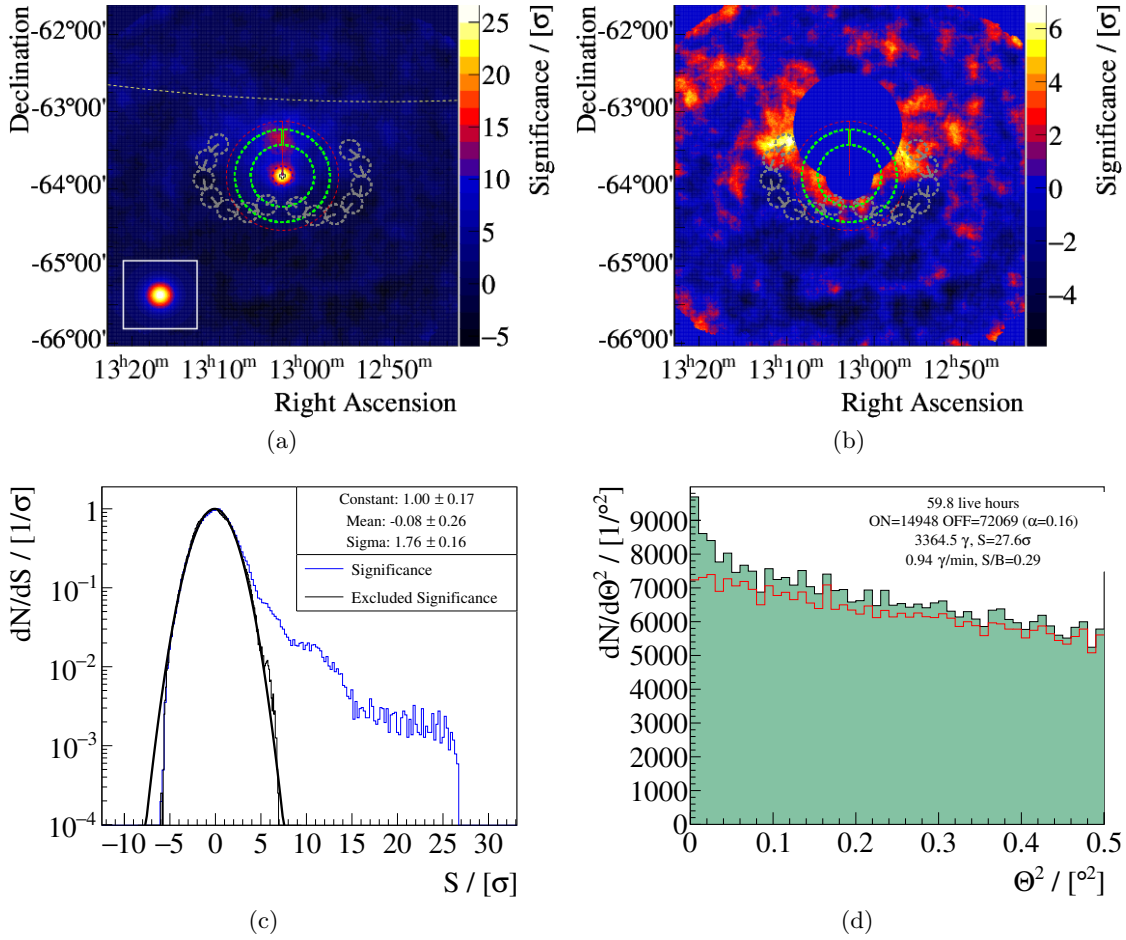


Figure 6.2: *Top left*: Significance distribution obtained from a monoscopic analysis of PSR B1259–63/LS 2883 data. The black cross marks the position of the source. The dashed blue circle indicates the ON region for both the reflected-background and the ring-background analysis techniques. Grey and green circles mark the corresponding OFF regions. The red dashed circle indicates the region used to calculate the Θ^2 distribution. The yellow dashed line represents the galactic plane. The PSF for this analysis is shown in the inset. *Top right*: The corresponding excluded significance map. *Bottom left*: Significance distribution for both the excluded and the non-excluded significance maps. *Bottom right*: Θ^2 distribution for ON events (black) and OFF events (red) obtained from the ring-background analysis.

shown in the mentioned figure is only an example, not a real ring used in the analysis.

Another feature that can be seen in the sky maps is a seemingly diffuse excess around both PSR B1259–63/LS 2883 and HESS J1303–631. In the excluded sky map shown in Fig. 6.2b the additional excess of up to 6.9σ can be seen more clearly, together with a negative excess with a statistical significance of up to -6σ . The positive excess

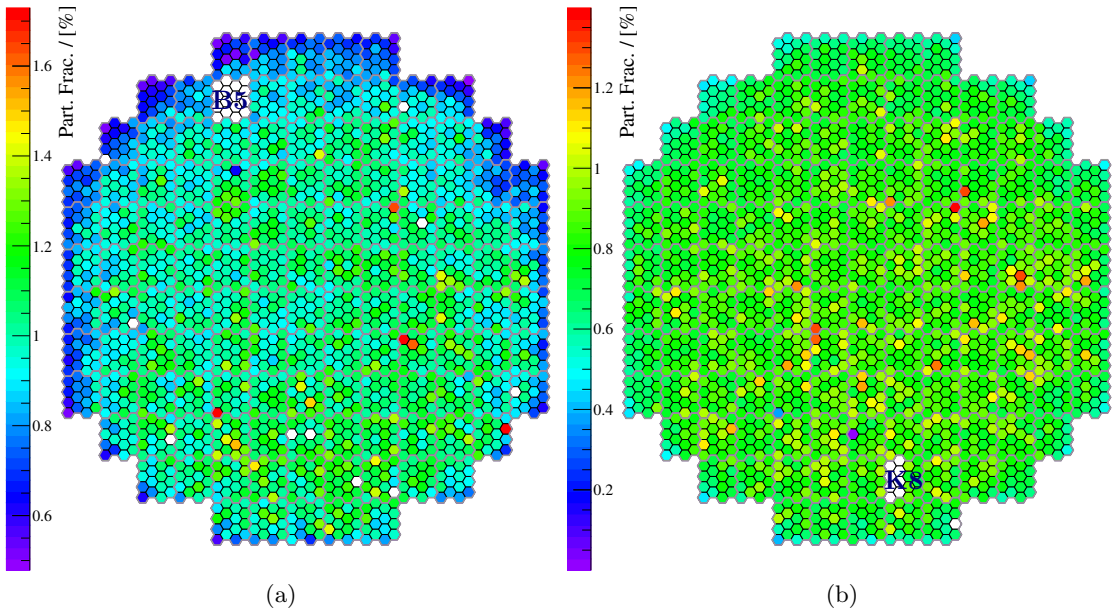


Figure 6.3: Participation fraction of each pixel in the CT5 camera in the events which triggered the camera. The images correspond to observation runs performed before (*left*) and after (*right*) the pixel gain adjustment. Malfunctioning pixels are displayed as blank fields. The drawers B5 and K8 are indicated by the respective labels.

extends significantly beyond the expected size of both known gamma-ray sources just mentioned, as indicated by the conservatively chosen sizes of the exclusion regions, and is not of physical origin. Instead it is caused mainly by two effects. A part of the effect is caused by one drawer named B5 that was malfunctioning during 113 of the total 134 runs used in this analysis. Due to the imaging properties of the telescope and the way the telescope is operated, a malfunctioning hardware in the top-left corner of the camera will, in general, cause a lack of intensities measured in the bottom-right part of the sky map, although the part of the sky imaged by the drawer changes during the course of an observation run. In Fig. 6.3a this drawer can be identified as the blank field in the top-left corner of the camera. In this figure, the fraction of pixels fulfilling the threshold criterion introduced in Sec. 3.3 among air showers which triggered the camera is shown. Apart from the missing drawer a gradient is visible in this plot. Pixels in the upper part of the camera participate less often in an event than pixels in the bottom half. Additionally, pixels at the camera edge tend to participate less as well. Both gradients are caused by a non-optimal configuration of the gains of the pixels and are not taken into account in the simulation of the experiment. In contrast, in the image shown in Fig. 6.3b no gradient is visible apart from a small lack of entries in the very corners of the camera, which is due to the fact that the trigger criteria are more difficult to fulfill if a shower image is located at the edge of the camera. In the run belonging to the image on the right-hand side, one scaler (half of the drawer K8) is missing. This scaler was

non-functional during 41 observation runs. There are no runs during which both this scaler and the drawer B5 worked properly. Other drawers or scalers were out of order during individual runs only, so the impact on the overall analysis results is limited.

From the overall scale of the participation fraction of $\varepsilon_{\text{Pix}} = \mathcal{O}(1\%)$, the average number of pixels contributing to a shower image can be estimated as $N_{\text{trig}}^{\text{CT}5} = \varepsilon_{\text{Pix}} N_{\text{Pix}}^{\text{CT}5} = 20$ given the number of pixels in CT 5 of $N_{\text{Pix}}^{\text{CT}5} = 2048$, which matches well the observed average number of pixels. Before applying gamma-ray selection cuts, the average number of pixels per shower is roughly 18, after applying selection cuts this number increases to 24 due to the enhanced suppression of small shower images discussed earlier. Furthermore, several pixels with a participation fraction $\sim 50\%$ higher than the average can be seen in Fig. 6.3. These are due to unstable camera electronics and high voltage supplies, and are transient problems appearing and disappearing from one run to the next.

Both the gradient and the broken drawers have an influence on the sky maps shown in Fig. 6.2. To identify the main contribution to the diffuse excess visible in Fig. 6.2b, the data set is split into several groups of runs. Ordering the runs by the state of the drawer B5 and the time before or after the gain adjustment, which was performed on May 22, 2014, results in the sky maps shown in Fig. 6.4–Fig. 6.11 in Tab. 6.3. The main conclusion that can be drawn from a comparison of the sky maps shown in this table is the fact that the diffuse excess is least prominent in Fig. 6.4 and the identical Fig. 6.5. In this plot, an excess with a significance of $> 4\sigma$ can be seen very close to the exclusion region covering HESS J1303–631, but the wing-like structure of the excess seen in, for example, Fig. 6.11 is not existent. Assuming an overall significance of the wing-like excess in Fig. 6.11 of 6σ , the expected significance can be estimated using the live times given in the captions of the figures in the table. In Fig. 6.4, a significance of 2.4σ would be expected, which is not seen. This supports the hypothesis that the main part of the diffuse excess is caused by either the gain gradient or the broken drawer B5.

The missing drawer will not be visible as one well-defined area in the sky with a lack of events but introduces a lack of events on a larger scale because the displacement parameter δ needs to be taken into account as well to reconstruct directions from the pixels in the shower images. Hence a lack of pixels with sufficient intensities in one area leads to an approximately circular area with a lack of events. The radius of this area is roughly equivalent to the maximum δ value, which is of order 1.6° . Given that the two telescope pointing positions invoked by the wobble offset observation strategy have an angular distance of 1° in right ascension, the malfunctioning drawer will have an influence in an area of 4.2° in right ascension and 3.2° in declination, not taking into account the size of the drawer itself. More than 68% of all events, however, have smaller δ values in the range of 0.34° – 0.86° . The size of the corresponding area is compatible with the negative excess in the lower halves of the sky maps shown in Tab. 6.3. Also the gain gradient will have a qualitatively similar effect, since the lack of events in the upper part of the camera translates to a lack of events in the bottom part of the sky maps.

To estimate the influence of the gain gradient, one can compare the sky maps shown in Fig. 6.9 and Fig. 6.10. Indeed the wing-like structure is seen in both images. It should be noted, though, that the live times corresponding to those plots are very different. To

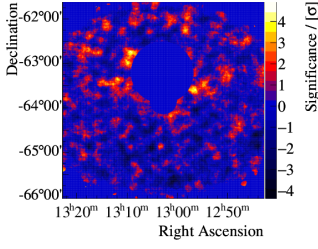
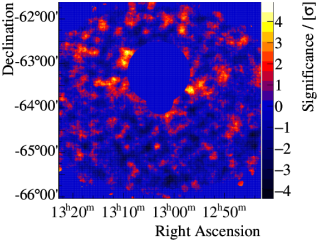
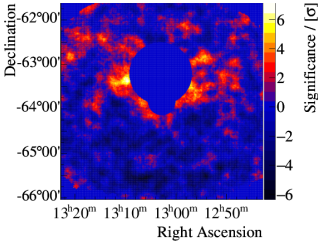
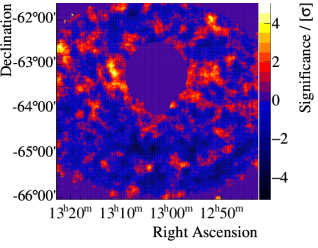
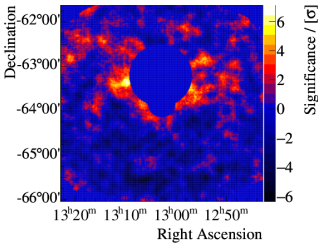
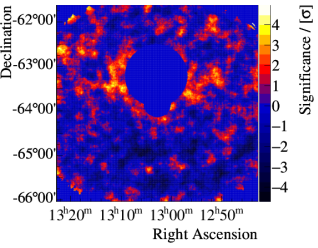
	Pre-gain adjustment	Post-gain adjustment	All times
Functional drawer B5	No such data	 <p>Figure 6.4: $t_L = 9.3$ h</p>	 <p>Figure 6.5: $t_L = 9.3$ h</p>
	Malfunctioning drawer B5	 <p>Figure 6.6: $t_L = 37.1$ h</p>	 <p>Figure 6.7: $t_L = 13.4$ h</p>
All states of drawer B5		 <p>Figure 6.9: $t_L = 37.1$ h</p>	 <p>Figure 6.10: $t_L = 22.7$ h</p>

Table 6.3: Sky maps resulting from monoscopic analyses with exclusion regions for different groups of runs, separated by the state of the drawer B5 and the time at which the observation runs used to create the sky maps were performed relative to the gain adjustment campaign. The corresponding live times t_L are given in the captions.

avoid scaling, subsets of the observation runs contributing to the plots shown in Tab. 6.3 are used to create excluded sky maps with similar live times. These maps are shown in Fig. 6.12. It can be seen that also the gain gradient has a large influence on the excluded sky map, causing a significant part of the excess seen around the excluded regions in Fig. 6.12a. The significance level seen in Fig. 6.12b is similar to the level seen in Fig. 6.12c, but the excess appears to be slightly more diffuse in the formerly mentioned map. More statistics and especially runs performed before the gradient adjustment with an intact drawer B5 would be needed to better quantify which effect is dominant in the

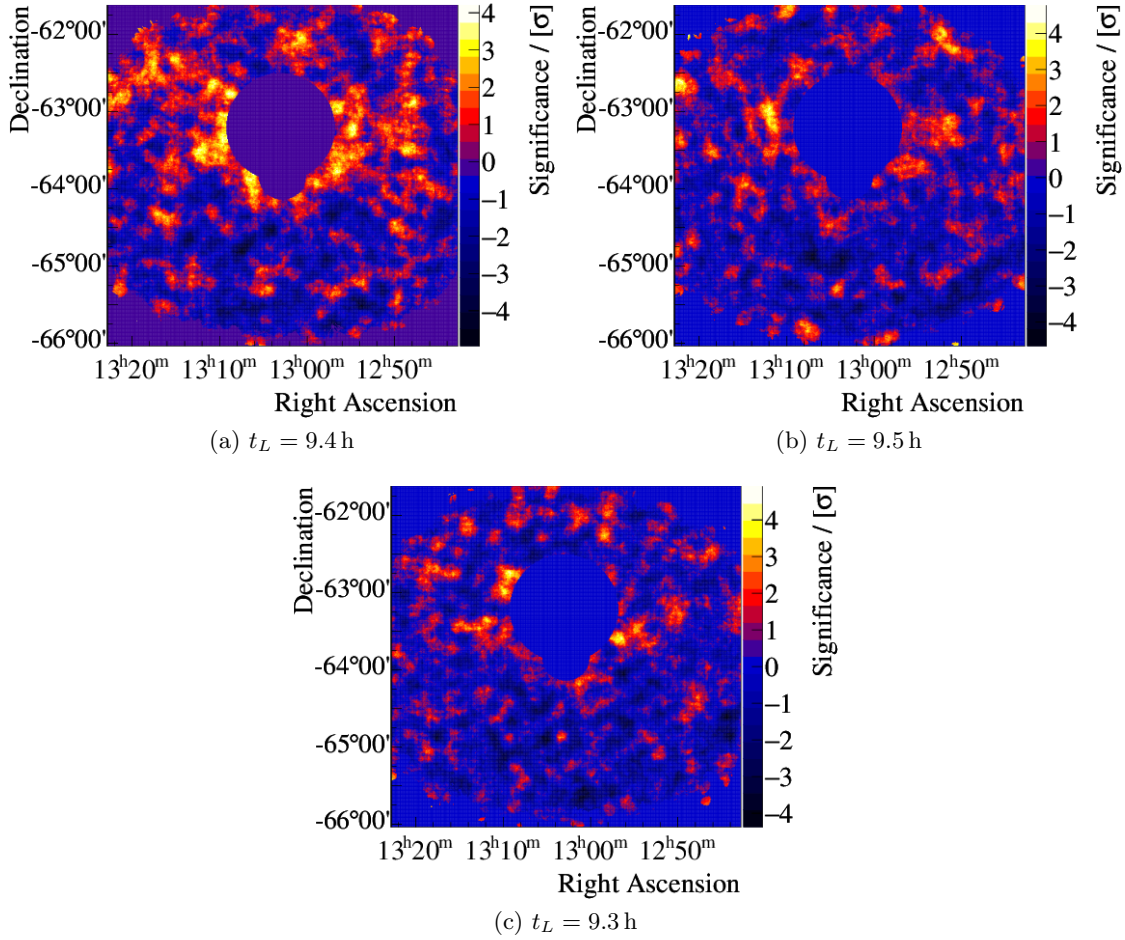


Figure 6.12: Excluded sky maps obtained from analyses of 21 observation runs each. Thus the corresponding live times are (9.4 ± 0.1) h each, as indicated in the captions. The drawer B5 was non-functional during the runs used to create the maps shown in the *top* row, while it was functional for the plot in the *bottom* row. The *top left/right* plots correspond to the pre-/post-gain adjustment phases. The *bottom* row plot uses data from the post-gain adjustment phase.

generation of the wing-like excess, but it is clear that these are the main reasons.

Due to the increased, artificial excess discussed above the excluded significance distribution shown in Fig. 6.2c deviates from the desired distribution. The excluded significance distribution is not compatible with a Gaussian distribution with a mean of zero and a width of one. Since the excess is due to the negative excess in the lower half of the sky map and not caused by a real, astrophysical source of VHE gamma rays, the distribution is still centred around zero with a mean value compatible with this number. The width, however, is incompatible with one with a significance of 4.8σ when ignor-

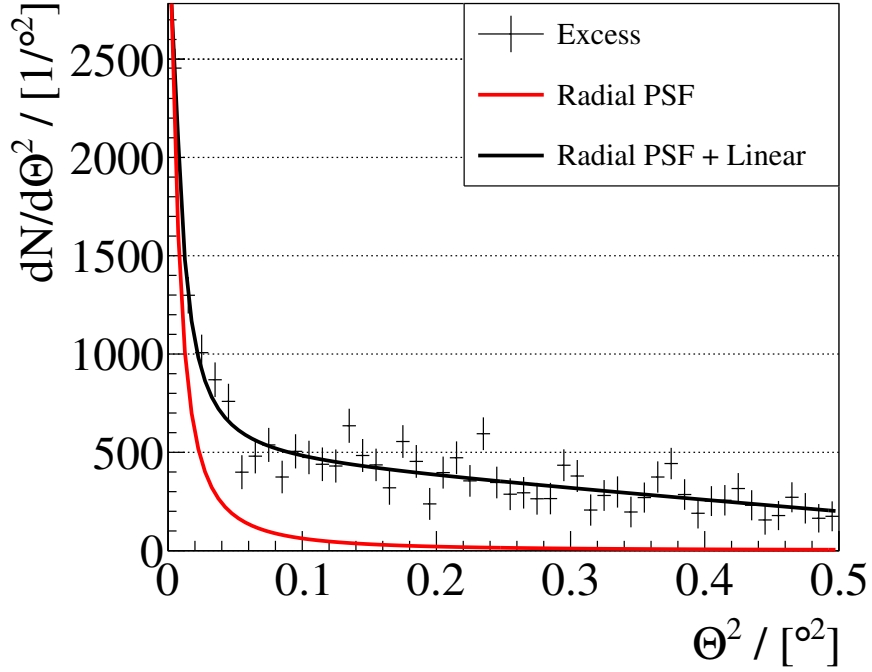


Figure 6.13: Excess events resulting from a monoscopic analysis as a function of Θ^2 . The red line is the radial PSF function following the King profile introduced in Eq. (5.1) scaled such that the integral of this function in the first bin equals the number of excess events in this bin. The black curve represents the same function added to a linear function. The excess distribution was fitted with the resulting function as described in the main text.

ing the correlation of the bin contents in the sky maps. The deviation from the ideal shape is asymmetric, though. While there is a large number of bins in the sky map with moderate negative excess enhancements, there are relatively few bins with positive excess enhancements, which then tend to be large. In the non-excluded significance distribution, a bump-like feature is seen around significance values below 15σ . This is caused by the source HESS J1303–631 introduced above. The Θ^2 distribution displayed in Fig. 6.2d is also influenced by the additional excess. At Θ^2 values close to zero a clear excess is visible nevertheless. With increasing Θ^2 values the excess decreases. As stated earlier, this is another manifestation of the wing-like excess discussed above, since the area sampled to create the Θ^2 plot covers a relevant part of the diffuse excess, as can be seen in Fig. 6.2a.

To investigate the question if PSR B1259–63/LS 2883 is extended or appears as a point-like gamma-ray source given the algorithm’s angular resolution, the excess as a function of Θ^2 can be compared to the PSF. The PSF calculated for the observation conditions of the data set analysed here is shown in Fig. 6.13 together with the number of excess events per bin. The PSF was scaled such that the integral of the PSF over the first bin is equal to the number of excess events in this bin. Due to the influence of the wing-like excess discussed above, the agreement between the PSF and the excess event

Parameter	Ξ	$\sigma / [^\circ]$	γ	$m / [(1^\circ)^{-4}]$	$n / [(1^\circ)^{-2}]$
Value	1.16	4.86×10^{-2}	1.68	-565 ± 81	478 ± 24

Table 6.4: Parameters of the function defined in Eq. (6.1), which describes the excess distribution as a function of Θ^2 . Parameters without errors are fixed, as described in the main text.

distribution is not satisfactory. This can be quantified by calculating the reduced χ^2 value, which takes into account the difference between the PSF function and the excess events. Here this value is 919. Thus the excess needs to be compared to a function with a different shape. Since the slope seen in Fig. 6.2d at large Θ^2 values is different from zero, the new function is constructed as a linear function added to the King-profile shape of the PSF introduced in Eq. (5.1). Hence the resulting function is defined as

$$K'(\Theta^2) = \frac{\Xi}{\pi\sigma^2} \left(1 - \frac{1}{\gamma}\right) \cdot \left[1 + \frac{1}{2\gamma} \cdot \frac{\Theta^2}{\sigma^2}\right]^{-\gamma} + m \cdot \Theta^2 + n. \quad (6.1)$$

The parameters σ and γ are not subject of the fitting procedure but are determined from the PSFs calculated for the relevant observation conditions from the Monte Carlo studies, hence they are identical to the original function $K(\Theta^2)$. The parameter Ξ is fixed by the scaling procedure described above. Only the parameters of the linear function are fitted, resulting in the values listed in Tab. 6.4. From the χ^2 value of 58.6, given the number of degrees of freedom of 48, the reduced χ^2 value of 1.2 is calculated, which corresponds to a p-value of 0.14. Thus it is concluded that, assuming that the excess can be modelled by a linear function, the excess is compatible with a point-like excess. It should be noted that for an extended source the width of the PSF would change instead of the absolute normalisation, thus the addition of a linear function with a moderate slope will not hide the effect of a source extension on the excess distribution, thus the conclusion is considered conservative.

Since monoscopic analyses are more susceptible to variations of the NSB level, the impact of the NSB on the sky maps shown above needs to be investigated. NSB rates can be calculated from data by investigating the current that needs to be provided to each pixel. For details of the calculation the reader is referred to Aharonian et al. [139]. In case of the area of the sky observed by CT5 during the PSR B1259–63/LS 2883 observation campaign, the map of the NSB rates is shown in Fig. 6.14. Since only NSB rates of regions of the sky within the FoV of the camera can be calculated, only information about areas which were included in the FoV at least once during the observation campaign is available. Averaged over the entire FoV, the mean NSB photoelectron rate is $(133 \pm 46) \times 10^6$ p.e. s⁻¹, where the given error represents the rms. Hence the overall NSB level is on the same order as the level assumed in the Monte Carlo simulations. Nevertheless, the level is significantly higher in certain regions in the FoV. The maximum NSB level in the FoV, found close to the bottom of the image, is 790×10^6 p.e. s⁻¹. This value is caused by the star HIP 64094, also called Theta Muscae, which has an

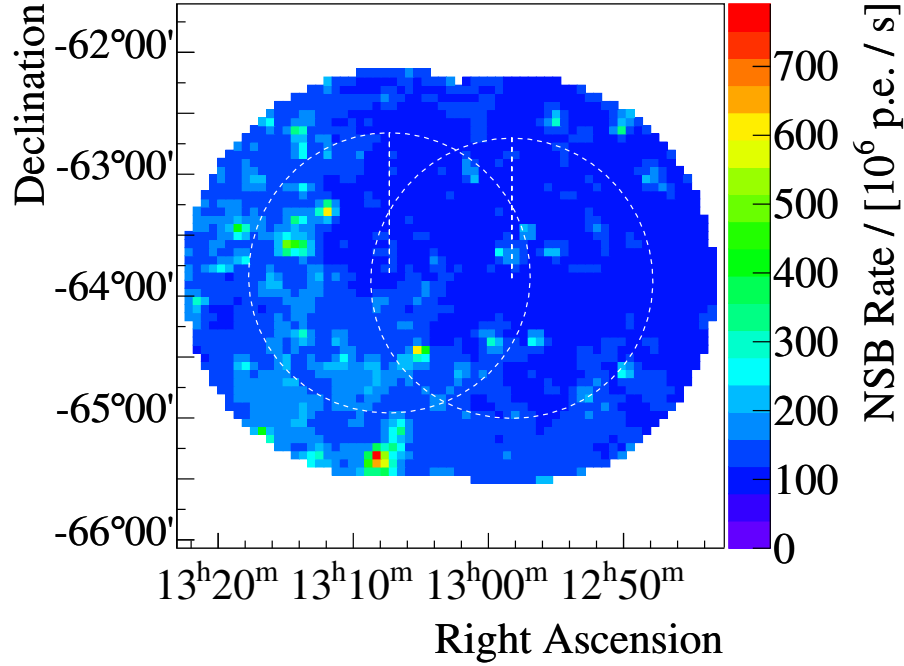


Figure 6.14: Average NSB rate per pixel, mapped to coordinates in the sky. No smoothing algorithm was applied. White, dashed circles illustrate the sizes of the circles defined by the nominal distance cut around the two observation positions.

apparent magnitude of 5.4. All other features in the NSB map are caused by stars as well, but all of those have apparent magnitudes of six or more. Hence the NSB level close to those stars is lower than the NSB level at the position of Theta Muscae. Close to Theta Muscae another star called HIP 63991 is located, contributing to the apparent elongation of the high-NSB region north-east of the formerly mentioned star. The extension of the elevated NSB level regions over several pixels around Theta Muscae and elsewhere in the field of view have two causes. Firstly, this might be a binning effect, and secondly, often two or more pixels in the camera will be illuminated by the light emitted by the respective star. The 80% containment diameter of the optical PSF of the telescope is $\lesssim 0.06^\circ$, which is comparable to the FoV of one pixel of the CT 5 camera of 0.07° . Therefore an enhanced NSB level is expected in several pixels in the sky map around the true position of a star.

The contribution of the enhanced NSB level around this brightest star to the measured intensity per pixel per readout window is estimated according to the description in Sec. 4.1 to be approximately 12.6 p.e. This has an influence on the measured intensity distribution in the camera and hence also on the distribution of reconstructed directions. Two cases need to be studied to understand the influence of the NSB on high-level results. In the first case, the NSB level in adjacent pixels is high enough to pass the image cleaning criterion. For this at least one pixel would need to measure NSB rates of at least $R_{10}^{\text{NSB}} = 625 \times 10^6 \text{ p.e. s}^{-1}$ to fulfill the higher image cleaning criterion, and at least one

adjacent pixel needs to measure rates exceeding $R_5^{\text{NSB}} = \frac{1}{2}R_{10}^{\text{NSB}} = 313 \times 10^6 \text{ p.e. s}^{-1}$. If this were the case, the distributions of basic parameters like the length or the width of the Hillas ellipses would deviate significantly between the pointing positions, since the bright star is only included in the FoV when pointing towards smaller right ascension values. These distributions, however, deviate only at the percent level, hence it is concluded that the high-NSB region does not contribute to the analysis in form of a separate cluster of pixels with intensities passing the image cleaning procedure. The reason why this criterion is not fulfilled despite the fact that the sky map pixels around Theta Muscae have a sufficient average NSB rate to pass the lower image cleaning threshold is that these rates are not high contemporaneously to the times when the maximum pixel exceeds the higher image cleaning threshold because the area illuminated by the star's light is distributed over two (or more) pixels at these times. However, in the second case, the high NSB level influences the intensities of pixels in the camera which are exposed to Cherenkov photons. In this case, for example the distribution of the COGs should show an increase towards the direction of the region exposed to the bright star. Since this region moves in the camera by approximately 0.2° during the course of one run, the COG distribution obtained from one third of a run is studied. The obtained COG distribution is radially symmetric, with mean values compatible with zero within one bin width of 0.02° and rms values in both the x - and y -directions deviating less than 1% from each other. Thus, the overall influence of the NSB present in the FoV discussed here on analysis results is found to be negligible.

When performing a stereoscopic analysis, the influence of the broken drawer in the CT5 camera is expected to be reduced, since information from the other cameras can be used to reconstruct directions even if the shower images were truncated by the malfunctioning drawer in the CT5 camera. In Fig. 6.15a, an excluded sky map resulting from an analysis of the 140 observation runs fulfilling quality criteria listed in Tab. 6.1 is shown. The analysis algorithm used here is a simple extension of the Hillas analysis presented in Aharonian et al. [164] enabling analyses of data taken with the H.E.S.S.-II array. A negative excess in the lower half of the excluded sky map can still be seen, but to a lesser extent than in case of the monoscopic sky map. Hence also the significance distribution shown in Fig. 6.15b is better compatible with the target distribution. The mean value of the significance distribution is zero, and also the width is compatible with one within two standard deviations. Interestingly, the overall significance with which PSR B1259–63/LS 2883 is detected here is slightly smaller than in the monoscopic case despite the much improved background suppression capabilities introduced by the use of stereoscopy. The simplicity of the stereoscopic analysis, which uses only cuts on Hillas parameters to discriminate between gamma-ray induced air showers and hadronic air showers, is the main reason for the limited sensitivity of that algorithm.

6.2 Spectrum

A fundamental property of any gamma-ray emitter is the differential photon spectrum. This quantity describes the photon flux per energy bin as a function of the energy. In

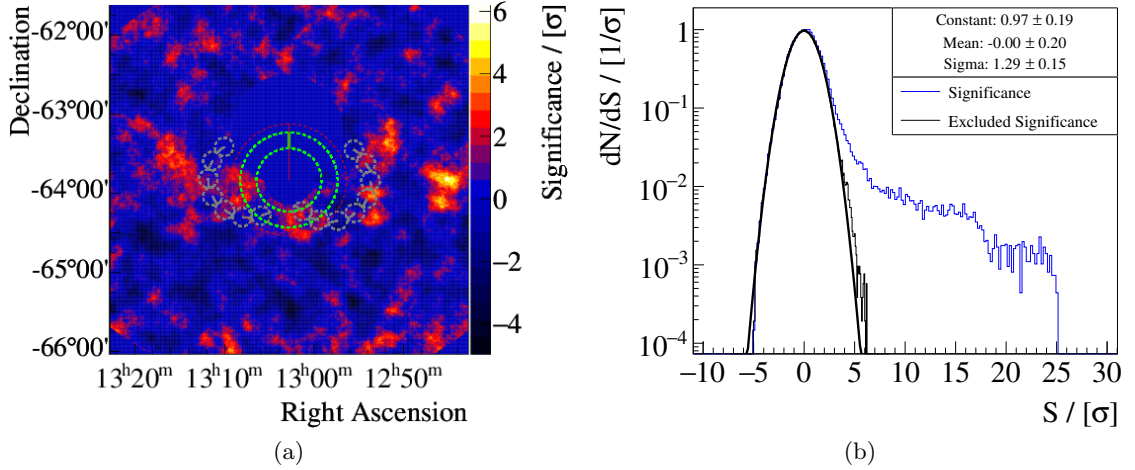


Figure 6.15: *Left*: Excluded significance map obtained from a stereoscopic analysis. See Fig. 6.2 for an explanation of the different elements shown in the plot. *Right*: Excluded and non-excluded significance distribution resulting from the stereoscopic analysis.

case of the HAP analysis framework used here, the spectrum reconstruction is based on the reflected-region background estimation technique. This technique, as discussed before, allows determining the number of ON, OFF and excess events. The distributions of those quantities as functions of the reconstructed energy are shown in Fig. 6.16. A general shape is common to all three distributions. At low energies, the number of events detected per energy bin after applying all cuts increases with energy. This is caused by the steep increase of the detection efficiency close to the energy threshold as discussed in Sec. 5.4. At higher energies the detection efficiency is relatively constant, but the gamma-ray spectrum of the source and the cosmic-ray spectrum decrease like a power-law with increasing energy. Therefore also the number of detected events in the ON and OFF regions and consequently the number of excess events decrease with energy. In case of the excess distribution, the shape is also influenced by the difference of the gamma- and hadron-acceptance of the cuts applied to the data, which is energy-dependent. Since the gamma-hadron separation is worst at low energies, the number of excess events exhibits an increase at the lower end of the displayed energy range. The energy threshold of the monoscopic analysis discussed here is shown in the plot, too. This threshold can be defined either as the energy at which the maximum of the ON distribution shown in the plot is found or as the energy at which the effective area reaches 10% of its maximum value. In the MonoReco algorithm presented before, the second definition is adopted, although by coincidence the threshold obtained from the first definition would be approximately the same. Since the value of the energy threshold depends on the observation conditions, the effective area is averaged over the entire data set, and the energy threshold is determined from the averaged function. In this case, the energy threshold is at 178 GeV, which is more than 50% lower than the lowest energy threshold of a PSR B1259–63/LS 2883 analysis published by the H.E.S.S. collaboration of 380 GeV

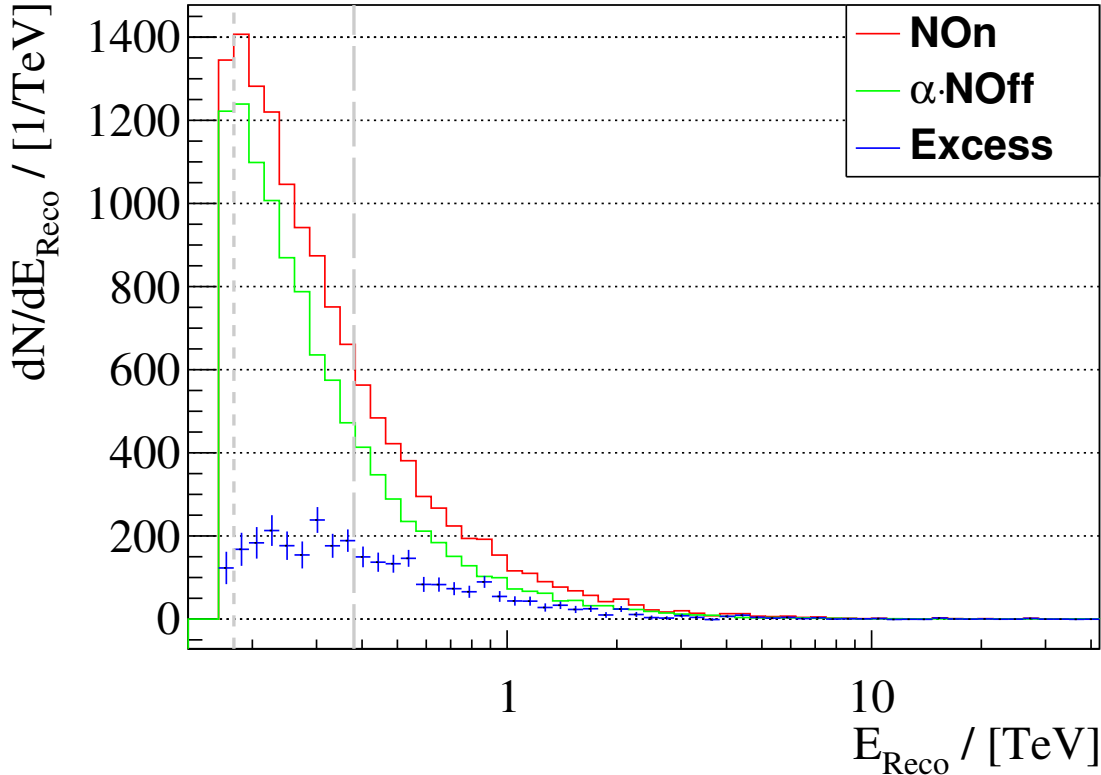


Figure 6.16: Distributions of the number of events in the ON and OFF regions, scaled to equal exposure, and the number of excess events in the ON region as functions of the reconstructed energy. The short-dashed grey line indicates the position of the energy threshold of the monoscopic analysis presented in this work, the long-dashed line indicates the position of the lowest threshold obtained from H.E.S.S. I analyses in the past.

[53]. In the energy range between these two thresholds, approximately 55 % of the excess events above the lower threshold are found, demonstrating the good performance of CT 5 and the MonoReco algorithm at previously inaccessible energies.

Before discussing the spectrum itself, the influences of the broken drawer and the gain gradient discussed in the previous section on the estimates of the number of ON and OFF events need to be discussed. In Fig. 6.2b, the positions of the OFF regions are indicated for both wobble offsets. The corresponding number of events in the OFF regions is shown in Fig. 6.17a, where the OFF regions are counted anti-clockwise starting from the north-western region. The numbers of events and their uncertainties are scaled to correspond to the total exposure of the ON region. It can be seen that the number of events in the OFF regions resembles the shape of the positions of the OFF regions in the sky map referenced above. This agrees well with the conclusion drawn above that there is a lack of events at the bottom of the sky map caused by the both the gain gradient and the broken drawer B5. To further investigate the correlation of the number of events with the location of the OFF region, in Fig. 6.17b the number of events

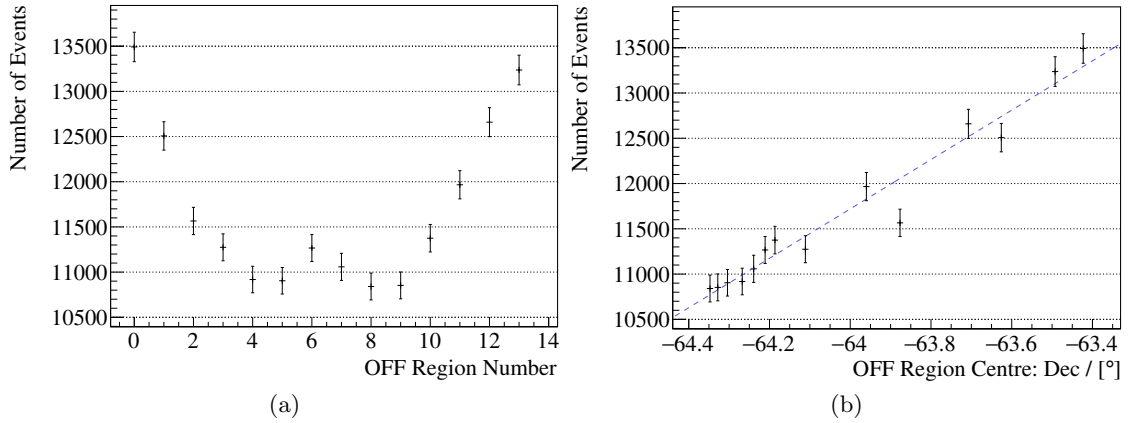


Figure 6.17: Number of events in the reflected-background OFF regions, scaled to correspond to the total exposure. The numbering of the regions given on the abscissa of the plot on the *left* is based on their positions in the sky. Counting starts in the north-western corner and is to be continued in an anti-clockwise direction. In the plot on the *right*, the same number of events in the OFF regions is shown as a function of the declination of the centres of the regions. The dashed blue line represents the best-fit linear function.

is shown as a function of the declination of the OFF region centres. A clear trend is observed, motivating a fit with a linear function yielding a slope of $(2700 \pm 100)/^\circ$ and a reduced χ^2 value of $19/12 = 1.6$. It should be noted, though, that this linear trend is not expected across the entire FoV, since in case of the ring-background technique the wing-like excess discussed above is observed instead of a linear gradient.

To study the influence of this gradient on the flux derived from the number of excess events, the linear fit can be used to estimate the number of background events expected at the declination of PSR B1259–63/LS 2883 given above. It should be noted that only the gradient observed in the sky map is relevant for the estimation of the number of background events in the on region, since a hypothetical, constant offset of the number of events in the region enclosed by the OFF regions will be eliminated by the background subtraction technique, and the statistical error of the event numbers does not impact absolute values of flux estimates. At the position of PSR B1259–63/LS 2883, a number of background events of 12179 is expected. This deviates from the number of events of 11926 given in Fig. 6.2d by only 2%, which is a fortunate coincidence. For example a different choice of the exclusion regions could lead to a larger deviation of the two numbers of events. Since the flux given in Eq. (5.14) is proportional to the excess, which in turn is proportional to $-N_{\text{OFF}}$, the fluxes calculated from the plain application of the reflected-region technique are estimated to be 2% too high, which is considered negligible given the much larger systematic effect of, for example, changing atmospheric conditions discussed in Sec. 2.9 on estimated fluxes. Hence no correction will be applied in the following to account for the effect of the gradient. Nevertheless an additional systematic error can be derived from the plots shown in Fig. 6.17. A conservative

estimate of a symmetric systematic error is derived by dividing the range of the number of background events, ranging from 10830 to 13500, in half, yielding a relative error on N_{OFF} and thus also on flux estimates of approximately 11 %.

The differential photon spectrum is calculated from the number of ON and OFF events using a forward-folding technique introduced briefly in Sec. 5.7. Based on the hypothesis that the spectrum follows a power law, a likelihood function is used to estimate the number of signal and background events per energy interval for each run given the measured numbers of ON and OFF events. During the calculation of the estimated numbers, the effective areas and the energy migration matrices corresponding to the observation conditions of the respective run are used. From these estimates, the expected number of excess events $\langle \frac{d\epsilon}{dE}(E) \rangle$ per energy bin dE and the expected differential photon flux $\langle \frac{dN}{dE}(E) \rangle$ as a function of the energy can be calculated. Using these results, the flux $\frac{dN}{dE}(E)$ is calculated as

$$\frac{dN}{dE}(E) = \frac{\frac{d\epsilon}{dE}(E)}{\langle \frac{d\epsilon}{dE}(E) \rangle} \cdot \left\langle \frac{dN}{dE}(E) \right\rangle. \quad (6.2)$$

The flux points resulting from this technique are shown in Fig. 6.18 together with the corresponding fit with a power-law function. Flux points are rebinned such that each point corresponds to a significance of at least 2σ . Since the significance of the last point is not sufficient, a flux upper limit is calculated for the energy range starting at the respective bin. Limits are placed at the flux corresponding to the upper end of the 99.7 % confidence interval of the flux calculated for the respective energy interval. The χ^2 value quantifying the deviation of the data points from the fit function is 17.0 for 15 degrees of freedom, so the reduced χ^2 value is 1.1. Since this χ^2 value indicates that the fit function is well-suited for this data set, no other spectral hypothesis was tested. The resulting fit parameters are given in the inset in Fig. 6.18. While the VHE part of the spectrum of PSR B1259–63/LS 2883 was known to be compatible with a power law down to 380 GeV only, it can now be concluded that the data points below this energy threshold agree well with a power-law fit. Nevertheless, a slight down-turn towards the lowest energies can be observed in the residuals plot shown in the figure, where the deviation from the fit function of four data points in a row decreases by, in total, 30 %. This effect does not affect the conclusion that the power-law fit describes the spectrum well, because the overall deviation of these data points is still below 20 % and compatible with the function within two standard deviations, but the observed trend might indicate the presence of a systematic effect instead of a statistical fluctuation. One reason for such a trend could be an underestimation of the energy bias at these energies, since then too few events are migrated from higher-energy bins to lower-energy bins. Also an underestimation of the energy resolution can lead to such an effect, since then the number of events with reconstructed energies in a higher-energy bin and real energies belonging to a lower-energy bin would be underestimated. Such a migration also occurs from lower-energy bins towards higher-energy bins, but due to the power-law decrease of the gamma-ray spectrum, too many events would then remain in higher-energy bins, leading to an observed lack of events at lower energies. Furthermore, also

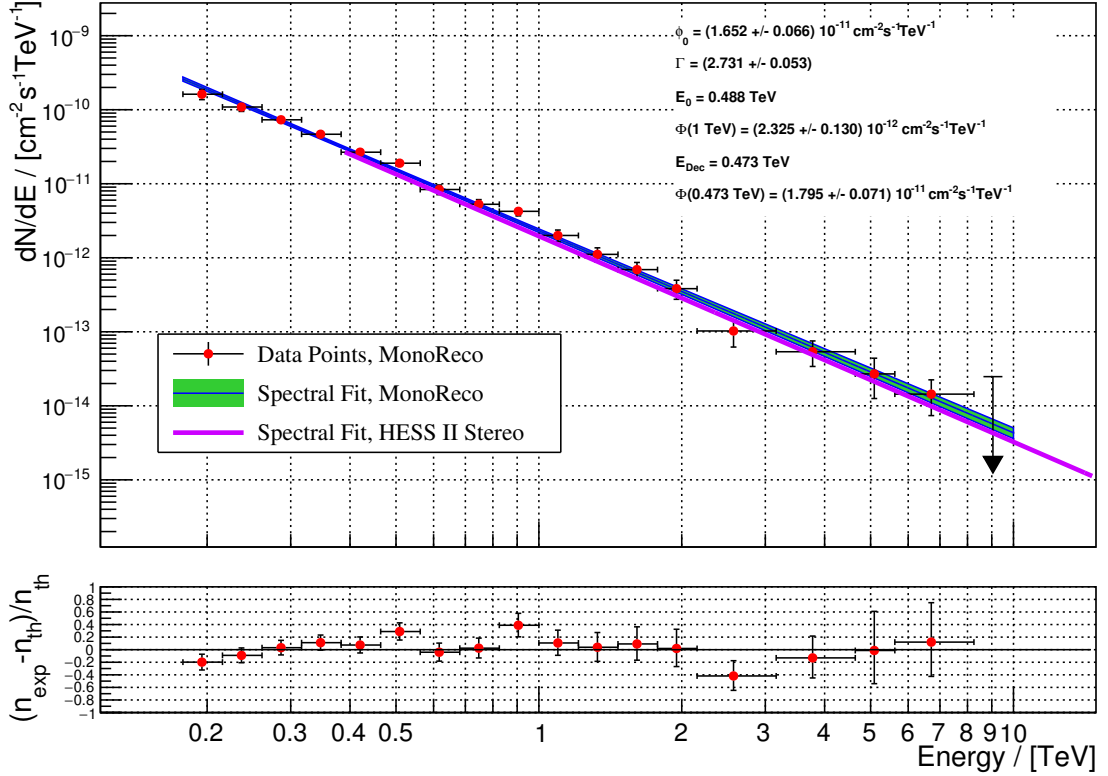


Figure 6.18: Differential photon spectrum obtained from a monoscopic analysis of PSR B1259–63/LS 2883 data. The blue line represents the best-fit power law, the green uncertainty band represents the statistical uncertainty of the spectral shape. The arrow represents a flux upper limit. The violet line represents the best-fit power-law function for data points obtained from a stereoscopic analysis of the 2014 data. The fit residuals are displayed in the lower panel as relative deviation of the flux points from the fit function.

an overestimation of the effective area at the respective energies can introduce such an effect, as can be seen from Eq. (5.14). Such an overestimation can be caused, for example, by too optimistic assumptions about the optical efficiency of the detector, the transmissivity of the atmosphere or the number of non-functional pixels in the camera. All these effects are more important at low energies, because there the showers are faint, leading to a large relative discrepancy of reconstructed shower properties from the real shower properties.

To put the obtained spectral parameters into perspective, a comparison with results from previous observation campaigns and also with results from a stereoscopic analysis of the 2014 data set can be made. All spectral indices listed in Tab. 6.5 agree with each other within errors, therefore a superorbital modulation of the spectral index can, for the years analysed here, be excluded. The agreement of the flux normalisations obtained from the previous observation campaigns with the flux normalisation resulting from analyses of the 2014 data set is not investigated here, because different parts of

	2004	2007	2010	2014 Mono	2014 Stereo
Γ	2.8 ± 0.1	2.8 ± 0.2	2.9 ± 0.3	2.73 ± 0.05	2.78 ± 0.08

Table 6.5: Spectral index Γ resulting from analyses of data obtained from different observation campaigns and, in case of the 2014 data set, from either a monoscopic or a stereoscopic analysis of the data. The spectral indices for the 2004–2010 data sets are taken from [53].

the orbit were sampled during the different observation campaigns. Thus altering flux normalisations are expected and will be discussed in the context of the light curves shown in Sec. 6.3. Whether the spectral index changes during the course of one orbit is also discussed in the next section. In case of the 2014 data set, apart from the spectral indices also the flux normalisations obtained from a monoscopic and a stereoscopic analysis are compatible with each other. The differential photon flux at 1 TeV obtained from a stereoscopic data analysis is $(2.0 \pm 0.1) \times 10^{-12} \text{ cm}^{-2} \text{ s}^{-1} \text{ TeV}^{-1}$, which is compatible with the flux given in Fig. 6.18 within two standard deviations.

6.3 Variability

As stated earlier, the binary system PSR B1259–63/LS 2883 exhibits flux variability at all wavelengths. In this section, the variability of the observed VHE gamma-ray flux and of the spectral index is discussed.

Fluxes above a certain energy threshold are calculated according to Eq. (6.2). They can be calculated for different periods of time, where the choice of time intervals should be motivated by the physics that is to be derived from the fluxes. Choosing very short time intervals, like the duration of a typical observation run of 28 min, yields very large relative statistical uncertainties of the fluxes, while very long time intervals, like a monthly binning, result in a too coarse picture of the flux variability, since the gamma-ray flux is expected to change on time scales of days. As a compromise, a weekly binning is chosen here. The choice of the energy threshold depends on the data set to be analysed. In case of the monoscopic analysis presented above, the threshold can be lowered to approximately 200 GeV, because the safe energy threshold for all but six observation runs is lower than this energy. In case of the remaining six observation runs, the safe threshold is 215 GeV. The threshold value of 200 GeV is contained in the energy bin below the bin starting at 215 GeV, hence the additional uncertainty introduced by choosing the given threshold value is considered negligible. Whenever the flux is calculated for an energy threshold below the safe threshold determined by the respective effective area curve, the calculated flux is an extrapolation of the flux calculated for energies above the safe energy threshold assuming a power-law shape of the spectrum. The spectral index is obtained from the spectral reconstruction presented above. The resulting flux above 200 GeV as a function of the time is shown in Fig. 6.19a. For reference, the disk crossing

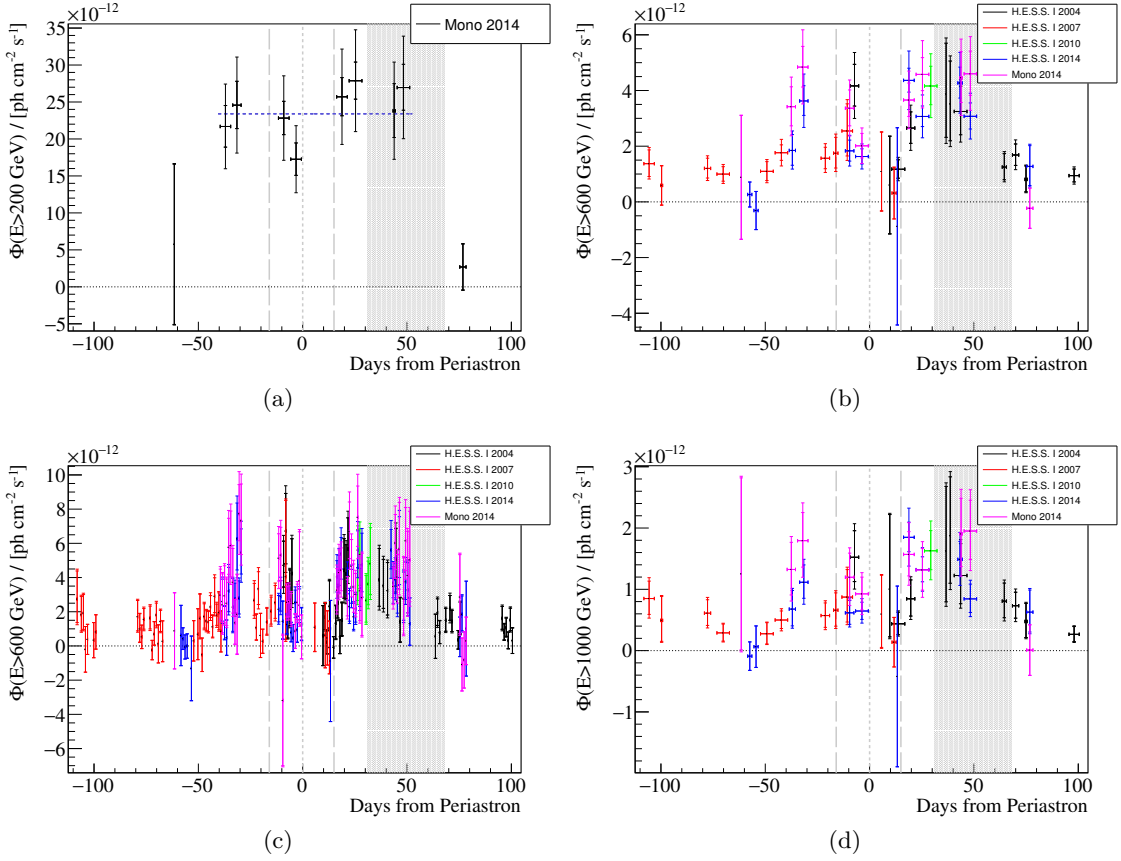


Figure 6.19: Integrated photon fluxes above energy thresholds of 200 GeV (*top left*), 600 GeV (*top right* and *bottom left*) and 1 TeV (*bottom right*) with a night-wise binning (*bottom left*) or a weekly binning (all other plots). Negative fluxes result from negative estimates of the number of excess photons. The times of the disk crossings and the periastron are marked by dashed grey lines as explained in the caption of Fig. 6.1. The time during which the Fermi flare occurred is indicated by the shaded grey area. H.E.S.S. I data from previous observation campaigns was re-analysed as explained in the main text. Horizontal error bars represent the time range during which the fluxes are averaged. Two types of vertical error bars are shown. The smaller bars represent statistical uncertainties only, larger error bars represent the quadratic sum of statistical and systematic uncertainties as explained in the main text. The dashed blue line in the *top left* plot represents a fit with a constant of the data points in the time range covered by the fit function.

times, the time of periastron and the time the Fermi flare was ongoing are highlighted as explained in the caption of the figure. The latter time range is defined by the time the flaring started in 2011 and by the time the flaring activity has vanished in 2014 [94]. The displayed statistical error bars represent the 68 % confidence intervals of the photon flux calculated with the method by Rolke et al. [173] from the number of ON and OFF events and the exposure ratio α . Since the number of excess photons can be negative due to upward fluctuations of the number of OFF events, also the photon flux calculated from the number of excess photons can be negative. Systematic uncertainties, which are also shown, are discussed below.

Approximately 60 d before periastron the flux shown in Fig. 6.19a is low, despite the fact that this conclusion is to be taken with care since the statistical errors are large because only one run contributed data to this flux point. The next two flux points, at approximately 37 d and 31 d before periastron, demonstrate that the flux is very high compared to the low flux measured far away from periastron at for example 70 d–80 d after periastron. The orbital phase approximately two weeks before the first disk crossing was not sampled before at VHEs. After the first disk crossing, the flux is high and decreases towards periastron, a trend that can also be seen in the night-wise light curve of fluxes above an energy threshold of 600 GeV shown in Fig. 6.19c. The last run contributing to the weekly flux point right before periastron ended approximately 13.5 h before the nominal time of periastron at an MJD of 56781.42 [57]. Shortly after the second disk crossing the flux is high, and also during the time of the Fermi flare a high flux, similar to the flux level at the time of the second disk crossing, is observed. This is the first time that such a high flux was observed for several days contemporaneously to observations performed with *Fermi*-LAT while the HE gamma-ray flare was ongoing. The last flux point at approximately 77 d after periastron indicates that the flux is very low after the time of the Fermi flare.

It was investigated whether the flux values between 41 d before periastron and 53 d after periastron are compatible with a constant by fitting these data points with a respective function. In the fitting procedure only statistical errors were considered. The resulting best-fit function, which corresponds to a value of 2.34×10^{-11} ph/cm²/s, is shown in Fig. 6.19a. From the reduced χ^2 value of $13.7/7 = 1.96$ the p-value can be calculated, which is 5.7 % in this case. Thus the described set of data points is just compatible with a constant at the 95 % confidence level. It should be noted that by fitting these data points it is not tried to claim that the flux is constant between the two given fiducial dates, since there are gaps in the time range covered by the data points. Only the fluxes shown in the plot were tested for compatibility.

For a more complete picture of the light curve, in Figs. 6.19b–6.19d the light curves obtained from re-analyses of data from previous observation campaigns are shown together with the 2014 light curve. A re-analysis of archival data was necessary to allow similar light curve binnings as the binning chosen for the monoscopic analysis. For the re-analyses, the multi-variate analysis technique by Ohm et al. [174] was used. Since the safe energy thresholds of the H.E.S.S.-I analyses are much higher than the fiducial value of 200 GeV used for the calculation of the fluxes shown in Fig. 6.19a, significantly higher thresholds of 600 GeV and 1 TeV are chosen, respectively. These thresholds are high

enough to further allow for calculations of fluxes from a H.E.S.S. I-type analysis of the 2014 data set, which are therefore included in the respective plots as well. In Fig. 6.19b it can be seen that between approximately 110 d and 40 d before periastron the measured flux is comparatively low and compatible with a constant. Between 42 d and 30 d before periastron, an increase of the flux by a factor κ of approximately 2.7 ± 0.8 can be observed in the results from a monoscopic analysis and, in a similar fashion, from a stereoscopic H.E.S.S.-I analysis of the 2014 data set. Flux levels obtained from these two analyses are compatible with each other within systematic uncertainties. To further strengthen the argument that the observed increase of the flux during the mentioned part of the orbit is not an artefact of the analysis or of the calibration of the detector, a cross-check was performed by other members of the H.E.S.S. collaboration using the Model++ analysis [146], which in addition makes use of an independent calibration procedure. Results from such an analysis show a similar flux enhancement at this part of the orbit, a result to be made available in a future publication. This cross-check indicates that the high flux state is not an artefact of calibration or analysis techniques. Such a flux increase has not been observed before. A 99.7% confidence interval of the flux increase factor κ can be calculated using a profile likelihood approach. It is assumed that the distribution of measured values Φ_i at a point in time T_i follows a Gaussian distribution around the true flux Φ_i^T . The second flux can be expressed in terms of the first flux via the relation

$$\Phi_2^T = \kappa^T \Phi_1^T. \quad (6.3)$$

The superscript T denotes the true value of a parameter. Then the profile likelihood function $\lambda(\kappa)$ can be defined as

$$\lambda(\kappa) = \frac{L(\hat{\varphi}_1, \kappa | \varphi_1, \varphi_2)}{L(\hat{\varphi}_1, \hat{\kappa} | \varphi_1, \varphi_2)}, \quad (6.4)$$

where L is a likelihood function and hats denote the maximum likelihood estimators of the respective quantities. The likelihood functions are constructed as the product of two Gaussian distributions of the two measured fluxes $\Phi_{1/2}$. Confidence intervals of κ can then be calculated from the quantity $-2 \log \lambda$, which follows a χ^2 distribution with one degree of freedom. In case of the two flux points mentioned above, the lower limit of the 99.7% confidence interval of the flux increase factor is 1.4. Thus the hypothesis that the flux is constant on the time scale of days at this part of the orbit can be rejected.

Between the time of the pulse disappearance during the first disk crossing and the end of the disk crossing at roughly 8 d before periastron, the flux again increases by a factor of 2.4 ± 1.2 , which is just compatible with a constant flux at the 2σ level. An exact time of the end of the disk crossing is not known yet. Here it was chosen to be the upper end of the first flux point of the 2004 data set, since this flux point represents the local maximum of the measured fluxes. Around the time of periastron the flux is lower than the maximum flux observed after the nominal time of the first disk crossing by a factor of 2.3 ± 1.1 , which is a new result since previous observation campaigns could not cover this part of the orbit.

Shortly after the second disk crossing, the flux increases to levels similar to the flux observed at the time of the first disk crossing. After the end of the second disk crossing

the Fermi flare occurred in 2011 and reoccurred in 2014, as mentioned in Sec. 2.8.6. During the H.E.S.S. observation campaign in 2010 and 2011, the coverage of this part of the orbit was limited, yielding approximately 2.5 h of live time during the time of the flare based on the data selection criteria listed in Tab. 6.2. In 2004, data worth another 5 h of live time were collected. The first two data points of the latter data set inside the time range corresponding to the Fermi flare indicate that the flux at this part of the orbit is on a similar level as shortly after the disk crossings. However, since no experiment covering the HE gamma-ray band observed PSR B1259–63/LS 2883 at this part of the orbit at that time, the existence of a flare in the respective energy band could not be inferred. The fluxes measured in 2014 are compatible with the fluxes obtained from the re-analysed data from 2004 and also indicate a high flux state at the time of the Fermi flare. Considering fluxes obtained with the monoscopic analysis only, the deviation of either of the fluxes inside the time range of the Fermi flare from the last flux measured before the start of the flare is less than 3%. At 99.7% confidence level, the flux increase factor is between 0.37 and 1.9. Hence it can be claimed that, while for the first time a high flux was measured in the VHE gamma-ray band contemporaneously with measurements in the HE gamma-ray band during a large part of the time of the flare, a flux increase of $\gtrsim 1.9$ can be excluded. At the end of the nominal time of the flare and later, the flux decreases to levels measured at the lower end of the time range displayed in Fig. 6.19b.

Most of the calculated photon fluxes shown in Fig. 6.19b obtained from different observation campaigns or from different analysis chains agree with each other within statistical errors when they correspond to similar parts of the orbit of PSR B1259–63/LS 2883. In addition to statistical uncertainties, also systematic uncertainties need to be taken into account when discussing the compatibility of flux points. In general, a systematic uncertainty on calculated fluxes of 20% is stated for H.E.S.S. results due to the influence of changing atmospheric conditions. This number is adopted also when comparing results from the same observation campaign but different analysis techniques, because the different quality criteria applied to select runs for either monoscopic or stereoscopic analyses yields non-identical sets of selected runs. Due to the short time scale of changing atmospheric conditions, like an increase or decrease of the relative humidity of the air or the presence of thin layers of clouds in the FoV of the telescopes, the atmospheric transparency can indeed change from run to run, so that the quoted value of the systematic uncertainty is considered to be a realistic choice. In addition, the systematic uncertainty introduced by the varying number of OFF events per circular OFF region, as discussed above, is estimated to be 11% in case of the monoscopic analysis. Adding these two systematic uncertainties in quadrature yields a total uncertainty of 23% in case of the monoscopic analysis. In case of the stereoscopic analyses also the fact that the safe energy thresholds for individual runs can be higher than the energy above which the fluxes are calculated is a cause of systematic uncertainties. The magnitude of this uncertainty is estimated to be 10%, yielding a total error of 22%.

Within uncertainties, all fluxes measured at similar parts of the orbit are compatible with each other apart from the last points of each of the 2014 analyses as shown in Fig. 6.19b. There are also several data points with only marginally overlapping confi-

dence intervals, for example at 38 d before periastron. One reason for this discrepancy could be a differing set of runs contributing to both analyses providing the two data points. To investigate this hypothesis, a light curve with a finer time binning can be discussed. A night-wise light curve using the same energy threshold above which fluxes are calculated as in Fig. 6.19b is shown in Fig. 6.19c. All night-wise fluxes obtained from the two analyses of 2014 data contributing to the mentioned weekly flux points at approximately 38 d before periastron are compatible with each other. However, it is noted that there is no counterpart for the first data point resulting from the monoscopic analysis in this time range. For each of the remaining nights, the fluxes are compatible, and no systematic shift between the fluxes obtained from the monoscopic analysis and the fluxes resulting from the stereoscopic analysis is apparent. This also holds for other parts of the orbit. Furthermore, the fact that for several nights the uncertainty intervals do not overlap is expected since only 68% intervals are shown. Among the 44 nights for which both monoscopic and stereoscopic flux points are available, the agreement is satisfactory. The reduced χ^2 value is $31.0/43 = 0.72$, and the distribution of the significances of the flux differences is best-fit with a Gaussian distribution with a mean value of $(0.25 \pm 0.24)\sigma$ and a width of $(1.10 \pm 0.29)\sigma$. This distribution is compatible with a Gaussian distribution with a mean of zero and a width of one, thus it is concluded that the deviation of the fluxes obtained from the two different analyses of the 2014 data set do not deviate more than expected due to statistical fluctuations. It was ignored that the data contributing to the two sets of flux points are mildly correlated.

Apart from the previous discussion of the agreement of fluxes obtained from different analyses of data from the same observation campaign, also the compatibility of the fluxes obtained from different years should be investigated. A χ^2 test can be performed to compare fluxes from nights with equal displacement from the respective periastron from any of the observation campaigns for which at least two fluxes are available. For the 2014 data, only the monoscopic fluxes are considered. The uncertainties used in the comparison were calculated as the average of the lower and upper ends of the total errors shown in Fig. 6.19c in order to convert the originally asymmetric errors into symmetric errors. In total there are 18 nights fulfilling the given criteria, covering times from approximately 30 d before periastron until approximately 75 d after periastron. Data from all years are included in the test after applying the selection. The resulting χ^2 value is 17.4. Given the number of degrees of freedom of 17 it is concluded that there is no indication of inter-orbital flux variability.

To investigate the energy-dependence of the light curve, fluxes at energies above 1 TeV are shown in Fig. 6.19d. The flux values obtained from the re-analyses of archival data are compatible with the published results for the 2004 and 2010/11 observation campaigns, whereas the results of the re-analysis of the 2007 data differ partially from the published results. The fluxes of the period labelled “April”, “June” and “August” in Fig. 4 in Aharonian et al. [52] are compatible with one of the weekly fluxes displayed in Fig. 6.19d which contribute to the respective monthly time bins. However, one of the respective weekly fluxes deviates from the published value at the 2σ level. Since the flux emitted by PSR B1259–63/LS 2883 is not constant in time, especially around the time of the flux increase before the first disk crossing, the exact choice of runs contributing to the

analysis is of importance. Since the run list used by the authors of the publication is not available, further compatibility tests could not be performed.

It can be seen that, while the overall flux level is lower at energies above 1 TeV than above 600 GeV, the most important properties of the light curve like the ratio of the high flux before the first disk crossing and the times before this flux increase, the similarity of the fluxes measured during the disk crossings and the Fermi flare or the fact that the flux is low between the two disk crossings remain unchanged. During the time of the Fermi flare, however, a discrepancy of $\lesssim 2\sigma$ between the flux points at approximately 48 d after periastron can be observed. This is the largest discrepancy observed between the two different analyses of the 2014 data sets, thus the reason of the deviation was investigated in more detail. The observation conditions during the respective nights were stable, and PSR B1259–63/LS 2883 was observed at favourable zenith angles around 40° , hence systematic effects occurring at large zenith angles can be excluded. Another possibility would be either an underestimation of the effective area of the monoscopic reconstruction algorithm or an overestimation of the stereoscopic reconstruction algorithm. To investigate the former hypothesis, photon fluxes were calculated for energies in a restricted range between 1 TeV and 3 TeV. Both reconstruction algorithms are expected to perform stably in this range. However, the observed fluxes changed on the level of a few percent only. Thus also an underestimation of the monoscopic effective area is considered unlikely to be the cause of the observed flux difference. An overestimation of the stereoscopic effective area could, for example, be caused by a large number of broken pixels in one or more of the cameras of CT 1–CT 4. This, however, is not the case during any of the runs contributing to the respective flux points. The fraction of broken pixels varies only marginally over the entire 2014 observation campaign. Thus the origin of the flux difference is assumed to be caused by statistical fluctuations.

Apart from the flux variability discussed above it was also investigated whether the spectral index is variable. As already discussed, the spectral indices obtained from analyses of the data from different years are compatible with each other, thus there is no evidence for inter-orbital index variability. For the 2014 data set analysed with the MonoReco algorithm, the spectral index as a function of the observation period is shown in Fig. 6.20a. Fitting the data points with a constant results in a χ^2 value of 7.3 for a number of degrees of freedom of three. These numbers can be converted to a p-value, which corresponds to the probability that the observed deviation of the indices from a constant value is due to fluctuations of the measured indices around the constant, true index. Here the p-value is 0.06, thus the measured spectral indices are compatible with a constant at the 2σ level.

In addition it was also tested if the spectral index is correlated with the integrated photon flux above energies of 1 TeV. Results from analyses of monthly periods of data from all available observation campaigns was used to provide the data shown in Fig. 6.20b. Published results were used for the data points from 2004, 2007 and 2010/11. Together with the data points, also a fit with a constant value and with a linear function are shown. The χ^2 value of the linear fit is 12.7 for a number of degrees of freedom of 10, yielding a reduced χ^2 value of 1.3. Fitting the data with a linear function improves the reduced χ^2 value marginally to approximately 1.1. In this case the resulting slope of the

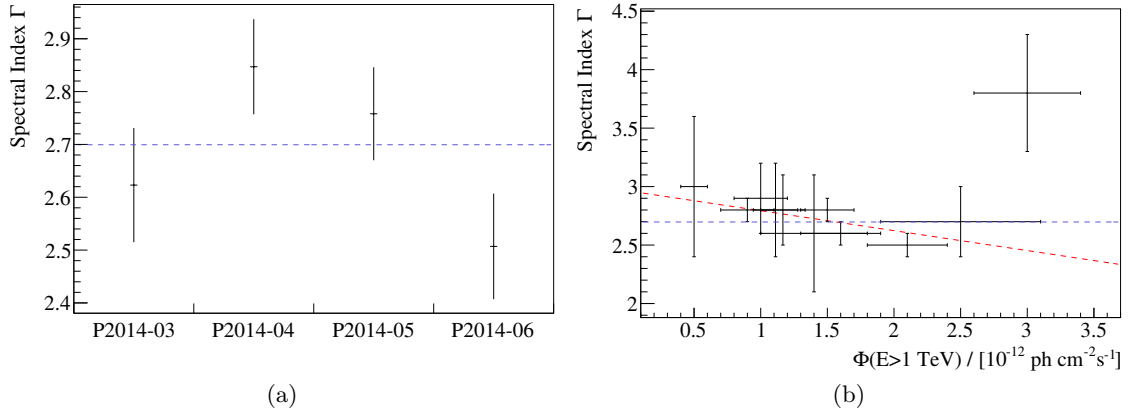


Figure 6.20: *Left*: Spectral index obtained from a monoscopic analysis of the 2014 data set as a function of time. *Right*: Spectral index as a function of the integrated photon flux above energies of 1 TeV. Results from analyses of data from all years were used as input for the latter plot. Data points were fitted with a constant value and, in case of the plot on the *right*, also with a linear function. Fit results are discussed in the main text.

linear function is $-0.2 \pm 0.1 / (10^{-12} \text{ ph/cm}^2/\text{s})$. It should be noted that the resulting deviation of the slope from $0 / (10^{-12} \text{ ph/cm}^2/\text{s})$ is entirely caused by one single data point at a flux value of approximately $2.1 \times 10^{-12} \text{ ph/cm}^2/\text{s}$. Excluding this data point from the fit leads to a fit function that has a slope of $0.0 \pm 0.2 / (10^{-12} \text{ ph/cm}^2/\text{s})$. This, together with the fact that the linear fit is only marginally preferred over the fit with a constant, leads to the conclusion that the spectral index is not correlated with the integrated photon flux.

6.4 Discussion

In this section, the results discussed above are put into context by comparing them to results from observations at other wavelengths. Results from contemporaneous observations by *Fermi*-LAT in the HE band are compared with the spectra and light curves obtained from H.E.S.S. observations around the 2014 periastron. From the measured fluxes, also the maximum energy deposited into VHE gamma-rays is calculated. In addition, measured light curves are also compared to two model predictions.

6.4.1 Multi-Wavelength Spectral Energy Distribution

The spectral energy distributions (SEDs), calculated as the differential photon fluxes multiplied by the squared energy corresponding to the mean of the respective bin, obtained from *Fermi*-LAT observations around the 2010 and the 2014 periastra [93], are shown in Fig. 6.21. These SEDs correspond to the times of the Fermi flare only. For comparison, also the VHE spectrum obtained from a monoscopic analysis of the data set

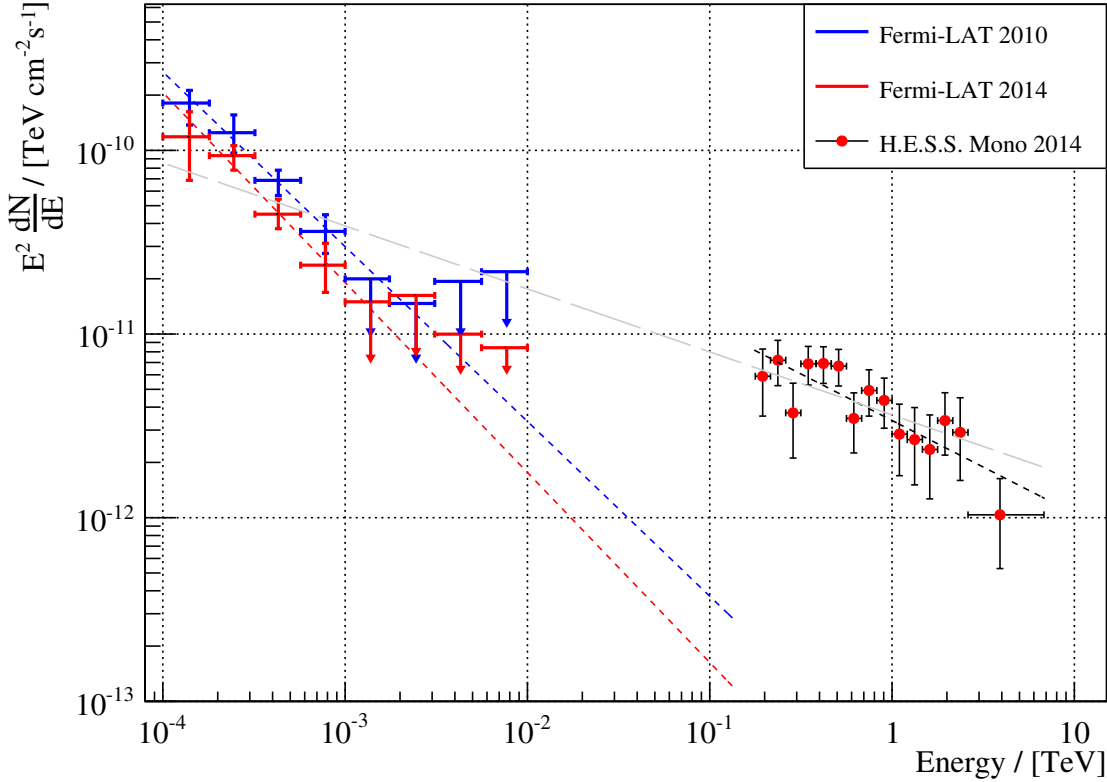


Figure 6.21: Spectral energy distributions resulting from analyses of *Fermi*-LAT data obtained during the 2010 and 2014 flare periods by Caliendo et al. [93] and from a monoscopic analysis of the H.E.S.S. data from observation period P2014-06. Best-fit power-law functions are shown for all distributions individually. Upper limits were not considered during the fitting procedure. Due to the large statistical uncertainties, the reduced χ^2 values are $0.14/2 = 0.07$ and $0.38/2 = 0.19$ for the 2010 and 2014 *Fermi*-LAT data sets, respectively. In case of the H.E.S.S. data, this value is $9.5/13 = 0.73$. The grey, long-dashed line represents the best-fit power-law function of the two 2014 data sets. Results of this fit are discussed in the main text.

obtained during observation period P2014-06 is shown in the plot. The latter data set corresponds to the central part of the time range covering the Fermi flare. Together with the data points, also fits of the SEDs with simple power-law functions are shown. In case of the fits of the *Fermi*-LAT results, upper limits were not taken into account in the fit. The best-fit index of the SED fits is 1.0 ± 0.3 for both data sets. This translates to an index of the differential photon spectrum of 3.0 ± 0.3 . For better visibility, the drawn energy ranges of the fit functions were extended to roughly 100 GeV. Together with the H.E.S.S. SED the fit function describing the differential photon flux multiplied by E^2 is shown. Hence the spectral index of the differential flux is 2.5 ± 0.1 as previously shown in Fig. 6.20. It can be seen that at an energy of 1 TeV, both *Fermi*-LAT fit functions deviate from the VHE curve by approximately two orders of magnitude. This is even a

conservative estimate, since often a convex curvature is assumed for the fit function of the *Fermi*-LAT data, as shown in Fig. 5 in the publication by the H.E.S.S. Collaboration et al. [53]. To further quantify the compatibility of the data points in the two energy regimes, a combined fit with a power-law function was performed, again not taking into account upper limits. The resulting fit function is also shown in Fig. 6.21. The χ^2 value of the power-law fit is 20.7 for 17 degrees of freedom, resulting in a reduced χ^2 value of 1.2. While this value indicates that the fit function describes the data points well, it should be noted that all upper limits are strongly violated by this function. As the displayed upper limits exclude fluxes higher than the limit at the 95 % confidence level, also the combined fit function can be excluded at this confidence level. A spectral fit function with a convex curvature was not tested since no improved fit quality is expected as the H.E.S.S. spectrum is harder than the *Fermi*-LAT spectra.

From the incompatibility of the HE and VHE data points it can be concluded that either different particle populations or different locations, and hence different physical environments, are involved in the production of emission in the respective energy domains. For the HE radiation, the origin of the emission is considered to be the unshocked pulsar wind according to Khangulyan et al. [175; 56]. An estimate of the bulk Lorentz factors of the electrons in the pulsar wind is derived by Khangulyan et al. [56] from a comparison of the model predictions with the measured HE gamma-ray SED. This Lorentz factor is on the order of $\Gamma_e = 10^4$. The average energy $\langle E_\gamma \rangle$ of photons after an IC scattering process with electrons of such Lorentz factors can be calculated as

$$\langle E_\gamma \rangle = \frac{4}{3} \Gamma_e^2 \cdot E_\gamma^0, \quad (6.5)$$

where E_γ^0 is the photon energy before the scattering process. To produce photon energies of $E_\gamma \approx 1$ TeV, target photon energies of $E_\gamma^0 \approx 10$ keV are required, corresponding to X-ray energies. The thermal components of the radiation fields created by the star and the circumstellar disk are dominated by infrared, optical and UV wavelengths and not by X-rays. X-ray photons can instead be created by non-thermal processes, most importantly via synchrotron radiation of electrons in strong magnetic fields. However, it has been argued by Kong et al. [176] that the gamma-ray luminosity of such a synchrotron self-Compton process is expected to be too low by several orders of magnitude. The expected HE gamma-ray luminosity below 1 GeV caused by IC scattering of electrons with Lorentz factors of 10^4 on stellar radiation fields is three orders of magnitude higher than the VHE gamma-ray luminosity invoked by the synchrotron self-Compton process involving the same electrons. According to the results shown in Fig. 6.21, however, it can be seen that the HE and VHE gamma-ray luminosities are roughly on the same order of magnitude. Hence the unshocked pulsar wind is not the source of the VHE emission, while the shocked pulsar wind electrons are believed to be responsible for the VHE gamma-ray production.

6.4.2 VHE Gamma-Ray Luminosity

Before comparing the VHE gamma-ray light curve to light curves measured at other wavelengths, several fundamental properties of the binary system can be calculated

from the observed flux levels. Assuming an isotropic emission of VHE gamma rays, the total luminosity L_{VHE} of this emission can be calculated from the distance to PSR B1259–63/LS 2883 of $d = (2.3 \pm 0.4)$ kpc and the measured energy flux Φ_E at a certain point in time as

$$L_{\text{VHE}}(E > E_0) = 4\pi d^2 \cdot \Phi_E(E > E_0), \quad (6.6)$$

where E_0 is a threshold energy above which the fluxes are measured. The energy flux Φ_E can be calculated from photon fluxes Φ based on the parameters of the gamma-ray spectrum. The conversion between the two types of fluxes is done according to the equation

$$\Phi_E = S_F \cdot \Phi. \quad (6.7)$$

The scaling factor is calculated as an average energy according to the formula

$$S_F = \frac{\int_{E_{\min}}^{E_{\max}} E \cdot \frac{dN}{dE}(E) dE}{\int_{E_{\min}}^{E_{\max}} \frac{dN}{dE}(E) dE}. \quad (6.8)$$

Since for all observation campaigns the spectra dN/dE were fitted with simple power-law functions, the evaluation of the integrals is trivial, so that the scaling factor can be expressed as

$$S_F = \frac{-\Gamma + 1}{-\Gamma + 2} \cdot \frac{E_{\max}^{-\Gamma+2} - E_{\min}^{-\Gamma+2}}{E_{\max}^{-\Gamma+1} - E_{\min}^{-\Gamma+1}}. \quad (6.9)$$

Spectral indices Γ are assumed to be positive here. The minimum energy E_{\min} is given by the energy threshold above which fluxes are calculated, the maximum energy E_{\max} is set to infinity. Since the flux is variable, also the calculated total luminosity will cover a range of values. Far away from periastron, the measured fluxes are compatible with or even below zero, hence the minimum luminosity is 0 erg s^{-1} . For fluxes measured at energies above a fiducial value E_0 obtained from the monoscopic analysis of the 2014 data set, the maximum luminosity $L_{\text{VHE}}^{\max}(E > E_0)$ is given in Tab. 6.6. For reference, the calculated VHE gamma-ray luminosities are also expressed as fractions of the pulsar luminosity $\dot{E} = 8.3 \times 10^{35} \text{ erg s}^{-1}$ and the stellar luminosity $L_{\text{star}} = 2.4 \times 10^{38} \text{ erg s}^{-1}$. For average PWNe detected at VHEs, the VHE gamma-ray luminosity corresponds to roughly 1% of the respective pulsar's spin-down power, but also values up to 10% were observed [5]. The value found here is consistent with these numbers. Since the stellar luminosity dominates the luminosity of the binary system, the VHE gamma-ray luminosity is not given separately as a fraction of the total luminosity of the binary system. Uncertainties were derived from the statistical uncertainties of the distance, the flux and the spectral index using a Gaussian error propagation approach. Systematic uncertainties are not included in the numbers given in the table, but can easily be calculated from the systematic uncertainty on the flux measurement of 23% introduced earlier.

Previous publications of the average integrated VHE gamma-ray luminosity above 1 TeV assumed a distance from Earth to PSR B1259–63/LS 2883 of 1.5 kpc [51; 52].

E_0	$L_{\text{VHE}}^{\text{max}}(E > E_0) / [\text{erg s}^{-1}]$	$L_{\text{VHE}}^{\text{max}}(E > E_0)/\dot{E}$	$L_{\text{VHE}}^{\text{max}}(E > E_0)/L_{\text{star}}$
200 GeV	$(1.3 \pm 0.6) \times 10^{34}$	$(1.6 \pm 0.7) \%$	$(5.4 \pm 2.5) \times 10^{-3} \%$
1 TeV	$(4 \pm 2) \times 10^{33}$	$(0.5 \pm 0.2) \%$	$(1.7 \pm 0.9) \times 10^{-3} \%$

Table 6.6: Maximum VHE gamma-ray luminosities $L_{\text{VHE}}^{\text{max}}(E > E_0)$ for energies exceeding the threshold energy E_0 . Values were derived from the monoscopic analysis of the 2014 data set. The maximum energy up to which fluxes are taken into account is 30 TeV. The obtained luminosities are also given as fractions of the pulsar’s spin-down power \dot{E} and the stellar luminosity L_{star} . Only statistical uncertainties are given. A distance to the system of 2.3 kpc was assumed.

Scaling the published results to the current distance estimate, the resulting luminosities are $(1.9 \pm 0.5) \times 10^{33} \text{ erg s}^{-1}$ and $(1.4 \pm 0.5) \times 10^{33} \text{ erg s}^{-1}$ for the 2004 and 2007 data sets, respectively. For the 2010 data set [53], no luminosity estimate was published, but it can be calculated from the spectral index and the measured photon flux according to the above prescription. From the published values, a luminosity of $(2.2 \pm 0.9) \times 10^{34} \text{ erg s}^{-1}$ is calculated. All these luminosity estimates are calculated from the respective average fluxes, thus the fact that the corresponding luminosities are lower than the maximum luminosities calculated for the 2014 data set is expected. In the latter case the maximum flux was chosen since the definition of an average flux is considered arbitrary given an uneven sampling of the light curve of a variable source, while the maximum VHE gamma-ray luminosity can be a parameter constraining theoretical models. The best agreement between the maximum luminosity from 2014 and an average luminosity from another year is found for the 2010 data set, which is expected since at that time the high-flux period between the second disk crossing and the Fermi flare was sampled. These two luminosities are compatible with each other within uncertainties.

6.4.3 Multi-Wavelength Light Curve

The VHE gamma-ray light curve presented above can also be compared to the fluxes measured at other wavelengths. In Fig. 6.22, results from 2014 observations at HEs and at X-ray energies are shown together with the equivalent width of the H_α line as a function of the time. In panel a of this figure, the HE gamma-ray light curve with a weekly binning as measured with *Fermi*-LAT around the previous two periastron passages is plotted. As discussed previously, the prominent flare after the second disk crossing is observed during both years. During the parts of the orbit before the flare, drawing conclusions is difficult as only flux upper limits could be placed except for one bin in 2010. Especially the time before the first disk crossing at which a high flux was measured at VHEs close to the 2014 periastron passage is of interest, since a detection of an increased flux at other wavelengths would help to identify the reason of the observed flux increase. In the HE gamma-ray light curve shown in the figure, it can be observed

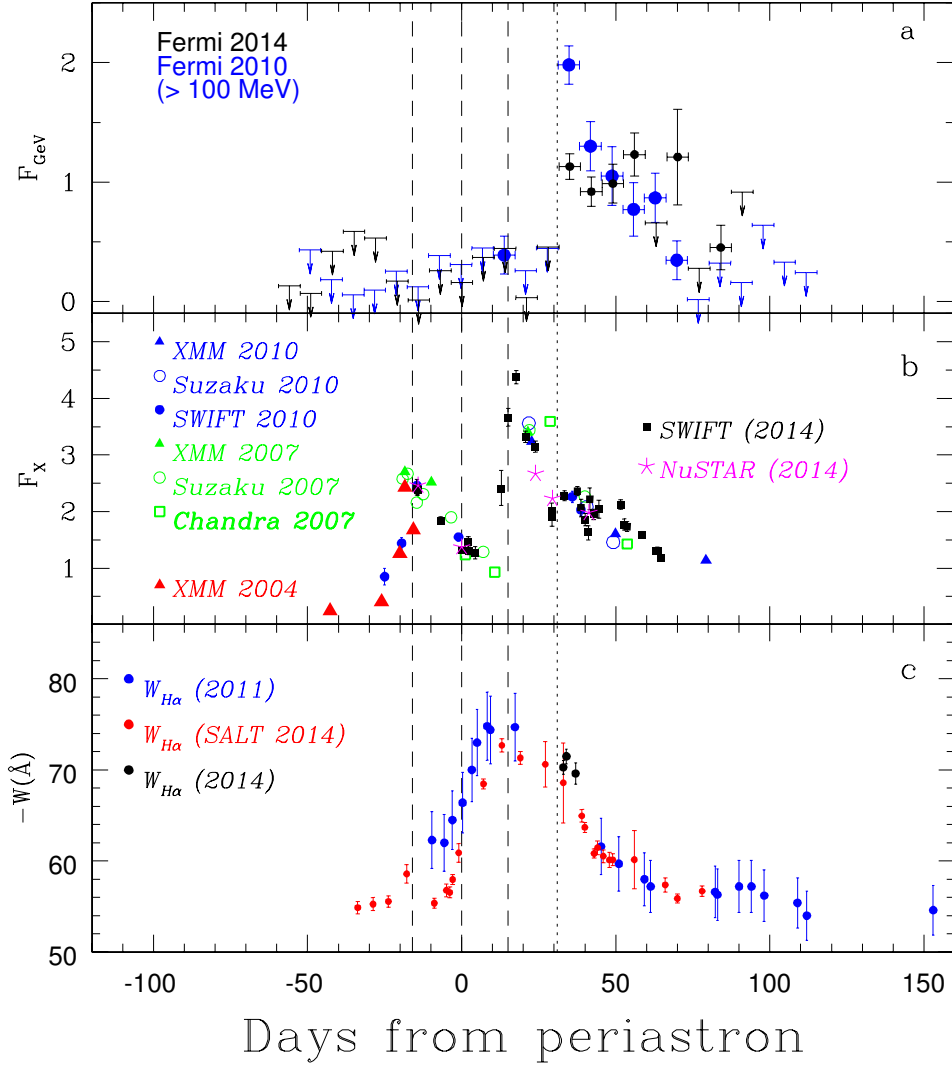


Figure 6.22: *Panel a*: HE gamma-ray light curves measured by *Fermi*-LAT around the 2010 and 2014 periastra. The unit of the displayed flux above 100 MeV is $10^{-6} \text{ cm}^{-2} \text{ s}^{-1}$. *Panel b*: X-ray light curves obtained from all years between 2004 and 2014 from measurements with the experiments listed in the legends. The flux unit is $10^{-11} \text{ erg cm}^{-2} \text{ s}^{-1}$. *Panel c*: Equivalent width of the $\text{H}\alpha$ line for the 2010 and 2014 periastra with either the SALT or the SAA0 telescopes. Taken from Chernyakova et al. [79].

that, in case of the 2014 data set, the flux upper limits are higher at the corresponding part of the orbit than before or after this period of time by a factor of approximately two to three. Given that the exposure is equal for all time bins before the time of the flare [93], this indeed indicates a higher number of HE gamma rays detected per time, but more statistics are needed to allow drawing firm conclusions. Furthermore the fact that in 2010 no such increased upper limits are found hints towards the conclusion that the higher

2014 upper limits are caused by statistical fluctuations if flux periodicity is assumed. In addition, in the biweekly-binned light curve shown in Fig. 2.7, there are several significant flux points around periastron and around the disk crossings, but only upper limits at the time of the high VHE gamma-ray flux state before the first disk crossing. These upper limits are at flux levels similar to or lower than the significant fluxes measured afterwards, further strengthening the argument that there was no increased HE gamma-ray flux at that part of the orbit in 2010. A higher sensitivity at HEs would be needed to investigate the question whether a light curve with a short-term structure similar to the one observed at VHEs is found. For future periastron passages, also an increase of the exposure accomplished by altering the pointing strategy of the *Fermi* satellite could lead to an increased number of significant flux points.

At X-ray energies, the part of the light curve before the first disk crossing is sampled sparsely, as shown in panel b of Fig. 6.22. Between 50 d and 30 d before periastron, only one flux point from 2004 is available, limiting the comparability of the VHE gamma-ray and X-ray light curves. This flux point does not correspond to a part of the orbit at which the high flux at VHEs is measured, thus no further conclusions about the presence or absence of a high X-ray flux can be drawn. During later parts of the orbit, the well-known double-peak structure is seen, as well as the absence of a flux increase at the time of the HE gamma-ray flare.

In panel c of Fig. 6.22, the equivalent width of the H_α line is shown. As already discussed in Sec. 2.8.4, this quantity can be interpreted as a measure of the growth or decay of the circumstellar disk. At the time of the high VHE gamma-ray flux before the disk crossing, there are no indications of a change of the equivalent width, which is expected since the distance of the pulsar from the star is still too large at this part of the orbit to have an effect on the disk structure.

6.4.4 Comparison of Energy Fluxes with Model Predictions

The VHE gamma-ray light curve for fluxes above 1 TeV can also be compared to model predictions. Here the measured light curve is compared to predictions from models by Khangulyan et al. [175], which is a successor of the model by Khangulyan et al. [100], and Zabalza et al. [177]. In both models, the VHE gamma-ray emission is assumed to be produced by electrons through IC scattering. The electrons themselves are thought to be produced by the pulsar, which emits such electrons as part of the pulsar wind. At the termination shock, the structure of which differs between the two models, the pulsar wind electrons can be accelerated to the required TeV energies. Several assumptions about the binary system's parameters are made. The pulsar wind is assumed to be isotropic, and the parameters of the massive star and of the orbit are assumed to be similar to those given in Sec. 2.8 if not specified differently here. The models were implemented by D. Khangulyan, who generously provided the author of this dissertation with the software package capable of calculating SEDs and light curves from theoretical assumptions. In this framework it is assumed that the generation of the non-thermal spectra happens in a quasi-steady regime in which the physical conditions encountered by the particles participating in the shock acceleration change on time scales that are

much longer than the time scales needed for the particles to be accelerated or to be cooled. In the following paragraphs, only the predicted VHE gamma-ray light curves will be compared to measurements. A comparison of predicted multi-wavelength SEDs with data is left for a future publication.

In the model by Zabalza et al. [177], two different locations of particle acceleration are proposed. As already discussed in Sec. 2.8.8, one shock front is formed at the contact discontinuity of the stellar and the pulsar winds, where the ram pressures of the winds emitted by the pulsar and by the star LS 2883 balance. In the model discussed here, this shock front is proposed to accelerate shocked pulsar wind electrons to GeV energies. A second shock front is thought to be formed in the opposite direction of the massive star as seen from the compact object. This shock formation is a result of the orbital motion of the pulsar around the star, which leads to a wind collision zone due to the fact that the relativistic pulsar wind catches up with the much slower stellar wind. This shock front is hypothesised to be able to accelerate electrons to TeV energies. In addition to the system's parameters given in Sec. 2.8, several other parameters were specified. The surface temperature of LS 2883 is assumed to be 30 000 K, and the stellar radius is assumed to be $8.6 R_{\odot}$. Both values are contained in the ranges of values given in the aforementioned section. Particle acceleration at the shock fronts is not simulated directly, but instead a power-law spectrum of the resulting electron population with an index of 1.8 was assumed. The energy flux Φ_E above 1 TeV as a function of time predicted for the given set of parameters is shown in Fig. 6.23, together with the data points converted from those shown in Fig. 6.19d. For each observation campaign the spectral index Γ listed in Tab. 6.5 is used. Due to the choice of the very hard electron spectrum the predicted maximum flux is on the correct order of magnitude. Nevertheless, the general shape of the predicted light curve is incompatible with observations. Especially the fact that the flux is maximal very close to periastron does not agree with the fact that a local flux minimum is observed at this part of the orbit. Variants of this model can predict the light curve of other binary systems like LS 5039 or LS I +61°303 in a satisfactory manner, but, as suspected by the authors of the model, the effect of the very different orbital parameters and especially the presence of a dense circumstellar disk around the host star render the model non-applicable to the case of PSR B1259–63/LS 2883.

The model by Khangulyan et al. [175] was studied as well. In this model, the existence of only one shock front is assumed, which is located at the wind collision zone between the two binary components. Furthermore, particle escape from the wind collision zone is also taken into account by simulating the effect of this on the system as adiabatic energy losses. A very important parameter is the index of the electron spectrum. As discussed in Sec. 2.8.8, the index of the electron spectrum Γ_e can be calculated from the observed gamma-ray spectral index Γ as $\Gamma_e = \Gamma - \frac{1}{2}$ under the assumption that the IC scattering takes place in the Klein-Nishina regime. From the fit of the monoscopic spectrum discussed in Sec. 6.2, an index of $\Gamma = 2.73 \pm 0.05$ was derived. This translates to an electron index of $\Gamma_e = 2.23 \pm 0.05$. It is noted that the index of 1.8 specified above for the model by Zabalza et al. [177] is not compatible with the anticipated value of 2.23, but this harder index was necessary to yield orders of magnitude of the predicted fluxes. Inserting the latter value into the model by Khangulyan et al. [175] yields fluxes

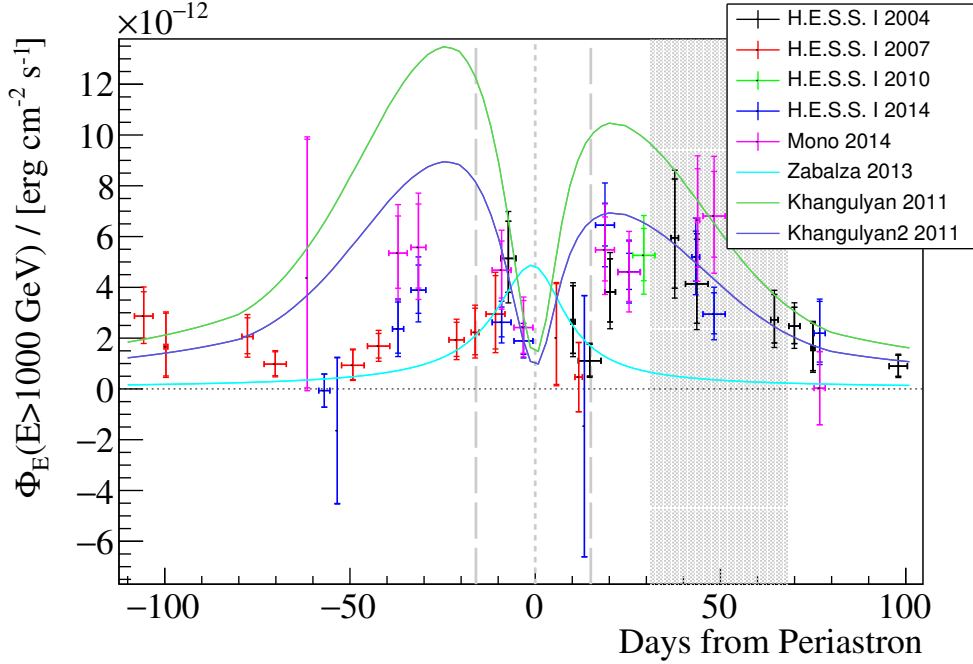


Figure 6.23: Energy fluxes above 1 TeV obtained from analyses of data taken around all periastron passages observed with the H.E.S.S. telescopes. Flux points are converted to energy fluxes from those shown in Fig. 6.19d. In addition, energy flux predictions obtained from the models by Zabalza et al. [177] and Khangulyan et al. [175] are displayed. The models labelled Khangulyan and Khangulyan2 differ only by the choice of the spectral index of the VHE electrons, as explained in the text. These indices are 2.23 and 2.3, respectively.

that are too high at several parts of the orbit, for example at the time of the second disk crossing. Altering the index to $\Gamma_e = 2.3$, however, results in a predicted light curve which matches the observed light curve better. Both simulated light curves are shown in Fig. 6.23. Several key features of the light curve, like the double-peak structure with maxima around the times of the disk crossings and a local minimum around the time of periastron, agree well with observations. Especially the second peak of the predicted light curve agrees very well with the data points, while the first peak is too high by factors of a few for large parts of the parts of the orbit before the first disk crossing. It should be noted, though, that the high flux values measured in 2014 before the first disk crossing are indeed predicted by this model. In contrast, the low fluxes measured in 2007 approximately 25 d–13 d before periastron are not predicted. Given the fact that this flux decrease happens so shortly before the nominal disk crossing suggests that a more complex interaction of the pulsar with the disk might cause this TeV flux decrease.

The general structure of the predicted light curve is a result of simulations taking into account the stellar and neutron star parameters mentioned above as well as geometrical aspects influencing the observed intensity of the VHE gamma rays produced by IC

scattering. Two different electron populations can participate in IC scattering processes. In the first case, the electrons in the unshocked pulsar wind can scatter off photons of the stellar and disk radiation fields, in the second case shock-accelerated electrons interact with the same photon fields. The increasing VHE gamma-ray flux levels are caused by the increase of the particle and photon densities as the pulsar approaches the star around the time of periastron. However, a local flux minimum is observed close to periastron, which is assumed to be caused, among other processes, by the effect of very intense photon fields interacting with the unshocked pulsar wind. Simulations suggest that due to such IC scattering processes the energy emitted in the direction of the star inside a cone with an opening angle of approximately 60° is reduced by up to 25%. This flux reduction is taken into account in terms of adiabatic energy losses in the simulation. In addition, also the effect of pair production by VHE gamma rays scattering off thermal photons reduces the observed luminosity. Depending on the location of the creation of VHE gamma rays and also depending on their energy, the gamma-ray flux can be attenuated by up to 60% [175]. On average, the attenuation is on the order of 10% only, though. Furthermore, the attenuation depends on the energy of the gamma-ray photons. It is maximal at roughly 500 GeV, while absorption effects are negligible at energies above several TeV. Hence the observed gamma-ray spectrum is harder than it is right after the shock acceleration process. This attenuation is considered in the model by Khangulyan et al. [175]. To fully take the effect of this attenuation into account when comparing simulated energy fluxes with measurements, also the inferred spectral index of the electrons needs to be corrected. Since the attenuation is largest at the low-energy end of the reconstructed VHE gamma-ray spectrum, the effect of the absorption was assumed to affect the low-energy data points of the differential photon spectrum only, while the highest-energy data points were not altered. Scaling the lowest-energy differential flux values by 10% in a positive direction yields a spectral index of 2.79. Hence the inferred index of electron spectrum is 2.29, which is in very good agreement with the value assumed above. Nevertheless, also the combined effect of the attenuations of the energy of the unshocked pulsar wind electrons and of the VHE gamma-ray flux are still too weak by a factor of approximately two to fully explain the observed flux decrease towards periastron.

It is remarked that no model is currently able to predict the various features of the light curves or spectral shapes of any gamma-ray binary system accurately. In most cases a model is considered successful if the observed trends can be reproduced and the right order of magnitude of observed fluxes is predicted. This is the case because binary systems are very complex, with many different processes playing a role, like the flow dynamics of the interacting winds, temperatures of the involved components, different particle populations, inhomogeneities or anisotropies of the winds and scattering processes, among others. Thus the observed discrepancy of the predicted fluxes and the measured fluxes before the first disk crossing is not considered to be a strong argument against the presented model by Khangulyan et al. [175]. Also the fact that the first peak flux is higher than the second peak flux, which is an effect of the orbital inclination of 23° and which is not observed, does not rule out the model, as this is a 30% effect only. The model by Zabalza et al. [177] is, however, considered incompatible with observations

due to the very different qualitative shape of the predicted VHE gamma-ray light curve.

6.4.5 Future Improvements

Future observations with the CTA observatory will certainly enable progress in the understanding of gamma-ray binaries. The sensitivity of this observatory is expected to be approximately one order of magnitude better than that of current-generation IACT experiments, so that detections of several new gamma-ray binaries are anticipated. This could enable population studies that lead to the identification of general properties of gamma-ray binaries, which would be crucial for the creation of better models of such systems. Furthermore, due to the better sensitivity a more accurate measurement of fluxes will be possible since the statistical uncertainties will be reduced significantly. In addition it would be important to sample the orbit of gamma-ray sources with complex light curves, such as PSR B1259–63/LS 2883, more evenly around each periastron passage, which could be enabled by allowing for observations during moonlit parts of the night. While this is an experimentally difficult task to accomplish, it was shown by e.g. the VERITAS collaboration that such measurements can be made [178]. Such an operation mode would help to close the gaps in the TeV light curve quickly, and the comparability of fluxes around individual periastra as well as the compatibility of fluxes measured around different periastra would be enhanced. To ease the comparison of results obtained from different years and different telescope configurations, being able to analyse all data sets within the HAP analysis framework with the same reconstruction chain would be desirable. Such an algorithm would decide on an event-by-event basis whether to perform a monoscopic or a stereoscopic reconstruction. With such an algorithm for example the differential photon spectrum could both extend down to lowest energies similar to the spectrum obtained from the MonoReco algorithm and at the same time make use of the concept of stereoscopy whenever possible. Such algorithms are being worked on, so that improved results are imminent soon.

Also the energy threshold of both the monoscopic and stereoscopic reconstruction algorithms could be lowered safely. As explained earlier, this threshold is defined using an average effective area curve. In case of the monoscopic analysis presented here, energy thresholds of 148 GeV are obtained for a significant fraction of the number of runs. It is possible to define the overall threshold as the lowest threshold of all runs, but such a threshold definition is currently not available in the HAP framework. Lowering the threshold this way is also possible for stereoscopic analyses.

7 Conclusion

During the course of the work presented here, a new algorithm capable of reconstructing all key parameters of VHE gamma rays from data recorded with CT 5, the largest Cherenkov telescope on Earth, was developed. These parameters comprise the direction and the energy of the initial gamma rays as well as the type of particle initiating the imaged air shower, which is important since the far more numerous background events formed by VHE hadrons need to be effectively distinguished from gamma-ray events. Artificial neural networks are used for the reconstruction of all three types of parameters. The most important feature of this reconstruction algorithm called MonoReco is the low energy threshold compared to values obtained from analyses of data recorded with the four H.E.S.S.-I telescopes, which typically are a factor of roughly two higher. All relevant performance curves were discussed, exhibiting a stable analysis results down to tens of GeV in case of small zenith angles. All performance measures were studied as a function of the energy, the zenith angle and the azimuth angle. The influences of the source offset angle and of the optical efficiency of the detectors were not presented here. Also the definition of different cut sets, optimised for different physics cases, was not discussed. It was shown that steady sources of VHE gamma rays with fluxes as low as 2% of the flux of the Crab Nebula can be detected within 50 h of observation time with a statistical significance of 5σ .

Applying the reconstruction algorithm to data recorded during observations of the Crab Nebula yields an energy threshold of 177 GeV, which is an unprecedentedly low value for observations of this source with the H.E.S.S. array. Former energy thresholds were as high as 440 GeV, indicating the great scientific prospects of having added such a large telescope to the H.E.S.S.-I array. The resulting spectra obtained from the new, monoscopic reconstruction algorithm and from H.E.S.S. I-style analyses are compatible with each other within systematic uncertainties. Also the resulting sky maps are found to be free of significant features, indicating that there are no systematics arising from poorly understood background event distributions.

Due to the stable and especially fast operation of the reconstruction algorithm it is now used in various situations. Apart from the fact that it is used by researchers to obtain high-level analysis results it is also used on-site in Namibia in the so-called real-time analysis and also in the WebSummary. The former analysis presents analysis results to the shift personnel in real time while the observations are ongoing. This enables a flexible reaction in case of, for example, flaring events. The WebSummary is available the next day also for researchers at their home institutes and makes use of a more accurate, but less fast calibration procedure, rendering the displayed results more accurate compared to the real-time analysis. In addition, the MonoReco algorithm is used to provide estimates of the gamma-ray parameters for the monoscopic version of

7 Conclusion

the more advanced ImPACT reconstruction algorithm, which provides more accurate energy and direction estimates, but relies on the particle identification performed by the MonoReco algorithm.

Despite the fact that the performance of the MonoReco algorithm is stable and competitive over a large energy range, and allows for measurements at energies previously not reachable by IACTs, there is still room for improvement. Especially at the lowest energies the performance of the particle discrimination algorithm could be improved, possibly by finding new variables that provide a better discrimination power. Also the general approach of using simple artificial neural networks for all parts of the reconstruction implicates limitations, since during the training process it is assumed that the input shower images are homogeneous. While this approach provides good results over a large parts of the energy range, the performance at the lowest energies cannot be tuned individually. Furthermore, the assumption of homogeneity is not valid in case shower images are cropped at the camera edges, which is a problem occurring frequently at the highest energies. To cover such cases, approaches as used in the aforementioned ImPACT algorithm could be used, albeit at the cost of a lower data analysis speed. Hence the algorithm presented here is a trade-off between very fast analysis speed and optimal results.

Data taken around the 2014 periastron passage of the gamma-ray binary system PSR B1259–63/LS 2883 were analysed with the MonoReco algorithm as well as with stereoscopic reconstruction algorithms. It was confirmed that the source is compatible with a point-like VHE gamma-ray source also when considering the energy range extended down to the lowest energies currently reachable. The influence of non-optimal data taking conditions, most notably missing drawers and a gain gradient in the camera, was studied. It was shown that both these conditions lead to a lack of reconstructed gamma rays in one part of the sky and to an enhanced excess of reconstructed gamma rays in other parts of the sky. Furthermore, the influence of the night sky background on the distribution of reconstructed events was discussed. It could be shown that the presence of a star with an apparent magnitude of 5.4 does not influence this distribution significantly.

From analyses of data taken around previous periastra it was known that the differential photon spectrum of PSR B1259–63/LS 2883 is well-fit by a power-law function. With the new data set it could be shown that the power-law hypothesis is also applicable when extending the energy range down to 178 GeV. The best-fit spectral index is 2.73 ± 0.05 . There is no significant variation of the spectral index over the course of the time range covered by observations, and the index is also not correlated with the flux normalisation.

PSR B1259–63/LS 2883 exhibits flux variability at all wavelengths. It was shown that also at VHEs the flux is not compatible with a constant at the 99.7% confidence level. While a double-peak structure of the light curve, with maxima measured shortly after the two disk crossings, was expected and confirmed with the most recent measurements, an additional flux increase before the first disk crossing by a factor of 2.7 ± 0.8 was observed at a part of the orbit not sampled before. Also the time of periastron was covered for the first time, and it was shown that the flux reaches a local minimum at this particular

part of the orbit. Furthermore, contemporaneous observations were performed with the H.E.S.S. telescopes and the *Fermi*-LAT satellite experiment over an extended period of time. It was shown that there is no significant flux increase at VHEs compared to the flux levels observed during the time of the second disk crossing, but instead the flux level is similar to the latter.

The VHE gamma-ray energy flux as a function of time was compared to predictions resulting from two different models. While the model by Zabalza et al. [177] is not compatible with the observed energy fluxes, the model by Khangulyan et al. [175] agrees well with observations. In this model, the VHE gamma-ray emission is thought to originate from electrons and positrons that were accelerated at the shock front between the pulsar and stellar winds, and the flux modulation is a result of the geometry of the binary system. In addition, the maximum fraction of the spin-down luminosity of the pulsar transferred into gamma rays with energies above 200 GeV was inferred. It was found that this fraction is $(1.6 \pm 0.7) \%$, which is compatible with the range of efficiencies observed in PWNe.

Despite the fact that PSR B1259–63/LS 2883 has been observed by the H.E.S.S. telescope array for four periastron passages in a row, there are still parts of the orbit not sampled yet. Future observation campaigns conducted with either the H.E.S.S. array or the CTA observatory should aim to close these gaps. Also already covered parts of the orbit should be re-observed to be able to study inter-orbital flux variability. Especially the better sensitivity the CTA observatory is foreseen to provide compared to current-generation IACT experiments could furthermore help to reduce statistical uncertainties of observables of gamma-ray binaries like the emitted VHE gamma-ray flux. It is expected that several new gamma-ray binaries will be discovered by CTA, which could allow for conducting population studies not possible today due to the limited number of identified sources. Given the unique environments found in gamma-ray binary systems, new discoveries and precision measurements are certain to provide fascinating physics results and a deeper understanding of fundamental processes occurring close to extreme objects like neutron stars and stellar-mass black holes.

Bibliography

- [1] V. F. Hess. Über Beobachtungen der durchdringenden Strahlung bei sieben Freiballonfahrten. *Physikalische Zeitschrift*, 13:1084–1091, November 1912.
- [2] H.E.S.S. Collaboration. H.E.S.S. High Energy Stereoscopic System. <http://www.mpi-hd.mpg.de/hfm/HESS/>, 2016.
- [3] S. Wakely and D. Horan. TeVCat, an Online Gamma-Ray Catalog. <http://tevcat.uchicago.edu/>, 2016.
- [4] T. C. Weekes, M. F. Cawley, D. J. Fegan, K. G. Gibbs, A. M. Hillas, P. W. Kowk, R. C. Lamb, D. A. Lewis, D. Macomb, N. A. Porter, P. T. Reynolds, and G. Vacanti. Observation of TeV gamma rays from the Crab nebula using the atmospheric Cerenkov imaging technique. *The Astrophysical Journal*, 342:379–395, July 1989. doi: 10.1086/167599.
- [5] S. Funk. The status of gamma-ray astronomy. *ArXiv e-prints*, April 2012.
- [6] J. A. Hinton and W. Hofmann. Teraelectronvolt Astronomy. *Annual Review of Astronomy & Astrophysics*, 47:523–565, September 2009. doi: 10.1146/annurev-astro-082708-101816.
- [7] HESS Collaboration, A. Abramowski, F. Aharonian, F. A. Benkhali, A. G. Akhperjanian, E. O. Angüner, M. Backes, A. Balzer, Y. Becherini, J. B. Tjüs, and et al. Acceleration of petaelectronvolt protons in the Galactic Centre. *Nature*, 531:476–479, March 2016. doi: 10.1038/nature17147.
- [8] R. Blandford, P. Simeon, and Y. Yuan. Cosmic Ray Origins: An Introduction. *Nuclear Physics B Proceedings Supplements*, 256:9–22, November 2014. doi: 10.1016/j.nuclphysbps.2014.10.002.
- [9] F. A. Aharonian, A. G. Akhperjanian, K.-M. Aye, A. R. Bazer-Bachi, M. Beilicke, W. Benbow, D. Berge, P. Berghaus, K. Bernlöhr, O. Bolz, C. Boisson, C. Borgmeier, F. Breitling, A. M. Brown, J. Bussons Gordo, P. M. Chadwick, V. R. Chitnis, L.-M. Chounet, R. Cornils, L. Costamante, B. Degrange, A. Djannati-Ataï, L. O. Drury, T. Ergin, P. Espigat, F. Feinstein, P. Fleury, G. Fontaine, S. Funk, Y. A. Gallant, B. Giebels, S. Gillessen, P. Goret, J. Guy, C. Hadjichristidis, M. Hauser, G. Heinzlmann, G. Henri, G. Hermann, J. A. Hinton, W. Hofmann, M. Holleran, D. Horns, O. C. de Jager, I. Jung, B. Khélifi, N. Komin, A. Konopelko, I. J. Latham, R. Le Gallou, M. Lemoine, A. Lemièrre, N. Leroy, T. Lohse, A. Marcowith, C. Masterson, T. J. L. McComb, M. de Naurois, S. J.

Bibliography

- Nolan, A. Noutsos, K. J. Orford, J. L. Osborne, M. Ouchrif, M. Panter, G. Pelletier, S. Pita, M. Pohl, G. Pühlhofer, M. Punch, B. C. Raubenheimer, M. Raue, J. Raux, S. M. Rayner, I. Redondo, A. Reimer, O. Reimer, J. Ripken, M. Rivoal, L. Rob, L. Rolland, G. Rowell, V. Sahakian, L. Saugé, S. Schlenker, R. Schlickeiser, C. Schuster, U. Schwanke, M. Siewert, H. Sol, R. Steenkamp, C. Stegmann, J.-P. Tavernet, C. G. Théoret, M. Tluczykont, D. J. van der Walt, G. Vasileiadis, P. Vincent, B. Visser, H. J. Völk, and S. J. Wagner. High-energy particle acceleration in the shell of a supernova remnant. *Nature*, 432:75–77, November 2004. doi: 10.1038/nature02960.
- [10] E. Amato. Particle Acceleration in Astrophysical Sources. *ArXiv e-prints*, March 2015.
- [11] K. Egberts, F. Brun, S. Casanova, W. Hofmann, M. de Naurois, O. Reimer, Q. Weitzel, for the H. E. S. S. Collaboration, and Y. Fukui. Diffuse TeV Gamma-Ray Emission in the H.E.S.S. Galactic Plane Survey. *ArXiv e-prints*, August 2013.
- [12] J. Holder. Ground-Based Gamma Ray Astronomy. *Brazilian Journal of Physics*, 44:450–464, October 2014. doi: 10.1007/s13538-014-0245-3.
- [13] F. Acero, M. Ackermann, M. Ajello, A. Albert, W. B. Atwood, M. Axelsson, L. Baldini, J. Ballet, G. Barbiellini, D. Bastieri, A. Belfiore, R. Bellazzini, E. Bissaldi, R. D. Blandford, E. D. Bloom, J. R. Bogart, R. Bonino, E. Bottacini, J. Bregeon, R. J. Britto, P. Bruel, R. Buehler, T. H. Burnett, S. Buson, G. A. Caliandro, R. A. Cameron, R. Caputo, M. Caragiulo, P. A. Caraveo, J. M. Casandjian, E. Cavazzuti, E. Charles, R. C. G. Chaves, A. Chekhtman, C. C. Cheung, J. Chiang, G. Chiaro, S. Ciprini, R. Claus, J. Cohen-Tanugi, L. R. Cominsky, J. Conrad, S. Cutini, F. D’Ammando, A. de Angelis, M. DeKlotz, F. de Palma, R. Desiante, S. W. Digel, L. Di Venere, P. S. Drell, R. Dubois, D. Dumora, C. Favuzzi, S. J. Fegan, E. C. Ferrara, J. Finke, A. Franckowiak, Y. Fukazawa, S. Funk, P. Fusco, F. Gargano, D. Gasparrini, B. Giebels, N. Giglietto, P. Giommi, F. Giordano, M. Giroletti, T. Glanzman, G. Godfrey, I. A. Grenier, M.-H. Grondin, J. E. Grove, L. Guillemot, S. Guiriec, D. Hadasch, A. K. Harding, E. Hays, J. W. Hewitt, A. B. Hill, D. Horan, G. Iafate, T. Jogler, G. Jóhannesson, R. P. Johnson, A. S. Johnson, T. J. Johnson, W. N. Johnson, T. Kamae, J. Kataoka, J. Katsuta, M. Kuss, G. La Mura, D. Landriu, S. Larsson, L. Latronico, M. Lemoine-Goumard, J. Li, L. Li, F. Longo, F. Loparco, B. Lott, M. N. Lovellette, P. Lubrano, G. M. Madejski, F. Massaro, M. Mayer, M. N. Mazziotta, J. E. McEnery, P. F. Michelson, N. Mirabal, T. Mizuno, A. A. Moiseev, M. Mongelli, M. E. Monzani, A. Morselli, I. V. Moskalenko, S. Murgia, E. Nuss, M. Ohno, T. Ohsugi, N. Omodei, M. Orienti, E. Orlando, J. F. Ormes, D. Paneque, J. H. Panetta, J. S. Perkins, M. Pesce-Rollins, F. Piron, G. Pivato, T. A. Porter, J. L. Racusin, R. Rando, M. Razzano, S. Razzaque, A. Reimer, O. Reimer, T. Reposeur, L. S. Rochester, R. W. Romani, D. Salvetti, M. Sánchez-Conde, P. M. Saz Parkinson, A. Schulz, E. J. Siskind, D. A. Smith, F. Spada, G. Spandre, P. Spinelli, T. E. Stephens, A. W.

- Strong, D. J. Suson, H. Takahashi, T. Takahashi, Y. Tanaka, J. G. Thayer, J. B. Thayer, D. J. Thompson, L. Tibaldo, O. Tibolla, D. F. Torres, E. Torresi, G. Tosti, E. Troja, B. Van Klaveren, G. Vianello, B. L. Winer, K. S. Wood, M. Wood, S. Zimmer, and Fermi-LAT Collaboration. Fermi Large Area Telescope Third Source Catalog. *The Astrophysical Journal, Supplement*, 218:23, June 2015. doi: 10.1088/0067-0049/218/2/23.
- [14] S. Funk. Space- and Ground-Based Gamma-Ray Astrophysics. *ArXiv e-prints*, August 2015.
- [15] M. Ackermann, M. Ajello, K. Asano, W. B. Atwood, M. Axelsson, L. Baldini, J. Ballet, G. Barbiellini, M. G. Baring, D. Bastieri, K. Bechtol, R. Bellazzini, E. Bissaldi, E. Bonamente, J. Bregeon, M. Brigida, P. Bruel, R. Buehler, J. M. Burgess, S. Buson, G. A. Caliandro, R. A. Cameron, P. A. Caraveo, C. Cecchi, V. Chaplin, E. Charles, A. Chekhtman, C. C. Cheung, J. Chiang, G. Chiaro, S. Ciprini, R. Claus, W. Cleveland, J. Cohen-Tanugi, A. Collazzi, L. R. Cominsky, V. Connaughton, J. Conrad, S. Cutini, F. D’Ammando, A. de Angelis, M. DeKlotz, F. de Palma, C. D. Dermer, R. Desiante, A. Diekmann, L. Di Venere, P. S. Drell, A. Drlica-Wagner, C. Favuzzi, S. J. Fegan, E. C. Ferrara, J. Finke, G. Fitzpatrick, W. B. Focke, A. Franckowiak, Y. Fukazawa, S. Funk, P. Fusco, F. Gargano, N. Gehrels, S. Germani, M. Gibby, N. Giglietto, M. Giles, F. Giordano, M. Giroletti, G. Godfrey, J. Granot, I. A. Grenier, J. E. Grove, D. Gruber, S. Guiriec, D. Hadasch, Y. Hanabata, A. K. Harding, M. Hayashida, E. Hays, D. Horan, R. E. Hughes, Y. Inoue, T. Jogler, G. Jóhannesson, W. N. Johnson, T. Kawano, J. Knödseder, D. Kocevski, M. Kuss, J. Lande, S. Larsson, L. Latronico, F. Longo, F. Loparco, M. N. Lovellette, P. Lubrano, M. Mayer, M. N. Mazziotta, J. E. McEnery, P. F. Michelson, T. Mizuno, A. A. Moiseev, M. E. Monzani, E. Moretti, A. Morselli, I. V. Moskalenko, S. Murgia, R. Nemmen, E. Nuss, M. Ohno, T. Ohsugi, A. Okumura, N. Omodei, M. Orienti, D. Paneque, V. Pelassa, J. S. Perkins, M. Pesce-Rollins, V. Petrosian, F. Piron, G. Pivato, T. A. Porter, J. L. Racusin, S. Rainò, R. Rando, M. Razzano, S. Razzaque, A. Reimer, O. Reimer, S. Ritz, M. Roth, F. Ryde, A. Sartori, P. M. S. Parkinson, J. D. Scargle, A. Schulz, C. Sgrò, E. J. Siskind, E. Sonbas, G. Spandre, P. Spinelli, H. Tajima, H. Takahashi, J. G. Thayer, J. B. Thayer, D. J. Thompson, L. Tibaldo, M. Tinivella, D. F. Torres, G. Tosti, E. Troja, T. L. Usher, J. Vandenbroucke, V. Vasileiou, G. Vianello, V. Vitale, B. L. Winer, K. S. Wood, R. Yamazaki, G. Younes, H.-F. Yu, S. J. Zhu, P. N. Bhat, M. S. Briggs, D. Byrne, S. Foley, A. Goldstein, P. Jenke, R. M. Kippen, C. Kouveliotou, S. McBreen, C. Meegan, W. S. Paciesas, R. Preece, A. Rau, D. Tierney, A. J. van der Horst, A. von Kienlin, C. Wilson-Hodge, S. Xiong, G. Cusumano, V. La Parola, and J. R. Cummings. Fermi-LAT Observations of the Gamma-Ray Burst GRB 130427A. *Science*, 343: 42–47, January 2014. doi: 10.1126/science.1242353.
- [16] H.E.S.S. Collaboration, A. Abramowski, F. Aharonian, F. Ait Benkhali, A. G. Akhperjanian, E. Angüner, G. Anton, S. Balenderan, A. Balzer, A. Barnacka, and

Bibliography

- et al. Search for TeV Gamma-ray Emission from GRB 100621A, an extremely bright GRB in X-rays, with H.E.S.S. *Astronomy & Astrophysics*, 565:A16, May 2014. doi: 10.1051/0004-6361/201322984.
- [17] D. D’Urso. Cosmic Ray Physics. *ArXiv e-prints*, November 2014.
- [18] G. Maier and J. Knapp. Cosmic-ray events as background in imaging atmospheric Cherenkov telescopes. *Astroparticle Physics*, 28:72–81, September 2007. doi: 10.1016/j.astropartphys.2007.04.009.
- [19] J. Aleksić, E. A. Alvarez, L. A. Antonelli, P. Antoranz, M. Asensio, M. Backes, J. A. Barrio, D. Bastieri, J. Becerra González, W. Bednarek, A. Berdyugin, K. Berger, E. Bernardini, A. Biland, O. Blanch, R. K. Bock, A. Boller, G. Bonnoli, D. Borla Tridon, I. Braun, T. Bretz, A. Cañellas, E. Carmona, A. Carosi, P. Colin, E. Colombo, J. L. Contreras, J. Cortina, L. Cossio, S. Covino, F. Dazzi, A. de Angelis, G. de Caneva, E. de Cea Del Pozo, B. de Lotto, C. Delgado Mendez, A. Diago Ortega, M. Doert, A. Domínguez, D. Dominis Prester, D. Dorner, M. Doro, D. Elsaesser, D. Ferenc, M. V. Fonseca, L. Font, C. Fruck, R. J. García López, M. Garczarczyk, D. Garrido, G. Giavitto, N. Godinović, D. Hadasch, D. Häfner, A. Herrero, D. Hildebrand, D. Höhne-Mönch, J. Hose, D. Hrupec, B. Huber, T. Jogler, H. Kellermann, S. Klepser, T. Krähenbühl, J. Krause, A. La Barbera, D. Lelas, E. Leonardo, E. Lindfors, S. Lombardi, M. López, A. López-Oramas, E. Lorenz, M. Makariev, G. Maneva, N. Mankuzhiyil, K. Mannheim, L. Maraschi, M. Mariotti, M. Martínez, D. Mazin, M. Meucci, J. M. Miranda, R. Mirzoyan, H. Miyamoto, J. Moldón, A. Moralejo, P. Munar-Adrover, D. Nieto, K. Nilsson, R. Orito, I. Oya, D. Paneque, R. Paoletti, S. Pardo, J. M. Paredes, S. Partini, M. Pasanen, F. Pauss, M. A. Perez-Torres, M. Persic, L. Peruzzo, M. Pilia, J. Pochon, F. Prada, P. G. Prada Moroni, E. Prandini, I. Puljak, I. Reichardt, R. Reinthal, W. Rhode, M. Ribó, J. Rico, S. Rügamer, A. Saggion, K. Saito, T. Y. Saito, M. Salvati, K. Satalecka, V. Scalzotto, V. Scapin, C. Schultz, T. Schweizer, M. Shayduk, S. N. Shore, A. Sillanpää, J. Sitarek, I. Snidaric, D. Sobczynska, F. Spanier, S. Spiro, V. Stamatescu, A. Stamerra, B. Steinke, J. Storz, N. Strah, T. Surić, L. Takalo, H. Takami, F. Tavecchio, P. Temnikov, T. Terzić, D. Tescaro, M. Teshima, O. Tibolla, D. F. Torres, A. Treves, M. Uellenbeck, H. Vankov, P. Vogler, R. M. Wagner, Q. Weitzel, V. Zabalza, F. Zandanel, and R. Zanin. Performance of the MAGIC stereo system obtained with Crab Nebula data. *Astroparticle Physics*, 35:435–448, February 2012. doi: 10.1016/j.astropartphys.2011.11.007.
- [20] J. R. Hörandel. On the knee in the energy spectrum of cosmic rays. *Astroparticle Physics*, 19:193–220, May 2003. doi: 10.1016/S0927-6505(02)00198-6.
- [21] W. Hanlon. Updated Cosmic Ray Spectrum. <http://www.physics.utah.edu/~whanlon/spectrum.html>, 2012.

- [22] M. Cardillo, M. Tavani, and A. Giuliani. The origin of Cosmic-Rays from SNRs: confirmations and challenges after the first direct proof. *Nuclear Physics B Proceedings Supplements*, 256:65–73, November 2014. doi: 10.1016/j.nuclphysbps.2014.10.007.
- [23] M. G. Baring. Diffusive Shock Acceleration : the Fermi Mechanism. In Y. Giraud-Heraud and J. Tran Thanh van, editors, *Very High Energy Phenomena in the Universe; Moriond Workshop*, page 97, 1997.
- [24] E. Fermi. On the Origin of the Cosmic Radiation. *Physical Review*, 75:1169–1174, April 1949. doi: 10.1103/PhysRev.75.1169.
- [25] D. Urošević. On the radio spectra of supernova remnants. *Astrophysics & Space Science*, 354:541–552, December 2014. doi: 10.1007/s10509-014-2095-4.
- [26] Mathieu De Naurois. *Very High Energy astronomy from H.E.S.S. to CTA. Opening of a new astronomical window on the non-thermal Universe*. Habilitation à diriger des recherches, Université Pierre et Marie Curie - Paris VI, March 2012. URL <https://tel.archives-ouvertes.fr/tel-00687872>.
- [27] A. R. Bell. The acceleration of cosmic rays in shock fronts. I. *Monthly Notices of the Royal Astronomical Society*, 182:147–156, January 1978. doi: 10.1093/mnras/182.2.147.
- [28] A. R. Bell and S. G. Lucek. Cosmic ray acceleration to very high energy through the non-linear amplification by cosmic rays of the seed magnetic field. *Monthly Notices of the Royal Astronomical Society*, 321(3):433–438, 2001. doi: 10.1046/j.1365-8711.2001.04063.x. URL <http://mnras.oxfordjournals.org/content/321/3/433.abstract>.
- [29] Stephen P. Reynolds. Supernova Remnants at High Energy. *Annual Review of Astronomy and Astrophysics*, 46(1):89–126, 2008. doi: 10.1146/annurev.astro.46.060407.145237. URL <http://dx.doi.org/10.1146/annurev.astro.46.060407.145237>.
- [30] E. Amato. The origin of galactic cosmic rays. *International Journal of Modern Physics D*, 23:1430013, May 2014. doi: 10.1142/S0218271814300134.
- [31] E. M. de Gouveia Dal Pino and G. Kowal. Particle Acceleration by Magnetic Reconnection. In A. Lazarian, E. M. de Gouveia Dal Pino, and C. Melioli, editors, *Magnetic Fields in Diffuse Media*, volume 407 of *Astrophysics and Space Science Library*, page 373, 2015. doi: 10.1007/978-3-662-44625-6_13.
- [32] D. Kuempel. Extragalactic Propagation of Ultra-High Energy Cosmic Rays. *ArXiv e-prints*, September 2014.
- [33] G. Di Sciascio and R. Iuppa. On the Observation of the Cosmic Ray Anisotropy below 10^{15} eV. *ArXiv e-prints*, July 2014.

Bibliography

- [34] P. Mertsch and S. Funk. Solution to the Cosmic Ray Anisotropy Problem. *Physical Review Letters*, 114(2):021101, January 2015. doi: 10.1103/PhysRevLett.114.021101.
- [35] A. A. Ivanov, A. D. Krasilnikov, M. I. Pravdin, and A. V. Sabourov. Large-scale distribution of cosmic rays in right ascension as observed by the Yakutsk array at energies above 10^{18} eV. *Astroparticle Physics*, 62:1–6, March 2015. doi: 10.1016/j.astropartphys.2014.07.002.
- [36] M. Fukushima. Recent results from telescope array. In *European Physical Journal Web of Conferences*, volume 99 of *European Physical Journal Web of Conferences*, page 04004, August 2015. doi: 10.1051/epjconf/20159904004.
- [37] R. Aloisio. Cosmic Rays: What Gamma Rays Can Say. *ArXiv e-prints*, December 2014.
- [38] M. de Naurois. The Very High Energy Sky from ~ 20 GeV to Hundreds of TeV - Selected Highlights. *ArXiv e-prints*, October 2015.
- [39] M. Ackermann, M. Ajello, A. Allafort, L. Baldini, J. Ballet, G. Barbiellini, M. G. Baring, D. Bastieri, K. Bechtol, R. Bellazzini, R. D. Blandford, E. D. Bloom, E. Bonamente, A. W. Borgland, E. Bottacini, T. J. Brandt, J. Bregeon, M. Brigida, P. Bruel, R. Buehler, G. Busetto, S. Buson, G. A. Caliandro, R. A. Cameron, P. A. Caraveo, J. M. Casandjian, C. Cecchi, Ö. Çelik, E. Charles, S. Chaty, R. C. G. Chaves, A. Chekhtman, C. C. Cheung, J. Chiang, G. Chiaro, A. N. Cillis, S. Ciprini, R. Claus, J. Cohen-Tanugi, L. R. Cominsky, J. Conrad, S. Corbel, S. Cutini, F. D’Ammando, A. de Angelis, F. de Palma, C. D. Dermer, E. do Couto e Silva, P. S. Drell, A. Drlica-Wagner, L. Falletti, C. Favuzzi, E. C. Ferrara, A. Franckowiak, Y. Fukazawa, S. Funk, P. Fusco, F. Gargano, S. Germani, N. Giglietto, P. Giommi, F. Giordano, M. Giroletti, T. Glanzman, G. Godfrey, I. A. Grenier, M.-H. Grondin, J. E. Grove, S. Guiriec, D. Hadasch, Y. Hanabata, A. K. Harding, M. Hayashida, K. Hayashi, E. Hays, J. W. Hewitt, A. B. Hill, R. E. Hughes, M. S. Jackson, T. Jogler, G. Jóhannesson, A. S. Johnson, T. Kamae, J. Kataoka, J. Katsuta, J. Knödlseeder, M. Kuss, J. Lande, S. Larsson, L. Latronico, M. Lemoine-Goumard, F. Longo, F. Loparco, M. N. Lovellette, P. Lubrano, G. M. Madejski, F. Massaro, M. Mayer, M. N. Mazziotta, J. E. McEnery, J. Mehault, P. F. Michelson, R. P. Mignani, W. Mitthumsiri, T. Mizuno, A. A. Moiseev, M. E. Monzani, A. Morselli, I. V. Moskalenko, S. Murgia, T. Nakamori, R. Nemmen, E. Nuss, M. Ohno, T. Ohsugi, N. Omodei, M. Orienti, E. Orlando, J. F. Ormes, D. Paneque, J. S. Perkins, M. Pesce-Rollins, F. Piron, G. Pivato, S. Rainò, R. Rando, M. Razzano, S. Razzaque, A. Reimer, O. Reimer, S. Ritz, C. Romoli, M. Sánchez-Conde, A. Schulz, C. Sgrò, P. E. Simeon, E. J. Siskind, D. A. Smith, G. Spandre, P. Spinelli, F. W. Stecker, A. W. Strong, D. J. Suson, H. Tajima, H. Takahashi, T. Takahashi, T. Tanaka, J. G. Thayer, J. B. Thayer, D. J. Thompson, S. E. Thorsett, L. Tibaldo, O. Tibolla, M. Tinivella, E. Troja, Y. Uchiyama, T. L. Usher, J. Vandenbroucke, V. Vasileiou, G. Vianello, V. Vitale,

- A. P. Waite, M. Werner, B. L. Winer, K. S. Wood, M. Wood, R. Yamazaki, Z. Yang, and S. Zimmer. Detection of the Characteristic Pion-Decay Signature in Supernova Remnants. *Science*, 339:807–811, February 2013. doi: 10.1126/science.1231160.
- [40] M. Tavani, G. Barbiellini, A. Argan, F. Boffelli, A. Bulgarelli, P. Caraveo, P. W. Cattaneo, A. W. Chen, V. Cocco, E. Costa, F. D’Ammando, E. Del Monte, G. de Paris, G. Di Cocco, G. di Persio, I. Donnarumma, Y. Evangelista, M. Feroci, A. Ferrari, M. Fiorini, F. Fornari, F. Fuschino, T. Froyland, M. Frutti, M. Galli, F. Gianotti, A. Giuliani, C. Labanti, I. Lapshov, F. Lazzarotto, F. Liello, P. Lipari, F. Longo, E. Mattaini, M. Marisaldi, M. Mastropietro, A. Mauri, F. Mauri, S. Mereghetti, E. Morelli, A. Morselli, L. Pacciani, A. Pellizzoni, F. Perotti, G. Piano, P. Picozza, C. Pontoni, G. Porrovecchio, M. Prest, G. Pucella, M. Rapisarda, A. Rappoldi, E. Rossi, A. Rubini, P. Soffitta, A. Traci, M. Trifoglio, A. Trois, E. Vallazza, S. Vercellone, V. Vittorini, A. Zambra, D. Zanello, C. Pittori, B. Preger, P. Santolamazza, F. Verrecchia, P. Giommi, S. Colafrancesco, A. Antonelli, S. Cutini, D. Gasparrini, S. Stellato, G. Fanari, R. Primavera, F. Tamburelli, F. Viola, G. Guarrera, L. Salotti, F. D’Amico, E. Marchetti, M. Crisconio, P. Sabatini, G. Annoni, S. Alia, A. Longoni, R. Sanquerin, M. Battilana, P. Concari, E. Dessimone, R. Grossi, A. Parise, F. Monzani, E. Artina, R. Pavesi, G. Marseguerra, L. Nicolini, L. Scandelli, L. Soli, V. Vettorello, E. Zardetto, A. Bonati, L. Maltecca, E. D’Alba, M. Patané, G. Babini, F. Onorati, L. Acquaroli, M. Angelucci, B. Morelli, C. Agostara, M. Cerone, A. Michetti, P. Tempesta, S. D’Eramo, F. Rocca, F. Giannini, G. Borghi, B. Garavelli, M. Conte, M. Balasini, I. Ferrario, M. Vanotti, E. Collavo, and M. Giacomazzo. The AGILE Mission. *Astronomy and Astrophysics*, 502:995–1013, August 2009. doi: 10.1051/0004-6361/200810527.
- [41] M. Tavani, A. Giuliani, A. W. Chen, A. Argan, G. Barbiellini, A. Bulgarelli, P. Caraveo, P. W. Cattaneo, V. Cocco, T. Contessi, F. D’Ammando, E. Costa, G. De Paris, E. Del Monte, G. Di Cocco, I. Donnarumma, Y. Evangelista, A. Ferrari, M. Feroci, F. Fuschino, M. Galli, F. Gianotti, C. Labanti, I. Lapshov, F. Lazzarotto, P. Lipari, F. Longo, M. Marisaldi, M. Mastropietro, S. Mereghetti, E. Morelli, E. Moretti, A. Morselli, L. Pacciani, A. Pellizzoni, F. Perotti, G. Piano, P. Picozza, M. Pilia, G. Pucella, M. Prest, M. Rapisarda, A. Rappoldi, E. Scalise, A. Rubini, S. Sabatini, E. Striani, P. Soffitta, M. Trifoglio, A. Trois, E. Vallazza, S. Vercellone, V. Vittorini, A. Zambra, D. Zanello, C. Pittori, F. Verrecchia, P. Santolamazza, P. Giommi, S. Colafrancesco, L. A. Antonelli, and L. Salotti. Direct Evidence for Hadronic Cosmic-Ray Acceleration in the Supernova Remnant IC 443. *The Astrophysical Journal, Letters*, 710:L151–L155, February 2010. doi: 10.1088/2041-8205/710/2/L151.
- [42] E. Amato. Particle acceleration and radiation in Pulsar Wind Nebulae. *ArXiv e-prints*, March 2015.
- [43] P. Eger, H. Laffon, P. Bordas, E. de Oña Whilhelmi, J. Hinton, and G. Pühlhofer.

Bibliography

- Discovery of a variable X-ray counterpart to HESS J1832-093: a new gamma-ray binary? *Monthly Notices of the Royal Astronomical Society*, 457:1753–1758, April 2016. doi: 10.1093/mnras/stw125.
- [44] R. H. D. Corbet, L. Chomiuk, M. J. Coe, J. B. Coley, G. Dubus, P. G. Edwards, P. Martin, V. A. McBride, J. Stevens, J. Strader, L. J. Townsend, and A. Udalski. A Luminous Gamma-ray Binary in the Large Magellanic Cloud. *ArXiv e-prints*, August 2016.
- [45] G. Dubus. Gamma-ray emission from binaries in context. *Comptes Rendus Physique*, 16:661–673, August 2015. doi: 10.1016/j.crhy.2015.08.014.
- [46] G. Dubus. Gamma-ray binaries and related systems. *Astronomy & Astrophysics Reviews*, 21:64, August 2013. doi: 10.1007/s00159-013-0064-5.
- [47] A. Lamberts. Gamma-ray binaries : a bridge between Be stars and high energy astrophysics. *ArXiv e-prints*, October 2014.
- [48] Q. Z. Liu, J. van Paradijs, and E. P. J. van den Heuvel. Catalogue of high-mass X-ray binaries in the Galaxy (4th edition). *Astronomy and Astrophysics*, 455: 1165–1168, September 2006. doi: 10.1051/0004-6361:20064987.
- [49] A. K. Harding. The neutron star zoo. *Frontiers of Physics*, 8:679–692, December 2013. doi: 10.1007/s11467-013-0285-0.
- [50] S. Johnston, R. N. Manchester, A. G. Lyne, L. Nicastro, and J. Spyromilio. Radio and Optical Observations of the PSR:B1259-63 / SS:2883 Be-Star Binary System. *Monthly Notices of the Royal Astronomical Society*, 268:430, May 1994. doi: 10.1093/mnras/268.2.430.
- [51] F. Aharonian, A. G. Akhperjanian, K.-M. Aye, A. R. Bazer-Bachi, M. Beilicke, W. Benbow, D. Berge, P. Berghaus, K. Bernlöhr, C. Boisson, O. Bolz, I. Braun, F. Breitling, A. M. Brown, J. Bussons Gordo, P. M. Chadwick, L.-M. Chounet, R. Cornils, L. Costamante, B. Degrange, A. Djannati-Ataï, L. O’C. Drury, G. Dubus, D. Emmanoulopoulos, P. Espigat, F. Feinstein, P. Fleury, G. Fontaine, Y. Fuchs, S. Funk, Y. A. Gallant, B. Giebels, S. Gillessen, J. F. Glicenstein, P. Goret, C. Hadjichristidis, M. Hauser, G. Heinzlmann, G. Henri, G. Hermann, J. A. Hinton, W. Hofmann, M. Holleran, D. Horns, O. C. de Jager, S. Johnston, B. Khélifi, J. G. Kirk, N. Komin, A. Konopelko, I. J. Latham, R. Le Gallou, A. Lemièrre, M. Lemoine-Goumard, N. Leroy, O. Martineau-Huynh, T. Lohse, A. Marcowith, C. Masterson, T. J. L. McComb, M. de Naurois, S. J. Nolan, A. Noutsos, K. J. Orford, J. L. Osborne, M. Ouchrif, M. Panter, G. Pelletier, S. Pita, G. Pühlhofer, M. Punch, B. C. Raubenheimer, M. Raue, J. Raux, S. M. Rayner, I. Redondo, A. Reimer, O. Reimer, J. Ripken, L. Rob, L. Rolland, G. Rowell, V. Sahakian, L. Saugé, S. Schlenker, R. Schlickeiser, C. Schuster, U. Schwanke, M. Siewert, O. Skjæraasen, H. Sol, R. Steenkamp, C. Stegmann, J.-P. Tavernet, R. Terrier, C. G. Théoret, M. Tluczykont, G. Vasileiadis, C. Venter, P. Vincent,

- H. J. Völk, and S. J. Wagner. Discovery of the binary pulsar PSR B1259-63 in very-high-energy gamma rays around periastron with HESS. *Astronomy & Astrophysics*, 442:1–10, October 2005. doi: 10.1051/0004-6361:20052983.
- [52] F. Aharonian, A. G. Akhperjanian, G. Anton, U. Barres de Almeida, A. R. Bazer-Bachi, Y. Becherini, B. Behera, K. Bernlöhr, A. Bochow, C. Boisson, J. Bolmont, V. Borrel, J. Brucker, F. Brun, P. Brun, R. Bühler, T. Bulik, I. Büsching, T. Boute-lier, P. M. Chadwick, A. Charbonnier, R. C. G. Chaves, A. Cheesebrough, L.-M. Chounet, A. C. Clapson, G. Coignet, M. Dalton, M. K. Daniel, I. D. Davids, B. Degrange, C. Deil, H. J. Dickinson, A. Djannati-Ataï, W. Domainko, L. O’C. Drury, F. Dubois, G. Dubus, J. Dyks, M. Dyrda, K. Egberts, D. Emmanoulopoulos, P. Espigat, C. Farnier, F. Feinstein, A. Fiasson, A. Förster, G. Fontaine, M. Füßling, S. Gabici, Y. A. Gallant, L. Gérard, D. Gerbig, B. Giebels, J. F. Glicenstein, B. Glück, P. Goret, D. Göring, D. Hauser, M. Hauser, S. Heinz, G. Heinzlmann, G. Henri, G. Hermann, J. A. Hinton, A. Hoffmann, W. Hofmann, M. Holleran, S. Hoppe, D. Horns, A. Jacholkowska, O. C. de Jager, C. Jahn, I. Jung, K. Katarzyński, U. Katz, S. Kaufmann, M. Kerschhaggl, D. Khangulyan, B. Khélifi, D. Keogh, D. Klochkov, W. Kluźniak, T. Kneiske, N. Komin, K. Kosack, R. Kossakowski, G. Lamanna, J.-P. Lenain, T. Lohse, V. Marandon, O. Martineau-Huynh, A. Marcowith, J. Masbou, D. Maurin, T. J. L. McComb, M. C. Medina, R. Moderski, E. Moulin, M. Naumann-Godo, M. de Naurois, D. Nedbal, D. Nekrassov, B. Nicholas, J. Niemiec, S. J. Nolan, S. Ohm, J.-F. Olive, E. de Oña Wilhelmi, K. J. Orford, M. Ostrowski, M. Panter, M. Paz Arribas, G. Pedalletti, G. Pelletier, P.-O. Petrucci, S. Pita, G. Pühlhofer, M. Punch, A. Quirrenbach, B. C. Raubenheimer, M. Raue, S. M. Rayner, M. Renaud, F. Rieger, J. Ripken, L. Rob, S. Rosier-Lees, G. Rowell, B. Rudak, C. B. Rulten, J. Ruppel, V. Sahakian, A. Santangelo, R. Schlickeiser, F. M. Schöck, U. Schwanke, S. Schwarzburg, S. Schwemmer, A. Shalchi, M. Sikora, J. L. Skilton, H. Sol, D. Spangler, L. Stawarz, R. Steenkamp, C. Stegmann, F. Stinzing, G. Superina, A. Szostek, P. H. Tam, J.-P. Tavernet, R. Terrier, O. Tibolla, M. Tluczykont, C. van Eldik, G. Vasileiadis, C. Venter, L. Venter, J. P. Vialle, P. Vincent, M. Vivier, H. J. Völk, F. Volpe, S. J. Wagner, M. Ward, A. A. Zdziarski, and A. Zech. Very high energy γ -ray observations of the binary PSR B1259-63/SS2883 around the 2007 Periastron. *Astronomy & Astrophysics*, 507:389–396, November 2009. doi: 10.1051/0004-6361/200912339.
- [53] H.E.S.S. Collaboration, A. Abramowski, F. Acero, F. Aharonian, A. G. Akhperjanian, G. Anton, S. Balenderan, A. Balzer, A. Barnacka, Y. Becherini, J. Becker Tjus, K. Bernlöhr, E. Birsin, J. Biteau, C. Boisson, J. Bolmont, P. Bordas, J. Brucker, F. Brun, P. Brun, T. Bulik, S. Carrigan, S. Casanova, M. Cerruti, P. M. Chadwick, R. C. G. Chaves, A. Cheesebrough, S. Colafrancesco, G. Cologne, J. Conrad, C. Couturier, M. Dalton, M. K. Daniel, I. D. Davids, B. Degrange, C. Deil, P. deWilt, H. J. Dickinson, A. Djannati-Ataï, W. Domainko, L. O. Drury, G. Dubus, K. Dutson, J. Dyks, M. Dyrda, K. Egberts, P. Eger, P. Espigat, L. Fallon, C. Farnier, S. Fegan, F. Feinstein, M. V. Fernandes, D. Fernan-

- dez, A. Fiasson, G. Fontaine, A. Förster, M. Füßling, M. Gajdus, Y. A. Gallant, T. Garrigoux, H. Gast, B. Giebels, J. F. Glicenstein, B. Glück, D. Göring, M.-H. Grondin, M. Grudzińska, S. Häer, J. D. Hague, J. Hahn, D. Hampf, J. Harris, S. Heinz, G. Heinzelmann, G. Henri, G. Hermann, A. Hillert, J. A. Hinton, W. Hofmann, P. Hofverberg, M. Holler, D. Horns, A. Jacholkowska, C. Jahn, M. Jamrozy, I. Jung, M. A. Kastendieck, K. Katarzyński, U. Katz, S. Kaufmann, B. Khélifi, S. Klepser, D. Klochkov, W. Kluźniak, T. Kneiske, D. Kolitzus, N. Komin, K. Kosack, R. Kossakowski, F. Krayzel, P. P. Krüger, H. Lan, G. Lamanna, J. Lefaucheur, M. Lemoine-Goumard, J.-P. Lenain, D. Lennarz, T. Lohse, A. Lopatin, C.-C. Lu, V. Marandon, A. Marcowith, J. Masbou, G. Maurin, N. Maxted, M. Mayer, T. J. L. McComb, M. C. Medina, J. Méhault, U. Menzler, R. Moderski, M. Mohamed, E. Moulin, C. L. Naumann, M. Naumann-Godo, M. de Naurois, D. Nedbal, N. Nguyen, J. Niemiec, S. J. Nolan, L. Oakes, S. Ohm, E. de Oña Wilhelmi, B. Opitz, M. Ostrowski, I. Oya, M. Panter, R. D. Parsons, M. Paz Arribas, N. W. Pekeur, G. Pelletier, J. Perez, P.-O. Petrucci, B. Peyaud, S. Pita, G. Pühlhofer, M. Punch, A. Quirrenbach, S. Raab, M. Raue, A. Reimer, O. Reimer, M. Renaud, R. de los Reyes, F. Rieger, J. Ripken, L. Rob, S. Rosier-Lees, G. Rowell, B. Rudak, C. B. Rulten, V. Sahakian, D. A. Sanchez, A. Santangelo, R. Schlickeiser, A. Schulz, U. Schwanke, S. Schwarzborg, S. Schwemmer, F. Sheidaei, J. L. Skilton, H. Sol, G. Spengler, L. Stawarz, R. Steenkamp, C. Stegmann, F. Stinzing, K. Stycz, I. Sushch, A. Szostek, J.-P. Tavernet, R. Terrier, M. Tluczykont, C. Trichard, K. Valerius, C. van Eldik, G. Vasileiadis, C. Venter, A. Viana, P. Vincent, H. J. Völk, F. Volpe, S. Vorobiov, M. Vorster, S. J. Wagner, M. Ward, R. White, A. Wierzholska, P. Willmann, D. Wouters, M. Zacharias, A. Zajczyk, A. A. Zdziarski, A. Zech, and H.-S. Zechlin. H.E.S.S. observations of the binary system PSR B1259-63/LS 2883 around the 2010/2011 periastron passage. *Astronomy & Astrophysics*, 551:A94, March 2013. doi: 10.1051/0004-6361/201220612.
- [54] I. Negueruela, M. Ribó, A. Herrero, J. Lorenzo, D. Khangulyan, and F. A. Aharonian. Astrophysical Parameters of LS 2883 and Implications for the PSR B1259-63 Gamma-ray Binary. *The Astrophysical Journal, Letters*, 732:L11, May 2011. doi: 10.1088/2041-8205/732/1/L11.
- [55] S. Johnston, R. N. Manchester, A. G. Lyne, M. Bailes, V. M. Kaspi, G. Qiao, and N. D’Amico. PSR 1259-63 - A binary radio pulsar with a Be star companion. *The Astrophysical Journal, Letters*, 387:L37–L41, March 1992. doi: 10.1086/186300.
- [56] Dmitry Khangulyan, Felix A. Aharonian, Sergey V. Bogovalov, and Marc Ribó. Post-periastron Gamma-Ray Flare from PSR B1259–63/LS 2883 as a Result of Comptonization of the Cold Pulsar Wind. *The Astrophysical Journal Letters*, 752(1):L17, 2012. URL <http://stacks.iop.org/2041-8205/752/i=1/a=L17>.
- [57] R. M. Shannon, S. Johnston, and R. N. Manchester. The kinematics and orbital dynamics of the PSR B1259-63/LS 2883 system from 23 yr of pulsar timing.

- Monthly Notices of the Royal Astronomical Society*, 437:3255–3264, February 2014. doi: 10.1093/mnras/stt2123.
- [58] N. Wang, S. Johnston, and R. N. Manchester. 13 years of timing of PSR B1259–63. *Monthly Notices of the Royal Astronomical Society*, 351(2):599–606, 2004. ISSN 1365-2966. doi: 10.1111/j.1365-2966.2004.07806.x. URL <http://dx.doi.org/10.1111/j.1365-2966.2004.07806.x>.
- [59] M. Tavani and J. Arons. Theory of High-Energy Emission from the Pulsar/Be Star System PSR 1259-63. I. Radiation Mechanisms and Interaction Geometry. *The Astrophysical Journal*, 477:439–464, March 1997.
- [60] A. Y Potekhin. The physics of neutron stars. *Physics Uspekhi*, 53:1235–1256, December 2010. doi: 10.3367/UFNe.0180.201012c.1279.
- [61] L. D. Landau. To the Stars theory. *Phys. Zs. Sowjet.*, vol.1, p.285, 1932 (*English and German*), 1:285, December 1932.
- [62] W. Baade and F. Zwicky. On Super-novae. *Proceedings of the National Academy of Science*, 20:254–259, May 1934. doi: 10.1073/pnas.20.5.254.
- [63] V. S. Beskin, S. V. Chernov, C. R. Gwinn, and A. A. Tchekhovskoy. Radio Pulsars. *Space Science Reviews*, 191:207–237, October 2015. doi: 10.1007/s11214-015-0173-8.
- [64] A. Hewish, S. J. Bell, J. D. H. Pilkington, P. F. Scott, and R. A. Collins. Observation of a Rapidly Pulsating Radio Source. *Nature*, 217:709–713, February 1968. doi: 10.1038/217709a0.
- [65] Mathieu De Naurois. *L'expérience CELESTE: Reconversion d'une centrale solaire pour l'astronomie gamma. Première observation de la Nébuleuse du Crabe et du Blazar Markarian 421 entre 30 et 300 GeV*. Theses, Université Pierre et Marie Curie - Paris VI, May 2000. URL <https://tel.archives-ouvertes.fr/tel-00004261>. Michel BAUBILLIER: Président Hélène SOL: Rapporteur François LE DIBERDER: Rapporteur David SMITH Patrick FLEURY Marie Claude COUSINOU René ONG.
- [66] Matthew Lynn Dalton. *Identification of the VHE Gamma-ray source HESS J1303-631 as a pulsar wind nebula through multi-wavelength observations*. PhD thesis, 2011. URL <http://edoc.hu-berlin.de/docviews/abstract.php?id=38003;urn:nbn:de:kobv:11-100186258>.
- [67] I. A. Grenier and A. K. Harding. Gamma-ray pulsars: A gold mine. *Comptes Rendus Physique*, 16:641–660, August 2015. doi: 10.1016/j.crhy.2015.08.013.
- [68] R. N. Manchester, G. B. Hobbs, A. Teoh, and M. Hobbs. The Australia Telescope National Facility Pulsar Catalogue. *The Astronomical Journal*, 129:1993–2006, April 2005. doi: 10.1086/428488.

Bibliography

- [69] P. Goldreich and W. H. Julian. Pulsar Electrodynamics. *Astrophysical Journal*, 157:869, August 1969. doi: 10.1086/150119.
- [70] M. J. Rees and J. E. Gunn. The origin of the magnetic field and relativistic particles in the Crab Nebula. *Monthly Notices of the Royal Astronomical Society*, 167:1–12, April 1974. doi: 10.1093/mnras/167.1.1.
- [71] R. Bühler and R. Blandford. The surprising Crab pulsar and its nebula: a review. *Reports on Progress in Physics*, 77(6):066901, June 2014. doi: 10.1088/0034-4885/77/6/066901.
- [72] A. K. Harding, E. Tadamaru, and L. W. Esposito. A curvature-radiation-pair-production model for gamma-ray pulsars. *Astrophysical Journal*, 225:226–236, October 1978. doi: 10.1086/156486.
- [73] E. Massaro and M. Salvati. Gamma-ray spectra expected from pulsars. *Astronomy and Astrophysics*, 71:51–54, January 1979.
- [74] K. S. Cheng, C. Ho, and M. Ruderman. Energetic radiation from rapidly spinning pulsars. I - Outer magnetosphere gaps. II - VELA and Crab. *Astrophysical Journal*, 300:500–539, January 1986. doi: 10.1086/163829.
- [75] J. Arons. Pair creation above pulsar polar caps - Geometrical structure and energetics of slot gaps. *Astrophysical Journal*, 266:215–241, March 1983. doi: 10.1086/160771.
- [76] A. G. Muslimov and A. K. Harding. High-Altitude Particle Acceleration and Radiation in Pulsar Slot Gaps. *Astrophysical Journal*, 606:1143–1153, May 2004. doi: 10.1086/383079.
- [77] B. van Soelen, P. Väisänen, A. Odendaal, L. Klindt, I. Sushch, and P. J. Meintjes. Optical spectroscopy of PSR B1259-63/LS 2883 during the 2014 periastron passage with the Southern African Large Telescope. *ArXiv e-prints*, November 2015.
- [78] G. G. Pavlov, J. Hare, O. Kargaltsev, B. Rangelov, and M. Durant. An Extended X-Ray Object Ejected from the PSRB1259-63/LS2883 Binary. *The Astrophysical Journal*, 806:192, June 2015. doi: 10.1088/0004-637X/806/2/192.
- [79] M. Chernyakova, A. Neronov, B. van Soelen, P. Callanan, L. O’Shaughnessy, I. Babyk, S. Tsygankov, I. Vovk, R. Krivonos, J. A. Tomsick, D. Malyshev, J. Li, K. Wood, D. Torres, S. Zhang, P. Kretschmar, M. V. McSwain, D. A. H. Buckley, and C. Koen. Multi-wavelength observations of the binary system PSR B1259-63/LS 2883 around the 2014 periastron passage. *Monthly Notices of the Royal Astronomical Society*, 454:1358–1370, December 2015. doi: 10.1093/mnras/stv1988.
- [80] J. M. Porter and T. Rivinius. Classical Be Stars. *Publications of the Astronomical Society of the Pacific*, 115:1153–1170, October 2003. doi: 10.1086/378307.

- [81] A. T. Okazaki, S. Nagataki, T. Naito, A. Kawachi, K. Hayasaki, S. P. Owocki, and J. Takata. Hydrodynamic Interaction between the Be Star and the Pulsar in the TeV Binary PSR B1259-63/LS 2883. *Publications of the Astronomical Society of Japan*, 63:893–901, August 2011. doi: 10.1093/pasj/63.4.893.
- [82] A. Melatos, S. Johnston, and D. B. Melrose. Stellar wind and stellar disc models of dispersion and rotation measure variations in the PSR B1259 - 63/SS2883 binary system. *Monthly Notices of the Royal Astronomical Society*, 275:381–397, July 1995. doi: 10.1093/mnras/275.2.381.
- [83] Simon Johnston, Lewis Ball, N. Wang, and R. N. Manchester. Radio observations of PSR B1259–63 through the 2004 periastron passage. *Monthly Notices of the Royal Astronomical Society*, 358(3):1069–1075, 2005. ISSN 1365-2966. doi: 10.1111/j.1365-2966.2005.08854.x. URL <http://dx.doi.org/10.1111/j.1365-2966.2005.08854.x>.
- [84] N. Kee, S. Owocki, R. Townsend, and H.-R. Müller. Pulsational Mass Ejection in Be Star Disks. *ArXiv e-prints*, December 2014.
- [85] W. C. G. Ho, C. M. Espinoza, D. Antonopoulou, and N. Andersson. Pinning down the superfluid and measuring masses using pulsar glitches. *ArXiv e-prints*, October 2015.
- [86] M. Chernyakova, A. A. Abdo, A. Neronov, M. V. McSwain, J. Moldón, M. Ribó, J. M. Paredes, I. Sushch, M. de Naurois, U. Schwanke, Y. Uchiyama, K. Wood, S. Johnston, S. Chaty, A. Coleiro, D. Malyshev, and I. Babyk. Multiwavelength observations of the binary system PSR B1259-63/LS 2883 around the 2010-2011 periastron passage. *Monthly Notices of the Royal Astronomical Society*, 439:432–445, March 2014. doi: 10.1093/mnras/stu021.
- [87] Javier Moldón, Simon Johnston, Marc Ribó, Josep M. Paredes, and Adam T. Deller. Discovery of Extended and Variable Radio Structure from the Gamma-ray Binary System PSR B1259–63/LS 2883. *The Astrophysical Journal Letters*, 732(1):L10, 2011. URL <http://stacks.iop.org/2041-8205/732/i=1/a=L10>.
- [88] S. Johnston, R. N. Manchester, A. G. Lyne, N. D’Amico, M. Bailes, B. M. Gaensler, and L. Nicastro. Radio observations of PSR B1259-63 around periastron. *Monthly Notices of the Royal Astronomical Society*, 279:1026–1036, April 1996. doi: 10.1093/mnras/279.3.1026.
- [89] George G. Pavlov, Chulhoon Chang, and Oleg Kargaltsev. Extended Emission from the PSR B1259–63/SS 2883 Binary Detected with Chandra. *The Astrophysical Journal*, 730(1):2, 2011. URL <http://stacks.iop.org/0004-637X/730/i=1/a=2>.
- [90] Chandra Collaboration. Chandra X-ray Observatory. <http://chandra.harvard.edu/>, 2016.

- [91] M. V. Barkov and V. Bosch-Ramon. The origin of the X-ray-emitting object moving away from PSR B1259-63. *Monthly Notices of the Royal Astronomical Society*, 456:L64–L68, February 2016. doi: 10.1093/mnras/slv171.
- [92] A. A. Abdo, M. Ackermann, M. Ajello, A. Allafort, J. Ballet, G. Barbiellini, D. Bastieri, K. Bechtol, R. Bellazzini, B. Berenji, R. D. Blandford, E. Bonamente, A. W. Borgland, J. Bregeon, M. Brigida, P. Bruel, R. Buehler, S. Buson, G. A. Caliandro, R. A. Cameron, F. Camilo, P. A. Caraveo, C. Cecchi, E. Charles, S. Chaty, A. Chekhtman, M. Chernyakova, C. C. Cheung, J. Chiang, S. Ciprini, R. Claus, J. Cohen-Tanugi, L. R. Cominsky, S. Corbel, S. Cutini, F. D’Ammando, A. de Angelis, P. R. den Hartog, F. de Palma, C. D. Dermer, S. W. Digel, E. d. C. e. Silva, M. Dormody, P. S. Drell, A. Drlica-Wagner, R. Dubois, G. Dubus, D. Dumora, T. Enoto, C. M. Espinoza, C. Favuzzi, S. J. Fegan, E. C. Ferrara, W. B. Focke, P. Fortin, Y. Fukazawa, S. Funk, P. Fusco, F. Gargano, D. Gasparri, N. Gehrels, S. Germani, N. Giglietto, P. Giommi, F. Giordano, M. Giroletti, T. Glanzman, G. Godfrey, I. A. Grenier, M.-H. Grondin, J. E. Grove, E. Grundstrom, S. Guiriec, C. Gwon, D. Hadasch, A. K. Harding, M. Hayashida, E. Hays, G. Jóhannesson, A. S. Johnson, T. J. Johnson, S. Johnston, T. Kamae, H. Katagiri, J. Kataoka, M. Keith, M. Kerr, J. Knödseder, M. Kramer, M. Kuss, J. Lande, S.-H. Lee, M. Lemoine-Goumard, F. Longo, F. Loparco, M. N. Lovellette, P. Lubrano, R. N. Manchester, M. Marelli, M. N. Mazziotta, P. F. Michelson, W. Mitthumsiri, T. Mizuno, A. A. Moiseev, C. Monte, M. E. Monzani, A. Morselli, I. V. Moskalenko, S. Murgia, T. Nakamori, M. Naumann-Godo, A. Neronov, P. L. Nolan, J. P. Norris, A. Noutsos, E. Nuss, T. Ohsugi, A. Okumura, N. Omodei, E. Orlando, D. Paneque, D. Parent, M. Pesce-Rollins, M. Pierbattista, F. Piron, T. A. Porter, A. Possenti, S. Rainò, R. Rando, P. S. Ray, M. Razzano, S. Razzaque, A. Reimer, O. Reimer, T. Reposeur, S. Ritz, H. F.-W. Sadrozinski, J. D. Scargle, C. Sgrò, R. Shannon, E. J. Siskind, P. D. Smith, G. Spandre, P. Spinelli, M. S. Strickman, D. J. Suson, H. Takahashi, T. Tanaka, J. G. Thayer, J. B. Thayer, D. J. Thompson, S. E. Thorsett, L. Tibaldo, O. Tibolla, D. F. Torres, G. Tosti, E. Troja, Y. Uchiyama, T. L. Usher, J. Vandenbroucke, V. Vasileiou, G. Vianello, V. Vitale, A. P. Waite, P. Wang, B. L. Winer, M. T. Wolff, D. L. Wood, K. S. Wood, Z. Yang, M. Ziegler, and S. Zimmer. Discovery of High-energy Gamma-ray Emission from the Binary System PSR B1259-63/LS 2883 around Periastron with Fermi. *The Astrophysical Journal, Letters*, 736:L11, July 2011. doi: 10.1088/2041-8205/736/1/L11.
- [93] G. A. Caliandro, C. C. Cheung, J. Li, J. D. Scargle, D. F. Torres, K. S. Wood, and M. Chernyakova. Gamma-Ray Flare Activity from PSR B1259-63 during 2014 Periastron Passage and Comparison to Its 2010 Passage. *The Astrophysical Journal*, 811:68, September 2015. doi: 10.1088/0004-637X/811/1/68.
- [94] G. A. Caliandro, C. C. Teddy Cheung, J. Li, D. F. Torres, and K. Wood. High energy γ -ray emission from PSR B1259–63 during 2014 and 2010 periastron passages. *ArXiv e-prints*, April 2015.

- [95] P. H. T. Tam, K. L. Li, J. Takata, A. T. Okazaki, C. Y. Hui, and A. K. H. Kong. High-energy Observations of PSR B1259-63/LS 2883 through the 2014 Periastron Passage: Connecting X-Rays to the GeV Flare. *The Astrophysical Journal, Letters*, 798:L26, January 2015. doi: 10.1088/2041-8205/798/1/L26.
- [96] A. Kawachi, T. Naito, J. R. Patterson, P. G. Edwards, A. Asahara, G. V. Bicknell, R. W. Clay, R. Enomoto, S. Gunji, S. Hara, T. Hara, T. Hattori, S. Hayashi, S. Hayashi, C. Itoh, S. Kabuki, F. Kajino, H. Katagiri, T. Kifune, L. Ksenofontov, H. Kubo, J. Kushida, Y. Matsubara, Y. Mizumoto, M. Mori, H. Moro, H. Muraishi, Y. Muraki, T. Nakase, D. Nishida, K. Nishijima, M. Ohishi, K. Okumura, R. J. Protheroe, K. Sakurazawa, D. L. Swaby, T. Tanimori, F. Tokanai, K. Tsuchiya, H. Tsunoo, T. Uchida, A. Watanabe, S. Watanabe, S. Yanagita, T. Yoshida, and T. Yoshikoshi. A Search for TeV Gamma-Ray Emission from the PSR B1259-63/SS 2883 Binary System with the CANGAROO-II 10 Meter Telescope. *The Astrophysical Journal*, 607:949–958, June 2004. doi: 10.1086/383604.
- [97] G. R. Blumenthal and R. J. Gould. Bremsstrahlung, Synchrotron Radiation, and Compton Scattering of High-Energy Electrons Traversing Dilute Gases. *Reviews of Modern Physics*, 42:237–271, 1970. doi: 10.1103/RevModPhys.42.237.
- [98] J. G. Kirk, L. Ball, and O. Skjæraasen. Inverse Compton emission of TeV gamma rays from PSR B1259-63. *Astroparticle Physics*, 10:31–45, January 1999. doi: 10.1016/S0927-6505(98)00041-3.
- [99] G. Dubus. Gamma-ray binaries: pulsars in disguise? *Astronomy & Astrophysics*, 456:801–817, September 2006. doi: 10.1051/0004-6361:20054779.
- [100] D. Khangulyan, S. Hnatic, F. Aharonian, and S. Bogovalov. TeV light curve of PSR B1259-63/SS2883. *Monthly Notices of the Royal Astronomical Society*, 380: 320–330, September 2007. doi: 10.1111/j.1365-2966.2007.12075.x.
- [101] I. Sushch and M. Böttcher. Role of the disk environment in the gamma-ray emission from the binary system PSR B1259-63/LS 2883. *ArXiv e-prints*, September 2015.
- [102] S. W. Kong, K. S. Cheng, and Y. F. Huang. Modeling the Multiwavelength Light Curves of PSR B1259-63/LS 2883. II. The Effects of Anisotropic Pulsar Wind and Doppler Boosting. *The Astrophysical Journal*, 753:127, July 2012. doi: 10.1088/0004-637X/753/2/127.
- [103] G. Dubus and B. Cerutti. What caused the GeV flare of PSR B1259-63? *Astronomy & Astrophysics*, 557:A127, September 2013. doi: 10.1051/0004-6361/201321741.
- [104] Fermi LAT Collaboration. The Fermi Large Area Telescope. <http://www-glast.stanford.edu/>, 2012.

Bibliography

- [105] W. B. Atwood, A. A. Abdo, M. Ackermann, W. Althouse, B. Anderson, M. Axelsson, L. Baldini, J. Ballet, D. L. Band, G. Barbiellini, and et al. The Large Area Telescope on the Fermi Gamma-Ray Space Telescope Mission. *The Astrophysical Journal*, 697:1071–1102, June 2009. doi: 10.1088/0004-637X/697/2/1071.
- [106] S. M. Mari, P. Montini, and for the ARGO-YBJ Collaboration. The Cosmic Ray p+He energy spectrum in the 3-3000 TeV energy range measured by ARGO-YBJ. *ArXiv e-prints*, February 2015.
- [107] Miguel Mostafa for the HAWC Collaboration. The High Altitude Water Cherenkov Observatory. *ArXiv e-prints*, October 2013.
- [108] M. F. Cawley, D. J. Fegan, K. Harris, P. W. Kwok, A. M. Hillas, R. C. Lamb, M. J. Lang, D. A. Lewis, D. Macomb, P. T. Reynolds, D. J. Schmid, G. Vacanti, and T. C. Weekes. A high resolution imaging detector for TeV gamma-ray astronomy. *Experimental Astronomy*, 1:173–193, May 1990. doi: 10.1007/BF00462039.
- [109] A. Daum et al. First results on the performance of the HEGRA IACT array. *Astropart. Phys.*, 8:1–11, 1997. doi: 10.1016/S0927-6505(97)00031-5.
- [110] MAGIC Collaboration. The MAGIC Telescopes. <http://www.magic.mppmu.mpg.de/>, 2012.
- [111] T. C. Weekes et al. VERITAS: The Very Energetic Radiation Imaging Telescope Array System. *Astropart. Phys.*, 17(2):221–243, 2002.
- [112] P. A. Cerenkov. Visible luminescence of pure fluids induced by gamma rays. *Ac. Sci. U.S.S.R.*, 8:451, 1934.
- [113] Yuen Tung Eunice Lo. Determining Atmospheric Clarity for the Calibration of Ground-Based Gamma-Ray Telescopes. Durham, April 2013.
- [114] K. Bernlöhr. Impact of atmospheric parameters on the atmospheric Cherenkov technique. *Astroparticle Physics*, 12:255–268, January 2000. doi: 10.1016/S0927-6505(99)00093-6.
- [115] I. M. Frank and I. E. Tamm. Coherent radiation of fast electron in medium. *Dokl. Akad. Nauk SSSR*, 14:107–113, 1937.
- [116] S. Funk, G. Hermann, J. Hinton, D. Berge, K. Bernlöhr, W. Hofmann, P. Nayman, F. Toussenel, and P. Vincent. The trigger system of the H.E.S.S. telescope array. *Astroparticle Physics*, 22:285–296, November 2004. doi: 10.1016/j.astropartphys.2004.08.001.
- [117] S. Funk and for the H. E. S. S. collaboration. Results from the H.E.S.S. Galactic Plane survey. volume 4 of *Proceedings of the 29th International Cosmic Ray Conference, Pune, India*, pages 123–126, 2005.

- [118] S. Carrigan, F. Brun, R. C. G. Chaves, C. Deil, A. Donath, H. Gast, V. Marandon, M. Renaud, and for the H. E. S. S. collaboration. The H.E.S.S. Galactic Plane Survey - maps, source catalog and source population. *ArXiv e-prints*, July 2013.
- [119] N. A. Fuchs. *The Mechanics of Aerosols*. Pergamon Press Limited, 1964.
- [120] Keith Hilton. *Process & pattern in physical geography*. London : Unwin Hyman, 2nd ed edition, 1986. ISBN 0713527242.
- [121] John Strutt. On the light from the sky, its polarization and colour. *Philosophical Magazine*, 41:107–120,274–279, 1871.
- [122] G. Mie. Beiträge zur Optik trüber Medien, speziell kolloidaler Metallösungen. *Annalen der Physik*, 330:377–445, 1908. doi: 10.1002/andp.19083300302.
- [123] M. K. Daniel, G. Vasileiadis, and H. E. S. S. Collaboration. Determining atmospheric aerosol content with an infra-red radiometer. In F. A. Aharonian, W. Hofmann, and F. M. Rieger, editors, *American Institute of Physics Conference Series*, volume 1505 of *American Institute of Physics Conference Series*, pages 717–720, December 2012. doi: 10.1063/1.4772360.
- [124] K. Bernlöhr, O. Carrol, R. Cornils, S. Elfahem, P. Espigat, S. Gillessen, G. Heinzelmann, G. Hermann, W. Hofmann, D. Horns, I. Jung, R. Kankanyan, A. Katora, B. Khelifi, H. Krawczynski, M. Panter, M. Punch, S. Rayner, G. Rowell, M. Tluczykont, and R. van Staa. The optical system of the H.E.S.S. imaging atmospheric Cherenkov telescopes. Part I: layout and components of the system. *Astroparticle Physics*, 20:111–128, November 2003. doi: 10.1016/S0927-6505(03)00171-3.
- [125] Arnim Balzer. *Crab flare observations with H.E.S.S. phase II*. PhD thesis, 2014.
- [126] S. Preuss, G. Hermann, W. Hofmann, and A. Kohnle. Study of the photon flux from the night sky at La Palma and Namibia, in the wavelength region relevant for imaging atmospheric Cherenkov telescopes. *Nucl. Instrum. Meth.*, A481:229–240, 2002. doi: 10.1016/S0168-9002(01)01264-5.
- [127] John M. Davies and Eugene S. Cotton. The Proceedings of the Solar Furnace Symposium Design of the quartermaster solar furnace. *Solar Energy*, 1(2):16 – 22, 1957. ISSN 0038-092X. doi: [http://dx.doi.org/10.1016/0038-092X\(57\)90116-0](http://dx.doi.org/10.1016/0038-092X(57)90116-0). URL <http://www.sciencedirect.com/science/article/pii/0038092X57901160>.
- [128] J. Bolmont, P. Corona, P. Gauron, P. Ghislain, C. Goffin, L. Guevara Riveros, J.-F. Huppert, O. Martineau-Huynh, P. Nayman, J.-M. Parraud, J.-P. Tavernet, F. Toussenel, D. Vincent, P. Vincent, W. Bertoli, P. Espigat, M. Punch, D. Besin, E. Delagnes, J.-F. Glicenstein, Y. Moudden, P. Venault, H. Zaghia, L. Brunetti, P.-Y. David, J.-M. Dubois, A. Fiasson, N. Geffroy, I. Gomes Monteiro, L. Journet, F. Krayzel, G. Lamanna, T. Le Flour, S. Lees, B. Lieunard,

Bibliography

- G. Maurin, P. Mugnier, J-L. Panazol, J. Prast, L.-M. Chounet, B. Degrange, E. Edy, G. Fontaine, B. Giebels, S. Hormigos, B. Khélifi, P. Manigot, P. Maritaz, M. de Naurois, M. Compin, F. Feinstein, D. Fernandez, J. Mehault, S. Rivoire, S. Royer, M. Sanguillon, and G. Vasileiadis. The camera of the fifth H.E.S.S. telescope. Part I: System description. *Nuclear Instruments and Methods in Physics Research Section A: Accelerators, Spectrometers, Detectors and Associated Equipment*, 761:46–57, 2014. ISSN 0168-9002. doi: 10.1016/j.nima.2014.05.093. URL <http://www.sciencedirect.com/science/article/pii/S0168900214006469>.
- [129] R. Chalme-Calvet, M. de Naurois, J.-P. Tavernet, and for the H. E. S. S. Collaboration. Muon efficiency of the H.E.S.S. telescope. *ArXiv e-prints*, March 2014.
- [130] P. Hofverberg, R. Kankanyan, M. Panter, G. Hermann, W. Hofmann, C. Deil, and F. Ait Benkhali. Commissioning and initial performance of the H.E.S.S. II drive system. In *Proceedings, 33rd International Cosmic Ray Conference (ICRC2013)*, 2013. URL <http://inspirehep.net/record/1243099/files/arXiv:1307.4550.pdf>.
- [131] C. Trichard, A. Fiasson, G. Maurin, G. Lamanna, and for the H. E. S. S. Collaboration. Enhanced H.E.S.S. II low energies performance thanks to the focus system. *ArXiv e-prints*, September 2015.
- [132] A. Balzer, M. Füßling, M. Gajdus, D. Göring, A. Lopatin, M. de Naurois, S. Schlenker, U. Schwanke, and C. Stegmann. The H.E.S.S. central data acquisition system. *Astroparticle Physics*, 54:67–80, February 2014. doi: 10.1016/j.astropartphys.2013.11.007.
- [133] A Balzer, M Füßling, M Gajdus, D Göring, A Lopatin, T Murach, M de Naurois, S Schlenker, U Schwanke, C Stegmann, and P Wagner. The H.E.S.S. data acquisition system. *Journal of Physics: Conference Series*, 513(1):012003, 2014. URL <http://stacks.iop.org/1742-6596/513/i=1/a=012003>.
- [134] Object Management Group. The common object request broker: Architecture and specification. Technical Report 2.0, 1995.
- [135] Sai-Lai Lo and Steve Pope. The implementation of a high performance orb over multiple network transports. In Nigel Davies, Seitz Jochen, and Kerry Raymond, editors, *Middleware'98*, pages 157–172. Springer London, 1998. ISBN 978-1-4471-1285-3. doi: 10.1007/978-1-4471-1283-9_10. URL http://dx.doi.org/10.1007/978-1-4471-1283-9_10.
- [136] Oracle. *MySQL. The world's most popular open source database*, 2015. URL <https://www.mysql.com/>.
- [137] Gluster Community. *GlusterFS. Storage for your Cloud*, 2015. URL <https://www.gluster.org/>.

- [138] NASA Goddard Space Flight Center. *GCN: The Gamma-ray Coordinates Network*, 2015. URL <http://gcn.gsfc.nasa.gov/>.
- [139] F. Aharonian et al. Calibration of cameras of the H.E.S.S. detector. *Astropart. Phys.*, 22:109–125, 2004. doi: 10.1016/j.astropartphys.2004.06.006.
- [140] T. Murach. A Mono Reconstruction Software for Phase II of the H.E.S.S. Experiment. Master’s thesis, Humboldt-Universität zu Berlin, 2012.
- [141] T. Murach, M. Gajdus, and R. D. Parsons. A Neural Network-Based Monoscopic Reconstruction Algorithm for H.E.S.S. II. *ArXiv e-prints*, September 2015.
- [142] Andreas Hoecker, Peter Speckmayer, Joerg Stelzer, Jan Therhaag, Eckhard von Toerne, and Helge Voss. TMVA: Toolkit for Multivariate Data Analysis. *PoS, ACAT:040*, 2007.
- [143] R. Brun and F. Rademakers. ROOT — An object oriented data analysis framework. *Nuclear Instruments and Methods in Physics Research A*, 389:81–86, February 1997. doi: 10.1016/S0168-9002(97)00048-X.
- [144] R. D. Parsons and J. A. Hinton. A Monte Carlo template based analysis for air-Cherenkov arrays. *Astroparticle Physics*, 56:26–34, April 2014. doi: 10.1016/j.astropartphys.2014.03.002.
- [145] R. D. Parsons, M. Gajdus, T. Murach, and for the H. E. S. S. collaboration. HESS II Data Analysis with ImPACT. *ArXiv e-prints*, September 2015.
- [146] M. de Naurois and L. Rolland. A high performance likelihood reconstruction of γ -rays for imaging atmospheric Cherenkov telescopes. *Astroparticle Physics*, 32: 231–252, December 2009. doi: 10.1016/j.astropartphys.2009.09.001.
- [147] K. Bernlöhr. Simulation of imaging atmospheric Cherenkov telescopes with CORSIKA and sim_telarray. *Astroparticle Physics*, 30:149–158, October 2008. doi: 10.1016/j.astropartphys.2008.07.009.
- [148] M. Szanecki, K. Bernlöhr, D. Sobczyńska, A. Niedźwiecki, J. Sitarek, and W. Bednarek. Geomagnetic field and altitude effects on the performance of future IACT arrays. *ArXiv e-prints*, May 2014.
- [149] D. Heck, J. Knapp, J. N. Capdevielle, G. Schatz, and T. Thouw. *CORSIKA: a Monte Carlo code to simulate extensive air showers*. February 1998.
- [150] V. Marandon and A Mitchell. HD Muon Reconstruction. <https://hess-confluence.desy.de/confluence/display/HESS/HD+Muon+Reconstruction>, 2016.
- [151] Konrad Bernlöhr. Recent changes to CT5 configuration for sim_telarray. https://www.mpi-hd.mpg.de/hfm/~bernlöhr/HESS/Software/sim_hessarray/mc-phase2b2-updates.pdf, December 2014.

Bibliography

- [152] A. Daum, G. Hermann, M. Heß, W. Hofmann, H. Lampeitl, G. Pühlhofer, F. Aharonian, A.G. Akhperjanian, J.A. Barrio, A.S. Beglarian, K. Bernlöhr, J.J.G. Beteta, S.M. Bradbury, J.L. Contreras, J. Cortina, T. Deckers, E. Feigl, J. Fernandez, V. Fonseca, A. Fraß, B. Funk, J.C. Gonzalez, G. Heinzelmann, M. Hemberger, A. Heusler, I. Holl, D. Horns, R. Kankanyan, O. Kirstein, C. Köhler, A. Konopelko, D. Kranich, H. Krawczynski, H. Kornmayer, A. Lindner, E. Lorenz, N. Magnussen, H. Meyer, R. Mirzoyan, H. Möller, A. Moralejo, L. Padilla, M. Panter, D. Petry, R. Plaga, J. Prah, C. Prosch, G. Rauterberg, W. Rhode, A. Röhring, V. Sahakian, M. Samorski, J.A. Sanchez, D. Schmele, W. Stamm, M. Ulrich, H.J. Völk, S. Westerhoff, B. Wiebel-Sooth, C.A. Wiedner, M. Willmer, and H. Wirth. First results on the performance of the HEGRA IACT array. *Astroparticle Physics*, 8(1–2):1 – 11, 1997. ISSN 0927-6505. doi: [http://dx.doi.org/10.1016/S0927-6505\(97\)00031-5](http://dx.doi.org/10.1016/S0927-6505(97)00031-5). URL <http://www.sciencedirect.com/science/article/pii/S0927650597000315>.
- [153] Andreas Hoecker, Peter Speckmayer, Joerg Stelzer, Jan Therhaag, Eckhard von Toerne, and Helge Voss. TMVA: Toolkit for Multivariate Data Analysis. *PoS, ACAT:040*, 2007.
- [154] C. G. BROYDEN. The Convergence of a Class of Double-rank Minimization Algorithms 1. General Considerations. *IMA Journal of Applied Mathematics*, 6(1):76–90, 1970. doi: 10.1093/imamat/6.1.76. URL <http://imamat.oxfordjournals.org/content/6/1/76.abstract>.
- [155] R. Fletcher. A new approach to variable metric algorithms. *The Computer Journal*, 13(3):317–322, 1970. doi: 10.1093/comjnl/13.3.317. URL <http://comjnl.oxfordjournals.org/content/13/3/317.abstract>.
- [156] Donald Goldfarb. A family of variable-metric methods derived by variational means. *Mathematics of computation*, 24(109):23–26, 1970.
- [157] David F Shanno. Conditioning of quasi-Newton methods for function minimization. *Mathematics of computation*, 24(111):647–656, 1970.
- [158] W. Hofmann, I. Jung, A. Konopelko, H. Krawczynski, H. Lampeitl, and G. Pühlhofer. Comparison of techniques to reconstruct {VHE} gamma-ray showers from multiple stereoscopic cherenkov images. *Astroparticle Physics*, 12(3):135 – 143, 1999. ISSN 0927-6505. doi: [http://dx.doi.org/10.1016/S0927-6505\(99\)00084-5](http://dx.doi.org/10.1016/S0927-6505(99)00084-5). URL <http://www.sciencedirect.com/science/article/pii/S0927650599000845>.
- [159] V. Marandon. *TeV observations of pulsar wind nebulae*. PhD thesis, APC CNRS/Universite Paris 7, 2010.
- [160] D. Berge, S. Funk, and J. Hinton. Background modelling in very-high-energy γ -ray astronomy. *Astronomy and Astrophysics*, 466:1219–1229, May 2007. doi: 10.1051/0004-6361:20066674.

- [161] T.-P. Li and Y.-Q. Ma. Analysis methods for results in gamma-ray astronomy. *Astrophysical Journal*, 272:317–324, September 1983. doi: 10.1086/161295.
- [162] W. Hofmann. Performance Limits for Cherenkov Instruments. *ArXiv Astrophysics e-prints*, March 2006.
- [163] M. Ackermann, M. Ajello, A. Albert, A. Allafort, W. B. Atwood, M. Axelson, L. Baldini, J. Ballet, G. Barbiellini, D. Bastieri, K. Bechtol, R. Bellazzini, E. Bissaldi, R. D. Blandford, E. D. Bloom, J. R. Bogart, E. Bonamente, A. W. Borgland, E. Bottacini, A. Bouvier, T. J. Brandt, J. Bregeon, M. Brigida, P. Bruel, R. Buehler, T. H. Burnett, S. Buson, G. A. Caliandro, R. A. Cameron, P. A. Caraveo, J. M. Casandjian, E. Cavazzuti, C. Cecchi, Ö. Çelik, E. Charles, R. C. G. Chaves, A. Chekhtman, C. C. Cheung, J. Chiang, S. Ciprini, R. Claus, J. Cohen-Tanugi, J. Conrad, R. Corbet, S. Cutini, F. D’Ammando, D. S. Davis, A. de Angelis, M. DeKlotz, F. de Palma, C. D. Dermer, S. W. Digel, E. d. C. e. Silva, P. S. Drell, A. Drlica-Wagner, R. Dubois, C. Favuzzi, S. J. Fegan, E. C. Ferrara, W. B. Focke, P. Fortin, Y. Fukazawa, S. Funk, P. Fusco, F. Gargano, D. Gasparrini, N. Gehrels, B. Giebels, N. Giglietto, F. Giordano, M. Giroletti, T. Glanzman, G. Godfrey, I. A. Grenier, J. E. Grove, S. Guiriec, D. Hadasch, M. Hayashida, E. Hays, D. Horan, X. Hou, R. E. Hughes, M. S. Jackson, T. Jogler, G. Jóhannesson, R. P. Johnson, T. J. Johnson, W. N. Johnson, T. Kamae, H. Katagiri, J. Kataoka, M. Kerr, J. Knödseder, M. Kuss, J. Lande, S. Larsson, L. Latronico, C. Lavalley, M. Lemoine-Goumard, F. Longo, F. Loparco, B. Lott, M. N. Lovellette, P. Lubrano, M. N. Mazziotta, W. McConville, J. E. McEnery, J. Mehault, P. F. Michelson, W. Mitthumsiri, T. Mizuno, A. A. Moiseev, C. Monte, M. E. Monzani, A. Morselli, I. V. Moskalenko, S. Murgia, M. Naumann-Godo, R. Nemmen, S. Nishino, J. P. Norris, E. Nuss, M. Ohno, T. Ohsugi, A. Okumura, N. Omodei, M. Orienti, E. Orlando, J. F. Ormes, D. Paneque, J. H. Panetta, J. S. Perkins, M. Pesce-Rollins, M. Pierbattista, F. Piron, G. Pivato, T. A. Porter, J. L. Racusin, S. Rainò, R. Rando, M. Razzano, S. Razzaque, A. Reimer, O. Reimer, T. Reposeur, L. C. Reyes, S. Ritz, L. S. Rochester, C. Romoli, M. Roth, H. F.-W. Sadrozinski, D. A. Sanchez, P. M. Saz Parkinson, C. Sbarra, J. D. Scargle, C. Sgrò, J. Siegal-Gaskins, E. J. Siskind, G. Spandre, P. Spinelli, T. E. Stephens, D. J. Suson, H. Tajima, H. Takahashi, T. Tanaka, J. G. Thayer, J. B. Thayer, D. J. Thompson, L. Tibaldo, M. Tinivella, G. Tosti, E. Troja, T. L. Usher, J. Vandenbroucke, B. Van Klaveren, V. Vasileiou, G. Vianello, V. Vitale, A. P. Waite, E. Wallace, B. L. Winer, D. L. Wood, K. S. Wood, M. Wood, Z. Yang, and S. Zimmer. The Fermi Large Area Telescope on Orbit: Event Classification, Instrument Response Functions, and Calibration. *The Astrophysical Journal, Supplement*, 203:4, November 2012. doi: 10.1088/0067-0049/203/1/4.
- [164] F. Aharonian, A. G. Akhperjanian, A. R. Bazer-Bachi, M. Beilicke, W. Benbow, D. Berge, K. Bernlöhr, C. Boisson, O. Bolz, V. Borrel, I. Braun, F. Breitting, A. M. Brown, R. Bühler, I. Büsching, S. Carrigan, P. M. Chadwick, L.-M. Chounet, R. Cornils, L. Costamante, B. Degrange, H. J. Dickinson, A. Djannati-

- Ataï, L. O’C. Drury, G. Dubus, K. Egberts, D. Emmanoulopoulos, P. Espigat, F. Feinstein, E. Ferrero, A. Fiasson, G. Fontaine, S. Funk, S. Funk, Y. A. Gallant, B. Giebels, J. F. Glicenstein, P. Goret, C. Hadjichristidis, D. Hauser, M. Hauser, G. Heinzelmann, G. Henri, G. Hermann, J. A. Hinton, W. Hofmann, M. Holleran, D. Horns, A. Jacholkowska, O. C. de Jager, B. Khélifi, N. Komin, A. Konopelko, K. Kosack, I. J. Latham, R. Le Gallou, A. Lemièrre, M. Lemoine-Goumard, T. Lohse, J. M. Martin, O. Martineau-Huynh, A. Marcowith, C. Masterson, T. J. L. McComb, M. de Naurois, D. Nedbal, S. J. Nolan, A. Noutsos, K. J. Orford, J. L. Osborne, M. Ouchrif, M. Panter, G. Pelletier, S. Pita, G. Pühlhofer, M. Punch, B. C. Raubenheimer, M. Raue, S. M. Rayner, A. Reimer, O. Reimer, J. Ripken, L. Rob, L. Rolland, G. Rowell, V. Sahakian, L. Saugé, S. Schlenker, R. Schlickeiser, U. Schwanke, H. Sol, D. Spangler, F. Spanier, R. Steenkamp, C. Stegmann, G. Superina, J.-P. Tavernet, R. Terrier, C. G. Théoret, M. Tluczykont, C. van Eldik, G. Vasileiadis, C. Venter, P. Vincent, H. J. Völk, S. J. Wagner, and M. Ward. Observations of the Crab nebula with HESS. *Astronomy & Astrophysics*, 457:899–915, October 2006. doi: 10.1051/0004-6361:20065351.
- [165] J. Aleksić, S. Ansoldi, L. A. Antonelli, P. Antoranz, A. Babic, P. Bangale, J. A. Barrio, J. Becerra González, W. Bednarek, E. Bernardini, B. Biasuzzi, A. Billand, O. Blanch, S. Bonnefoy, G. Bonnoli, F. Borracci, T. Bretz, E. Carmona, A. Carosi, P. Colin, E. Colombo, J. L. Contreras, J. Cortina, S. Covino, P. Da Vela, F. Dazzi, A. De Angelis, G. De Caneva, B. De Lotto, E. de Oña Wilhelmi, C. Delgado Mendez, M. Doert, D. Dominis Prester, D. Dorner, M. Doro, S. Einecke, D. Eisenacher, D. Elsaesser, M. V. Fonseca, L. Font, K. Frantzen, C. Fruck, D. Galindo, R. J. García López, M. Garczarczyk, D. Garrido Terrats, M. Gaug, N. Godinović, A. González Muñoz, S. R. Gozzini, D. Hadasch, Y. Hanabata, M. Hayashida, J. Herrera, D. Hildebrand, J. Hose, D. Hrupec, W. Idec, V. Kadenius, H. Kellermann, K. Kodani, Y. Konno, J. Krause, H. Kubo, J. Kushida, A. La Barbera, D. Lelas, N. Lewandowska, E. Lindfors, S. Lombardi, M. López, R. López-Coto, A. López-Oramas, E. Lorenz, I. Lozano, M. Makariev, K. Mallot, G. Maneva, N. Mankuzhiyil, K. Mannheim, L. Maraschi, B. Marcote, M. Mariotti, M. Martínez, D. Mazin, U. Menzel, J. M. Miranda, R. Mirzoyan, A. Moralejo, P. Munar-Adrover, D. Nakajima, A. Niedzwiecki, K. Nilsson, K. Nishijima, K. Noda, N. Nowak, R. Orito, A. Overkemping, S. Paiano, M. Palatiello, D. Paneque, R. Paoletti, J. M. Paredes, X. Paredes-Fortuny, M. Perisic, P. G. Prada Moroni, E. Prandini, S. Preziuso, I. Puljak, R. Reinthal, W. Rhode, M. Ribó, J. Rico, J. Rodriguez Garcia, S. Rügamer, A. Saggion, T. Saito, K. Saito, K. Satalecka, V. Scalzotto, V. Scapin, C. Schultz, T. Schweizer, S. N. Shore, A. Sillanpää, J. Sitarek, I. Snidaric, D. Sobczynska, F. Spanier, V. Stamatescu, A. Stamerra, T. Steinbring, J. Storz, M. Strzys, L. Takalo, H. Takami, F. Tavecchio, P. Temnikov, T. Terzić, D. Tesaro, M. Teshima, J. Thaele, O. Tibolla, D. F. Torres, T. Toyama, A. Treves, M. Uellenbeck, P. Vogler, R. M. Wagner, R. Zanin, D. Horns, J. Martín, and M. Meyer. Measurement of the Crab Nebula

- spectrum over three decades in energy with the MAGIC telescopes. *Journal of High Energy Astrophysics*, 5:30–38, March 2015. doi: 10.1016/j.jheap.2015.01.002.
- [166] M. Wood, R. Caputo, R. Rando, E. Charles, S. Digel, and L. Baldini. Fermi LAT Performance. https://www.slac.stanford.edu/exp/glast/groups/canda/lat_Performance.htm, June 2016.
- [167] C. F. Kennel and F. V. Coroniti. Magnetohydrodynamic model of Crab nebula radiation. *The Astrophysical Journal*, 283:710–730, August 1984. doi: 10.1086/162357.
- [168] A. P. Lobanov, D. Horns, and T. W. B. Muxlow. VLBI imaging of a flare in the Crab nebula: more than just a spot. *Astronomy & Astrophysics*, 533:A10, September 2011. doi: 10.1051/0004-6361/201117082.
- [169] F. Piron, A. Djannati-Atai, M. Punch, J.-P. Tavernet, A. Barrau, R. Bazer-Bachi, L.-M. Chounet, G. Debais, B. Degrange, J.-P. Dezalay, P. Espigat, B. Fabre, P. Fleury, G. Fontaine, P. Goret, C. Gouiffes, B. Khelifi, I. Malet, C. Masterson, G. Mohanty, E. Nuss, C. Renault, M. Rivoal, L. Rob, and S. Vorobiov. Temporal and spectral gamma-ray properties of $\text{jASTROBJ}_i\text{Mkn 421}_i/\text{ASTROBJ}_i$ above 250 GeV from CAT observations between 1996 and 2000. *Astronomy & Astrophysics*, 374:895–906, August 2001. doi: 10.1051/0004-6361:20010798.
- [170] J. Hahn, H. Gast, R. de los Reyes, C. Deil, K. Bernlöhner, K. Kosack, V. Marandon, and P. Hofverberg. Heidelberg Data Quality Selection. H.E.S.S. internal note, February 2013.
- [171] F. Aharonian, A. G. Akhperjanian, K.-M. Aye, A. R. Bazer-Bachi, M. Beilicke, W. Benbow, D. Berge, P. Berghaus, K. Bernlöhner, C. Boisson, O. Bolz, I. Braun, F. Breitling, A. M. Brown, J. Bussons Gordo, P. M. Chadwick, L.-M. Chounet, R. Cornils, L. Costamante, B. Degrange, A. Djannati-Ataï, L. O’C. Drury, G. Dubus, D. Emmanoulopoulos, P. Espigat, F. Feinstein, P. Fleury, G. Fontaine, Y. Fuchs, S. Funk, Y. A. Gallant, B. Giebels, S. Gillessen, J. F. Glicenstein, P. Goret, C. Hadjichristidis, M. Hauser, G. Heinzlmann, G. Henri, G. Hermann, J. A. Hinton, W. Hofmann, M. Holleran, D. Horns, O. C. de Jager, B. Khelifi, N. Komin, A. Konopelko, I. J. Latham, R. Le Gallou, A. Lemièrre, M. Lemoine-Goumard, N. Leroy, T. Lohse, O. Martineau-Huynh, A. Marcowith, C. Masterson, T. J. L. McComb, M. de Naurois, S. J. Nolan, A. Noutsos, K. J. Orford, J. L. Osborne, M. Ouchrif, M. Panter, G. Pelletier, S. Pita, G. Pühlhofer, M. Punch, B. C. Raubenheimer, M. Raue, J. Raux, S. M. Rayner, I. Redondo, A. Reimer, O. Reimer, J. Ripken, L. Rob, L. Rolland, G. Rowell, V. Sahakian, L. Saugé, S. Schlenker, R. Schlickeiser, C. Schuster, U. Schwanke, M. Siewert, H. Sol, R. Steenkamp, C. Stegmann, J.-P. Tavernet, R. Terrier, C. G. Théoret, M. Thuczykont, D. J. van der Walt, G. Vasileiadis, C. Venter, P. Vincent, H. J. Völk, and S. J. Wagner. Serendipitous discovery of the unidentified extended

Bibliography

- TeV γ -ray source HESS J1303-631. *Astronomy & Astrophysics*, 439:1013–1021, September 2005. doi: 10.1051/0004-6361:20053195.
- [172] H.E.S.S. Collaboration, A. Abramowski, F. Acero, F. Aharonian, A. G. Akhperjanian, G. Anton, S. Balenderan, A. Balzer, A. Barnacka, Y. Becherini, J. Becker, K. Bernlöhr, E. Birsin, J. Biteau, A. Bochow, C. Boisson, J. Bolmont, P. Bordas, J. Brucker, F. Brun, P. Brun, T. Bulik, I. Büsching, S. Carrigan, S. Casanova, M. Cerruti, P. M. Chadwick, A. Charbonnier, R. C. G. Chaves, A. Cheesebrough, G. Cologna, J. Conrad, C. Couturier, M. Dalton, M. K. Daniel, I. D. Davids, B. Degrange, C. Deil, H. J. Dickinson, A. Djannati-Ataï, W. Domainko, L. O. Drury, G. Dubus, K. Dutton, J. Dyks, M. Dyrda, K. Egberts, P. Eger, P. Espigat, L. Fallon, C. Farnier, S. Fegan, F. Feinstein, M. V. Fernandes, A. Fiasson, G. Fontaine, A. Förster, M. Füßling, M. Gajdus, Y. A. Gallant, T. Garrigoux, H. Gast, L. Gérard, B. Giebels, J. F. Glicenstein, B. Glück, D. Göring, M.-H. Grondin, S. Häffner, J. D. Hague, J. Hahn, D. Hampf, J. Harris, M. Hauser, S. Heinz, G. Heinzlmann, G. Henri, G. Hermann, A. Hillert, J. A. Hinton, W. Hofmann, P. Hofverberg, M. Holler, D. Horns, A. Jacholkowska, C. Jahn, M. Jamroz, I. Jung, M. A. Kastendieck, K. Katarzyński, U. Katz, S. Kaufmann, B. Khélifi, D. Klochov, W. Kluźniak, T. Kneiske, N. Komin, K. Kosack, R. Kossakowski, F. Krayzel, H. Laffon, G. Lamanna, J.-P. Lenain, D. Lennarz, T. Lohse, A. Lopatin, C.-C. Lu, V. Marandon, A. Marcowith, J. Masbou, G. Maurin, N. Maxted, M. Mayer, T. J. L. McComb, M. C. Medina, J. Méhault, U. Menzler, R. Moderski, M. Mohamed, E. Moulin, C. L. Naumann, M. Naumann-Godo, M. de Naurois, D. Nedbal, D. Nekrassov, N. Nguyen, B. Nicholas, J. Niemiec, S. J. Nolan, S. Ohm, E. de Oña Wilhelmi, B. Opitz, M. Ostrowski, I. Oya, M. Panter, M. Paz Arribas, N. W. Pekeur, G. Pelletier, J. Perez, P.-O. Petrucci, B. Peyaud, S. Pita, G. Pühlhofer, M. Punch, A. Quirrenbach, M. Raue, A. Reimer, O. Reimer, M. Renaud, R. de los Reyes, F. Rieger, J. Ripken, L. Rob, S. Rosier-Lees, G. Rowell, B. Rudak, C. B. Rulten, V. Sahakian, D. A. Sanchez, A. Santangelo, R. Schlickeiser, A. Schulz, U. Schwanke, S. Schwarzburg, S. Schwemmer, F. Sheidaei, J. L. Skilton, H. Sol, G. Spengler, L. Stawarz, R. Steenkamp, C. Stegmann, F. Stinzing, K. Stycz, I. Sushch, A. Szostek, J.-P. Tavernet, R. Terrier, M. Tluczykont, K. Valerius, C. van Eldik, G. Vasileiadis, C. Venter, A. Viana, P. Vincent, H. J. Völk, F. Volpe, S. Vorobiov, M. Vorster, S. J. Wagner, M. Ward, R. White, A. Wiercholska, M. Zacharias, A. Zajczyk, A. A. Zdziarski, A. Zech, and H.-S. Zechlin. Identification of HESS J1303-631 as a pulsar wind nebula through γ -ray, X-ray, and radio observations. *Astronomy & Astrophysics*, 548:A46, December 2012. doi: 10.1051/0004-6361/201219814.
- [173] W. A. Rolke, A. M. López, and J. Conrad. Limits and confidence intervals in the presence of nuisance parameters. *Nuclear Instruments and Methods in Physics Research A*, 551:493–503, October 2005. doi: 10.1016/j.nima.2005.05.068.
- [174] S. Ohm, C. van Eldik, and K. Egberts. γ /hadron separation in very-high-energy

- γ -ray astronomy using a multivariate analysis method. *Astroparticle Physics*, 31: 383–391, June 2009. doi: 10.1016/j.astropartphys.2009.04.001.
- [175] D. Khangulyan, F. A. Aharonian, S. V. Bogovalov, and M. Ribó. Gamma-Ray Signal from the Pulsar Wind in the Binary Pulsar System PSR B1259-63/LS 2883. *The Astrophysical Journal*, 742:98, December 2011. doi: 10.1088/0004-637X/742/2/98.
- [176] S. W. Kong, Y. W. Yu, Y. F. Huang, and K. S. Cheng. Modelling the multiwavelength light curves of PSR B1259–63/SS 2883. *Monthly Notices of the Royal Astronomical Society*, 416(2):1067–1076, 2011. doi: 10.1111/j.1365-2966.2011.19103.x. URL <http://mnras.oxfordjournals.org/content/416/2/1067.abstract>.
- [177] V. Zabalza, V. Bosch-Ramon, F. Aharonian, and D. Khangulyan. Unraveling the high-energy emission components of gamma-ray binaries. *Astronomy & Astrophysics*, 551:A17, March 2013. doi: 10.1051/0004-6361/201220589.
- [178] S. Griffin and for the VERITAS Collaboration. VERITAS Observations under Bright Moonlight. *ArXiv e-prints*, August 2015.

List of Figures

2.1	Differential diffuse cosmic ray flux as a function of the energy per nucleus. Different experiments have contributed data to this graph according to the respective energy ranges. The graph was taken from Hanlon [21]. . . .	5
2.2	Sketch of a shock front between two flows of different directions and velocities u_1 and u_2 in the shock rest frame. The speed of a particle in the upstream region is denoted as v_0	7
2.3	Sketch of a hadronic spectral energy distribution for a source of an age of 1000 yr. A magnetic field strength of $30 \mu\text{G}$ was assumed. At the top of the figure, the proton SED is shown. A spectral index of 2.0 and a cut-off energy of 100 TeV were assumed. The higher-energy peak of the gamma-ray SED is caused by π^0 decay. The shape of the peak depends on the proton spectral index Γ_p . The proton spectrum cut-off is reproduced by the gamma-ray spectrum. The much weaker low-energy peak is caused by synchrotron emission from secondary electrons which have been produced in the scattering processes between protons and target particles. Adapted from Funk [14].	11
2.4	Sketch of a leptonic spectral energy distribution. At the top, an electron SED with a spectral index of 2 with a cut-off at 100 TeV is shown (grey band) together with an alternative scenario in which cooling effects are taken into account (dashed grey line). The IC gamma-ray peak is visible at high energies. Scenarios taking into account IC scattering of different photon fields are displayed as well. At low energies, a stronger and broader peak can be seen. The corresponding photons have been produced via synchrotron radiation. For both peaks, a source with an age of 1000 yr and a relatively high magnetic field strength of $100 \mu\text{G}$ has been assumed. An alternative scenario with a weaker magnetic field of $3 \mu\text{G}$ is shown as well in light grey. Adapted from Funk [14]	13
2.5	Sketch of the PSR B1259–63/LS 2883 binary system configuration. The pulsar orbits the star counterclockwise along the sketched white line. The shock structure is indicated in dark red. During most parts of the orbit, a bow-like structure is found, but during the disk crossings a cavity forms. The length of the pulsar wind zone in the direction of the observer is indicated as blue lines. Adapted from Khangulyan et al. [56].	19

List of Figures

2.6	Sketch of a pulsar. The rotational axis Ω and the magnetic field axis μ are shown. Closed magnetic field lines are indicated by solid lines enclosing a grey area, open field lines are shown as dashed lines. The last open field line defines the location of the light cylinder at a distance R_L from the rotational axis. Figure taken from De Naurois [65].	22
2.7	Light curves from several periastron passages for different wavelength bands are shown. In panel <i>a</i> the VHE flux, in panel <i>b</i> the HE gamma-ray flux, in panel <i>c</i> the X-ray flux and in panel <i>d</i> the radio flux is shown. Panel <i>e</i> is not relevant for the discussion here. Upper limits are marked by arrows. Black, dashed lines indicate, from left to right, the times of the first disc crossing, the periastron and the second disc crossing. Figure taken from Chernyakova et al. [86].	27
2.8	X-ray images showing the movement of a bright object away from the binary. The second image (<i>top right</i>) was recorded 519 d after the first image (<i>top left</i>). The last image was taken another 265 d later. All images in colour coded form are overlaid in the last picture (<i>bottom right</i>). Image taken from Pavlov et al. [78].	28
2.9	Sketch of an imaging atmospheric Cherenkov telescope called CT 5 with a spherical mirror. The Cherenkov photons emitted at different angles are focussed onto the pixelated camera, where the intensity distribution is measured and recorded. See the main text for details of the telescope setup and the measurement process.	35
2.10	Simulated air showers initiated by gamma rays (<i>top</i>) and protons (<i>bottom</i>), each with an energy of 300 GeV. The unit of the values on both axes is kilometres. Green lines represent photons, blue is for electrons and positrons, thick red lines are for protons, other colors stand for muons, pions and other particles. The much larger irregularity and intrinsic spread of proton showers is obvious. Figure taken from De Naurois [65].	36
3.1	The H.E.S.S. array on a hazy day. From left to right there are CT 4, CT 3, CT 5, CT 2 and CT 1. CT 1 to 4 are parked in, whereas CT 5 is pointing towards the south for tests of the drive system. The building in front of the array hosts the control room and the local computing farm.	40
3.2	Sketch of the states of hardware controllers and software processes used in the DAQ. The transitions between the states are indicated by arrows.	45
3.3	ADC count distribution for a single pixel recorded during a SinglePhoto-Electron run [139]. See main text for details.	48
4.1	Simulated radius around the shower axis within which the simulated telescope array was placed as a function of the zenith angle at which the gamma rays were simulated. The points are connected for better visibility.	56

4.2	Energy distributions at the stage of simulating gamma rays (black) and after passing trigger criteria (blue). These distributions follow from simulated observations at 20° zenith, 0° azimuth and a source offset of 0.5° during MuonPhase 200.	57
4.3	Sketch of a neural network as used in this work. The displayed network is used for reconstructing the energies of gamma rays. Input parameters are fed into the input layer on the left, the network's output can be retrieved from the neuron in the output layer on the right. The names of the input parameters are listed on the left. The neurons' activation functions are sketched in the centres of the nodes. The colours of the node connections represent the synapse weight values according to the colour scale shown in the top right corner.	59
4.4	Sketch of an elliptical shower image in the camera plane. Brighter colours represent higher intensities measured by individual pixels. The centre of gravity (COG) of the intensity distribution as defined in the main text and the direction of the initial gamma ray are both shown as points along the major axis of the ellipse. Their angular distance is called δ	62
4.5	Correlations between the input parameters to the MLP networks used to reconstruct the direction and the energy of primary gamma rays given in percent. The logarithm of the amplitude is abbreviated as lgAmp in this plot. This histogram results from a training process corresponding to a zenith angle of 20° , an azimuth angle of 0° , an offset angle of 0.5° and a MuonPhase of 200.	65
4.6	Correlations between the input parameters to the MLP network used to differentiate between gamma ray- and hadron-induced shower images given in percent. This histogram results from a training process for a zenith angle of 20° , an azimuth angle of 0° , an offset angle of 0.5° and a MuonPhase of 200.	70
4.7	Input parameter distributions for the particle discrimination network. Blue histograms represent gamma-ray air shower parameters, red histograms represent the OFF data parameters. The histograms result from a training process corresponding to a zenith angle of 20° , an azimuth angle of 0° , an offset angle of 0.5° and a MuonPhase of 200.	71
4.8	Distributions of the discriminant variable ζ for signal (blue) and background (red) events. The histograms result from a training process for a zenith angle of 20° , an azimuth angle of 0° , an offset angle of 0.5° and a MuonPhase of 200.	72
4.9	Two-dimensional distribution of gamma-ray air shower parameters. The abscissa is the corresponding input parameter of the neural network performing the particle separation, the ordinate is the discriminant variable ζ . Units are similar to those given in Fig. 4.7.	73

List of Figures

4.10	Discriminant variable ζ as a function of the simulated energy E_{True} . The points denote the average ζ value per bin in logarithmic energy. Vertical error bars represent the standard deviation of the ζ distribution around the average value per bin in energy. Only shower images passing the basic cuts introduced in Sec. 4.3 are considered in this plot.	74
4.11	Sketch of the camera plane with indicated ON and OFF regions. Each of these regions is displaced from the camera centre by an offset o . The ON region is centred at the location of the previously known position of the (potential) gamma-ray source. The radius of each region is called Θ_0 . The number of OFF regions depends on the choice of Θ_0	75
4.12	Significance S as a function of the ζ_0 and Θ_0^2 cut values. The colour code represents the values on the vertical axis. This surface results from an optimisation procedure performed with a size cut of $A_0 = 60$ p.e.	77
4.13	Illustration of the interpolation algorithm. In this example the displacement value δ , introduced in Sec. 4.3, at the current observation position θ_C, φ_C and o_C needs to be determined. For each of the neighbouring angle configurations consisting of triples of the angles $\theta_{\text{MC}}^{1/2}, \varphi_{\text{MC}}^{1/2}$ and $o_{\text{MC}}^{1/2}$, the neural networks that have been trained for these angles are used to determine the corresponding δ values. In this sketch the brightness and the size of the spheres in each corner represent the respective value of δ	79
5.1	Reconstructed directions in the camera plane for shower images induced by simulated gamma rays (<i>left</i>) and by real, charged cosmic ray particles (<i>right</i>). The gamma rays were simulated at a zenith angle of 20° , an azimuth angle of 0° , an offset of 0.5° and a MuonPhase of 200. The distribution on the right results from 23 runs during which source-free regions of the sky were observed. These runs were conducted at zenith angles between 10° and 25° and azimuth angles between 110° and 250° . Most of these runs belong to MuonPhase 200, only four runs belong to MuonPhase 201.	82
5.2	Angular resolution as a function of the energy of simulated gamma rays. The curves for simulated gamma-ray source positions at azimuth angles of 0° (<i>left</i>) and 180° (<i>right</i>) and zenith angles of $20^\circ, 40^\circ$ and 55° are shown. The offset of the direction of the gamma-ray source from the observation direction is 0.5° , and the MuonPhase is 200 in all cases.	83
5.3	Reconstruction bias of the parameter δ needed for the direction reconstruction as a function of the true value of δ inferred from Monte Carlo simulations (<i>left</i>) and as a function of the simulated energy of the primary gamma ray (<i>right</i>). Error bars indicate the width of the bias distribution per bin on the abscissa. The plots correspond to a simulated zenith angle of 55° , an azimuth of 0° , an offset of 0.5° and a MuonPhase of 200.	84

- 5.4 Reconstructed energy E_{Reco} as a function of the simulated gamma-ray energy E_{True} . The dashed line represents the identity relation. Colours denote the number of events per bin. The shown distribution corresponds to a zenith angle of 20° , an azimuth angle of 0° , an offset angle of 0.5° and a MuonPhase of 200. 86
- 5.5 Energy reconstruction bias curves (*top left* and *top right*) and energy resolution distributions (*bottom left* and *bottom right*) for several zenith angles as indicated in the legends. Plots on the left (*right*) side correspond to azimuth angles of 0° (180°). The MuonPhase is 200 in all cases. Error bars denote the statistical error on the bias and on the resolution, respectively. 88
- 5.6 *Left*: Efficiency with which signal-type and background-type air shower images pass the cut on the ζ variable as functions of the cut parameter ζ_0 . In this plot also the purity is shown, which is defined as the fraction of signal events in the total sample of events passing the cut on ζ_0 . A ratio of the input number of signal events to the input number of background events of 10^{-3} was assumed. *Right*: Efficiency with which background events pass the cut on the ζ variable as a function of the signal efficiency. All distributions correspond to a zenith angle of 20° , an azimuth angle of 0° , an offset angle of 0.5° and a MuonPhase of 200. 89
- 5.7 Effective area as a function of the simulated gamma-ray energy for three different zenith angles and an azimuth angle of 0° (*left*) or 180° (*right*). All distributions correspond to an offset angle of 0.5° and a MuonPhase of 200. 91
- 5.8 Radial acceptance in arbitrary units, scaled to have maximum values equal to one, as a function of the squared angular distance between the reconstructed direction of an air shower and the centre of the camera $\Delta\Psi$. Distributions are shown for four different zenith angles. Observational data from observations at various azimuth angles and MuonPhases contribute to each of these distributions. 93
- 5.9 Differential and integrated sensitivity as a function of the reconstructed energy for a zenith angle of 20° , an azimuth angle of 180° , an offset angle of 0.5° , a MuonPhase of 200 and an observation time of 50 h. Curves obtained from the MonoReco algorithm are shown together with the distributions resulting from the H.E.S.S.-I Model++ analysis. Also the differential sensitivity of the *Fermi*-LAT satellite experiment for ten years of operation for detections of sources in the galactic plane is shown. . . . 97

List of Figures

5.10 *Top left:* Significance distribution obtained with the ring-background technique. The black cross marks the position of the Crab pulsar. The inset in the lower left corner represents the PSF for comparison. *Top right:* The same distribution, with the difference that three regions, including the position of the Crab Nebula, are excluded. *Bottom left:* Distribution of the squared angular distances of the reconstructed directions from the test position for ON (black) and OFF events (red) obtained from the ring background algorithm. The numbers given in the inset are explained in the main text. *Bottom right:* One-dimensional significance distributions obtained from the top-left and top-right distributions. 99

5.11 Differential energy spectrum obtained from observations of the Crab Nebula. Data points and the green uncertainty band correspond to the analysis conducted with the MonoReco algorithm, the purple line shown for comparison represents the spectrum published by the H.E.S.S. collaboration in 2006. The lower panel shows the fit residuals for the MonoReco analysis. Residuals are calculated as the relative deviation of the fit function from the data points. 101

6.1 Visibility of PSR B1259–63/LS 2883 around the 2014 periastron in hours per night with zenith angles θ smaller than 50° and 45° . The time of the periastron passage is marked with a short-dashed line, the times of the disk crossings, here defined as the times the radio pulsations disappear, are marked by long-dashed lines. For reference, the monthly-binned fluxes above energies of 1 TeV obtained from a re-analysis of archival data around the previous periastron passages indicated in the legend are shown as well. Also the names of the periods during which observations were conducted in 2014 are displayed. 104

6.2 *Top left:* Significance distribution obtained from a monoscopic analysis of PSR B1259–63/LS 2883 data. The black cross marks the position of the source. The dashed blue circle indicates the ON region for both the reflected-background and the ring-background analysis techniques. Grey and green circles mark the corresponding OFF regions. The red dashed circle indicates the region used to calculate the Θ^2 distribution. The yellow dashed line represents the galactic plane. The PSF for this analysis is shown in the inset. *Top right:* The corresponding excluded significance map. *Bottom left:* Significance distribution for both the excluded and the non-excluded significance maps. *Bottom right:* Θ^2 distribution for ON events (black) and OFF events (red) obtained from the ring-background analysis. 107

6.3 Participation fraction of each pixel in the CT 5 camera in the events which triggered the camera. The images correspond to observation runs performed before (*left*) and after (*right*) the pixel gain adjustment. Malfunctioning pixels are displayed as blank fields. The drawers B5 and K8 are indicated by the respective labels. 108

6.4	$t_L = 9.3$ h	110
6.5	$t_L = 9.3$ h	110
6.6	$t_L = 37.1$ h	110
6.7	$t_L = 13.4$ h	110
6.8	$t_L = 50.5$ h	110
6.9	$t_L = 37.1$ h	110
6.10	$t_L = 22.7$ h	110
6.11	$t_L = 59.8$ h	110
6.12	Excluded sky maps obtained from analyses of 21 observation runs each. Thus the corresponding live times are (9.4 ± 0.1) h each, as indicated in the captions. The drawer B5 was non-functional during the runs used to create the maps shown in the <i>top</i> row, while it was functional for the plot in the <i>bottom</i> row. The <i>top left/right</i> plots correspond to the pre-/post-gain adjustment phases. The <i>bottom</i> row plot uses data from the post-gain adjustment phase.	111
6.13	Excess events resulting from a monoscopic analysis as a function of Θ^2 . The red line is the radial PSF function following the King profile introduced in Eq. (5.1) scaled such that the integral of this function in the first bin equals the number of excess events in this bin. The black curve represents the same function added to a linear function. The excess distribution was fitted with the resulting function as described in the main text.	112
6.14	Average NSB rate per pixel, mapped to coordinates in the sky. No smoothing algorithm was applied. White, dashed circles illustrate the sizes of the circles defined by the nominal distance cut around the two observation positions.	114
6.15	<i>Left</i> : Excluded significance map obtained from a stereoscopic analysis. See Fig. 6.2 for an explanation of the different elements shown in the plot. <i>Right</i> : Excluded and non-excluded significance distribution resulting from the stereoscopic analysis.	116
6.16	Distributions of the number of events in the ON and OFF regions, scaled to equal exposure, and the number of excess events in the ON region as functions of the reconstructed energy. The short-dashed grey line indicates the position of the energy threshold of the monoscopic analysis presented in this work, the long-dashed line indicates the position of the lowest threshold obtained from H.E.S.S. I analyses in the past.	117
6.17	Number of events in the reflected-background OFF regions, scaled to correspond to the total exposure. The numbering of the regions given on the abscissa of the plot on the <i>left</i> is based on their positions in the sky. Counting starts in the north-western corner and is to be continued in an anti-clockwise direction. In the plot on the <i>right</i> , the same number of events in the OFF regions is shown as a function of the declination of the centres of the regions. The dashed blue line represents the best-fit linear function.	118

List of Figures

- 6.18 Differential photon spectrum obtained from a monoscopic analysis of PSR B1259–63/LS 2883 data. The blue line represents the best-fit power law, the green uncertainty band represents the statistical uncertainty of the spectral shape. The arrow represents a flux upper limit. The violet line represents the best-fit power-law function for data points obtained from a stereoscopic analysis of the 2014 data. The fit residuals are displayed in the lower panel as relative deviation of the flux points from the fit function. 120
- 6.19 Integrated photon fluxes above energy thresholds of 200 GeV (*top left*), 600 GeV (*top right* and *bottom left*) and 1 TeV (*bottom right*) with a night-wise binning (*bottom left*) or a weekly binning (all other plots). Negative fluxes result from negative estimates of the number of excess photons. The times of the disk crossings and the periastron are marked by dashed grey lines as explained in the caption of Fig. 6.1. The time during which the Fermi flare occurred is indicated by the shaded grey area. H.E.S.S. I data from previous observation campaigns was re-analysed as explained in the main text. Horizontal error bars represent the time range during which the fluxes are averaged. Two types of vertical error bars are shown. The smaller bars represent statistical uncertainties only, larger error bars represent the quadratic sum of statistical and systematic uncertainties as explained in the main text. The dashed blue line in the *top left* plot represents a fit with a constant of the data points in the time range covered by the fit function. 122
- 6.20 *Left*: Spectral index obtained from a monoscopic analysis of the 2014 data set as a function of time. *Right*: Spectral index as a function of the integrated photon flux above energies of 1 TeV. Results from analyses of data from all years were used as input for the latter plot. Data points were fitted with a constant value and, in case of the plot on the *right*, also with a linear function. Fit results are discussed in the main text. 128
- 6.21 Spectral energy distributions resulting from analyses of *Fermi*-LAT data obtained during the 2010 and 2014 flare periods by Caliendo et al. [93] and from a monoscopic analysis of the H.E.S.S. data from observation period P2014-06. Best-fit power-law functions are shown for all distributions individually. Upper limits were not considered during the fitting procedure. Due to the large statistical uncertainties, the reduced χ^2 values are $0.14/2 = 0.07$ and $0.38/2 = 0.19$ for the 2010 and 2014 *Fermi*-LAT data sets, respectively. In case of the H.E.S.S. data, this value is $9.5/13 = 0.73$. The grey, long-dashed line represents the best-fit power-law function of the two 2014 data sets. Results of this fit are discussed in the main text. . 129

6.22 *Panel a*: HE gamma-ray light curves measured by *Fermi*-LAT around the 2010 and 2014 periastra. The unit of the displayed flux above 100 MeV is $10^{-6} \text{ cm}^{-2} \text{ s}^{-1}$. *Panel b*: X-ray light curves obtained from all years between 2004 and 2014 from measurements with the experiments listed in the legends. The flux unit is $10^{-11} \text{ erg cm}^{-2} \text{ s}^{-1}$. *Panel c*: Equivalent width of the H_α line for the 2010 and 2014 periastra with either the SALT or the SAA0 telescopes. Taken from Chernyakova et al. [79]. 133

6.23 Energy fluxes above 1 TeV obtained from analyses of data taken around all periastron passages observed with the H.E.S.S. telescopes. Flux points are converted to energy fluxes from those shown in Fig. 6.19d. In addition, energy flux predictions obtained from the models by Zabalza et al. [177] and Khangulyan et al. [175] are displayed. The models labelled Khangulyan and Khangulyan2 differ only by the choice of the spectral index of the VHE electrons, as explained in the text. These indices are 2.23 and 2.3, respectively. 136

List of Tables

2.1	Overview over the five binary systems known to emit VHE gamma rays, together with two newly identified gamma-ray binary candidates listed in the two bottom rows. P_{orb} is the orbital period of the binary. Adapted from Dubus [45].	16
4.1	Angles specifying the directions of the simulated gamma rays used in the presented reconstruction algorithm. θ is the zenith angle, φ is the azimuth angle and o is the offset angle. Also the MuonPhases are listed. See the main text for a definition of these quantities. Simulations for all possible combinations of these values are used in this work.	53
4.2	List of input parameters to the MLP network used for the reconstruction of the direction of gamma rays together with the correlation coefficients ρ introduced in Eq. (4.6). The listed variables are introduced in the main text. The correlation coefficients describe the correlation of the input parameters with the output parameter δ . The given variable ranking and the correlation coefficients in particular are valid for a training configuration corresponding to a zenith angle of 20° , an azimuth angle of 0° , an offset angle of 0.5° and a MuonPhase of 200.	64
4.3	List of input parameters to the MLP network used for the reconstruction of the energy of gamma rays together with the correlation coefficients ρ introduced in Eq. (4.6). The listed variables are introduced in the main text. The given variable ranking and the correlation coefficients in particular are valid for a training configuration corresponding to a zenith angle of 20° , an azimuth angle of 0° , an offset angle of 0.5° and a MuonPhase of 200.	67
4.4	List of input parameters to the MLP network used for the discrimination between gamma-ray and hadronic air showers. The listed importance I is introduced in Eq. (4.12). The given variable ranking and the importance values are valid for a training configuration corresponding to a zenith angle of 20° , an azimuth angle of 0° , an offset angle of 0.5° and a MuonPhase of 200.	69
4.5	Optimised cut values for the three cut parameters A_0 , ζ_0 and Θ_0^2 . These values are derived using a zenith angle of 20° , an azimuth angle of 0° , an offset angle of 0.5° and a MuonPhase of 200.	78

List of Tables

6.1	Number of available good-quality runs N_{Runs} , selected using the criteria for monoscopic and stereoscopic analyses detailed in the main text, corresponding live times t_L and the mean zenith angles of the ON region $\bar{\theta}$. Numbers are given for each observation period and also summed to give the total value.	105
6.2	Quality criteria which have to be met in order to pass the run selection for each telescope and for the entire array for monoscopic, stereoscopic and H.E.S.S. I-type analyses. The criteria are explained in the main text.	105
6.3	Sky maps resulting from monoscopic analyses with exclusion regions for different groups of runs, separated by the state of the drawer B5 and the time at which the observation runs used to create the sky maps were performed relative to the gain adjustment campaign. The corresponding live times t_L are given in the captions.	110
6.4	Parameters of the function defined in Eq. (6.1), which describes the excess distribution as a function of Θ^2 . Parameters without errors are fixed, as described in the main text.	113
6.5	Spectral index Γ resulting from analyses of data obtained from different observation campaigns and, in case of the 2014 data set, from either a monoscopic or a stereoscopic analysis of the data. The spectral indices for the 2004–2010 data sets are taken from [53].	121
6.6	Maximum VHE gamma-ray luminosities $L_{\text{VHE}}^{\text{max}}(E > E_0)$ for energies exceeding the threshold energy E_0 . Values were derived from the monoscopic analysis of the 2014 data set. The maximum energy up to which fluxes are taken into account is 30 TeV. The obtained luminosities are also given as fractions of the pulsar’s spin-down power \dot{E} and the stellar luminosity L_{star} . Only statistical uncertainties are given. A distance to the system of 2.3 kpc was assumed.	132

Selbstständigkeitserklärung

Ich erkläre, dass ich die Dissertation selbständig und nur unter Verwendung der von mir gemäß §7 Abs. 3 der Promotionsordnung der Mathematisch-Naturwissenschaftlichen Fakultät, veröffentlicht im Amtlichen Mitteilungsblatt der Humboldt-Universität zu Berlin Nr. 126/2014 am 18.11.2014 angegebenen Hilfsmittel angefertigt habe.

Berlin, den 30.09.2016,
Thomas Murach